TECHNISCHE UNIVERSITÄT MÜNCHEN
Lehrstuhl für Angewandte Mechanik

Design and Realization of a Humanoid Robot for Fast and Autonomous Bipedal Locomotion

Entwurf und Realisierung eines Humanoiden Roboters für Schnelles und Autonomes Laufen

Dipl.-Ing. Univ. Sebastian Lohmeier

Vollständiger Abdruck der von der Fakultät für Maschinenwesen der
Technischen Universität München zur Erlangung des
akademischen Grades eines

Doktor-Ingenieurs (Dr.-Ing.)

genehmigten Dissertation.

Vorsitzender: Univ.-Prof. Dr.-Ing. Udo Lindemann

Prüfer der Dissertation:

1. Univ.-Prof. Dr.-Ing. habil. Heinz Ulbrich
2. Univ.-Prof. Dr.-Ing. Horst Baier

Die Dissertation wurde am 2. Juni 2010 bei der Technischen Universität München eingereicht und durch die Fakultät für Maschinenwesen am 21. Oktober 2010 angenommen.

Colophon

The original source for this thesis was edited in GNU Emacs and AUCTeX, typeset using PDFLaTeX in an automated process using GNU make, and output as PDF. The document was compiled with the LaTeX 2$_\varepsilon$ class AMdiss (based on the KOMA-Script class scrreprt). AMdiss is part of the AMclasses bundle that was developed by the author for writing term papers, Diploma theses and dissertations at the Institute of Applied Mechanics, Technische Universität München. Photographs and CAD screenshots were processed and enhanced with THE GIMP. Most vector graphics were drawn with CorelDraw X3, exported as Encapsulated PostScript, and edited with psfrag to obtain high-quality labeling. Some smaller and text-heavy graphics (flowcharts, etc.), as well as diagrams were created using PSTricks. The plot raw data were preprocessed with Matlab. In order to use the PostScript-based LaTeX packages with PDFLaTeX, a toolchain based on pst-pdf and Ghostscript was used. The bibliography was prepared with biblatex.
The fonts in this thesis are the light versions of the Kp-Fonts by the Johannes Kepler project.

Author contact: `robots@loh-fi.de`

This thesis is also available as a printed book published by
Verlag Dr. Hut München, Germany (ISBN 978-3-86853-734-5).

To my parents

The danger of the past was that men became slaves. The danger of the future is that men may become robots. True enough, robots do not rebel. But given man's nature, robots cannot live and remain sane, they become 'Golems,' they will destroy their world and themselves because they cannot stand any longer the boredom of a meaningless life.

—Erich Fromm, *The Sane Society*

Abstract

This thesis covers the mechatronic conception, design and realization of a humanoid walking robot. Weighing approximately 60 kg, the robot stands 180 cm tall and has 25 actuated degrees of freedom in a redundant configuration. The mechanical structure is characterized by the consistent lightweight design with high effective stiffness. The lightweight servo actuators combine high-dynamic brushless servo motors with precision gearings and sensors into a compact package. Moreover, the resultant inertia of the legs is minimized by a sophisticated design of the structure and drive mechanisms, resulting in a superior acceleration behavior. The sensor layout comprises angular sensors for direct measurement of the joint angles, a high-precision inertial measurement system and force/torque sensors in the feet. Using the trajectory generation and control system which is not in the scope of this work, the current speed of locomotion is 3.34 km/h.

Keywords: humanoid robots, anthropomorphic robots, legged locomotion, mechatronics, robot design, sensors

Zusammenfassung

Diese Arbeit beschreibt die mechatronische Konzeption, Konstruktion und Realisierung eines humanoiden Laufroboters. Der Roboter ist 180 cm groß, wiegt zirka 60 kg und verfügt über 25 angetriebene Freiheitsgrade in einer redundanten Konfiguration. Die mechanische Struktur ist durch den extremen Leichtbau mit hoher effektiver Steifigkeit charakterisiert. Die hochdynamischen Gelenkantriebe kombinieren bürstenlose Servomotoren, Untersetzungsgetriebe und Sensorik zu kompakten Einheiten. Daneben werden die Massenträgheitsmomente der Beine durch konstruktive Maßnahmen minimiert. Daraus resultiert ein überragendes Beschleunigungsverhalten. Neben Winkelsensoren zur direkten Messung der Gelenkwinkel verfügt der Roboter über ein hochgenaues inertiales Messsystem und Kraftsensoren in den Füßen. Mit dem Bahnplanungs- und Regelungssystem, das nicht Bestandteil dieser Arbeit ist, konnte bisher eine Maximalgeschwindigkeit von 3,34 km/h erreicht werden.

Stichworte: humanoide Roboter, anthropomorphe Roboter, zweibeiniges Laufen, Mechatronik, Konstruktion, Sensorik

Acknowledgments

This thesis summarizes my research carried out at the Institute of Applied Mechanics, Technische Universität München. Developing the humanoid robot *Lola* almost from scratch has been a unique opportunity and certainly one of the biggest challenges in my life so far. Many people have contributed to this thesis and I would like to use the opportunity to express my gratitude to some of them.

First and foremost I want to express my deep and sincere gratitude to my advisor Professor Heinz Ulbrich for the excellent research environment and giving enough freedom for own creativity. His patience and irrefutable confidence in my skills were beneficial for the success of this research.

I also wish to express my warm and sincere thanks to Professor Friedrich Pfeiffer, the former head of the institute, for a lot of good advice and ideas and many helpful discussions.

I warmly thank our academic director, Dr. Thomas Thümmel, for his support and continuing commitment to the robotics group. Thomas managed our project resources and largely kept us free from most administrative and formal burdens.

Starting off with only two doctoral candidates, the *Lola* project was divided simply into “Software” and “Hardware.” I am particularly indebted to Thomas Buschmann, my co-worker and good friend, who took over the “Software” part. His theoretically accurate and thorough works on the robot simulation and controller were one of the foundations for the success of the project. To me, working together with Thomas was a stroke of luck as our ways of thinking and working were quite similar and, where not, complemented each other.

I really need to thank Markus Schwienbacher and Valerio Favot who joined the team in a later project phase. In his Diploma thesis Markus developed, assembled and calibrated the force/torque sensors with enthusiasm and great attention to detail. I appreciate his efforts in resolving *Lola*’s teething problems. Markus, thank you so much for the fruitful discussions and competent suggestions! Valerio tested the PCBs for the local controllers and wrote all the code for them. Also, special thanks are due to Mathias Bachmayer, who developed the DSP boards for *Lola*’s decentralized controllers.

The official presentation of *Lola* at the *HANNOVER MESSE 2010* was the grand finale before turning in this dissertation. Regarding our trade fair presence, I thank Alexander Ewald for taking over all the organizational stuff. And my thanks go to the developers of *Lola*’s visual perception system, Dr. Felix von Hundelshausen and Gerhard Rohe from the Institute of Autonomous Systems Technology, University of the Bundeswehr, München, for the pleasant cooperation.

During my first year at the institute I have had the pleasure to work with Dr. Klaus Löffler, the developer of *Johnnie*’s balance controller. Klaus shared the office with me and has always been a competent and excellent advisor as I took my first tentative steps into the field of humanoid robotics. Thank you for the collaboration

during the countless public performances of *Johnnie* in 2003/04. The designer of *Johnnie*'s mechatronic system, Dr. Michael Gienger, had already left the institute before I started. Nevertheless, he was a competent advisor and always there to discuss about biped robots. Klaus and Michael, your results and experience were more than helpful and contributed substantially to this research!

I warmly need to thank Dr. Andreas Zagler for getting me excited about robotics and for encouraging me to take up this position.

The countless customized mechanical and electronic components would not have been possible without the enthusiasm and willingness of the institute's mechanical and electronic workshops. My sincere thanks are due to Wilhelm Miller, Walter Wöß, Simon Gerer, Philipp Schneider and Tobias Schmid. I very much appreciated their amazing skills to machine even the most complex parts with unparalleled precision. Until his retirement, Walter was a great help during the assembly of *Lola*. Wilhelm Miller, the former manager of the mechanical workshop, deserves a special mention. He fostered the manufacturing with optimism and never ending perseverance. He was always there to talk about my ideas and solve any unsolvable problems concerning precision mechanics. I have fond memories of numerous discussions—be it technical or non-technical. Sadly, he was not given the time to see *Lola* walking: he passed away during the first weeks of assembly. I am also greatly indebted to our electronics engineer, Georg Mayr, for numerous helpful discussions and for developing most of the electronics hardware. His experience and openness for my ideas were beneficial.

For this dissertation I would like to thank my proof-readers: Michael, Markus, Thomas Buschmann, Dr. Martin Schwaiger and Valerio for their time, interest and many helpful comments.

I would also like to thank the other two members of my dissertation committee, the second advisor Professor Horst Baier and the chairman Professor Udo Lindemann, for their time and insightful questions.

I gratefully acknowledge the funding sources that made my dissertation possible. For most of the time I was funded by the German Research Foundation (DFG) within the project-cluster „Natur und Technik Intelligenten Laufens"(PAK-146, grant UL 105/29).

Putting a lot of effort into sophisticated hardware design is very expensive and makes it difficult for a small university group like ours to compete with larger research groups and companies with considerable financial support. I like to thank all companies that supplied us with customized components to very good conditions. I particularly thank Arne Laugwitz and his colleagues at ACTech GmbH, Freiberg, who manufactured the investment castings. I appreciated their collaboration and enthusiasm to pushing the limits of current casting and machining technologies. *Lola*'s leg architecture would not have been possible without their generous support.

Finally, in deep gratitude I want to thank my parents, Gertraud and Hans, for their never-ending love, encouragement and support in all my efforts.

And most of all for my loving, encouraging and patient wife Veronika who reminded me that there is a life besides research. Her faithful support during the final stages of this dissertation is so appreciated.

Contents

1 Introduction

> *In the Fifties, it was predicted that in 5 years robots would be everywhere. In the Sixties, it was predicted that in 10 years robots would be everywhere. In the Seventies, it was predicted that in 20 years robots would be everwhere. In the Eighties, it was predicted that in 40 years robots would be everywhere . . .*
>
> —Marvin Minsky

No matter whether one believes in God's creation or theory of evolution: everyone will agree that nature is fascinating and in a sense "perfect." We are surrounded by highly developed creatures that are fully adapted to their environment and able to react to any kind of environmental influence. What we take for granted by nature is extremely difficult to realize in technical systems. For example, the complexity of everyday tasks like "going straight on"—"put one foot in front of the other . . . just walk!" is anything but simple! Accordingly, interaction between the "walking tool" leg and the body is highly complex: the body must be kept in balance at any time; environmental influence such as wind or the nature of the walking surface must be taken into consideration; the goal is to be focussed, potential obstacles must be identified and alternative paths must be assessed.

The term "robot" (Czech for "worker") in its today's meaning was invented in 1920 by the Czech author KAREL ČAPEK He wrote satires on technological progress. In his fictional play "R.U.R.—Rossum's Universal Robots," the first robots were shaped like humans and created for factory work [72]. Eighty-nine years later, human-shaped robots are still rare, although the number of research groups worldwide has increased exponentially during the recent years. Some Japanese companies have been conducting research on humanoid robots for a long term. They began delivering them in 2004 as human companions for performing typical everyday tasks. But, according to a study of the International Federation of Robotics [80], only about 100 are in use, most of them in research laboratories. Recent studies notwithstanding acknowledge that humanoid service robots might be an emerging application area in the near future [80, 150]. The anthropomorphic structure is one reason why such devices are ideal general-purpose robots to assisting humans at everyday tasks: the human-like structure allows them to easily operate in and interact with human-built environments. Other scenarios include medical engineering and prosthetics, the entertainment industry and academic education and research. For all such tasks in production, office or home environments robust, fast and agile locomotion is a basic skill. Moreover, research on walking robots can be seen as a driver of technology in the field of mechatronics, pushing lightweight drive systems and components, sensors, and automatic control engineering.

Despite extensive research in the fields of biomechanics and movement sciences, the question how humans solve the highly complex problem of three-dimensional bipedal locomotion with unparalleled robustness is not well understood to this day. Although the biomechanics of human walking and running has been investigated quite well [129, 142], the mechanisms of balance control are not very well understood. For a long time posture control during standing and walking has been considered an automatic or reflex-controlled task. However, recent research suggests that postural stability is also achieved by high-level neural feedback mechanisms that primarily utilize visual, vestibular, and proprioceptive sensory information [143].

The traditional approach to building a walking robot combines classical control systems engineering with a sophisticated hardware system which is characterized by high performance and accuracy. It does not try to copy biological systems, rather, it benefits from the advantages of well-proven technology and design methods. The fundamental difference between technical and biological systems brings up the question whether the hardware and control design of a versatile, multi-purpose humanoid robot can actually benefit from the biological sciences. From the author's point of view, biological designs currently serve as a source of inspiration. The aim is to collect suggestions for technical designs, test them for transferability into technical systems, and realize them using state-of-the-art mechatronics technology.

Research on humanoid robots is more and more focusing on complex, higher-level scenarios such as human-robot interaction and manipulation. Regarding the locomotion capabilities of biped robots, however, there are still numerous unsolved problems. For example, higher speeds of locomotion and flexible motion generation still remain challenging. Since of them do not necessarily require the development of new hardware, the highest degree of attention and development is often given to the control system, while almost no importance is attached to the mechatronic hardware and its significance for control performance.

The review of current humanoid robot projects in Section 1.1 shows certain "convergence" in the hardware design and component selection, suggesting that the "ideal" architecture is found. However, research on reliable biped robots with high performance and human-like walking capabilities still faces numerous problems regarding the kinematic structure, mass distribution, actuators and drive mechanisms, and sensor layout. Moreover, robots that effectively combine the advantages of full actuation (Section 1.1.1) and the biologically inspired approach of passively compliant structures (Section 1.1.3) is not in sight.

In conclusion, balance control and robot hardware must be seen as tightly coupled parts of a highly integrated mechatronic system. The judicious and concurrent design of both parts is paramount to the realization of a high-performance walking robot.

1.1 Literature Review

Two fundamentally different approaches are dominating in the bipedal locomotion community. Besides fully actuated humanoid robots using classical control theory

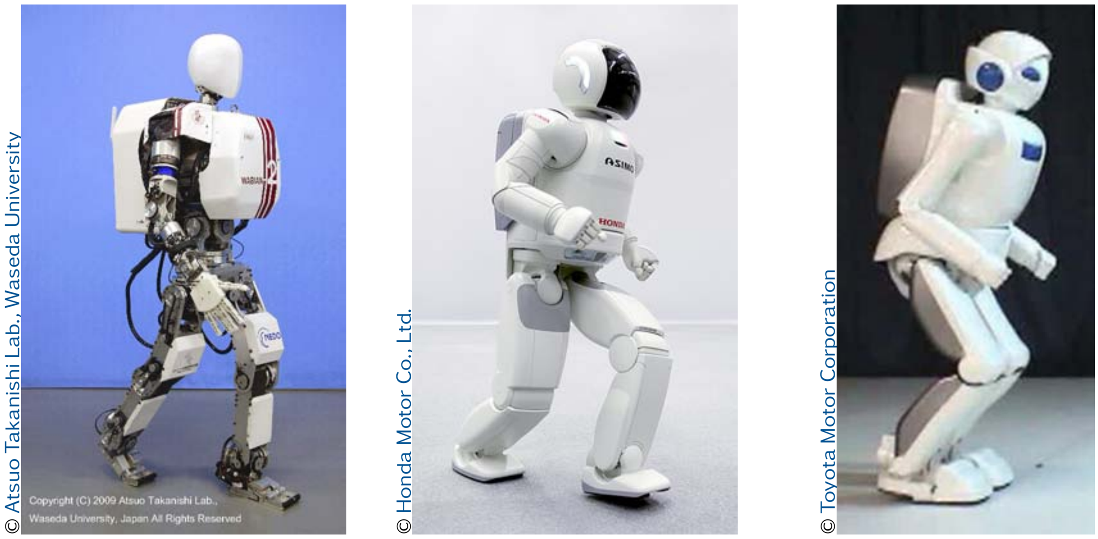

(a) Wabian-2R (b) Asimo (c) Toyota running robot

Figure 1.1: Humanoid robots, part 1

and mechatronic design, another concept based on the idea of passive dynamic walking is emerging. Although humanoid robots are a comparatively new self-contained research field, the literature is tremendous. Without attempting to review all research projects, this section describes the ones that are considered to be the most relevant. More specific details on the servomechanisms, sensors and electronics are given throughout this work. Aiming for a comprehensive review, the *Springer Handbook of Robotics* provides two contributions on legged [85] and humanoid [97] robots. Gienger [46] provides interesting statistical evaluations of relevant characteristics of current robot platforms.

1.1.1 Fully Actuated Biped Walking Robots

Speaking of fully actuated systems, significant advances in enabling technologies (sensors, drive and computer technology) has allowed the realization of numerous humanoid robots with advanced capabilities.

The pioneering work in the field of fully actuated biped robots was achieved by Kato at Waseda University, Japan. In the year 1973 he created *WABOT-1*, the world's first full-scale anthropomorphic robot [106]. From 1986 to 1990, a hydraulic biped robot was developed within the *WL-12* family. The robot has a trunk and a waist with two degrees of freedom (DoFs) for more natural motions [106]. In 1999, Yamaguchi et al. [204] presented the 15-DoF robot *WL-12RVI* that employs a complex foot mechanism with elastic pads to absorb impact and contact forces. Using these feet, the robot was able to walk over uneven terrain. Waseda's current robot generation, *Wabian-2* (41 DoFs, size 1.53 m, mass 64.5 kg), shows some specialties in its kinematic configuration: unlike other robots the legs have seven DoFs with internal/external rotation axes of the ankle joints, allowing rotation of the legs relative to the feet along the vertical axis [130]. The developers expect improved gait pattern generation as the spatial orientation of the knee joint and foot is independent. Especially passing over obstacles, through narrow spaces, or climbing a ladder are expected to be simplified. Also, *Wabian-2* is equipped with a two-DoF pelvis joint and an additional two-DoF joint in the upper body [135]. Using the pelvis joint, the upper body can be bent forward, backward and sidewards. The refined version *Wabian-2R*, Figure 1.1*a*, is equipped with passive toe joints that enable walking with stretched knees and heel-off gait patterns [132]. Furthermore, *Wabian-2R* is able to mimic various human motions and can be used for testing rehabilitation devices. The robot can provide quantitative information about the effectiveness of these instruments. The top speed of the *Wabian* robots is currently 0.75 km/h. Sugahara et al. [176] develop the multi-purpose locomotion system *WL-16* where the legs are designed as Stewart platforms. The robot is able to carry a heavy payload and suitable as a locomotion platform for humans.

One of the most advanced humanoid robots is being developed by Honda Motor Corporation. To the surprise of all research groups Honda presented the outstanding robot *P2* after 10 years of secret research and several prototypes [65] in December 1996. *P2* is 1.82 m tall and weighs 210 kg. Having a total of 30 DoFs, it was the first self-contained robot that is able to walk, climb stairs and perform simple manipulation tasks. Besides encoders for joint position measurement, the sensor layout comprises fiber-optic gyroscopes, inclination sensors, ground reaction force sensors and four cameras. Its successor *P3* [64] was presented in 1997 (30 DoFs, size 1.60 m, mass 130 kg). In the year 2000, Honda presented the robot *Asimo*, Figure 1.1*b*, which was reduced in size and mass (26 DoFs, height 1.20 m, mass 52 kg). The control system architecture called "i-Walk" allows the robot to change its direction of movement arbitrarily and provides greater stability against unexpected disturbance. Besides a stereo vision system for dynamic environment detection, *Asimo* integrates speech recognition and is able to detect the speaker's location, enabling the robot to take over simple tasks in a human environment. The current research model *Asimo-R* (34 DoFs, height 1.30 m, mass 54 kg) employs additional DoFs in its arms and hands to extend the robot's manipulation capabilities. At the end of 2005 Honda announced that *Asimo-R* can *run* straight on and in a slalom course at maximum speeds of 6 km/h and 5 km/h, respectively. According to publicly available data[1], the maximum *walking* speed is 2.7 km/h. As its predecessors, *Asimo-R* relies on a highly accurate and responsive hardware which is improved by employing high-dynamic servo actuators with high performance and a lightweight yet rigid leg structure. Furthermore, the balance controller is extended by bending and twisting of the torso. In late 2009, Honda published some details on their research on walking and running, e. g., [185]. Using a robot with similar size as *Asimo*, the authors achieve running at 10 km/h. Although many details on the mechatronic system are not yet disclosed, these impressive results can be regarded as a proof of concept that fully actuated robots with rigid structure are capable of fast bipedal locomotion.

Until Honda's new top mark, Toyota's running robot, Figure 1.1*c*, used to be the fastest humanoid robot at a top speed of 7 km/h, but walking and running is only feasible on flat surfaces [178]. It has a total of 15 DoFs: each leg has seven

---

[1] `http://world.honda.com/ASIMO/technology/spec.html`, accessed on 05/30/2010

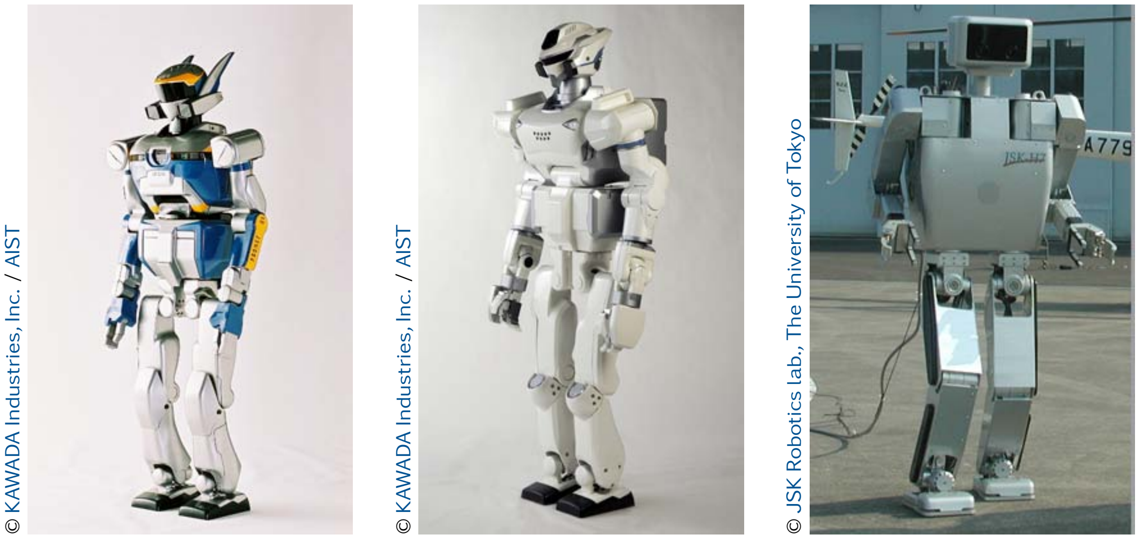
© KAWADA Industries, Inc. / AIST

© KAWADA Industries, Inc. / AIST

© JSK Robotics lab., The University of Tokyo

(a) HRP-2 (b) HRP-3 (c) H7

Figure 1.2: Humanoid robots, part 2

DoFs including an actuated toe joint and a one-DoF pelvis joint. The robot stands 1.30 m tall and weighs 50 kg. Toyota's research focuses on developing new forms of mobility for elderly care and assistance robots in manufacturing and household environments. The goal is to achieve close interaction with humans by exploiting morphological similarities of humans and humanoids. Notably, Toyota's running robot is, to the author's knowledge, the only robot that implements compliance control for absorbing the landing impacts without force or torque measurement in the feet and joints. Instead, controlled compliance of some joints is utilized. The landing impacts are attenuated by adjusting the feedback gains under the assumption of a flat ground [178].

The "Humanoid Robotics Project" (HRP) funded by the Japanese Ministry of Economy, Trade and Industry (METI) is definitely one of the largest humanoid robotics projects worldwide. The *HRP* robot hardware is developed in cooperation of the National Institute of Advanced Industrial Science and Technology (AIST) and Kawada Industries. The self-contained robot *HRP-2*, Figure 1.2*a*, has a total of 30 DoFs, including six-DoF arms, one-DoF hands, a two-DoF waist, six-DoF legs, and a two-DoF head with stereo cameras. The robot is 1.54 m tall and weighs 58 kg [95]. The angular workspace of the joints allows the robot to lay down on the floor and get up again. The three-DoF hip joint is a specialty within the kinematic structure of the robot: the adduction/abduction joint[2] are arranged very close to the sagittal plane of the robot, reducing the hip joint loading due to the small distance to the center of mass. However, the contribution of the adduction/abduction joints to increasing the step length is limited. Moreover, the resultant hip joint stiffness is determined by the cantilevered design with a single-side bearing of the flexion/extension axis. The top speed of *HRP-2* is $2.5\,\mathrm{km/h}$ [95]. Kajita et al. [87] present an experimental study of running motion using

---

[2] see Figure A.1 on page 176 for an explanation of the anatomical terminology

the 12-DoF leg module *HRP-2P*. The maximum running speed is considerably lower than the top speed of *HRP-2*. In another study on running, Kajita et al. [90] develop spring-loaded, passive toe joints for the 12-DoF leg module *HRP-2LT*. The successor model prototype *HRP-3P* stands 1.60 m tall and weighs 65 kg including batteries. The most important distinctions to *HRP-2* are additional DoFs in the arms and hands, making a total of 36 DoFs, and the sealed body shell, protecting the robot against ingress of liquid, solid foreign objects and dust [3]. Furthermore, the on-board PC unit is complemented by several decentralized computer nodes for motor control and sensor data processing. The computers are connected by a proprietary real-time Ethernet protocol. *HRP-2*'s actual successor is shown in Figure 1.2*b*. *HRP-3* is 1.61 m tall, weighs 68 kg and has a total of 42 DoFs [96]: the legs have six DoFs each, head and pelvis two DoFs each, and the arms and hands have seven DoFs and six DoFs, respectively, improving the manipulation capabilities. As its prototype, *HRP-3* has a dust-proof outer shell. The electronics architecture is modified: now, *HRP-3* has a centralized control system for the arms and head, while decentralized nodes are applied to the legs, pelvis and hands, using a CAN-based communication architecture [96]. In December 2009, Kaneko et al. [93] presented the "cybernetic human" *HRP-4C*. Standing 158 cm tall and weighing 43 kg (including batteries), the robot has 43 DoFs. The underlying technology (actuation, electronics, etc.) is basically identical to previous *HRP* models, but the proportions and appearance are very human-like.

The JSK lab at the University of Tokyo is another major robotics laboratory. The former robots *H5*, *H6* and *H7* [126] were built by Kawada Industries. The robots were planned as experimental research platforms for autonomous locomotion and whole-body motion [41]. The joint motion ranges are adjusted such that the robots can kneel down and climb stairs to maximum step height of 25 cm. Using the integrated stereo camera vision system of *H7* shown in Figure 1.2*c*, advanced path planning methods for locomotion in unknown environments with various fixed and movable obstacles were developed [127]. Nishiwaki et al. [128] implement actuated toe joints in the robots *H6* und *H7*. Walking speed increases significantly which is mainly due to reduced angular velocities in the knee joints. One major focus of current activities at JSK is developing technologies for multi-purpose household assistance robots. Using several *HRP-2* robots, which were partly developed at JSK and modified in some details, methods for whole-body motion planning and vision-based environment recognition are evaluated experimentally. Another focus is the development of whole-body musculoskeletal humanoids with flexible spines. The aim of this novel and—at this time—unique approach to designing humanoid robots is to realize human-like natural motion using a flexible spine. The "anatomy" of these robots is based on the human skeleton and manufactured from plastic by rapid prototyping techniques. All joints are driven by redundant tendon-shaped actuators, each of which is composed of a tension sensor and a spring-loaded motor-gear unit. Using the tension sensors, joint stiffness is adjustable. The latest robot *Kojiro* (height 1.40 m, mass 45 kg) has a total of 82 DoFs that are actuated by 109 spring-loaded motors [124]. *Kojiro*, Figure 1.3*a*, employs a new spherical shoulder joint mechanism [175]. The highly redundant actuation and sensor system of these multi-DoF robots with a highly

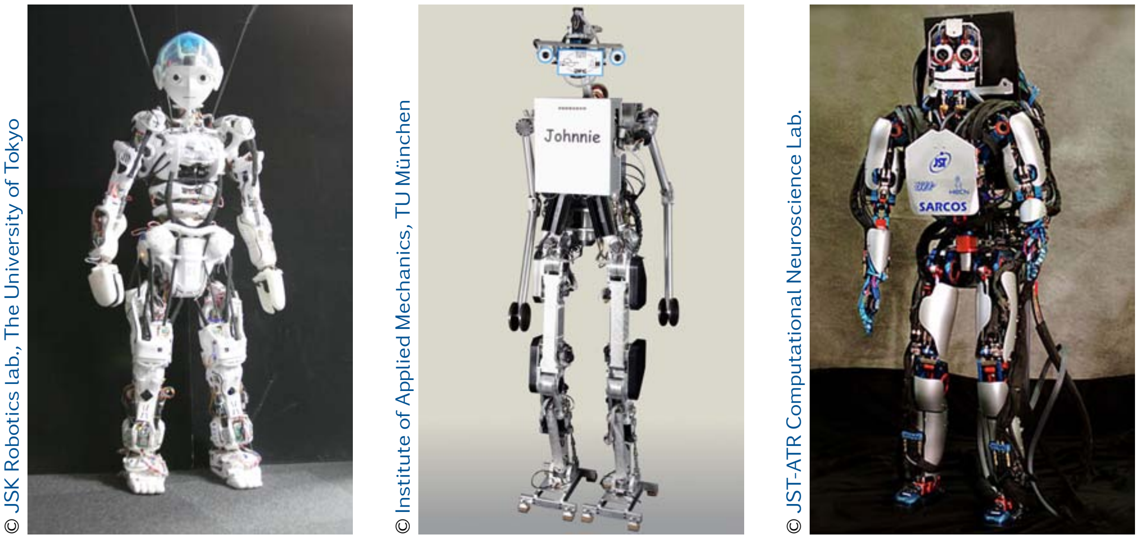
© JSK Robotics lab., The University of Tokyo
© Institute of Applied Mechanics, TU München
© JST-ATR Computational Neuroscience Lab.

(a) Kojiro *(b) Johnnie* *(c) CB-i*

Figure 1.3: Humanoid robots, part 3

complex structure is indeed challenging, both in building and control.

The biped robot *Johnnie*, Figure 1.3*b*, was developed by Gienger [46] and Löffler [109] at the Institute of Applied Mechanics, Technische Universität München, as part of the priority program "Autonomous Walking."[3] The goal was the realization of fast, dynamically stable walking on even and uneven ground. At a step length of 0.55 m, a maximum walking speed of 2.4 km/h was achieved. *Johnnie* is also able to take turns and climb up stairs. The second focus was autonomous, vision-guided walking. Using computer vision techniques that were developed by another institute [169], *Johnnie* was able to perceive its environment and to reactively adapt its step sequences to navigate obstacles and climb stairs. *Johnnie*'s proportions correspond to a male human with a body height of 1.80 m. The total mass is about 50 kg. The robot has 17 actuated joints: each leg has six DoFs, three in the hip, one in the knee and two in the ankle. The pelvis segment has one DoF about its vertical axis. For compensation of the overall momentum each shoulder incorporates two DoFs. However, the pelvis and shoulder adduction/abduction joints were mechanically blocked and not used in the gait patterns, so that 14 DoFs are actually used. Like most other biped robots, the joints are actuated by DC brush motors through Harmonic Drive gears. Only the ankle joints are actuated by parallel mechanisms with ballscrews [47]. *Johnnie* is autonomous to a far extent, only energy is supplied by cables. The joint angles and angular velocities are measured by incremental encoders on the motor shafts. *Johnnie* is equipped with two customized six-axis force/torque sensors in its feet. Upper body orientation and angular velocity are determined by a customized inertial measurement system composed of three gyroscopes and three accelerometers. Using a centralized on-board computer system, *Johnnie* is computationally autonomous. An external PC is necessary only for monitoring purposes and to submit basic operating

---

[3] The priority program SPP 1039 was funded by the German Research Foundation (DFG) from 1998–2003. A comprehensive overview of all projects is given in [145].

commands in case the vision system is not connected.

The Korea Advanced Institute of Science and Technology (KAIST) is currently working on its fourth generation of humanoid robots. The robot *HUBO* (developing name *KHR-3*) is an improved version of its predecessors *KHR-1* and *KHR-2* [100, 140]. *HUBO* weighs 56 kg and is 1.25 m tall. It has a total of 41 DoFs, including legs and arms with 6 DoFs each and five-DoF hands. Similar to *Johnnie*, all core technologies (servo actuators, force/torque sensors, inertial measurement system, power amplifiers) are custom developments. The robot employs a distributed real-time control system using CAN communication. The maximum walking speed of *HUBO* is 1.25 km/h [139]. KAIST's current robot *HUBO2* (40 DoFs, height 1.30 m, mass 45 kg) is being developed since 2008. Each leg and arm has six DoFs and seven DoFs, respectively. The pelvis joint has one DoF, the hands have ten DoFs each and the head has three DoFs in the neck. According to the project website[4], *HUBO2* can walk with stretched legs at 1.4 km/h and run at 3.3 km/h.

Measuring only 0.58 m, the robot *SDR-3X* [83] is not full-sized, still Sony's research activities on humanoid robots are notable. The robot weighs only 5 kg and has 24 actuated DoFs. As with the robot dogs *Aibo* Sony's marketing activities were focused on the entertainment area, which explains the size of the robot. The improved version *SDR-4X* with a total of 38 DoFs has been presented in 2004 and later renamed to *QRIO* [84]. *QRIO* is built with modular servo actuators, comprising a custom-developed brushless motor, planetary gears and control electronics. These so-called "intelligent servo actuators" [40, 82] are employed in three different sizes and seem to be optimized for mass production. *QRIO* can move arbitrarily but also sit down and get up and—as is well known—it was the world's first running biped at a speed of 0.83 km/h [84]. In 2006 Sony announced the discontinuation of *Aibo* and *QRIO* at the same time.

In Germany the development of the robot *BARt-UH* at the University of Hannover should be emphasized. *BARt-UH* (six DoFs, size 0.70 m, mass 4.5 kg) is a planar biped without upper body. It is capable of statically and dynamically stable walking. Each leg incorporates actuated joints in the hip, knee and ankle that are driven by DC brush motors through Harmonic Drive gears [5]. The maximum walking speed of *BARt-UH* is unknown. With a total of 12 actuated DoFs the robot *LISA* (height 1.24 m, mass 40 Kg) is a lower limb robot without any actuated DoFs in its upper body. Having three-DoF hip joints, one-DoF knee joints, two-DoF ankle joints and passive toe joints, the robot is able to walk in arbitrary directions. The joints are driven by DC brush motors through Harmonic Drive gears. A specialty of *LISA*'s kinematic structure is the hip joint, which is designed as a ball-and-socket joint with parallel actuation. All hip motors are attached to the upper body [70]. The sensor system comprises six-axis force/torque sensors in the feet and three inertial measurement systems on the trunk and thighs. *LISA* employs a distributed on-board computer system using CAN communication. The current robot *BART III* was presented in late 2009 [153]. The robot stands 1.25 m tall and weighs 35 kg. 19 active joints divide up into six DoFs per leg, three per arm and one in the pelvis. *BART III* employs absolute angular sensors in its joints, four load cells for measuring the ground reactions in each foot and an

---

[4] `http://hubolab.kaist.ac.kr/hubo(khr-4).php`, accessed on 05/30/2010

inertial measurement system in the upper body. The robot is again controlled by a distributed system comprising DSP-controlled power electronics and an external main controller which are connected by CAN bus.

Although discontinued at the end of 2002, the anthropomorphic biped robot *BIP2000* (size 1.80 m, mass 105 kg) developed at the French institute INRIA Grenoble is worth mentioning as it features some interesting details in its mechanical structure. *BIP2000* consists of two legs with six DoFs each and a three-DoF pelvis joint, making a total of 15 active joints [35]. All joints are actuated by DC brushless motors. Five joints are driven through Harmonic Drive gears, the other ones employ linear actuators based on planetary roller screws: the knee joint and hip joint flexion/extension axis are actuated by slider-crank mechanisms. Two-DoF parallel slider-crank mechanisms are applied to the ankle joint and parts of the pelvis joint. The joint angles are measured by resolvers on the motor shafts. Three load cells per foot allow the measurement of the vertical ground reaction force and two lateral moments. Two-axis inclinometers are mounted on the feet to measure their inertial orientation. The orientation of all other links including the upper body is then calculated by inverse kinematics. *BIP2000* is controlled by an on-board computer system based on VME-bus components.

A very sophisticated anthropomorphic robot with hydraulic actuation is designed by Sarcos Research Corporation for ATR Computational Neuroscience Laboratories, Japan. The robot *CB* is 1.58 m in height and 92 kg in mass [23]. It has an active head with seven DoFs, seven-DoF arms and legs, a three-DoF upper body and six-DoF hands, making 50 DoFs in total. The sensor layout is rather complex and includes position and velocity sensing at all joints, and torque sensors on the main joints of the arms, legs, torso and neck. Foot force sensors measure the ground reactions and two inertial measurement systems on the head and pelvis provide the orientations of the head and overall system, respectively. Walking control and force-based balance control run on an on-board computer system, any processing requiring substantial computing power (vision processing, etc.) are performed remotely on a cluster of PCs. The robot is supplied by an external hydraulic pump. The succeeding model *CB-i*, Figure 1.3*c*, has a total of 51 DoFs, measuring 1.55 m and weighing 85 kg. The joints are actuated either electrically (cameras), pneumatically (hands), or hydraulically (all other joints).

The robot *PETMAN* built by Boston Dynamics is another hydraulically driven biped robot that is aimed for testing chemical protection clothing used by the US Army. The legs look similar to Boston Dynamics' four-legged robot *BigDog*. Despite its non-anthropomorphic leg structure with four links, *PETMAN* has a human-like shape and size. According to a video on the company website[5], it is capable of heel-to-toe walking and currently achieves a walking speed of 7.08 km/h.

Pratt and Krupp [147] present the 12-DoF 3-D walking robot *M2V2*. The robot is developed by Yobotics, a spinoff from M.I.T.'s former Leg Laboratory. *M2V2* has the traditional leg structure with six DoFs per leg and no actuated DoFs in the upper body. The leg joints are powered by "Series Elastic Actuators." These electric linear actuators are based on ballscrews and incorporate coil springs in series between the screw output and the load. The output force is controlled

---

[5] `http://www.bostondynamics.com/robot_petman.html`, accessed on 04/01/2010

by controlling the compression of the springs which is measured by quadrature encoders, hence the springs basically act as load cells. The authors expect to use mechanisms that are used in passive dynamic walkers (cf. Section 1.1.3).

Some very sophisticated and unique designs of humanoid robots and its components are developed by the Nakamura lab at the University of Tokyo. Nakamura et al. [123] develop the robot *UT-θ* (height 1.50 m, mass 45 kg). *UT-θ* has a total of 23 DoFs (neck three, arm four, leg six DoFs). The joints are driven by DC brush motors through Harmonic Drive gears. The lightweight design is mainly due to the main structure which is cast from magnesium alloy. The sensor layout comprises incremental encoders for joint position sensing, four six-axis force/torque sensors at the elbows and ankles and an inertial measurement system at the trunk. The kinematic structure of *UT-θ* has some distinctive features: the mobility of the human shoulder is mimicked by a parallel mechanism with two-DoF prismatic and a one-DoF rotational joint. The so-called "cybernetic shoulder" [133] allows the continuous movement of the shoulder's center of rotation. Considerable passive compliance is achieved by a flexible link that can absorb impacts at a collision with obstacles and reduce the risk of damage to objects or people. The "double spherical hip joint" [134] is composed two spherical hip joints with shared center of rotation. The authors expect advantages in the stabilization of the robot by separating the upper and lower body motion such that the upper body motion is controlled independently from foot placement. The knee joint is equipped with a "backlash clutch" [134] that adds large backlash between the thigh and shank. Torque is transmitted unilaterally to the shank, allowing to accelerate the shank, while shank advancement occurs virtually passive. The current robot *UT-θ2* (20 DoFs, height 1.50 m, mass 45 kg) features basically the same design as its predecessor, except that structural stiffness is increased and the servo actuators are more powerful. Also, the concept of the double spherical joint [134] is adopted to the shoulder joints, enabling a large workspace of the arms.

Other developments that should be mentioned include the *HOAP* robots series [117] by Fujitsu (now Miyachi Systems), *ETL-Humanoid* [121], the robots *BHR-1* and *BHR-2* from the Beijing Institute of Technology [105], *Mahru-III* developed by Samsung [104], *REEM-B* from PAL-Robotics [186], and the 0.57 m tall robot *NAO* from Aldebaran Robotics [53]. *NAO* has been selected to replace the *Aibo* robots in the RoboCup standard league.

1.1.2 Balance Control of Fully Actuated Biped Robots

This work does not deal with biped walking control. Since the control strategy also affects the mechatronic design concept, this section briefly describes the most relevant control methods. For a more comprehensive review of biped walking control and trajectory generation the reader is referred to an article by Kajita and Espiau [85].

In the early 1970s Vucobratović formulated the zero moment point (ZMP) theory as a stability criterion for biped robots [196]. Since then, ZMP theory has established as the basis for gait pattern generation and control for many biped robots. The ZMP, $\boldsymbol{r}_{ZMP} = (r_x, r_y, 0)^{\mathsf{T}}$, is defined as the point in the walking surface where the moment $\boldsymbol{M}$ due to the ground reaction force, $\boldsymbol{F}_G = (f_x, f_y, f_z)^\mathsf{T}$, corresponds to the ground reaction moment, $\boldsymbol{M}_G = (m_x, m_y, m_z)^\mathsf{T}$, and is thus identical to the center of pressure: $\boldsymbol{M} = \boldsymbol{M}_G - \boldsymbol{r}_{ZMP} \times \boldsymbol{F}_G = (0, 0, m_z)^\mathsf{T}$. Note that the condition of zero moment about the vertical axis of the contact plane, $m_z = 0$, is not necessary in general: this moment is compensated by the friction force as the feet can be assumed not to slide during ground contact. The contact between the ground and the support leg is stable if the ZMP lies within the foot support polygon. During normal gait, it is undesirable to have the ZMP on or close to the edges of the support polygon as an additional moment would easily cause instability. A common interpretation of this theory is therefore to treat the distance between ZMP and the edges of the support polygon as a measure for the reserve of stability.

For now, a large number of approaches for balance control of biped robots have been proposed and a number of similar ideas have been successfully implemented on full-size biped robots. A very common approach to maintaining balance is controlling the contact torques at the feet [89, 110]. These are usually measured by a multi-component force/torque sensor or several load cells and controlled via position control of the ankle joints. Another method is to accelerate the CoM [127, 178] to create a reaction force that stabilizes the robot. Other possible strategies utilize upper body inclination or foot positions. Reducing the landing impacts involves the combination of passive and active mechanisms. Many robots incorporate active control of the vertical contact forces [89, 110]. Large impacts are avoided by using low gain joint position control in combination with gain scheduling [127] or inverse dynamics feed forward control [178].

These control components are normally developed independently, so that unwanted interference is possible if they are combined. But interference can be avoided by using an integrated control approach. Löffler [109] proposes an integrated, model-based approach for the biped *Johnnie* that is based on feedback linearization. Unfortunately, the performance of this method is limited by the available sensor bandwidth, computational power, and model accuracy [110]. A more fundamental issue is the fact that the computed torque method requires joint torque control, which is difficult without joint torque sensors.

Buschmann [17, 18, 114] proposes a real-time walking control system for the robot *Lola* that plans the walking trajectories on-line using a simplified robot model. The trajectories are then modified by hybrid position/force control in task space based on a resolved motion rate scheme. Inertial stabilization is achieved by modifying the contact force trajectories. Comparable to most other bipeds, a multi-layered, hierarchical control concept is implemented, with a high gain joint position control loop on the lowest level [18].

1.1.3 Passive Dynamic Walkers

The idea of fully passive walking mechanisms that rely on precisely tuned natural dynamics was pioneered by McGeer [116]. Descending a shallow slope without any control and actuation but gravity, these mechanisms generate a periodic gait with a high energetic efficiency. A more recent development are passive walking mechanisms which are partly actuated in few joints, thus they do not have to walk down an incline to accommodate the energetic losses. These minimally controlled mechanisms contain passive elements like springs and dampers that utilize inertia and collisions for legged locomotion at minimal power consumption. Since the natural trajectories of a passive walker are basically determined by its mechanical structure, they are less versatile and robust than fully actuated biped robots. Moreover, most of these walkers are designed as planar mechanisms, and some of them are physically constrained to the sagittal plane. In consequence, stability must be considered only in the sagittal plane since falling sideward is not possible. Due to fundamental differences between the stabilization of planar (2-D) and free (3-D) walking, the comparison between the approaches of passive walkers and fully actuated biped robots is limited. Nevertheless, there are some interesting current machines that are only partly passive.

The walkers *Denise* [201] and *Flame* [69] developed at Delft University are "semi-passive dynamic walkers" with partial actuation. *Denise* (size 1.50 m, mass 8 kg) is pneumatically powered and has five DoFs in the hip, knees and ankles. The ankles and knees are completely passive, only the hip joint is actuated by pneumatic muscles. *Denise* can walk with a velocity of 1.44 km/h. The latest robot *Flame* (seven DoFs, mass 15 kg, size 1.30 m) is a 3-D robot with series elastically actuated hips, knees and ankles. Cable transmissions are employed to reduce the mass of the legs by placing all electric motors in the torso. The actuated joints employ series elastic elements that allow joint torque control. The joint angles are measured by incremental encoders and the inclination of the upper body is estimated by an inertial sensor. The control loop runs on an on-board PC and implements torque and/or position control. *Flame* is able to place its feet sideways. Currently, it walks at a speed of 1.62 km/h.

At Carnegie Mellon University Robotics Institute, HURST et al. [74] develop the four-DoF planar walker *BiMASC* to study the role of controllable compliance in running and control strategies that utilize the leg springs. The robot is driven by actuators with mechanically adjustable series compliance and designed to resemble the "Spring Loaded Inverted Pendulum" (SLIP) model, a mathematical model widely used in biomechanics. Despite structural similarities to the "Series Elastic Actuators" used for example in the robot *M2V2* (see Section 1.1.1), the actuators of *BiMASC* are large enough to store the energy of a running gait, whereas the former are primarily intended for sensitive and robust force control. Moreover, the spring stiffness is mechanically adjustable and can be tuned for a particular gait or ground surface.

A similar approach is investigated by VANDERBORGHT et al. [191] at the Vrije University Brussels. The robot *Lucy* (mass 30 kg, size 1.50 m) is actuated by pneumatic muscles. Due to adjustable compliance of the pneumatic actuators, the natural dynamics of the system can be changed according to the situation. Having a total of six DoFs, *Lucy* can only walk in the sagittal plane. A guiding mechanism prevents the robot from falling sideward.

FÖRG and ULBRICH [37] investigate the influence of elastic mechanisms on technical, bipedal locomotion by the example of a 3-D multibody simulation model of a 15-DoF robot that is equipped with rubber straps. The parameters of the elastic elements are identified by numerical optimization using different objective functions. The behavior of the resulting configuration is explored in terms of biomechanics.

1.1.4 Other Relevant Developments

The broad experience of the Institute of Applied Mechanics in the development of walking machines [144] including the six-legged walking robot *Max*, the eight-legged pipe crawler *Moritz*, and the biped *Johnnie*, served as an important basis for the current robot development.

Though originally designed for crawling not walking, the *iCub* project funded by the European Commission is notable. The project aims at providing a research platform in the area of cognitive systems, interaction and robotics. At a mass of 22 kg *iCub* is 1.04 m tall, corresponding to the size of a 3.5 year old child [188]. It has 53 DoFs which are mainly located in the upper part of the body. *iCub* can crawl on all fours and sit up. The entire technology (i. e., mechanical structure, electronics, software) is distributed open source.

Sophisticated lightweight robotic arms with seven DoFs are developed at the Institute of Robotics and Mechatronics, German Aerospace Center (DLR) [66–68]. The latest generation, *LWR-III*, is characterized by its modular design and a distributed motion control architecture. The joints are driven by customized RoboDrive motors whose characteristics are tailored to the needs of robotic applications. Local joint control is implemented on DSP boards and allows to control output torque, position, or impedance independent. Each joint employs motor-side position sensing, and torque and position sensing at the output. Cartesian control runs out on a central computer which is connected to the joint controllers over the fiber-optic *SERCOS interface*. In 2006, Ott et al. [137] presented the two-arm system *Justin* which is composed of a newly developed upper body, two torque-controlled lightweight robot arms *LWR-III*, and two four-fingered hands. *Justin* has 43 actuated DoFs, including seven-DoF arms, 12-DoF hands, and a five-DoF torso. The overall mass is 45 kg. The robot is mounted on an omnidirectional platform. *Justin* is used to test programming and control concepts for bimanual mobile manipulation.

A similar system is developed within the collaborative research center SFB-588 at the University of Karlsruhe. The main focus of this research is human-robot interaction within a household environment. The latest robot *ARMAR-III* weighs 30 kg [4, 7] and has 43 actuated DoFs: the head has seven, the waist has three, each arm and hand has seven and eight DoFs, respectively. Some drive mechanisms have a rather complicated structure. For example, the shoulder joint is a series of three joints driven by brushed DC motors through Harmonic Drive gears. In addition, the shoulder adduction/abduction and upper arm internal/external rotation joints employ worm gear transmissions. The motors for the elbow and wrist joints are located in the upper body, driving the joints through wire ropes. The computer system has a distributed architecture with several PCs and local DSP modules for sensing and low-level control. The local controllers connect to the higher-ranking controller via several CAN bus lines.

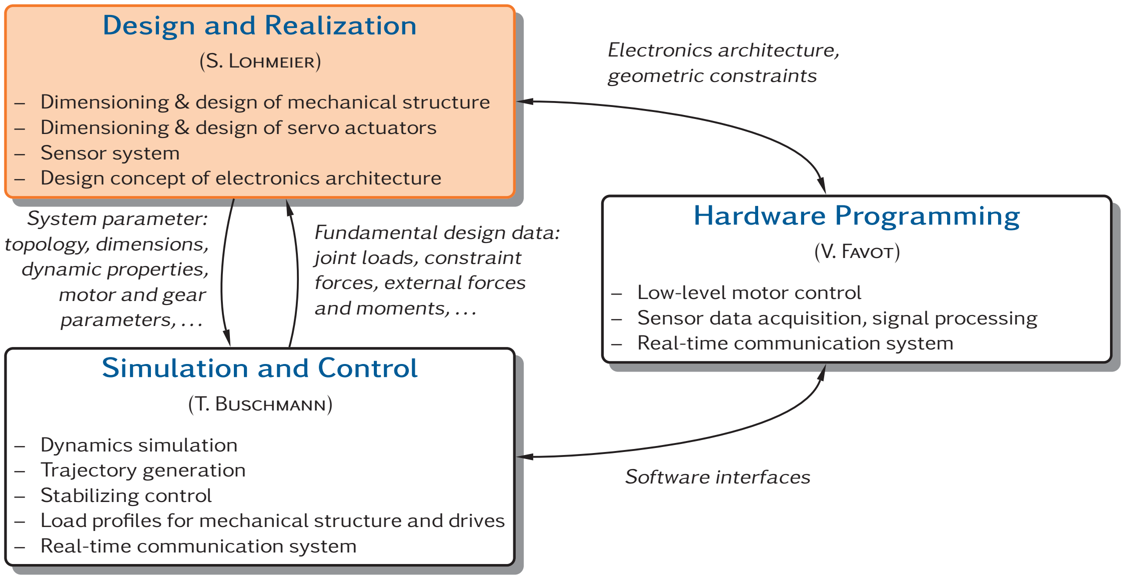

Figure 1.4: Integration of the sub-project "design and realization" in the overall project

1.2 Contributions of this Thesis

This work involves the mechatronic conception, mechanical design and realization of a dynamically stable walking robot with high performance and autonomous walking capabilities. It is part of the project cluster PAK-146 „Natur und Technik Intelligenten Laufens“[6] High walking performance includes more natural walking motion, human-like walking speed, flexible gait patterns for high mobility and agility, and a high degree of autonomy. The maximum walking speed is targeted at approximately 5 km/h which corresponds to the average walking speed of a human but is currently achieved by only few robots. The necessary performance of the mechanical system must be balanced with a minimal system mass. Hence the design of servo actuators with a high power density is paramount. Autonomy of the system is related to the drives, sensors and computer system. Since the robot is mainly operated within a laboratory environment, energy is supplied from an external source for the benefit of lower system mass. The robot should provide a reliable platform for testing different control methods, including vision-guided autonomous walking in arbitrary and realistic scenarios.

Figure 1.4 outlines the overall project organization: the robot is developed in collaboration of two major sub-projects, "Simulation and Control" and "Design and Realization", which are worked on iteratively and in parallel. The third sub-project, "Hardware Programming", was initiated in a later project phase. The sub-projects "Simulation and Control" and "Hardware Programming" are dealt by Buschmann [17–20] and Favot, respectively.

A well thought-out and holistic design concept of the mechatronic system is paramount for the robot's dynamic performance and agility. The hardware

---

[6] "Biological and Technical Aspects of Intelligent Locomotion." Group website: `http://www.uni-koeln.de/math-nat-fak/zoologie/tierphysiologie/dfgGruppe.html`, accessed on 05/20/2010

development relies on the "classical" approach, using well-proven and state-of-the-art mechatronics technology. Yet, inspiration from biological sciences is applied wherever appropriate. The employed machine elements and design methodologies are not generally new. Also, improving system dynamics by optimizing the mass distribution is a well-known approach in the field of industrial robotics and handling devices. However, global system dynamics of such conventional manipulators differ significantly from biped robots: manipulators are normally fixed to the environment and often have a with serial-link structure. Biped robots, on the other hand, contact ground unilaterally constrained using their feet. Hence the contact situation changes continuously and severely limits the amount of forces and moments that can be transferred to the ground for propulsion and balancing. The existing knowledge of designing fixed-base industrial robots can therefore not be applied directly but must be adapted to the specifics of biped robots. To the author's knowledge there are no scientific publications on biped robots that explicitly treat the global layout of the mechanical system (Section 2.4), kinematic structures of individual joints (Section 2.6), and the use of parallel mechanisms as design parameters for improving the dynamic properties of a fully actuated biped. The kinematic structures of the knee and ankle joints proposed in Section 2.6, on pages 53–56, aim at minimizing the resultant inertia of the legs and are indeed novel to the field of humanoid robotics. Also, the foot design for more effective impact attenuation (Section 2.3) is new. In summary, the key issues of this work are:

1. Redundant kinematic configuration of the locomotor system
2. Consistent lightweight design, considering sufficient static and dynamic stiffnesses of the mechanical structures and drive mechanisms
3. Development of a high-dynamic leg architecture with powerful yet lightweight drives and optimized mass distribution in the legs
4. Development of a foot dynamics concept that ensures reliable ground contact and effectively attenuates impact transients
5. High performance sensor layout to support the implementation of model-based control methods
6. Assisting control performance from a technological point of view by distributed low-level joint control and sensor data processing

The mechatronic design concept of the robot is developed in Chapter 2, with focus on the mechanical configuration, joint mechanisms, sensor layout, and computer architecture. After developing the topology of the kinematic chain, the foot dynamics concept is pointed out and general requirements on a high-dynamic leg architecture are discussed.

Chapter 3 presents the mechanical design of the machine. The distinguishing characteristics are the redundant kinematic structure with seven-DoF legs, the consistent lightweight construction and a modular joint design with high power density. The mass distribution of the legs is improved to achieve good dynamic performance. After compiling general design rules, the torque and stiffness-based dimensioning of the drive mechanisms is presented. The empirical approach to designing structural components is compared to an approach based on topology optimization and followed by strength assessment and elastodynamic analysis of critical components. The overall system is split into modular subsystems. The design of these sub-assemblies is explained in great detail. The parameter identification through kinematic calibration and CAD-based link inertial parameter estimation is described. Finally, the mass distribution is discussed and the dynamic performance of the implemented leg architecture is compared with other approaches.

The sensor system described in Chapter 4 is able to acquire the complete system state. The joint sensors for motor control and link position sensing are explained. Specific requirements and weight restrictions demand the development of customized force/torque sensors for measuring the ground reactions. They are complemented by contact sensors to disambiguate the contact state of the feet. The orientation and angular velocities of the upper body are estimated by a high-precision inertial measurement system.

The computer system is crucial to the performance of the robot. Although electronics hardware development and programming are not part of this work, Chapter 5 briefly sketches the electronics architecture and its components. The central control unit, local DSP nodes and the real-time communication system are presented. The chapter concludes with an overview of hardware security functions.

The experience gathered from the design and initial operation of the robot are analyzed in Chapter 6. Based on the lessons learned useful recommendations for future robot developments are made.

Chapter 7 finally summarizes the results and gives an outlook on future work.

2 Mechatronic Design Concept

> *Creativity requires the courage to let go of certainties.*
> —Erich Fromm

Humanoid robots are prime examples of mechatronic systems. They consist of a basic (mechanical) system, actuators and power transmissions, sensors, control electronics and control software. Before designing individual components, the overall design concept of the robot is developed. This chapter explains the aspects that must be considered in the realization of a high-dynamic and powerful robot with high walking performance (i. e., fast, agile and natural motions) and autonomy, and is particularly related to the

1. Mechanical configuration
2. Design concept of the joint mechanisms
3. Sensor layout
4. Computer architecture

All aspects imply several fundamental design decisions throughout the development process that affect the shape and performance of the overall system. Design decisions are based on own considerations, a comprehensive study of related literature and the results of the *Johnnie* project [46, 109]. To gain a deeper understanding of the requirements and constraints of the mechatronic system, a thorough hardware analysis of *Johnnie* is conducted during the conception phase. Finally, experience of the Institute of Applied Mechanics gathered from former walking machine projects is beneficial [144].

System complexity is rather high due to the interdisciplinary nature of the project and a high part diversity. Moreover, exacting demands on lightweight design severely limit the use of purchased components but call for the custom development of a broad spectrum of components, including servo actuators, structural components, sensors and electronics. In order to cope with the huge development effort within an acceptable timeframe, it is essential to adopt a systematic procedure throughout the development process (Section 2.1).

The topology of the kinematic chain is developed in Section 2.2. The foot dynamics concept which is paramount for the walking performance is introduced in Section 2.3, and Section 2.4 points out further requirements to achieve high-dynamic performance of the mechanical system, including good acceleration capabilities of the legs. The requirements on the joint mechanisms are discussed in Section 2.5. Types of actuators and precision gears with high dynamics and power density that satisfy the kinematic and kinetic requirements are selected. The drive mechanisms of the leg joints are developed in Section 2.6. The sensor layout is developed in Section 2.7 such that it is able to acquire the complete system state, allowing the implementation of model-based control schemes. Section 2.8 concludes with the conceptual design of the computer architecture. The

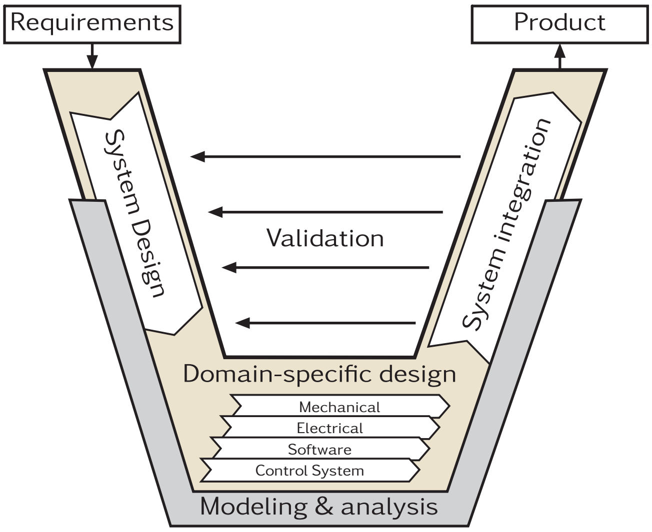

Figure 2.1: General workflow in the development of mechatronic systems according to the guideline VDI 2206 [192]

motivation for supplementing the central control unit with decentralized units for motor control and data processing are stressed and the requirements on the real-time communication system are discussed.

2.1 Systematic Approach to Managing Complexity

The development of a complex mechatronic system such as a humanoid robot demands for a systematic and goal-oriented procedure. High system complexity arises from the interdisciplinary nature of the problem and the high part count and diversity (number of actuators, sensors, electronic components). Two different aspects have to be considered in order to manage the project efficiently and within an acceptable timeframe. Content-related development methods involve the design methodology which is employed to structure the different stages of robot development. Organizational measures comprise the timing and scheduling of individual work stages using project planning tools throughout the development and realization phases.

2.1.1 Methodology in the Development Process

The procedure described by the guideline VDI 2206 "*Design methodology for mechatronic systems*" [192] forms the macro-cycle within the guiding framework of the robot development process. It is connected to the flexible approach of the "Munich Procedural Model" which describes the planning and design process during individual development phases [107].

Figure 2.1 shows the macro-cycle workflow of the guideline VDI 2206. It is a general model for the development of mechatronic systems, describing the entire range of required tools and activities. In the first step, a holistic and integrative concept of the entire system is developed on basis of the objectives stated in the research proposal. The robot's physical and logical structure are described on system-level and decomposed into sub-functions. Suitable active principles and/or functional elements are assigned to each sub-function and the goal achievement is

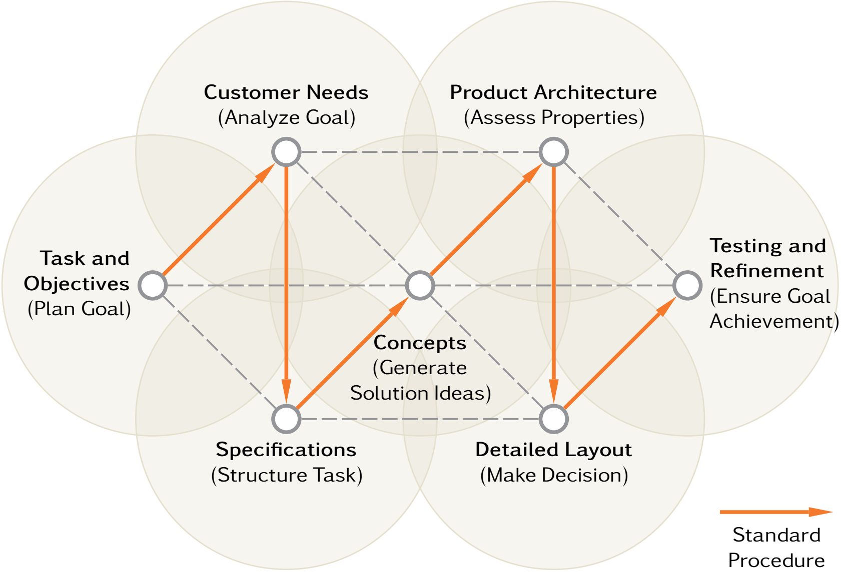

Figure 2.2: Overview of the Munich Procedural Model (adapted from [107])

again verified on system-level. The design process then divides into smaller development lines. Actual implementation of the subsystems and single components is carried out in a domain-specific manner. The development lines can be handled independently and simultaneously, nevertheless, synchronization is important throughout the development process. Finally, the development lines get merged into the complete system, where the interaction of the various components is verified. The development progress must be validated continuously with respect to the overall design concept. Thus, all phases of development are supported by the analysis of system properties by means of simulation models, taking into account either the complete system, subsystems, or single components. Like engineering design in general, the robot design process is iterative and open-ended and usually requires more than one macro-cycle.

For problem solving within the micro-cycles, the “Munich Procedural Model,” Figure 2.2, is adopted as the underlying procedural model [107]. It can be traced back to the four well-known steps to solving technical problems: task planning and clarification, conceptual design, embodiment design and detail design. Although a standard procedure is proposed, the network-like connections enable iterations or recursions.

2.1.2 Project Planning

The experience from the *Johnnie* project suggests that at least four years should be set for the design and realization of a complex humanoid robot and the necessary control software. Organizational planning of the project is the second element to keep track of progress and to better cope with complexity in the development process. The first step is to develop the work breakdown structure of the project. The common approach in product development is to use an object-related WBS. The product structure is defined, necessary work packages are shaped, logical and/or chronological dependencies among work packages are identified, and the activity duration is estimated. All work packages are then transferred into a Gantt chart of the project. The activities are represented by time-scaled bars and precedence relationships between them are shown as arrows. Besides the scheduling of activities, resources can be coordinated, e. g., manufacturing in the in-house machine shop, or the acquisition of procured items.

2.2 Kinematic Structure

The first tasks in the robot design process [163] are to determine the topology of the kinematic chain and the geometric dimensions of the links underlying the mechanical structure. The geometric proportions of the robot structure presented in Section 2.2.1 correspond to a human adult. The kinematic chain is derived in Section 2.2.2 using a well-known model of human gait. Finally, the expected advantages of the newly introduced DoFs (head, arms, pelvis, toes) are described in Sections 2.2.3 to 2.2.6.

This thesis relies on the same reference planes used in human anatomy and biomechanics to describe body regions and the relative movement of body structures. A short overview of the anatomic and biomechanical fundamentals of human locomotion is given in Appendix A. Furthermore, the Rancho Los Amigos Convention is used to divide the gait cycle into stance (loading response, mid-stance, terminal stance, pre-swing) and swing (initial swing, mid-swing, terminal swing) phases, see for example [142].

2.2.1 Geometric Dimensions of the Links

The geometric proportions are based on the human anatomy as far as possible. There are numerous studies and statistics on anthropometry. Henze [63] aggregates statistical data about the distribution of body dimensions from surveys by NASA and the German Institute for Standardization (DIN) [30, 31] in the computer program calcman3d. Specifying gender, and body size and mass, the software determines an average link geometry and mass and inertia parameters. The measurements are based on these sources and correspond to an adult that stands 180 cm tall and weighs 75 kg.

2.2.2 Topology of the Kinematic Chain

Though published over 55 years ago, the “Major Determinants of Human Gait” defined by Saunders et al. [162] still guide many researchers’ thinking about human gait. Based on the hypothesis that minimizing vertical and lateral movements of the center of mass (CoM) during gait minimizes the metabolic cost, the authors identified six basic motion patterns which reduce and smooth CoM vertical and lateral movement: Pelvic rotation, pelvic obliquity (i. e., motion in the coronal plane), knee flexion in the stance phase, knee and ankle interaction and lateral pelvis displacement. Recent investigations, however, raise the question whether the reduction in CoM displacement actually results from these six determinants.

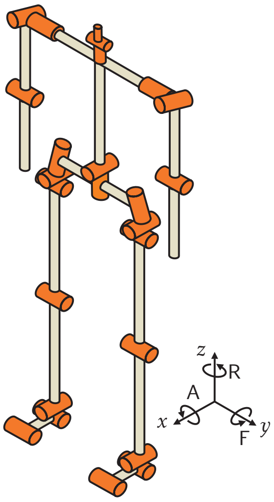

Figure 2.3: Kinematic scheme of the robot (R=internal/external rotation, A=adduction/abduction, F=flexion/extension)

Gard and Childress [43] find that pelvic obliquity and knee flexion do not reduce CoM vertical displacement as much as originally described, but they are believed to provide shock absorption during loading response. Croce et al. [25] quantified the contribution of pelvic rotation in reducing CoM vertical displacement to only 10 %, suggesting that pelvic rotation is only a minor determinant of gait. But the authors state that heel rise during terminal stance is probably the most important motion in reducing CoM displacement. Nevertheless, Saunders' "six determinants of gait" provide a clear and useful basis to determine the leg topology. Moreover, the hypothesis of minimal CoM motion is in line with established biped walking control strategies: most of them are based on the assumption that the CoM is kept at a constant height to decouple its fore-aft and lateral dynamics [88].

The goal of this research is the development of a humanoid robot with human-like proportions, range of motion, and kinematic structure. The robot should be able to move in arbitrary directions with human-like gait and speed of locomotion. The topology is thus mainly determined by the characteristics of human walking. Starting from the topology of *Johnnie*, a suitable joint structure is developed, taking into account literature on human gait analysis and coordination. Since the number of actuated degrees of freedom considerably influences the robot's complexity and weight, *Johnnie* achieves the desired mobility with a minimum number of DoFs [46]. Although this approach still applies to the new design, simulations and experiments suggest that additional DoFs in a redundant configuration allow to implement more natural and flexible gait patterns and, more generally, extend the abilities of the robot. Moreover, kinematic redundancies can reduce the joint loads, provided that appropriate algorithms for redundancy resolution are used. The kinematic scheme for the robot is therefore planned with 25 actuated DoFs, forming a tree-structure topology with the upper body as the root link. Figure 2.3 shows the proposed robot topology. The trunk has two and the head three joints, the arms have six joints (three each) and the legs 14 joints (seven each). Regarding the joints of leg and pelvis, the kinematic chain of the upper body with respect to the stance foot is redundant with nine DoFs.

During experiments with *Johnnie* it became evident that testing new controller

Table 2.1: Angular workspaces of the joints

Joint	# DoFs	Axis	Workspace [°]
Head	3	Pan	±115
		Tilt	-15~55
		Vergence	0~50
Shoulder	2	Flexion/extension	-180~45
		Adduction/abduction	-180~5
Elbow	1	Flexion/extension	-150~5
Pelvis	2	Internal/external rotation	±30
		Adduction/abduction	±15
Hip*	3	Internal/external rotation	±25
		Adduction/abduction	-50~22.5
		Flexion/extension	-110~45
Knee	1	Flexion/extension	-5~125
Ankle*	2	Adduction/abduction	±35
		Dorsiflexion/plantarflexion	-62~45
Foot (toe)	1	Flexion/extension	-65~5
Total	**25**		

* The hip and ankle joint workspaces are non-rectangular

concepts and gait patterns can benefit from larger workspaces. For instance, moving over obstacles and climbing stairs were not considered in the design and limited the robot's agility to smaller obstacles and steps. Moreover, the maximum step length was limited by the workspace of the ankle joints. For high mobility and agility, the joint motion ranges are therefore enlarged. Table 2.1 lists the angular workspaces of the joints.

2.2.3 Camera Head

As the robot should be able to cope with complex and realistic scenarios at considerable walking speed, close interaction of the vision and path planning system and the balance controller is necessary. The head DoFs are integrated to the controller structure of the overall system so that the kinematic redundancies can be utilized advantageously for gaze control.

Most humanoid robots have rather simple head designs where a stereo camera pair is mounted on a two-DoF pan-tilt unit, such as *Johnnie* [26] and the *HRP* robots [95, 96]. The camera head of *Johnnie* was operated as a self-contained unit within the vision and path planning system. Gaze direction was controlled independently from the robot posture. A patent application filed by Honda proposes two-DoF pan-tilt unit, where the field of view in the tilt axis is extended by a four-link neck mechanism [207]. Some humanoid robots show more complex designs. *HUBO* has a six-DoF head, with two DoFs in the neck and independent pan-tilt axes for both cameras [139]. The head of *iCub* has six DoFs, too, but the neck has three DoFs. The cameras have independent pan axes but share a common tilt axis [11]. *ARMAR-III* has almost the same configuration but a four-DoF neck, making seven DoFs in total [7]. *CB* has seven DoFs with three DoFs in the neck. Each camera is actuated by a two-DoF parallel mechanism, enabling independent pan and tilt movements [23].

Design Approach

The stereo camera pair for the new robot is mounted on a two-DoF pan-tilt platform, enabling both smooth pursuit and saccadic camera motions. The stereo basis is manually adjustable. In addition, camera vergence (the simultaneous rotation of both cameras in opposite directions) is adjustable, enabling stereo vision of objects close to the robot.

2.2.4 Arm Joints

Most humanoids have six or seven-DoF arms and hands for manipulation and whole-body activities [97]. Since this research is focused on bipedal locomotion, the arm structure must enable the compensation of total body momentum and is kept as simple as possible.

Arm motion in human gait occurs spontaneously in opposition to the legs [142]. Especially at higher walking speeds arm swing provides a meaningful counterforce to leg momentum and contributes to reducing the total body momentum about the fore-aft axis and avoiding stance foot slippage [16]. A recent study by UMBERGER [190] on the importance of arm swing for gait kinematics, kinetics and metabolic cost, confirmed the function of arm movement. While joint angles, angular velocities, and ground reaction forces are almost identical for walking with and without arm swing, some kinetic variables—in particular, the vertical momentum between foot and ground—show greater differences for walking with and without arm swing.

Johnnie has arms with two-DoF shoulder joints, but the adduction/abduction joints are blocked and not used in the gait patterns. The elbow joint is hinged and manually adjustable. The arm endpoints accept different balance weights, allowing to vary mass and inertia [46].

Design Approach

Each arm is equipped with three actuated DoFs, including flexion/extension and adduction/abduction joints in the shoulder and flexion/extension in the elbow. Since manipulation capabilities are not considered within this project, the arms are planned with balance weights at their endpoints. Introducing elbow joints is advantageous for higher walking speeds as they permit translational movement of the arm endpoints which is also observed in human gait [142]. Translational arm swing allows for an effective compensation of the total body momentum about the vertical axis because it does not affect the normal forces of the foot-ground contact. Though not relevant in straight walking, arm motion in the coronal plane is important for arbitrary movement and makes the gait look more aesthetic and natural. For example, the two-DoF shoulder joints can be utilized during sideward walking to avoid collisions of the arms and legs while compensating the total body momentum. Moreover, the resultant arm inertia is dynamically adjustable using the elbow and shoulder joints. Using the elbow joints, the position of the arm endpoints can serve as an additional parameter for controlling the CoM height.

2.2.5 Pelvis Joint

During normal gait the pelvis moves asynchronously in all three dimensions but only a very small motion arc accounts for pelvic flexion/extension compared to pelvic adduction/abduction and internal/external rotation [200]. Humans utilize pelvic rotation to lengthen the step at walking speeds above 3 km/h, which is also referred to as the "pelvic step" [16]. Moreover, upper body rotation is another parameter to compensate the total body momentum. In human walking, however, the contribution of upper body rotation is small compared to the contributions of the legs and arms [16].

Johnnie has a one-DoF pelvis joint which is blocked and not used in the gait patterns. *HRP-2* [95] has a two-DoF pelvis joint with flexion/extension and internal/external rotation joints. This configuration is especially useful for extending the workspace of the arms, e. g., when reaching distant objects. Also, it enables the robot to stand up from lying on the ground [39]. OMER et al. [135] propose a two-DoF pelvis joint combined with a two-DoF upper body joint for *Wabian-2*. The kinematic redundancy makes pelvis movement independent from upper body orientation, thus the robot is able to grasp something (e. g., a handrail), or to lean against an object without causing a statically indeterminate situation.

Design Approach

Neglecting pelvic flexion/extension, a joint with two actuated DoFs in the adduction/abduction and internal/external rotation axis is implemented between the trunk and the pelvis. Hence upper body orientation becomes almost independent from pelvic orientation. The pelvis joint allows to lengthen the steps and extends the robot's motion capabilities for sideways walking and other motion patterns. Moreover, the adduction/abduction joint enables walking with a stretched stance leg, while CoM is kept at an almost constant height [142].

2.2.6 Toe Joint

A common approach to gait generation for biped robots is to prescribe the upper body position and orientation and to calculate the joint angles accordingly. In general, six actuated joints per leg are sufficient to define the six rigid-body DoFs of the trunk. Hence most existing full-size biped robots have six actuated DoFs per leg—three in the hip, one in the knee and two in the ankle joint. The feet are usually one-piece segments without further segmentation, cf. Section 2.3. Higher speeds of locomotion are generally achieved by lower cycle times and/or larger step lengths. The cycle time is mainly restricted by actuator performance, and step length limitations arise from the leg topology, joint workspaces and stance leg singularity at initial contact. An approach to further enlarging the step length is rolling the feet from heel to toe. However, heel lift-off with monolithic feet is barely feasible: the robot is underactuated due to the line contact of the foot leading edge and the floor and, thus, marginally stable.

In human walking the toes play an important role in enlarging the weight-bearing area of the feet and are in contact for about 75 % of the gait cycle. During the gait cycle the center of pressure moves from the heel to the toes, so that about 40 % of the body weight is imposed on the toes in the final gait phases [73]. As figured out by Kerrigan et al. [98], heel rise in human gait contributes a considerable portion of the reduction in CoM vertical displacement. Heel rise occurs during terminal stance, shortly before the swing leg touches ground [142]. An experimental study by Takao et al. [180] with humans wearing mechanically constrained shoes shows that one-segment feet are clearly inferior to feet with toe segments both for straight and slalom walking. Typical models of human gait treat the feet as rigid links and provide six DoFs per leg, combining all movements of the toes and other foot joints into the ankle joint. Since the anatomical structure of the human foot is by far more complex, such simplifications are not valid for faster locomotion and running [129]. A more detailed model proposed by Carson et al. [22] separates the foot into three links: the hindfoot, forefoot and hallux, the latter representing the toes.

Due to the importance of stance leg heel rise in human walking, the idea of implementing toe joints on a humanoid robot is not new. One can basically distinguish between robots with passive and active toe joints. A simulative study by Sellaouti et al. [170] proves the relevance of toe joints for step length augmentation. By comparing gait patterns for flat and toed feet, the authors increase the walking speed by 50 % for feet with passive toes. Ogura et al. [132] implement passive toe joints in the robot *Wabian-2R* to walk with stretched knees and heel-off gait patterns. Kajita et al. [90] develop spring-loaded, passive toe joints for *HRP-2LT* to retrieve kinetic energy during running. The advantages of passive toe joints are obvious: they are simple and lightweight in design, and heel rise occurs automatically due to the whole-body dynamics. Like monolithic feet, however, heel-off with passive toe joints cause an underactuated phase at the end of single support because moments about the lateral axis cannot be transferred to the ground. These problems are overcome by actively driven toe joints. But the foot design gets more complex and the need for a motor-gear unit increases the weight of the foot significantly. To the author's knowledge, there are only three full-size humanoid robots with active toe joints. The robots *H6* and *H7* use actuated toe joints to reduce knee joint velocity during double support phase. In an experiment with *H6*, Nishiwaki et al. [128] increase the walking speed by 80 %. Toyota's running robot [178] is able to run as fast as 7 km/h by using active toe joints. Yamamoto et al. [206] develop a toe joint for the miniature humanoid robot *UT-μ2* using a parallel four-bar mechanism. The robot contacts ground with the toe tips and a non-movable part of the toe segment which allows to decrease the required joint torques and the actuator mass. The kinematics of the mechanism yield a foot displacement in the fore-aft direction that depends on the toe angle and the radii of the contact elements and must be taken into account in the trajectory planning algorithms.

Design approach

For reduced joint loading and larger step lengths, an additional link is implemented between the forefoot and heel, equivalent to the human toes. Figure 2.4 illustrates the benefits of actuated toe joints. The major advantage is the larger step length. Heel lift-off is feasible and allows the swing leg to be in a more extended configuration during mid-swing. The actively controlled area contact of

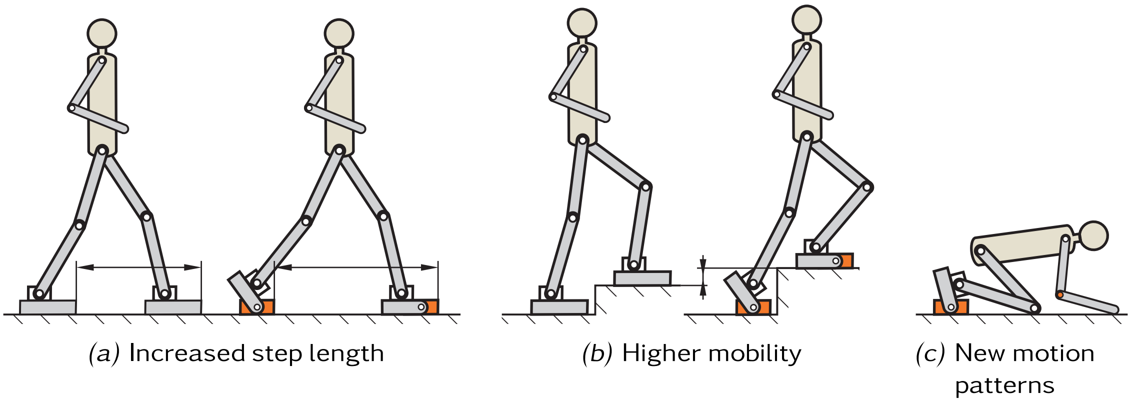
(a) Increased step length (b) Higher mobility (c) New motion patterns

Figure 2.4: Advantages of actuated toe joints to motion generation

the toe segment allows to transfer stabilizing moments about the axes tangential to the ground. Moreover, the joints facilitate rolling the feet from heel to toe which reduces the joint loads in the hip and knee, as opposed to the conventional six-DoF leg configuration. In general, actuated toe joints augment the robot's mobility, it is able to climb higher steps, and can execute more complex, or all new motion patterns.

2.3 Foot Dynamics

The feet are key components in the mechanical structure of the robot. During normal locomotion, they are the only parts of the robot which are subjected to external loads. At initial contact they must withstand shock loads of up to a multiple of the robot's weight. Since the stabilizing controller is based on the assumption that the robot does not slip and that tangential contact stiffness is high, the feet must ensure proper ground contact during the support phases in order to effectively transmit the necessary stabilizing forces and moments. The feet are the end links of the legs and undergo the largest accelerations. The design concept must therefore put emphasis on the mechanical design to be as lightweight as possible, yet robust enough to accept high impact loading.

Despite the obvious fact that the foot mechanism has a strong influence on the walking performance, there is surprisingly few detailed literature. YAMAGUCHI et al. [205] develop a complex foot mechanism for the biped robot *WL-12RVI*. It has four discrete contact points and is able to both attenuate landing impacts and adapt to unknown, uneven floor. The elastic layers are made from an open-cell foam material with nonlinear properties. Linear potentiometers measure the deformation of the feet. An additional passive DoF, whose configuration depends on the contact state of the foot, stabilizes the walking motion. Although some current robots have divided feet with toe joints, see Section 2.2.6, monolithic feet are the state-of-the-art in full-size humanoid robots. They normally consist of a monolithic base plate covered with rubber or plastic to increase friction. The feet have either four discrete contact points or area contact with the ground. Most often compression/shear mounts are used for shock absorption [64, 94]. The stiffness of these elements under shear loading is considerably lower than under pressure loading which limits the bandwidth of transferable forces and moments and, thus, the performance of force control. Moreover, the material properties of these rubber-metal elements is mainly elastic but damping is rather low. The shear stiffness is increased in a refined version of the *HRP-2* foot by a combination of compression/shear mounts with ring mount elements [136]. Honda filed several patent applications on design features of humanoid robot feet. The foot structure of the robot *P3* holds several elastic elements for shock attenuation. Position sensors measure the displacement of the outer sole with respect to the main foot segment [182]. Another approach improves shock absorption by means of a reinforced elastomer layer with viscoelastic insets at the heel [49]. A more recent patent application claims an ultra-lightweight foot design with plate springs made from fiber-reinforced plastic and damping material, assembled in a sandwich-like structure [184]. Another foot system which is adaptable to uneven terrain is developed by Hashimoto et al. [62]. The contact elements are attached to each corner of the foot and act as vertical sliding mechanisms. The sliders are locked after they are adjusted to a surface. Gienger et al. [47] develop a foot structure for the robot *Johnnie* which is similar to the foot mechanism of *WL-12*: it has four chamfered ground contact elements coated with rubber. A large block-shaped damper made from viscoelastic material is integrated between the upper and lower foot plates to reduce landing impacts. Linear potentiometers measure the deformations of the damping layer. A passive rotational DoF between the leading and rear contact elements makes the foot-ground contact statically determinate and allows to compensate smaller unevenness. However, the damper block is rather compliant under shear and pressure loading which easily causes instability. In particular, deformation of the damper by lateral moments considerably limits controller bandwidth. Therefore, this design was replaced by a simplified foot system with four point-contact elements. Each contact element comprises a viscoelastic damping layer and a high-wear contact layer. Shear of the contact elements due to tangential forces is omitted by a sliding contact bearing, allowing only vertical compliance.

2.3.1 Biomechanics of the Human Feet

Due to numerous conflicting requirements, the development of a functional foot design is not trivial. Hence the main functions of the human foot are discussed before specifying the requirements on the robotic foot. Without oversimplifying the foot motion during walking, the complex anatomical structure of the human foot can be reduced to three functional units: *(a)* hindfoot, *(b)* forefoot, *(c)* hallux [22]. Key elements are the toe joint discussed in Section 2.2.6, the subtalar and midtarsal joints [203], and the heel pad [157].

It is obvious that several mechanisms—both active and passive—are involved to protect the human body from the large impact forces during initial contact [199]. Active mechanisms are muscle contraction and joint movement[1] at initial contact. It is supposed that the use of knee flexion and ankle joint plantarflexion is not to

---

[1] In particular, knee flexion, ankle joint plantarflexion, and pronation of the subtalar joint.

reduce the impact force itself but the rate at which body weight is transferred to the stance foot [199]. The motion of the subtalar joint lowers the ankle and leg, increasing the time over which the foot is decelerated and energy is dissipated [13]. Due to their reaction time, however, active mechanisms can only attenuate impacts of a certain bandwidth. Passive shock attenuators are body tissues in the heel pad and the joints with viscoelastic properties, acting as low-pass filters by absorbing higher-frequency components of the transient forces [146]. The heel pad is between 10 mm and 20 mm thick and spreads the load over the whole plantar surface [157]. The compression during initial contact ranges from 3 mm to 8 mm [199].

During initial contact and early stance, the human foot is required to be a flexible and adaptable structure to accommodate to unevenness in the terrain. Conversely, during the propulsive phase it must perform as a rigid lever to transmit effectively the propulsive forces which are applied to it. These apparently contradictory functions are accomplished by a complex interaction of the subtalar and midtarsal joint [13]. In addition, the progressive material properties of the heel pad tissue ensure ground contact during stance [157].

2.3.2 Design Concept of the Robotic Feet

To ensure the effectiveness and performance of force control, the feet must be able to reliably transmit the contact forces and moments and provide high grip on different surfaces. The impact forces at initial contact can range up to a multiple of the body weight. In addition, higher impact forces result from disturbances like structural vibrations of the leg structure, or kinematic or positioning errors. Such errors let the ground contact of the swing leg occur too early or too late and can cause instability of the robot. Therefore, certain compliance of the foot structure must provide essential shock absorption to enable a smooth and stable walking motion. Adaptation to uneven terrain, on the other hand, may require complex mechanisms such as the human subtalar/midtarsal joint complex [13]. However, the ability to adapt to rough and inclined surfaces is not mandatory in a first version of the foot design because most experiments are conducted within the laboratory environment. Instead, it is sufficient to compensate smaller irregularities of the ground.

Furthermore, there are some requirements on top of the properties of the human feet. Empirical testing and modification are important steps in the development of a sophisticated foot design. Moreover, the mechanical structure must be modifiable and expandable, enabling the experimental validation of different foot concepts. For an easy replacement of the heel and toe segments the feet must show a modular structure. Finally, the systematic lightweight design is crucial as the feet are the end links of the leg kinematic chain. In summary, the requirements on the robotic feet are:

- Provide high grip on different surfaces to ensure proper ground contact
- Rigid mechanical structure to transmit the propulsive forces at a bandwidth sufficient for system stabilization
- Compensate smaller unevenness

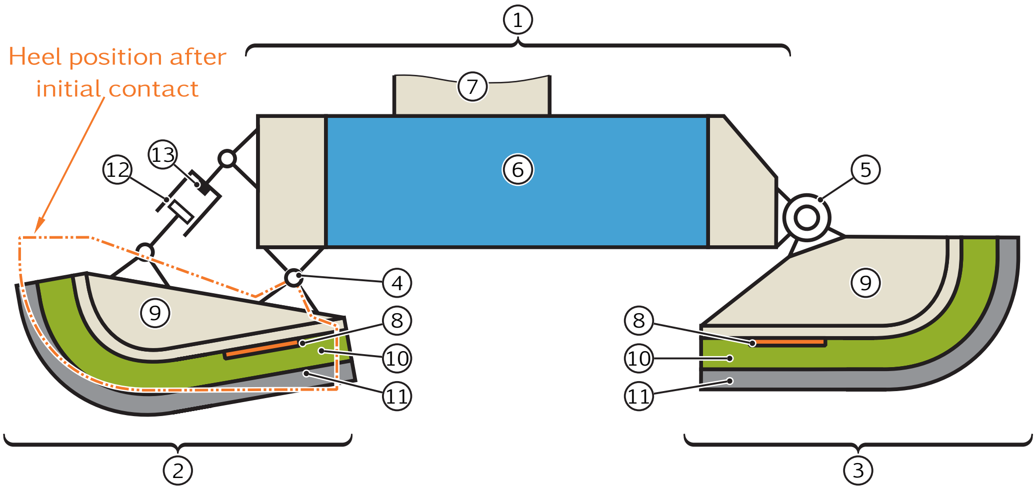

1	Forefoot
2	Heel
3	Hallux
4	Heel joint (passive)
5	Toe joint (active)
6	Force/torque sensor
7	Ankle joint flange
8	Contact sensor
9	Contact element (rigid)
10	Viscoelastic layer
11	Wear-resistant outsole
12	Hydraulic shock absorber
13	Mechanical end stop

Figure 2.5: Design concept of the robotic feet. The passive heel segment and hydraulic damper account for effective for shock attenuation at initial contact.

- Passively compliant elements with good damping characteristics for shock attenuation at initial contact
- Progressive spring characteristics at ground contact ensures effectiveness of stabilizing control
- Minimal weight
- Keeping the anthropometric dimensions, if possible
- Modular mechanical configuration, simplifying the replacement of heel and toe segments and/or other components

Based on these requirements, the design concept of the robotic feet is derived as shown in Figure 2.5. The foot is composed of three segments with the forefoot (1) as the base link. The heel (2) and hallux (3) segments are connected to the forefoot (1) by the heel joint (4) and the toe joint (5), respectively. The heel joint (4) is a passive joint that corresponds to the subtalar joint of the human foot [13]. The toe joint (5) is actuated in the original concept, but the modular mechanical structure facilitates different foot concepts, for example monolithic feet or feet with passive toe joints. The force/torque sensor (6), cf. Section 2.7.3, is an integral part of the forefoot (1) and interfaces to the ankle joint flange (7). Each contact element of the heel and hallux holds a contact sensor (8) to acquire the contact state of the feet, cf. Section 2.7.4. The contact forces and moments are transferred to the ground by area contact of the contact elements (9–11) for improved stiffness of the foot structure, compared to designs with point contact elements. Each contact element is composed of the rigid base body (9), the viscoelastic layer (10) and the outsole (11). The viscoelastic layer (9) corresponds to the fat pads in the human heel and toes [146]. It shows good damping characteristics, no significant compression set, long lasting ability to provide shock attenuation, and certain elasticity to recover from deformations. The outsole (11) is made from wear-resistant, high-friction rubber. Both layers are connected without any rigid part in between. Thus, the feet interact with the environment only via viscoelastic elements and can easily adapt to the ground surface by deformation.

Several mechanisms are combined for effective shock attenuation at initial contact, acting as mechanical low-pass filters for the transferred forces. Besides the viscoelastic contact elements (9–11), the passive heel segment (2) and hydraulic shock absorber (12) account for additional energy dissipation, similar to the human hindfoot. The mechanical end stop (13) determines the heel position after initial contact and thus ensures proper transmission of the propulsive forces and stabilizing moments during ground contact. Although necessary for the performance of force control, the compliant foot-ground contact bounds the mechanical bandwidth of the ground reaction forces and moments. The mechanisms for passive shock absorption are thus limited by the bandwidth required by the balance controller and must be complemented by active mechanisms. Possible approaches are vertical impedance control of the foot touching the ground [18], or joint servo gain scheduling of the swing leg [127].

2.4 General Requirements on a High-Dynamic Leg Architecture

Without doubt, many open questions make the control of fast bipedal locomotion very challenging. High dynamic stability and robustness against disturbances are the key mechanisms to maintain balance in different situations. The integrated control approach developed by Buschmann [18, 114] combines the stabilization of global dynamics by manipulation of the contact forces and hybrid force/position control in task space.

On the other hand, it is often neglected that the performance of balance control also relies on the mechatronic hardware. While considerable effort is paid to the development of powerful computer architectures (cf. Section 2.8), the effects of mechanical system dynamics are often disregarded in the design concepts of biped robots. Indeed, sophisticated control strategies may compensate for some limitations of the mechanical structure, and sophisticated planning algorithms are able to optimize the trajectories, e. g., for minimal speed and acceleration patterns, and take into account constraints, such as saturation effects of control variables. However, principal limitations of system performance can arise from fundamental reasons, that is, reasons based on the physics of a poor mechanical architecture. For example, fast motions of the swing leg produce large vertical contact moments in the stance foot that can easily cause slippage in the foot-ground contact, if the mass distribution in the legs is disadvantageous and—accordingly—leg inertia is high.

"Dynamic performance" of fixed-base robotic manipulators is defined as traditional performance criteria, e. g., actuator limits [6]. Regarding the specifics of legged robots, further performance limitations arise from the constraints associated with unilateral foot-ground contact. Viscoelastic contact elements at the feet make the robot underactuated and put severe limitations on the transferable

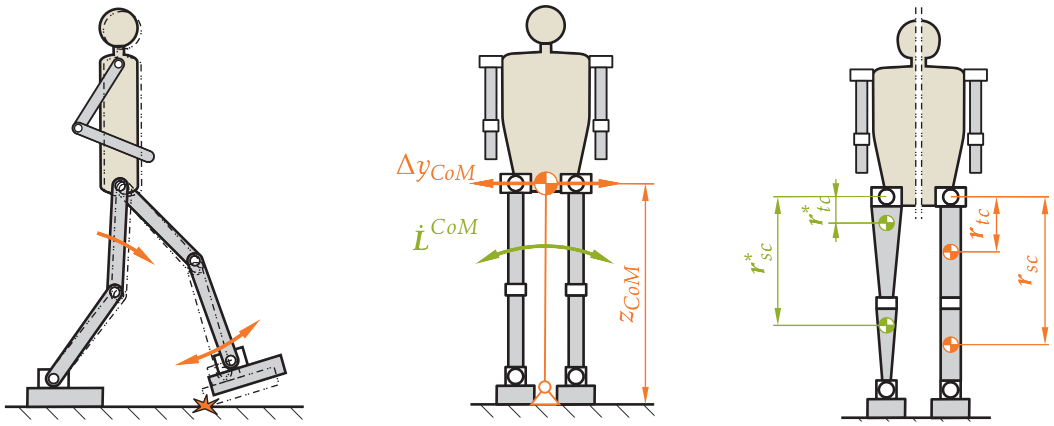

(a) Stiffness *(b)* CoM height *(c)* Link and leg inertia

Figure 2.6: Design objectives for improved dynamic behavior of the locomotor system at higher speeds of locomotion. *Left to right:* high effective stiffness; maximal height of the robot's center of mass; low-inertia design of the leg links.

forces and moments necessary for propulsion and to stabilize the upper body DoFs. In summary, the most important indices for evaluating the dynamics of fully actuated biped robots are:

- Mobility (topology of the kinematic chain, space of motion of the legs and arms, degree of redundancy, cf. Section 2.2)
- Agility (speed and acceleration capability)
- Force capability (magnitude of propulsive and stabilizing forces bounded by the compliant unilateral ground contact, cf. Section 2.3)
- Actuator limits (joint torque limits)
- Mechanical properties (structural stiffnesses, natural frequencies, mass, amount of moving masses)
- Accuracy

The acceleration capability of the locomotor system is closely related to the actuator limits and mechanical properties. Evidently, lightweight mechanical structures contribute to better dynamic properties, which are usually penalized by added weight. Moreover, they allow for smaller servo actuators, which in turn yield additional weight savings.

Focusing on stiffness and damping properties, Rivin [154] addresses critical aspects of the mechanical design of fixed-base robotic systems. Most of these approaches can be adapted to the specifics of biped robots. In addition, three basic design objectives aiming at high-dynamic behavior of the locomotor system are illustrated in Figure 2.6 and discussed in the following subsections: *(a)* high effective stiffness; *(b)* maximal height of the robot's total CoM; *(c)* low-inertia design of the leg links.

2.4.1 High Effective Stiffness

The effects of structural link flexibility and joint elasticity are often neglected under the assumption of a "rigid" mechanical structure. However, in terms of the above "traditional" criteria, mechanical compliance (whether introduced intentionally or not) normally degrades the robot's performance. For example, link deflections and joint compliance arising from the lightweight and slender design of the mechanical structure can severely limit the static (steady-state error) and dynamic (structural vibrations, deviations from desired trajectories) performance of the locomotor system. Further, if the foot-ground contact occurs too early due to mechanical compliance, Figure 2.6*a*, the walking performance degrades and may at worst destabilize the robot. The problem gets more emphasized at higher walking speeds, as the propulsive forces and landing impacts increase significantly.

Only few publications deal with effects of structural compliance on the walking performance of fully actuated bipeds, which makes it difficult to find reference values for the required stiffnesses. Carbone et al. [21] analyze the elastostatic performance of the robot *Wabian-RIV*. The robot is modeled as an elastic multibody system using linear and torsional springs. Neglecting backlash of the gears and joint bearings, the stiffness matrix is determined experimentally by measuring the linear and angular displacements for known static wrenches applied at the feet. According to the explanation of the experimental procedure, it seems that the joints were position-controlled during the experiment, hence, the performance of the joint position controllers is reflected in the stiffness parameters. Kwon et al. [104] conduct a numerical modal analysis to estimate the elastodynamic behavior of individual components, however, the dynamics of the overall system are not considered.

Unlike conventional robotic manipulators the locomotor system of a biped robot is subjected to topology changes throughout the walking cycle, depending on the contact state with its environment: during single and double support the legs respectively form an open and closed kinematic chain. Further, alternating kinematic configurations of the stance and swing phases, Figures 2.7*b* and 2.7*c*, put different requirements on the links and joints. Moreover, resultant load-side inertia of the stance leg drives is significantly higher due to contributions of upper body and swing leg. It is important to take these effects into account when developing the stiffness and weight requirements on the leg joints and links.

Structural Compliance

The legs of a biped robot normally are serial-link mechanisms with cantilever structure. Each link pivots about a transverse axis at one end, relative to the preceding link. Using the analytical model of a cantilevered beam, Rivin [154] discusses general requirements on links of industrial robots that rotate about a transverse axis. In general, such links require *(a)* high stiffness in both bending and torsion to reduce deflections of the feet due to gravity and inertia forces; *(b)* high natural frequencies to achieve fast rate of decay of vibrations caused by transient motions. Figure 2.7*a* illustrates shear Q, moment m and displacement u of a cantilever beam under constant angular acceleration. Consequently, a well-designed link tapers in cross section and/or wall thickness to reduce gravity and inertial loading. However, the need to provide space for electric cables, actuators, power transmission components, etc., as well as space requirements for the joint connecting the succeeding link often limit the use of variable cross sections.

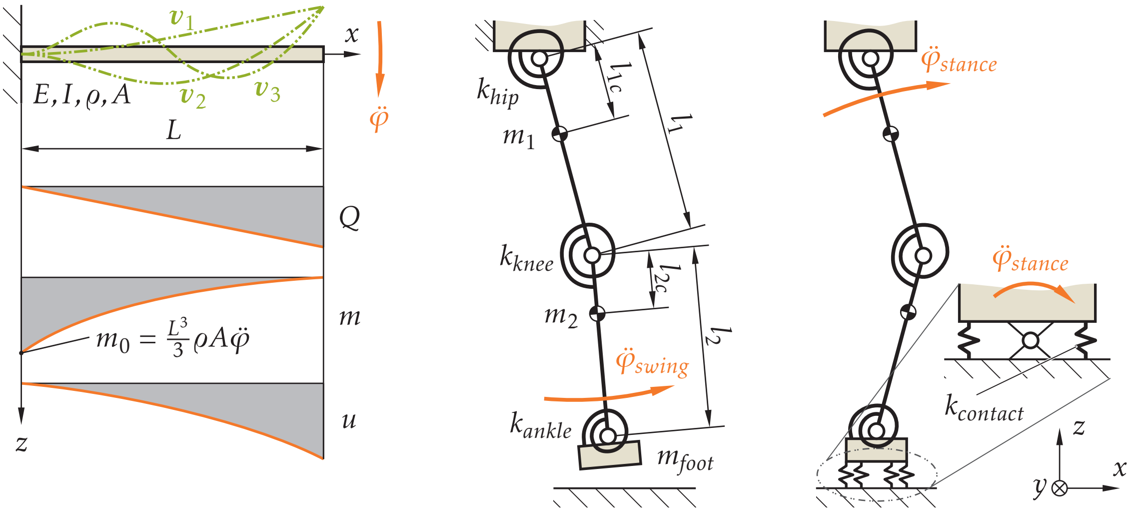

(a) Cantilever beam *(b)* Swing leg *(c)* Stance leg

Figure 2.7: Requirements on the leg structure for high stiffness. *Left:* elastic cantilever beam; *right:* changing kinematic configuration of the legs during the swing and stance phases.

For an industrial manipulator arm, these results suggest high stiffness of the proximal link, while low weight is more emphasized for distal links. In the case of a biped robot with structure-varying topology, however, this design approach would at a first glance alternately apply to the thigh and shank links. From robot simulations, however, it can be seen that the highest link accelerations occur in swing phase, hence this phase puts higher demands on leg dynamics than stance phase, where the load-bearing capability is more relevant. Moreover, since a timely ground contact of the stance leg is critical for walking stability, minimizing deviations from the desired swing leg trajectory is an important design goal.

Although the roles of material, cross-sectional properties and support in altering the fundamental frequency are limited, the influence of these parameters on lateral vibrations can be studied using the dynamic beam equation:

$$\frac{\partial^2}{\partial x^2}\left(EI\frac{\partial^2 u}{\partial x^2}\right) + \varrho A \frac{\partial^2 u}{\partial t^2} = f(x) \tag{2.1}$$

Here E is the Young's modulus, I the second moment of area, A the cross-sectional area, ϱ the material density and $f(x)$ an external load. For a uniform beam, $E, I, \varrho, A = \text{const.}$, of length L the natural frequencies for free vibration, $f(x) = 0$, can be computed from Eq. (2.1) as

$$\omega_i = \lambda_i^2 \sqrt{\frac{EI}{\varrho A L^4}}. \tag{2.2}$$

Here the eigenvalues λ_i^2 relate to the boundary conditions of Eq. (2.1) and the particular mode i of interest. The corresponding mode shapes, $\boldsymbol{v}_i$, for the first three solutions are illustrated in Figure 2.7*a*.

The relationship between beam support, material and geometric parameters and the fundamental mode of vibration can be seen from Eq. (2.2). While λ_i^2 could only be increased by providing additional support, the cantilever support naturally limits beam stiffness. Length L is constant and given by anthropometric data, so that the only parameters for maximizing the natural frequencies are material and geometry. The material properties, denoted by specific modulus E/ϱ, suggest the use of high specific modulus materials, e. g., fiber-reinforced composites (cf. Section 3.10). Beam cross-sectional geometry is represented by I/A. This ratio is evidently maximized for geometries showing high second moment at small cross-sectional area. In other words, the links should be designed with large, closed cross sections and minimum wall thickness.

Joint and Drive Compliance

Joints, actuators and drive mechanisms are critical design components, since they typically represent the largest part of total compliance of robotic structures [154]. Optimization of effective stiffness must therefore include compliance of joint and transmission components.

Linkage joints must accommodate constraint forces and moments between the links. Greater stiffness is achieved with rolling bearings in backlash-free arrangements. O-arrangements with adjusted clearance or preload are preferred for joints subjected to large tilting moments due to the increased “virtual” bearing distance (cf. Section 3.2). Another major concern is the weight of a joint. An optimal tradeoff is often achieved by using thin-section bearings with reduced cross sections but larger bore diameters and greater number of rolling elements. The issues related to an optimal selection and design of actuators and drive mechanisms are addressed in Section 2.5.2.

In the following, effects of the structure-varying kinematic chain on the leg joints are analyzed using a simplified 2-D model. For the sake of simplicity it is assumed that the deflection of the leg endpoint due to link elasticity is small compared to joint compliance. The leg is approximated as a planar mechanism of two rigid links, $i = 1, 2$, each with length l_i, mass m_i and CoM position l_{ic}. The foot is modeled as a lumped mass m_{foot} attached to the free end of the second link. Links and foot are connected by flexible joints with stiffnesses k_{hip}, k_{knee} and k_{ankle}. During swing and stance phase, the leg rotates about its base joint with constant angular acceleration, $\ddot{\varphi}_{swing}$ and $\ddot{\varphi}_{stance}$, respectively.

For the swing leg, the upper body is assumed fixed in space and the hip joint is the base joint of the leg (Figure 2.7*b*). Then deviations of the desired foot motion are mainly due to hip and knee joint compliances, while the effects of ankle joint elasticity are less emphasized. By analogy with the above considerations of the analytical bending beam, the hip joint stiffness must be the highest, followed by the knee and ankle joint stiffnesses: $k_{hip} > k_{knee} \gg k_{ankle}$.

Conversely, the stance leg contacts ground with its free end (i. e., the viscoelastic layer at the foot) to support the upper body, as illustrated in Figure 2.7*c*. Without loss of validity the foot-ground contact is considered as a passive pivot with stiffness $k_{contact}$, forming the “base joint” during stance phase. Contrary to the swing leg, the foot-ground contact and ankle joint must show the highest stiffnesses in order to minimize upper body deviations, while the knee and hip joint stiffnesses are less critical: $k_{contact} \geq k_{ankle} > k_{knee} > k_{hip}$. However, contact stiffness is rated to effectively attenuate impacts (cf. Section 2.3) and ensure performance of ankle joint torque control, and distinctly lower than the stiffnesses of the hip joint and other leg components: $k_{contact} \ll k_{hip}$. Indeed, upper body deviations during stance are dominated by compliance in the foot-ground contact.

As with the link structures, alternating leg topologies during the gait cycle yield conflicting requirements on the leg joints. However, since the highest accelerations occur during swing phase, the hip joint must evidently show the highest torsional stiffness. Though torsional stiffness of the the knee and ankle joints can be distinctly lower, yet large enough to ensure good control performance and high bandwidth of the torque controller.

Design Approach

In summary, the leg structure must meet the following requirements to achieve high stiffness and minimal deflection from the desired trajectories:

- Generally high stiffness of link structures in bending and torsion
- High stiffness of the thigh link. The shank link should be designed extremely lightweight with less strict requirements to stiffness.
- Thin-walled cross sections with high second moment of area. Additionally, links should taper in cross section and/or wall thickness to reduce associated gravity and inertial loading (see also Section 3.2).
- High torsional stiffness of the hip joint, followed by the knee and ankle joints
- Joint drive mechanisms and their auxiliary transmission components designed for high acceleration capability and sufficient bandwidth, see Section 2.5.2
- Linkage joints in backlash-free arrangements, preferably O-arrangements with adjusted clearance or preload
- Very lightweight foot design, see Section 2.3

2.4.2 Total Center of Mass Height

Unlike humans, the largest portion of a biped robot's mass resides in the legs since the motors and gears account for approximately a third of the overall mass [46]. Hence the total CoM height is typically at a level with the hip joint or even below. During single support phase, the dominant dynamics of a biped robot can be described by an inverted pendulum. Assuming that the robot mass is lumped in the CoM which is constrained to move at constant height, one gets a set of two decoupled differential equations for sagittal and lateral CoM motion. This approach developed by Kajita et al. [88] is known as the "Three-Dimensional Linear Inverted Pendulum Mode" (3D-LIPM). It illustrates the influence of total CoM height on the lateral swing of the upper body during walking. One possible solution for CoM lateral motion are pieces of hyperbolic curves:

$$\Delta y_{CoM} \propto \cosh\left(\sqrt{\frac{g}{z_{CoM}}}\, T_s\right). \tag{2.3}$$

According to this approximation, the CoM lateral swing Δy_{CoM} decreases with higher CoM positions z_{CoM} for a given single support period T_s. Lower lateral swing augments the stability of the robot at higher walking speeds because the angular momentum about the fore-aft axis is reduced. Maximizing the height of the robot's CoM is therefore a basic design guideline.

Moreover, achieving a human-like mass distribution by concentrating the mass in the upper part of the robot would be desirable. As pointed out in Section 2.6, most servo actuators typically are in the robot's legs. Considering the resultant mass distribution, it seems unlikely to shift the total CoM above the hip joint without adding masses to the upper body, cf. Figure 2.6*b*. In particular, arranging parts of the leg drive mechanisms in the upper body is very difficult. This approach normally leads to very complex drive mechanisms with various transmission components, spanning several links and multi-DoF joints. Moreover, the longer transmission distance increases the motor-side inertia and may introduce backlash. In summary, the practical influence on CoM height is limited. Shifting the total CoM as close as possible to the hip joint is nevertheless an important design guideline, provided that the robot's performance is not affected by complicated drive mechanisms.

2.4.3 Low-inertia Design of the Leg Links

Higher speeds of locomotion normally yield large step lengths at high step frequencies. Conversely, if the robot moves autonomously in realistic scenarios, sudden and arbitrary changes of the walking speed and direction may occur. Both tasks benefit from a greater acceleration capability of the locomotor system which is achieved by a low-inertia design of the leg links. As illustrated in Figure 2.6*c*, the mass distribution in the leg links directly affects a variety of robot characteristics, including the CoM position, the resultant inertia of the legs, and the elastodynamic behavior of the drivetrains. Therefore, the judicious design of the leg links and their drive mechanisms is important to achieve *(a)* high dynamic performance of the overall system and *(b)* support the performance and robustness of balance control.

Regarding the robot's agility and speed of locomotion, a high dynamic performance of the locomotor system is one of the most fundamental design objectives. The naïve approach is to simply design the servo actuators for high torque and speed bandwidths. But drive power must be increased very carefully since more powerful actuators are normally heavier and may in turn easily detract from the robot's dynamic behavior. High-performance servo actuators are nevertheless appropriate, yet with limited benefit if no accompanying measures are taken. In this light, it is proposed to reduce the inertia and gravity loading of the *individual leg links* to improve the acceleration capability of the leg actuators. This is basically achieved by minimizing the masses of the highly accelerated leg links. In addition, arranging heavier component parts, in particular the servo motors and gearboxes, close to the articulated joints of the individual links further contributes to improved acceleration behavior of the locomotor system. Taking this approach to its logical conclusion, systematically minimizing the resultant inertia of the *entire* *leg apparatus* and nonlinear effects due to varying inertia can further improve the acceleration capability of the entire leg. Ideally, the individual link inertias should decrease from the base to the end link. However, in many conventional biped robot designs the actuator of a leg link is located at or close to the articulated joint of the link. Hence the entire leg apparatus becomes heavy and bulky which detracts from the desired dynamic performance. It is therefore proposed to locate heavier component parts not only close to the articulated joint of an individual link but near the pivot point of the hip joint, whenever possible.

Note that also the elastodynamic behavior of the drivetrains benefits from lower link inertias since the load inertia enters the calculation of the natural frequency and antiresonance of a drive mechanism, Eq. (3.17) on page 89. The problem is becomes evident in the hip joint: the flexion/extension drive is subjected to high torque loading and alternating speeds with high accelerations. Reducing the load-side inertia increases the antiresonance frequency, along with the capability of the actuator to compensate disturbances and respond to desired actions. Further details are discussed in Footnote 6.

Finally, the performance and robustness of balance control can benefit from a sophisticated leg design. Balance control and real-time trajectory generation are currently only feasible by using simplified models. Most of them rely on an "inverted pendulum model" approach, treating the robot as a single point mass. The modeling error is mainly due to swing leg dynamics and leads to oscillations of the upper body. Although more exact models, e. g., [17], may compensate for some of these errors, the stability margin available for balance control is narrowed by poor leg dynamics if a certain amount of stability reserves accounts for compensating modeling errors. Conversely, greater stability reserves are available for actual disturbances of the robot if the locomotor system is optimized for low disturbances by leg angular momentum and other nonlinear effects.

2.5 Joint Mechanisms

The mechatronic servo systems are among the core units of a walking robot and composed of four major components: *(a)* actuators, *(b)* drive mechanisms, *(c)* state sensors, *(d)* motor electronics (servo controller and drive). In general, operating performance and suitability mainly rely on how well these components are matched. Hence they must be considered simultaneously, along with the kinematic structure of the drive mechanism.

Servo systems for walking robots must cover a large angular velocity range and have high overload capability to cope with task uncertainty. Since joint positions are often held for a certain time, it is desirable to have low-wear when the drives are in reversing operation around zero speed. General requirements on servo systems also apply, including high efficiency and good behavior in steady-state and transient operation. Good steady-state operational behavior is achieved by designing the mechanical hardware for linear system behavior whenever possible. Incorporating transmission components which are free from backlash and stick-slip improves positioning accuracy and enables jerk-free acceleration even at lower speeds. The transient operational behavior is improved by selecting actuators with small time constants and sufficient torque capacity.

This section focuses on the actuators and transmission components which are determined by the loads and the kinematic and mechanical structures of the joints. After discussing the relevant state of the art, the performance and efficiency of different actuator types are analyzed in Section 2.5.1. Suitable precision gears with high reduction ratios and auxiliary transmission components are introduced in Section 2.5.2. The state sensors and motor electronics are discussed in Sections 2.7.2 and 2.8.3, respectively.

Related Work

The prevalent actuation principle of current fully actuated humanoids is the combination of electric motors and reduction gears. Other solutions like fluidic actuators (hydraulic or pneumatic) are rarely used. Gienger [46] showed that servo actuators make almost 31 % of a biped robot's mass: 22.7 % account for the electric motors and another 7.9 % for the reduction gears. Although early prototypes of Honda's biped robots employed ballscrew drives [65], the combination of DC brush motors and Harmonic Drive gears is the de-facto standard for fully actuated humanoid robots, for example [95, 100, 126, 130]. The joints of *Asimo* [65] and *ETL-Humanoid* [122] are driven by both DC brush motors and DC brushless motors[2] through Harmonic Drive gears. *Johnnie* is actuated by DC brush motors and Harmonic Drive gears but the ankle joints are driven by parallel mechanisms with ballscrews [47]. The robot *BIP 2000* [35] is equipped with brushless motors that drive the joints through Harmonic Drive gears or planetary roller screws. The robots *SDR-4X* and *QRIO* are actuated by "intelligent servo actuators," comprising brushless motor, planetary gear and electronics. The units are characterized by high backdrivability and seem to be optimized for mass production [40, 82]. A very interesting concept is realized in DLR's torque-controlled seven-DoF robotic arm *LWR-III* [67]. The joints are driven by very efficient brushless motors called "RoboDrive" through Harmonic Drive gears. These motors are optimized for the demands of robotic applications and recently became commercially available. Only few humanoid robots are actuated by fluidic actuators, for example, hydraulic cylinders [23], or pneumatic muscles [191]. Kaminaga et al. [91] propose a highly backdrivable electro-hydraulic knee actuator with low mechanical impedance for better interaction with human beings.

2.5.1 Actuators

Although the literature survey in the previous section suggests certain "convergence" towards the combination of electric motors and Harmonic Drive gears, it is worth considering other actuation principles for humanoid robots [81]:

Pneumatic actuators have a rather poor power density and are compliant due to air compressibility which makes them unsuitable for position-controlled servo applications.

---

[2] See the clarification of brushless motor terminology in Footnote 3 on the facing page.

Hydraulic actuators have an unmatched power density and a high-dynamic behavior. However, the hydraulic power unit and the auxiliary system makes them rather complex and bulky. Provided that the entire hydraulic system must be integrated on the robot in order to maintain mobility, the power-to-weight ratio of these actuators decreases rapidly.

The support system of an electric motor on the other hand, consists of the power electronics and a controller unit and is normally by far less bulky. Therefore, electric motors are chosen to actuate the robot. Brushed DC motors and electronically commutated motors are most suitable for servo applications requiring high power density:

Brushed DC motors (BDCM) The windings of a BDCM are attached to the rotor, the permanent magnets to the stator. Mechanical commutation allows the control of motor speed by applying a pulse-width modulated voltage. Several designs with optimized speed and positioning performance are available for servo applications: the bar-armature, disc-armature and bell-type armature motors. The latter two have an ironless rotor and a winding molded with epoxy in the shape of a disc or tube. The advantages are low inertia, no iron losses, and smooth output with low torque ripple. However, duty-cycle limitations arise from the low thermal capacity and limited thermal paths to the motor housing. The mechanical commutation principally limits the maximum speed and output of a BDCM and severely narrows the permissible peak torque.

Electronically commutated motors (EC motors) Unlike BDCM, the rotor carries permanent magnets with a certain number of pole pairs. The stator assembly consists of stacked steel laminations holding the phase windings. Hence EC motors are synchronous motors excited by permanent magnets. EC motors exhibit iron losses and cogging torque, the latter can be minimized by a skewed stator and larger pole count. Though multiphase motors are advantageous for some applications that require low-speed operation with high torque as well as high-speed operation, the typical winding arrangement is a three-phase configuration in either star or delta connection. EC Motors can be distinguished by the shape of the back-electromotive force (back-EMF): motors with trapezoidal and sinusoidal back-EMF are referred to as *Brushless DC Motors* (BLDCM) and *AC Permanent Magnet Synchronous Motors* (PMSM), respectively[3]. For constant torque output trapezoidal and sinusoidal currents must be applied to the BLDCM and PMSM, respectively.

The decided advantages of EC motors over BDCM are the better robustness and reliability, significantly higher power density and acceleration capability due to the large torque and speed bandwidths. The continuous stall torque rating of EC motors is significantly higher due to excellent cooling properties and low thermal resistance to the environment. Moreover, electronic commutation permits larger

---

[3] Several ill-defined terms are used and mixed up in the literature and technical documents on EC motors: since “AC servo motors” are often referred to as induction motors, the term “AC Permanent Magnet Synchronous Motor” (PMSM) is used for EC motors with sinusoidal back-EMF. EC motors with trapezoidal back-EMF are referred to as “Brushless DC Motors” (BLDCM).

peak torques for longer intervals which is of particular importance when the motors are in reversing operation around zero speed. Although EC motors are simpler in design than BDCM, they require more complex controllers and motor electronics. But the integration level of current power and control electronics allows the cost-effective and extremely compact design of the necessary electronics, making EC motors the de-facto standard for high-performance servo motors in industrial applications.

Comparing the different types of EC motors, BLDCM are apparently easier in control and rotor position sensing: three Hall sensors provide six different switch combinations per (electrical) revolution. The rotating field for a PMSM is usually generated by field-oriented control [149, 166] and requires high-resolution rotor position feedback (encoder or resolver). Both motor types are comparable in small-signal and large-signal dynamic behavior. At higher speeds the commutation torque ripples of a BLDCM are damped out effectively by rotor inertia but severely affect low-speed performance. In particular, the accuracy and repeatability of position-servo performance deteriorates [166]. PMSM on the other hand, have the advantage of lower acoustic noise and torque ripple and are therefore preferred in high-performance speed and position-servo applications.

Servo Motor Selection Rationale

Volume and size of the motors are critical factors in high-performance applications such as robotics. In order to realize the desired motion patterns, the motors must exhibit high power density and provide sufficiently large torque and speed bandwidths. Before actually dimensioning the servo motors (see Section 3.3.2), a motor family is selected by comparing the technical data using different indices.

Several performance measures for robotic servo systems were proposed. For example, the "joint quality measure" by Hirzinger et al. [66] takes into account peak torque, maximum velocity and mass of the servo motor and transmission components. Gienger [46] proposes the "specific dynamic continuous torque" which takes into account motor mass, motor and gear inertia, gear ratio and gear friction. Both indices are based on parameters that can only be determined from the final design. Thus, they are of limited use for component selection in an early design stage, where only catalog data are available. For the pre-selection of a motor family, benchmarks based on publicly available data are necessary. Again, various selection criteria exist [103], and the most relevant ones are:

1. Power density
2. Acceleration capability
3. Efficiency and overall performance

Power density P/m_m [W/kg] cannot be determined reliably if the motor phase voltage is not known yet. Therefore, the ratio of continuous stall torque and motor mass τ_c/m_m [Nm/kg], referred to as "specific continuous torque," is proposed to indicate power density. The motor's acceleration capability can be seen from the peak-torque-to-inertia ratio τ_p/J_m [rad/s^2]. The so-called "dynamic factor" indicates motor acceleration at maximum torque without external load. Usually the inverter is not rated to deliver the current corresponding to the peak torque τ_p, hence the continuous-torque-to-inertia ratio τ_c/J_m $[\mathrm{rad/s^2}]$ is the more reliable figure. Though almost not present in the scientific literature, the motor constant K_m $[\mathrm{Nm}/\sqrt{\mathrm{W}}]$ is very useful for comparing the efficiency and overall performance of permanent magnet motors. Assuming a motor at stall, the current I produces a certain peak torque τ_p but no output power. Then ohmic losses are the only significant power dissipation mechanism and K_m is defined as the ratio of τ_p to the square root of input power, $P_s = I^2R$. Hence K_m is also the ratio of the torque constant K_τ to the winding resistance R:

$$K_m = \frac{\tau_p}{\sqrt{P_s}} = \frac{K_\tau}{\sqrt{R}}\,. \tag{2.4}$$

Although originally defined with respect to larger direct drive motors operating at stall or at very low speeds, the motor constant gives an idea of motor efficiency and is useful for comparing different motors.

Note that all proposed indices are generally winding-independent for a given size motor. The winding is determined by the phase voltage and current requirements, whereas the motor size (diameter and stack length) and power (torque and speed) are determined by the load and performance requirements.

PMSM/BDCM Market Survey

Figure 2.8 compares servo motors from different manufacturers[4]. Figure 2.8(a) and (b) show the specific continuous torque τ_c/m_m as a measure of power density and the continuous-torque-to-inertia ratio τ_c/J_m indicating the acceleration capability, respectively. Figure 2.8(c) shows the motor constant K_m which relates to the motor efficiency. For the best power-to-weight ratio, only motors using rare-earth magnetic material (NdFeB, SmCo) are considered. All motors have an inner rotor design, that is, the rotor is designed inside the stator. This design is preferred in incremental motion applications where low inertia and fast response are required.

Note that the analysis considers both frameless and housed motors. Frameless motors (or kit motors) are delivered as individual components (stator, rotor, feedback sensor) and allow for very compact and lightweight actuator designs. Motor housing and cooling can be tailored to the application, enabling the tight integration into the mechanical structure. The motor shaft and bearing arrangement are designed in the same manner, matching the precise needs of the application. In many cases the direct coupling of frameless motor and reduction gear is feasible and eliminates auxiliary transmission components such as belts, pulleys, auxiliary gears and couplings. Hence the drivetrain is less complex, free from backlash and slip, and the resultant stiffness and bandwidth increase. The housings of commercial motors, on the other hand, are industrially ruggedized and typically made from steel. Also, the rotor inertia of a housed motor includes the shaft and bearings, whereas the inertia of a frameless motor only considers the permanent

---

[4] The analysis compares commercially available BDCM and PMSM from Aerotech [1, 2], Axsys [8, 9], Kollmorgen [28], Maxon [115], Parker Bayside [141], RoboDrive [156], and Wittenstein [202]

(a) Specific continuous torque

(b) Continuous-torque-to-inertia ratio

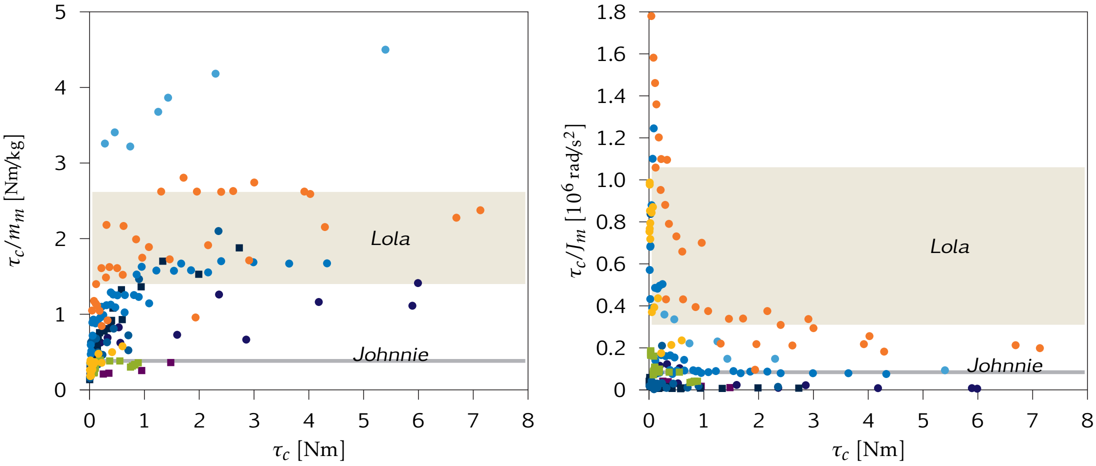

(c) Motor constant

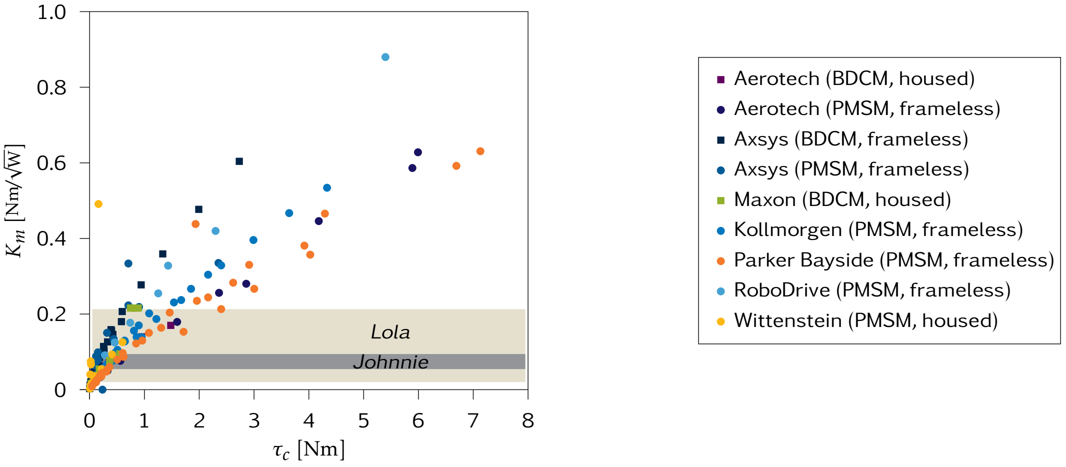

Figure 2.8: Power density, acceleration capability and efficiency of commercial BDCM and PMSM, represented by the *(a)* specific continuous torque; *(b)* continuous-torque-to-inertia ratio; *(c)* motor constant.

magnets. Thus, the comparison between frameless and housed motors using mass-relateed benchmarks is limited. Nevertheless, servo actuators using frameless motors are supposed to have a significantly higher power-to-weight ratio and acceleration capability than actuators based on standard framed motors with the same power rating.

Obviously, PMSM are clearly superior to BDCM both in specific continuous torque and continuous-torque-to-inertia ratio. RoboDrive [156] offers frameless PMSM in a segmented lamination design with a high pole count that are optimized for robotic applications. The motors are characterized by a high torque capacity at low power consumption and losses. Due to the high pole count, these motors are optimized for high torque delivery and efficiency at low and medium speeds. However, motors with high torque and speed bandwidths are required for a humanoid walking robot which is targeted to achieve human-like speeds of locomotion. Frameless PMSM from Parker Bayside [141], on the other hand, show excellent dynamic capabilities at a power density comparable to RoboDrive. Ripple and cogging torque of these motors are minimized by a skewed stator design. Moreover, the large variety of available winding configurations offers great flexibility in matching the motor to the application. Therefore, this motor series is chosen for all joint of the robot, except for the camera head where only very low torque capacity is required.

Compared to the robot *Johnnie*, the power density and acceleration capability rise substantially as indicated by the shaded areas in Figure 2.8. The hip and knee joints are driven by two Maxon motors RE-40 each [115]. As a straightforward measure for enhancing the performance, Gienger [46] proposes to install a third RE-40 motor in parallel. The power density remains constant in this case but, according to Eq. (2.4), K_m only increases by factor $\sqrt{2}$ and $\sqrt{3}$, respectively, if two or three motors are used in parallel. Conversely, the specific continuous torque of *Lola*'s servo motors increases by factor 3.7 for low-performance up to 6.8 for high-performance motors. The acceleration capability increases by factor 3.7 to 12.6 at comparable efficiency.

2.5.2 Drive Mechanisms

The drive mechanism interfaces the motor to the robot link through the joint. It is composed of the main transmission (typically a reduction gear) which interfaces to the joint, and—depending on the structure of the mechanism—additional components for power transmission such as coupler links, belts, or angular gears. The proper placement, sizing and design of the drive mechanisms sets the stiffness, mass, and overall operational performance of the robot [163]. Obviously, all transmission components have to provide the desired torque rating and keep certain overloading capacity, combined with good dynamic performance and sufficient torsional stiffness. Additionally, they must have compact dimensions, low mass and low inertia. Another important factor to achieve high efficiency and reduce the risk of damage in an emergency, is backdrivability[5] of the drive mechanism. In the following, the main transmissions and auxiliary components for power transmission are introduced.

Direct Drives

The kinematically simplest actuation mechanism interfaces an EC motor with high-torque and low-speed characteristics between the links without any reduction gear. Since mechanical gearing is completely eliminated, drive stiffness is high, friction is significantly reduced, and mechanical backlash and hysteresis are removed. Direct drives are fully backdrivable which would be particularly relevant for the sagittal plane joints: similar to human walking [142], the knee and hip actuators would accelerate the links at selected intervals of the gait cycle, while

---

[5] Backdrivability is the ability to move the output of the drive mechanism throughout the workspace without opposition. It is usually characterized by the *backdriving friction* of the mechanism. Backdrivability is usually reduced by certain elements, such as gears and friction in the motors and drive mechanisms.

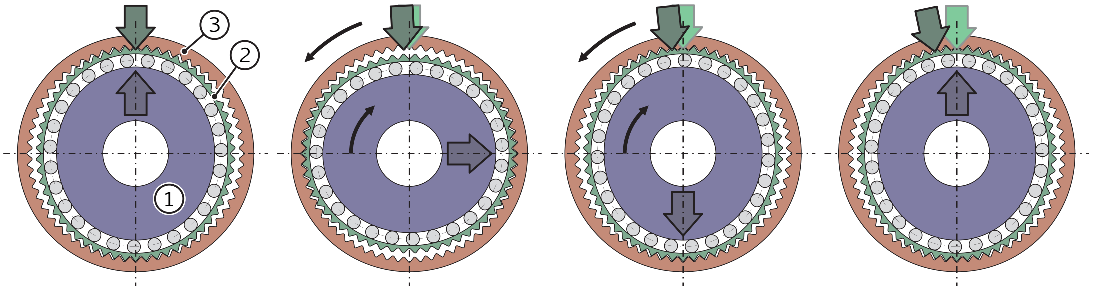

1 Wave Generator | 2 Flexspline | 3 Circular Spline

Figure 2.9: Working principle of the Harmonic Drive gear. The Circular Spline is fixed to the environment and the Wave Generator is driven by an actuator. The arrows indicate the relative position of the Wave Generator and Flexspline.

limb advancement would occur virtually passive. Despite excellent dynamic properties, direct drive motors are heavier and have larger physical dimensions, compared to conventional motor-gear units and require more accurate position sensors and controllers. Therefore, motor-gear units are currently the drive of choice for humanoid robots.

Harmonic Drive Gears

As stated above, Harmonic Drive (HD) gears are the de-facto standard for full-size humanoid robots. The principle of operation is described in detail in [59] and it is summarized here for clarity. The gear consists of three principal components shown in Figure 2.9. The elliptical Wave Generator (1) with ball bearing is usually driven by an electric motor. The Flexspline (2) is a flexible steel cylinder with external toothing, and the Circular Spline (3) a steel ring with internal toothing. The Flexspline has two fewer teeth than the Circular Spline. It is held in an elliptical shape by the Wave Generator, so that its teeth engage with the Circular Spline across the major axis of the ellipse. If the Wave Generator rotates, the zone of tooth engagement travels with the major elliptical axis, and each clockwise turn of the Wave Generator moves the Flexspline two teeth anti-clockwise with respect to the Circular Spline. The advantages of HD gears are well known and include excellent positioning accuracy and repeatability, high torque capacity and superior torque-to-weight ratio, compared to other gear types. HD gears have high single-stage reduction ratios ($30 \leq N \leq 160$), may operate with zero backlash[6], and exhibit high torsional stiffness over the full speed range. Although they can achieve efficiencies of up to 85 %, the frictional behavior is complex and depends for instance on manufacturing and assembly tolerances [177]. HD units are reversible and backdrivable. However, efficiency decreases significantly when in backdriving: a comparison of catalog data shows that the "no-load backdriving torque" is approximately 23 % higher than the "no-load starting torque" required to commence rotation of the Wave Generator with no load applied to the output.

---

[6] The gear teeth of HD gears have no backlash. But there are hysteresis losses (typically <3 arc min) and so-called "lost motion" (typically <1 arc min), resulting from the torsional stiffness in the low-torque region [59].

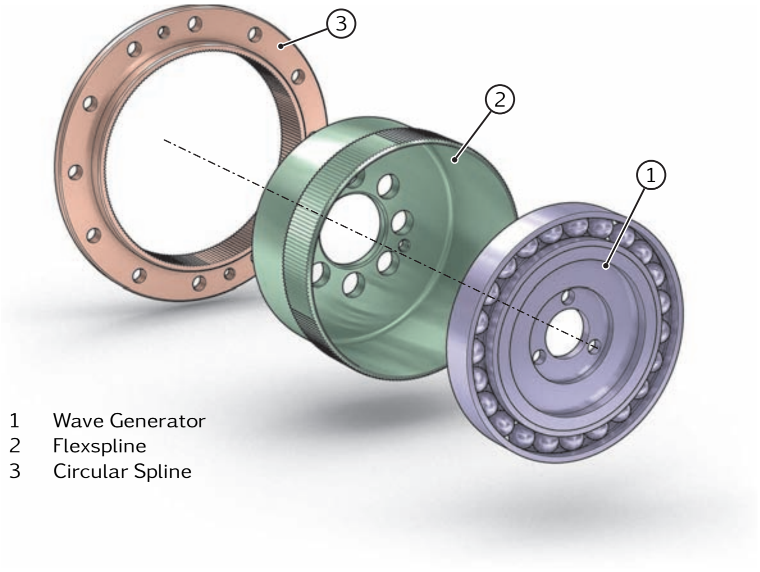

Figure 2.10: Harmonic Drive component set in a customized lightweight version. The Circular Spline has a T-shaped cross section, the Wave Generator plug is a solid body made from aluminum without Oldham coupling.

Due to the many advantages, HD gears are employed as speed reducers in most joints. As shown in Figure 2.10 the customized lightweight versions have a T-shaped Circular Spline to reduce weight and inertia while maintaining high radial stiffness. The solid Wave Generator plug has an optimized geometry and omits the Oldham coupling of the standard versions. To further reduce weight and inertia, special aluminum with almost the same thermal expansion coefficient as steel is used for the Wave Generator plug of some gears. Compared to other experimental lightweight solutions [174], these modifications are an economically justifiable tradeoff between weight and load rating. During the robot development, the new *CPL Series Lightweight Component Sets* [57] became available as off-the-shelf products, showing basically the same design features as the custom-made lightweight versions used in the robot. For joints that are subjected to smaller loads (e. g., the camera head), off-the-shelf gearboxes are the best choice with regard to weight and compactness: the *CSF Mini Series Gearboxes* [58] are very compact, standardized gearboxes with integrated rigid four-point contact output bearing. The *RSF supermini servo actuators* [60] combine gearbox, AC servo motor and encoder in a very compact package.

Ballscrews and Planetary Roller Screws

The drive mechanisms of knee and ankle joint (cf. Section 2.6 on pages 53–56) require the transformation of the motor's rotary motion into translational movement. Ballscrews and planetary roller screws are perfectly suited for such applications. They are characterized by high efficiency, smooth and silent operation without jerk, and no stick-slip:

Ballscrews use balls as rolling members to transfer the load between the screw and nut. These machine elements are widely used in mechanical engineering

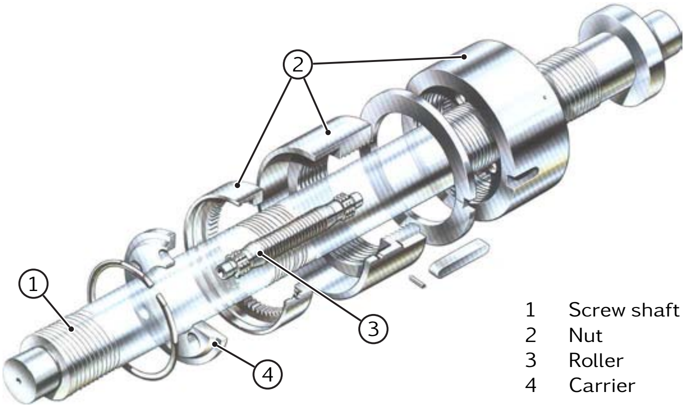

Figure 2.11: Mechanical design of a planetary roller screw (adapted from [78])

so that a large variety of types is available, e. g., [173], including special and application-specific designs (actuated nut systems, large-lead screws, etc.). The permissible rotational speed is limited by the ball recirculation system in the nut housing. The static and dynamic load rating are determined by the number of contacts and the contact areas between the balls and the nut or screw, respectively. As the number of contact points is limited by the ball size and other design factors, the obvious way of increasing the load capacity is to select a screw with larger diameter. For joints that must cover a wide speed range and are subjected to high loads (such as the knee joints), however, shaft inertia and weight increase significantly. A very expensive measure is to employ customized hollow-bored screw shafts which have reduced inertia and weight and higher critical rotating speed but lower axial stiffness and maximum permissible compressive load.

Planetary roller screws have grooved rollers as rolling members and are less common than ballscrews. The components are shown in Figure 2.11. The screw shaft (1) has a multi-threaded profile. The nut (2) has an internal thread which is complementary to that of the screw shaft. The rollers (3) have a single-threaded profile and are constantly engaged with the screw (1) and the nut (2). In addition, rollers and nut are geared together to avoid slip and the rollers are supported by carrier (4) to insure equal spacing. The operating mechanism of a planetary roller screw is analogous to the motion of a planetary gear, and one revolution of the screw shaft results in an axial displacement on the nut corresponding to its lead [78]. The number of contact points is significantly higher than at similar-sized ballscrews and goes along with considerably higher static and dynamic load ratings. Moreover, the large number of contact points results in greater axial stiffness and better tolerance against shock loading. Since there is no recirculation system necessary for the rolling members, the rotational speed is limited only by the centrifugal forces in the nut. Planetary roller screws can therefore be operated at higher speeds and can withstand higher acceleration and deceleration rates.

For minimal inertia it is advisable to actuate the lead screw shaft and move the nut along the shaft. The rolling contact makes ballscrews and planetary roller

Table 2.2: Comparison chart of Harmonic Drive gears, ballscrews and planetary roller screws

Criterion	Harmonic Drive	Ballscrew	Planetary roller screw
Load ratings	++	+	++
Lifetime	++	○	++
Output speed	+	++	+
Positioning accuracy	++	++	++
Backlash	No[*]	No[†]	No[†]
Backdrivability	○	+	+
Stiffness	+	+[†]	++[†]
Shock loads	○	○	++
Space requirements	++	+	++
Available range of reduction ratios	+	++	+
Efficiency at nominal torque	≥ 85 %	≥ 90 %	≥ 90 %
Backdriving efficiency	○	++[‡]	++[‡]
Power density	++	+	++

[*] There are hysteresis losses and so-called "lost motion" in the low-torque region.
[†] Pre-loaded nuts eliminate backlash and increase stiffness.
[‡] The backdriving efficiency depends on the pre-load, screw diameter and pitch.

screws backdrivable under almost all circumstances. The frictional behavior of ballscrews and planetary roller screws is similar: efficiency depends on the working conditions (e. g., load, speed, lubrication, preload) and is typically above 90 %. The "direct efficiency" which defines the torque required to transform the rotation of one member into the translation of the other, and "indirect efficiency" which relates to the axial load required to transform the translation of one member into the rotation of the other one, differ by less than 0.5 %. Hence the reversal of movement is much more efficient than at Harmonic Drive gears. The nuts can be preloaded to eliminate backlash and/or to increase axial stiffness, however, internally preloaded screws exhibit higher friction.

The key characteristics of ballscrews and planetary roller screws are compared to Harmonic Drive gears in Table 2.2. In conclusion, planetary roller screws are employed as main transmissions of the knee and ankle joint drives (cf. Section 2.6), whose design is particularly constrained by space and weight. In addition, their robustness against shock loads makes planetary roller screws particularly suitable for the robot's legs. The higher load rating allow to use smaller screws opposite to ballscrews which finally yields additional weight savings. Due to the reduced diameter, the buckling at compression loading and the critical rotating speed of the screw shaft have to be considered in the dimensioning of the drivetrain and selection of the bearing arrangement.

Other Precision Gear Types with High Reduction Ratios

In addition, two other high-reduction gear types for position servo applications shall be mentioned. However, these gear types are only relevant for higher power ranges because lightweight design are barely feasible:

Planetary gears: through the uniform load sharing of several gears, planetary gears are a very compact solution with high torque ratings and low backlash (typically in the range of 4 arc min or even ≤1 arc min for position servo applications) at efficiencies up to 97 %. Multi-stage planetary gear trains can achieve reduction ratios well over 100. Despite these advantageous characteristics, planetary gears are not suitable as main reduction gears because of an unfavorable power-to-weight ratio. On the other hand, the overall torque-to-weight ratio of an actuator can be improved by integrating a planetary pre-stage within the Wave Generator of a Harmonic Drive gear [174]. Such units provide high reduction ratios in a compact space envelope, enabling the use of high-speed motors with a high power density.

Cycloidal gear reducers are widely used in the joints of industrial robots. They are characterized by high torsional stiffness, compact measurements and a high efficiency resulting from the rolling contact of all major load transmitting components.

Auxiliary Transmissions

Actuator placement is a tradeoff between weight, link inertia, compliance and complexity of the drive mechanisms. The early actuation concept of the robot aimed at the direct coupling of electric motor and gear unit without any couplings and other auxiliary transmission components in between. Besides reduced weight, such drivetrains are free from backlash and slip and have higher stiffness and system bandwidth. On the other hand, the considerations made in Section 2.4 suggest that actuator relocation by means of auxiliary transmissions is essential to optimize the mass distribution of the legs for high acceleration capability. The longer transmission distance reduces inertia and gravity loading but can introduce compliance and backlash effects. System stiffness and transmission accuracy may be impaired and oscillations of the servo drivetrain may occur. In summary, the positive effects of actuator relocation on global system dynamics are much more significant than the weight savings and greater drivetrain stiffness in the case of the direct coupling of motor and gear unit. Possible transmission elements for actuator relocation are band drives, cable drives, synchronous drive belts, bevel gears and coupler links:

Band drives (e. g., steel, titanium, or aramid cord belt) are generally very stiff and accurate transmission members. They are widely used in industrial applications for the transmission of limited-travel rotational and translational movements, e. g., in SCARA-type robots. Because of the high stiffness and load rating, band drives are usually implemented at the output of a torque motor or conventional motor-gear unit, allowing to separate the entire servo actuator from the joint axis. Using a band drive, it is difficult to span one or more joint axes.

Cable drives are similar to band drives but steel wire ropes or bowden cables are used as transmission members. Cable transmissions are used as tendons in the *WAM Arm* built by Barrett Technology[7] and some humanoids [7, 188], allowing for a low-inertia design and the actuation of multi-DoF joints in a

---

[7] Available at: `http://www.barrett.com/`

differential arrangement. Although it is possible to span one or more joint axes, the stiffness of cable drives is considerably lower than of band drives. Also, it is difficult to achieve a backdrivable wire-driven joint which is free from backlash.

Synchronous drive belts, or timing belts[8], transmit torque and motion from a driving to a driven pulley. They are free from backlash and slip and provide an accurate way for modest speed reductions with an efficiency of 95 % or above. Belt drives are mostly used for power transmission between the motor shaft and the input of a reduction gear, enabling the spatial separation between the electric motor and main transmission, as well as the space-saving integration of the motors into the robot structure. Synchronous belt drives add considerable damping to the system which allows higher gain settings of the motor controller. A disadvantage of belt drives is the added inertia of the belt and pulleys, the latter can be minimized by modifying standard pulleys made from aluminum or plastic. Moreover, synchronous belts add compliance to the drivetrain which can impair transmission accuracy and cause oscillations, if not designed and installed properly [24]. The resultant stiffness of a belt drive is composed of the belt stiffness of the entering (tight) and leaving (slack) sides of the driven pulley, and the belt teeth and cords along the arc of tooth meshing. The most important measure to limit compliance effects is to choose belts with high tensile strength and optimized tooth profile, for example *HTD Synchronous Drive Belts* [24]. In addition, belt pre-tension must be set by an adjustable pulley or idler in order to prevent the belt from sagging and ensure proper tooth meshing under all circumstances. Proper belt pre-tension also increases the tooth stiffness along the arc of tooth meshing.

Angular gears: the drive mechanism of the ankle joint requires the redirection of the axis of rotation from the knee joint axis to the longitudinal direction of the shank (cf. Section 2.6.3). Spiral-toothed precision bevel gears designed for servo applications are used [55] because of smooth power transmission, high load rating at an efficiency ranging from 94 % up to 97 %. Spiral bevel gears have the benefit of very favorable meshing characteristics (in terms of high contact ratio) and curved teeth which are considerably more resistant to distortion than straight or helical teeth.

Coupler links are used in the parallel mechanisms of the ankle joints to connect the outputs of the linear actuators to the foot segment. Under normal operating conditions, coupler links are only subjected to normal forces, enabling a very slender and lightweight design that must only be dimensioned for buckling. Coupler links normally employ spherical and/or universal joints with plain bearings at their ends. Because plain bearings normally introduce backlash which impairs the performance of the joint controller, bearings with reduced clearance must be chosen.

---

[8] Although the term “timing belt” originates from combustion engine technology, it is widely used in mechanical engineering. Still, the term “synchronous belt” which originates from industrial power transmission is used throughout this thesis.

2.6 Kinematic Structure of the Leg Joints

In this section the kinematic structures of the leg joints are developed with special emphasis on the design objectives devised in Section 2.4. The kinematic structure of the robot comprises single-DoF revolute joints and multi-DoF joints. Single-DoF revolute joints, such as the knee and toe joints, can be actuated by either rotary or linear drives. Multi-DoF joints, for example the hip and ankle joints, can be actuated either in a serial or parallel configuration.

Rotary versus Linear Actuation of Single-DoF Revolute Joints

The standard actuation principle for single-DoF revolute joints is the rotary drive where a Harmonic Drive gear that is coaxially with the joint axis interfaces the motor to the robot link. In this case the output bearing of the reduction gear coincides with the joint. Depending on the surrounding construction and/or stiffness requirements, this bearing is designed either as single bearing that can accommodate loads in all directions (radial, axial, moments) or a bearing arrangement (adjusted or locating/non-locating). Spatial separation between the motor and gear unit is rather simple by using auxiliary transmissions, e. g., synchronous drive belts. Moreover, relocation of the whole servo actuator (motor and gear unit) from the articulated joint is accomplished, for instance, by a parallel-crank mechanism that interfaces the gear output to the driven link. Rotary drives based on Harmonic Drive gears are simple in design and control due to the linear relationship of input and output. All rotary drives of the robot can be built on the unit construction principle, thus, they share the identical design but differ in size and output. In conventional leg designs all joints are driven by such “conventional” revolute joints, forming an open kinematic chain of a series of cantilever beams. While the mechanical design is rather simple, the mass distribution of such structures is adverse, if the motors are coaxial or co-located with the articulated joints. Moreover, insufficient static and dynamic stiffness of the structure and transmission components (cf. Sections 3.3.2 and 3.3.3) can severely limit the dynamic performance of the locomotor system, or at worst destabilize the robot.

It is alternatively proposed to drive a single-DoF revolute joint through a mechanism based on a linear actuator. The actuator connects to the driven link for example by a slider-crank mechanism or acting as a length-variable coupler within a four-bar mechanism. Again, this approach enables the spatial separation between the entire drive from the joint to reduce its inertial contribution. The transfer behavior of such mechanisms is nonlinear which makes joint control more difficult since the nonlinearities must be taken into account. On the other hand, the non-uniform transmission ratio can be utilized advantageously by adjusting the mechanism to the torque-speed characteristics of typical movements of the robot. For example, the mechanism can be designed such that the transmission ratio increases where higher joint torques occur, and decreases in ranges of higher speeds. Moreover, the stiffness of the joint and surrounding structure increases as the leg link and the linear actuator and the mechanism form a closed kinematic chain. However, four-bar mechanisms are more complex in design and manufacturing, and the several bearings may introduce backlash.

Serial versus Parallel Actuation of Multi-DoF Joints

In case of serial actuation the individual joint axes are treated as single-DoF joints, so that the above considerations apply here, too. Since each axis of rotation is actuated independently, the kinematics are easy to control. Mechanical end stops can be applied easily and the unit construction principle of the motor-gear units simplifies the mechanical design.

Driving a multi-DoF joint in a parallel arrangement often results in a more uniform load distribution among the actuators, hence the drives can be smaller in size compared to the serial arrangement, which goes along with additional weight savings and less power consumption. Parallel kinematics can be actuated by rotary and/or linear drives which are often situated on the base link. In contrast to a serial configuration, the moving mass and inertial contribution are reduced significantly. The stiffness of parallel structures is usually high but depends on variable lever arms that result from the moving articulation points of the mechanism. The workspace is to a large extent constrained by the mechanism itself, i. e., by kinematic singularities and self-collisions. Hence the ratio of the workspace to the size of the mechanism is sometimes poor. Also, self-collisions determine the shape of the workspace, which is typically non-rectangular. In consequence, mechanical end stops are difficult to apply and of limited use. Rather, the software-based monitoring of the workspace is necessary to avoid self-collisions. The design, manufacturing and assembly of parallel mechanisms are more involved due to the higher part count and a large number of bearings. It is thus more difficult to achieve the same accuracy as with a serial mechanism.

The kinematics of parallel mechanisms are typically described as a set of non-linear equations. Calculating the manipulated variables for motor control in real-time is computationally expensive, in particular if no closed-form solution exists. Therefore, the solution is often obtained off-line and read out from lookup tables in real-time mode.

2.6.1 Hip Joint Actuation

The three-DoF hip joint is the root joint of the cantilever leg structure. Situated between the thigh and pelvis, it allows three independent rotations of the thigh. During locomotion, the hip joints are subjected to high moment loadings that result from the high impact forces at initial contact and the propulsive forces and angular momentum of the swing leg. Therefore, a well thought-out design of the kinematics and mechanical structure are crucial to the dynamic performance of the legs. In particular, high stiffness of the hip joint structure and bearings minimizes oscillations of the leg endpoints that may at worst destabilize the robot.

Related Work

All full-size humanoid walking robots incorporate three-DoF hip joints. As an example, the hip joint of the robot *Johnnie* is built in a serial configuration. The internal/external rotation joint is screwed to the pelvis. For better power distribution among the drives this joint is inclined 15° to the vertical axis [46]. It is followed by the adduction/abduction joint and the flexion/extension joint which interfaces to the thigh. While the first two joint axes intersect in one point, the adduction/abduction and flexion/extension axes are offset from one another for simplified mechanical design and easier integration of the actuators. A different structure is applied to the robots *HRP-2* and *HRP-3*. The internal/external rotation axis is situated close to the sagittal plane, resulting in a cantilever structure of the hip joint. The so-called "cantilevered crotch joint" reduced collisions between the thighs and allows for walking in confined areas [95, 96]. Nakamura et al. [123] propose a "double spherical joint" for the robot *UT-θ*. The spherical hip joints of both legs have a shared center of rotation in the sagittal plane to fully decouple the movements of the trunk and legs. To the author's knowledge, very few robots have a parallel mechanism applied to at least two hip joint DoFs. Konno et al. [102] adopt a mechanism to the robot *ROBIAN*. A parallel mechanism composed of two linear actuators drives the abduction/adduction and internal/external rotation joints. The flexion/extension joint is driven independently by a rotary drive. Hofschulte et al. [70] develop a three-DoF spherical parallel hip joint for the robot *LISA*. All motors are situated in the pelvis. A spherical ball bearing unloads the mechanism from the robot's mass. The complex mechanism is composed of several spatial links and shows considerable compliance. The three-DoF hip joint of the robot *iCub* uses a two-DoF cable differential mechanism in the flexion/extension and abduction/adduction axes, the internal/external rotation of the thigh is actuated independently [188]. Finally, Rosheim [158] provides an extensive survey of three-DoF wrist designs for industrial robots on the basis of serial and parallel actuation principles, which can serve as a source of inspiration.

Solution Approach

The individual axes of the hip joint show very different loading profiles (see Appendix D). While the internal/external rotation and adduction/abduction axes are subjected to moderate torque loadings at small motion arcs, the flexion/extension axis is among the highest loaded leg joints. These characteristics suggest the use of a parallel mechanism for the hip joint. However, the large angular workspace of the flexion/extension axis makes the realization of a reliable three-DoF parallel mechanism very difficult. The problem is reduced by combining a two-DoF parallel mechanism with a third axis that is driven independently. While the comparatively small angular ranges of the internal/external rotation and adduction/abduction axes allow the design of a mechanism without considerable posture-dependent stiffness variations, this architecture does not fully utilize the advantage of load distribution. The highly loaded flexion/extension axis with is large motion arc is actuated outside the parallel structure. Conversely, a mechanism comprising the adduction/abduction and flexion/extension axes avoids these shortcomings, however, the large workspace of the flexion/extension axis makes the realization very difficult. Moreover, the posture-dependent stiffness may cause unacceptable deflections or structural vibrations at higher loads.

The positive experience of the *Johnnie* project, on the other hand, suggests to actuate the hip joint in a serial configuration. The proper kinematic and mechanical design ensures a high static and dynamic stiffness and can improve the load distribution among the drives. Three serial drives compose a spherical joint with all axes intersecting in a single point. The principle axes arrangement is identical to the robot *Johnnie* because it avoids singular configurations in the desired range of motion: *(a)* internal/external rotation, *(b)* adduction/abduction, *(c)* flexion/extension. Furthermore, the inclination of the rotation joints is kept for a better power distribution among the drives [46].

In conclusion, serial actuation is preferred for the hip joint because the mechanical design is less complex compared to parallel mechanisms. The development risk is low, provided that the connecting links and joint bearings are designed for high stiffness and direct force flux.

2.6.2 Knee Joint Actuation

The knee is the second highly loaded joint in the kinematic chain of the leg. The goal is to develop an actuation principle which allows to enhance actuator performance while thigh inertia is kept minimal.

Related Work

The knees of all full-size humanoid robots are designed as one-DoF hinge joints and mostly actuated by Harmonic Drive gears. Using synchronous belt transmissions, the electric motors are situated either in or close to knee joint axis, e. g., [46, 140] or close to the hip joint, e. g., [94, 127]. A very different concept is realized in the robot *UT-θ*: the knee joint allows only unilateral torque transmission from the knee actuator to the shank. The so-called “backlash clutch” allows the shank to swing freely, exploiting its passive dynamics [134]. Espiau and Sardain [35] employ slider-crank mechanisms in the knee joints of the robot *BIP 2000*. The planetary roller screw drive is fixed to the thigh and connects to the shank with a coupler link. A linear bearing is required to keep the roller screw free from radial loads. A patent application filed by Honda [51] claims another approach to reduce thigh inertia: the rotary drive (motor-gear unit) for knee actuation is placed close to the hip joint. The output torque is transmitted to the knee joint by a parallel-crank mechanism. Another patent application by Honda [181] proposes a counterbalancing system based on a gas spring, similar to the mechanisms employed in industrial robots. The gas spring acts in parallel to the knee actuator and serves to minimize the moments generated about the knee axis when the knee is in motion and at rest.

Solution Approach

In the following, different kinematic configurations of the knee joint are analyzed in terms of dynamic properties and simplicity of design. Figure 2.12 depicts four possible kinematic chains. Although all mechanisms in question have a planar structure the kinematic analysis is conducted in 3-D, taking into account manufacturing and mounting tolerances, as well as elastic deformations during operation. Kutzbach-Gruebler’s equation is used to calculate the degree of freedom or mobility of a kinematic chain:

$$m = 6(n-1-j) + \sum_{k=1}^{j} f_k \,. \tag{2.5}$$

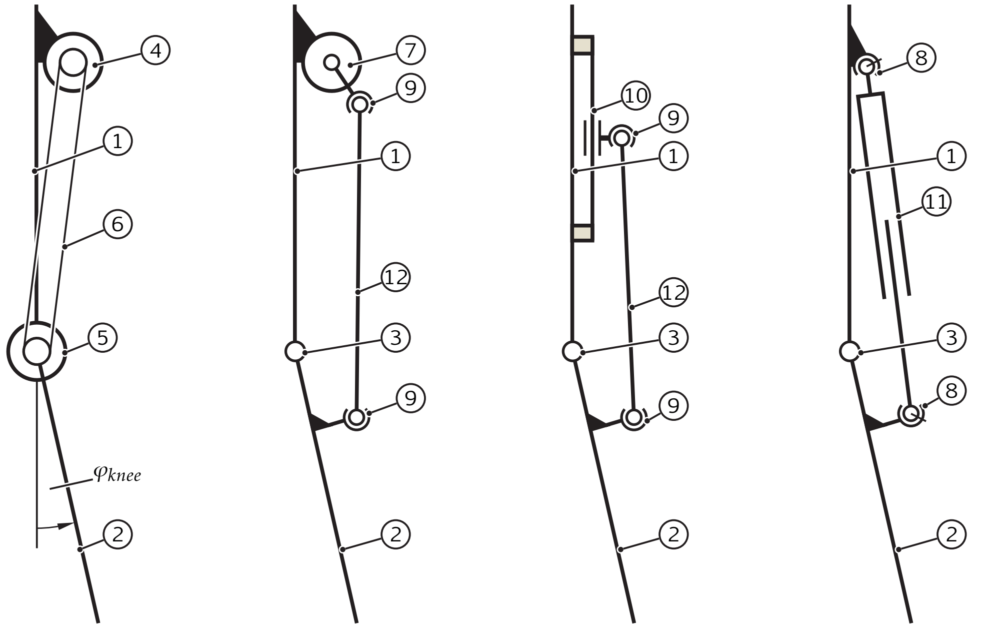

(a) Solution K1 (b) Solution K2 (c) Solution K3 (d) Solution K4

1	Thigh	5	Gear unit ($b = 1$)	9	Spherical joint ($b = 3$)
2	Shank	6	Belt drive ($b = 1$)	10	Linear carriage ($b = 1$)
3	Knee joint ($b = 1$)	7	Motor-gear unit ($b = 1$)	11	Linear actuator ($b = 2$)
4	Electric motor ($b = 1$)	8	Universal joint ($b = 2$)	12	Coupler link

Figure 2.12: Kinematic actuation principles for the knee joint

Here n is the number of links, j the number of joints and f_k the number of DoFs of joint k. The chain is statically determinate for $m = 0$ and indeterminate for $m < 0$. The chain may move for $m \geq 1$ where m denotes the number of independent motion variables that governs the motion of the mechanism.

The first solution approach K1 shown in Figure 2.12*a* is the conventional design which is well-known from nearly all humanoid robots. The electric motor (4) is placed near the hip joint and connected to the gear unit (5) in the knee axis via the synchronous belt drive (6). Similar configurations with a coaxial assembly of motor and gear in the joint axis are not considered because of unacceptable dynamic properties. Placing the motor near the hip joint significantly reduces the thigh inertia, yet the gear unit remains coaxially with the articulated joint axis. Thus, this solution is unfavorable because the high joint loading requires a large and rather heavy gear unit. Compared to a motor-gear unit situated in the knee joint, thigh inertia is reduced only marginally, and a considerable portion of the hip joint performance must spent on accelerating the heavier thigh.

Solution idea K2, Figure 2.12*b*, complies with a claim in [51]. The structure of the mechanism[9] is $\underline{R}SUR$ with mobility $m = 1$. It comprises a rotary motor-gear unit (7) located next to the hip joint. The knee (3) is driven by a parallel-crank

---

[9] The common notation for lower kinematic pairs is as follows: R – revolute pair ($f = 1$); P – prismatic pair ($f = 1$); H – helical pair or screw pair ($f = 1$); U – universal pair ($f = 2$); C – cylindrical pair ($f = 2$); S – spherical pair ($f = 3$). If the joint is actuated, the corresponding letter is underlined, e. g., $\underline{R}$ or $\underline{H}$.

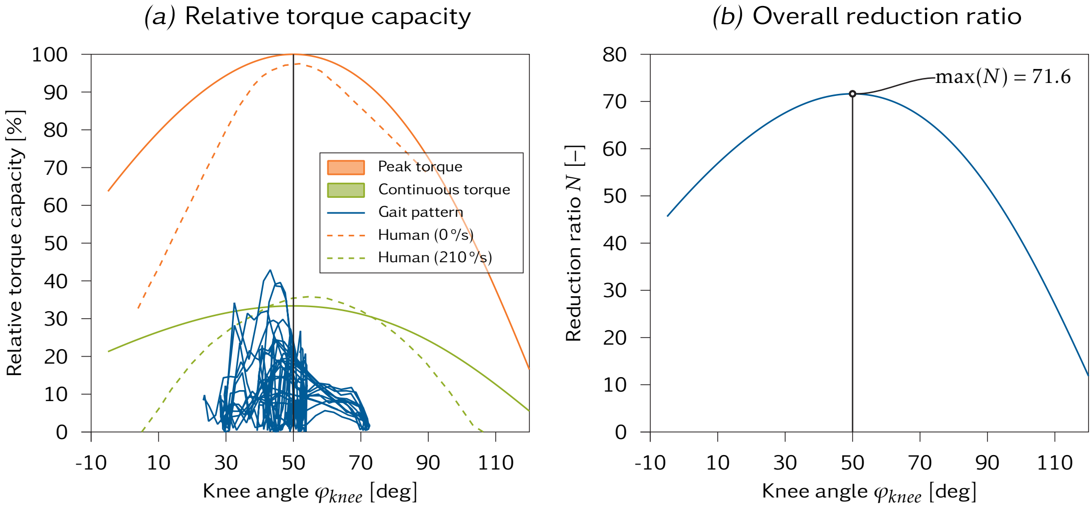

Figure 2.13: Torque-speed characteristics of the knee joint mechanism. The knee joint angle definition complies with Figure 2.12*a*. The human torque capacity data in plot *(a)* are adapted from [142].

mechanism. The coupler link (12) comprises spherical bearings (9) at its ends[10]. Kinematic singularities limit the angular range of the gear output to less than half a rotation. Furthermore, the four-bar mechanism induces high bending moments in the crank and follower links and high tension/compression forces in the coupler link. The output bearing of the motor-gear unit must therefore show high load carrying capability and tilting rigidity.

Solution approach K3 illustrated in Figure 2.12*c* is a slider-crank mechanism. The mechanism has the structure $\underline{P}SUR$ with mobility $m = 1$ and is similar to the design proposed in [35]. The linear guide (10) is fixed to the thigh (1) and connects to the shank (3) by the coupler link (12) which employs spherical bearings (9) at its ends. The actuator of the linear carriage (7) is either based on a ballscrew or planetary roller screw, and omitted here for clarity.

Solution approach K4, Figure 2.12*d*, proposes another four-bar mechanism. Assuming the thigh (1) as the fixed member of the linkage, the linear actuator (11) comprises the two intermediary links of the mechanism. The linear actuator (11) is universally mounted (8) in the thigh (1) and shank (2) and acts as length-variable coupler. Hence the structure is $S\underline{H}UR$ with mobility $m = 1$. As with the two previous approaches, this solution shifts the large proportion of the drive's mass close to the hip and knee joint performance is increased while the thigh moment of inertia is kept low. Therefore, this solution approach is adopted in the design of the robot. The torque-speed characteristic of this "muscle-like" mechanism K4 is nonlinear and corresponds to the human knee [142]. As illustrated in Figure 2.13, the torque depends on the link position and has its maximum at around 55°, which is advantageous for typical gait patterns of the robot. Conversely, the maximum speed increases at a stretched leg configuration, where they are needed.

---

[10] Spherical bearings simplify the mechanical design but allow rotation of the coupler link about its axis. Since this rotation does not affect general mobility of the mechanism, it is considered as a passive or redundant degree of freedom and neglected.

2.6.3 Ankle Joint Actuation

The two-DoF ankle joint connects the foot and shank of the robot. Its motion must allow for shock absorption and weight support and ensure reliable foot-ground contact during stance. The dynamic performance of the ankle joint not only affects gait velocity, rather, it must allow the precise control of the foot torques which are important control variables for robot stabilization [18]. Hence the drive mechanism must be free from stick-slip, it should show only minimal backlash and have good friction behavior (preferably rolling friction). Finally, an appropriate range of motion of the ankle joint is necessary as the dexterity of the foot determines step length and the ability of the robot to step over obstacles and to climb stairs.

Related Work

The ankle joints of almost all full-size humanoids are actuated in a serial arrangement through Harmonic Drive gears, forming a universal joint. plantarflexion/dorsiflexion is followed by the adduction/abduction axis which are fixed to the shank and foot, respectively. This structure allows to easily reduce shank inertia: as granted in a patent by Honda [50], the plantarflexion/dorsiflexion motor can be placed near the knee joint without any additional transmission but a synchronous belt. Most other robots have the plantarflexion/dorsiflexion motor situated close to the ankle joint. The adduction/abduction motor is typically mounted concentrically in the joint axis [50, 94], on the ankle joint segment [127, 130, 140] or — less frequent—near the knee joint [119]. In this case an angular gear is necessary to redirect the motor axis. Another patent application by Honda [118] describes a low-inertia serial structure, where both ankle joint motors are mounted on the thigh segment. The plantarflexion/dorsiflexion gear unit is located on the shank below the knee joint and connects to the ankle joint through a parallel-crank mechanism. The adduction/abduction gear unit is concentric to the joint axis and driven by the motor through synchronous belt transmissions and an angular gear. Ogura et al. [130] propose a serial three-DoF ankle joint for the robot *Wabian-2 LL* with internal/external rotation axis. The kinematic redundancy can be utilized for avoiding obstacles or passing through confined spaces.

Only few robots have a parallel structure implemented in the ankle joints. Espiau and Sardain [35] develop a two-DoF parallel slider-crank mechanism with linear actuators (structure[11] 2-DoF $2-\underline{P}SU$) for the robot *BIP 2000*. The linear drives employ planetary roller screws. They are fixed to the shank and connect to the feet with coupler links. Linear bearings keep the screws free from radial loads. A patent application filed by Honda [51] claims a parallel mechanism based on rotary drives. Two Harmonic Drive gears are mounted coaxially in the knee joint axis. The output shafts on the left and right hand side of the knee drive the ankle joint through spatial four-bar mechanisms (2-DoF $2-\underline{R}SU$). The

---

[11] Parallel mechanisms with identical kinematic chains are denoted as $n-\langle chain\rangle$ where n is the number of kinematic chains, and $\langle chain\rangle$ denotes the type of the kinematic chains, with the last letter denoting the kinematic pair at the end-effector (cf. Footnote 9 on page 54). Since the information on the type of kinematic chains and the number of actuators is not sufficient for determining the mobility of the mechanism, the latter is stated explicitly.

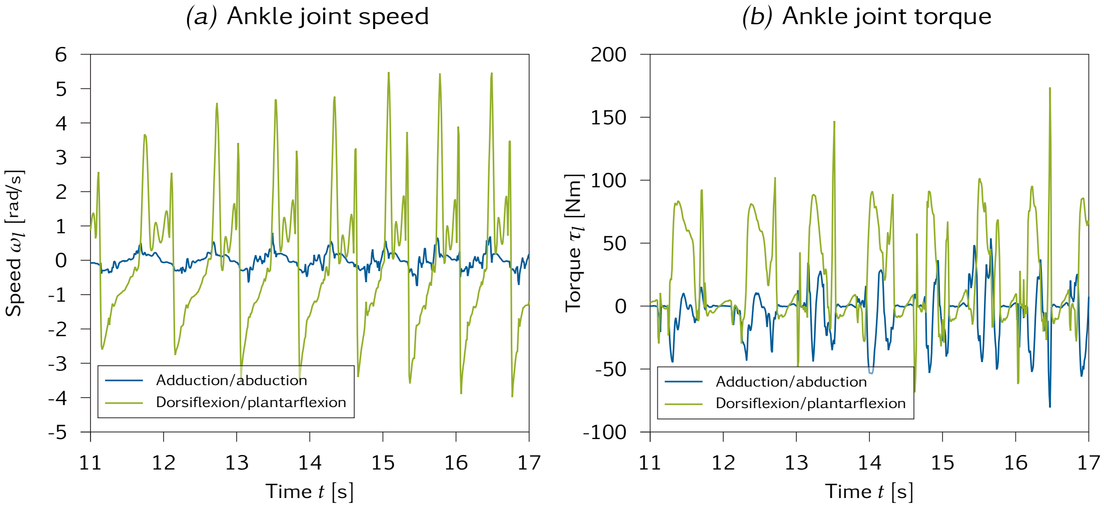

Figure 2.14: Torque-speed requirements of the two-DoF ankle joint at a walking speed of 5.55 km/h

motors are mounted on the thigh close to the hip joint and connected to the gear input shafts by synchronous belt transmissions. Regarding leg dynamics and lightweight design, this is undoubtedly an excellent solution. GIENGER [46] develops a parallel mechanism by for the robot *Johnnie* which has the structure 2-DoF $2-\underline{H}SS$. Ballscrew-based linear drives are mounted on the shank and drive two push rods which connect to the foot via coupler links. Each push rod is guided by linear ball bearings to keep the ballscrew free from radial loads. Due to the parallel structure the joint torques are distributed almost equally among the two motors, which is the main advantage over Harmonic Drive-based serial structures. Furthermore, torque control of the ankle joint which is an important mechanism in balance control of the robot,benefits from the very low rolling friction without stick-slip and the backdrivability of the ballscrews. During operation the mechanism showed a few shortcomings. The angular workspace is designed for normal walking and “jogging.” But self-collisions limit the maximum step length and the robot’s ability to pass over obstacles and climb stairs: the push rods move in the longitudinal axis of the shank and collide with the robot structure at certain postures of the ankle joint. The push rod bearing arrangement has a cantilever structure where the free length of the push rod depends on the ankle joint posture. Especially for larger plantarflexion/dorsiflexion angles the free length of the push rods increases and increases the inclination of the coupler links with respect to the push rods. The induced bending moments cause considerable deformations of the push rods and severely limit the lifetime of the push rods and their bearings.

Solution Approaches

Figure 2.14 shows the torque and speed characteristics of the ankle joint at an approximate walking speed of 5.55 km/h, obtained from the dynamics simulation model (see Section 3.3.1). Because of apparently different lateral and sagittal dynamics of the robot, both axes differ in their torque-speed characteristics. The peak torques in the adduction/abduction and plantarflexion/dorsiflexion axes are

75 Nm and 175 Nm, respectively, the maximum joint velocities are approximately 1 rad/s and 5.5 rad/s, respectively.

If the ankle joint is actuated in a serial arrangement, a rather powerful drive is required for the plantarflexion/dorsiflexion axis while a less powerful one is sufficient to drive the adduction/abduction axis. Although it is possible (and reasonable) to design tailored drives for both axes which differ in the motor performance and gear output, it is unlikely to achieve significant weight reductions. During stance the kinematic configuration of the leg in ground contact changes and the ankle joint becomes its root joint. The gear units in both axes of the ankle joint must show high torsional stiffness in order to avoid oscillations of the stance leg and to minimize deflection (cf. Footnote 6). Hence the gear size in the adduction/abduction axis cannot be reduced accordingly.

On the other hand, parallel actuation concepts can reduce the motor peak torques significantly. Since the peak loads of both axes do not occur simultaneously, the loads are distributed almost equally among the actuators. Thus, the motors can be identical and smaller in size. Due to positive experience with ballscrew-based parallel mechanisms in the ankle joints of the robot *Johnnie*, all solution approaches considered in the following employ actuators based on ballscrews or planetary roller screws. Figure 2.15 presents three possible kinematic structures for the ankle joint that are based on linear actuators.

Solution approach A1 illustrated in Figure 2.15*a* allows to place almost the entire drivetrain on the thigh. The linear carriages (10) are situated on either sides of the thigh and driven by actuators based on ballscrews or planetary roller screws. For clarity the screws are omitted in the figure. The carriage (10) drives the foot (3) via the coupler links (11) and (12) and the ternary link (13) which rotates about the knee joint axis (4). According to Eq. (2.5), the mechanism has two DoFs and the structure is 2-DoF 2−$\underline{P}SSRSS$. This solution allows an extremely low-inertia design of the legs since most transmission components (in particular, the motors, screws and linear carriages) are housed on the thigh (1). Only the coupler links (12) are assigned to the shank (2). However, the large angular workspace of the knee joint impairs the feasibility of this concept. A rather large stroke of the linear guides (10) is needed in addition to the ankle joint motion to compensate the knee motion. Moreover, the ternary link (13) may cause singularities at larger knee angles. Solution approach A2,Figure 2.15*b*, has originally been proposed in [113]. Its kinematics is similar to the knee joint mechanism presented in Section 2.6.2. The linear actuators (9) act as length-variable couplers and are connected to the shank (2) and foot (3) by the universal joints (7), resulting in the structure 2-DoF 2−$U\underline{H}U$. The mechanism is designed such that only tension and compression loads act upon the drives, enabling the lightweight design of all components. The structure of the drivetrain is rather simple and built from only a small number of components. The linear actuators (9) are identical in design to reduce manufacturing effort and part diversity. The shank length limits the length of the linear actuators (9) and thus the angular workspace of the mechanism. The entire drivetrain is housed on the shank which detracts from the low-inertia leg design. On the other hand, relocating the motors to the thigh is unlikely because the drivetrain would have to span the gimbal-mounting of the actuator (9). Finally, the linear actuators (9)

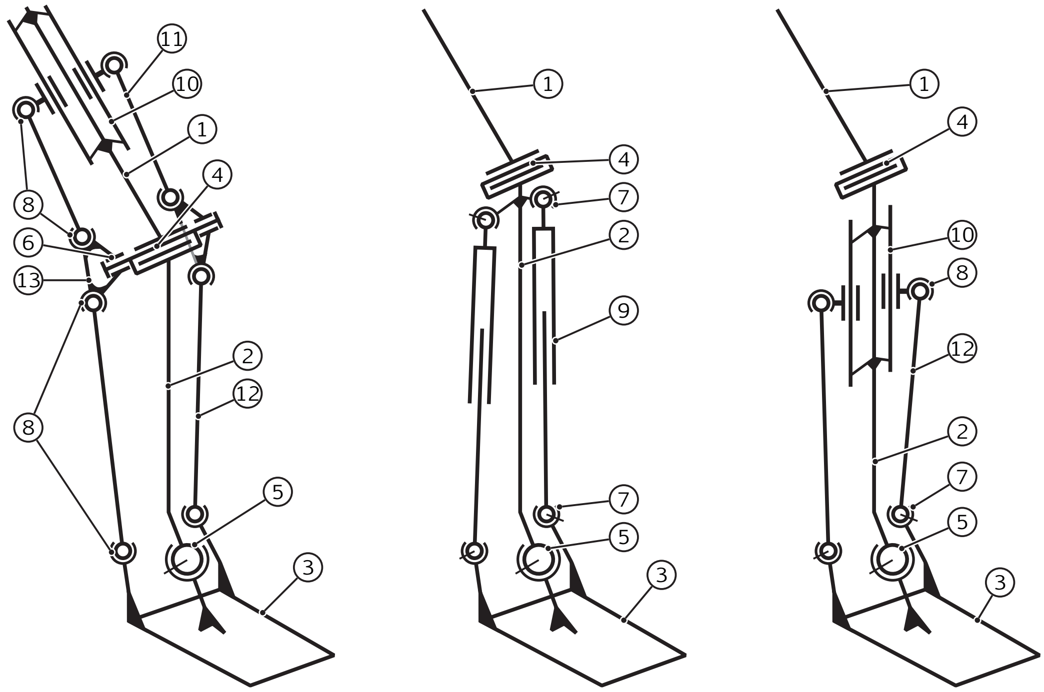

(a) Solution A1 (b) Solution A2 (c) Solution A3

1	Thigh	5	Ankle joint ($b = 2$)	9	Linear actuator ($b = 2$)
2	Shank	6	Revolute joint ($b = 1$)	10	Linear carriage ($b = 1$)
3	Foot	7	Universal joint ($b = 2$)	11,12	Coupler link
4	Knee joint ($b = 1$)	8	Spherical joint ($b = 3$)	13	Coupler plane (ternary link)

Figure 2.15: Kinematic actuation principles for the ankle joint (knee joint actuator omitted for clarity)

are exposed on the back of shank (2) and are easily be damaged in the case of collisions. Solution approach A3 shown in Figure 2.15*c* was first proposed in [111] and is similar to the design adopted to the robot *Johnnie*. The linear carriage (10) is mounted on the shank (2) and actuated by a screw (not shown). It drives the foot by two coupler links (11) which are connected to the carriage (10) and the foot (3) by spherical joints (8) and universal joints (7), respectively. This configuration results in the structure 2-DoF $2-\underline{P}SU$. The main advantage of this solution is that the screws are housed on the shank and protected from collisions. The workspace can be larger than in the previous solution because collisions with the shank are reduced by the slender design of the coupler links (11). Therefore, mechanism A3 is chosen for the ankle joints of the robot.

Until now, Figure 2.15 has considered only the principal structure of the mechanism. The motors and auxiliary transmissions to connect the motors to the mechanism have been neglected and is worked out in the following. Figure 2.16 presents two variants of mechanism A3. Mechanism A3.1 shown in Figure 2.16*a* is the simplest solution. The motors (6) are housed on the shank and connected to the planetary roller screws (9) by synchronous drive belts (7). The posture-dependent inclination of the coupler link (13) induces radial and moment loads to the screw (9). To avoid non-axial loading of the screw, the linear bearing (10) is used to accommodate these loads. The entire drive mechanism A31 is mounted

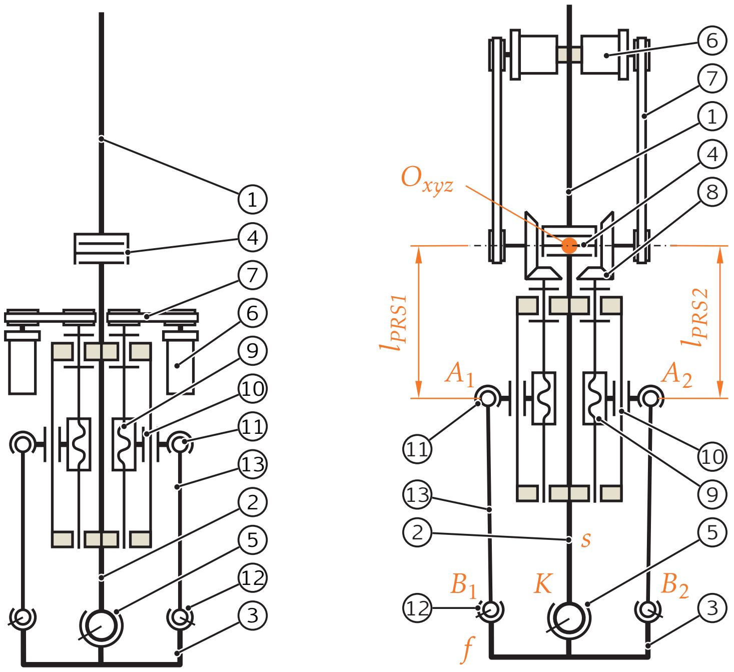

(a) Drive mechanism A3.1 *(b)* Drive mechanism A3.2

1	Thigh	6	Motor	10	Linear carriage
2	Shank	7	Synchronous belt drive	11	Spherical joint
3	Foot	8	Angular gear	12	Universal joint
4	Knee joint	9	Planetary roller screw	13	Coupler link
5	Ankle joint				

Figure 2.16: Possible drive mechanisms for ankle joint mechanism A3. For clarity the mechanisms are projected into the drawing plane.

on the shank which corresponds to the design adopted to the robot *Johnnie* [47]. Although the motors are situated close to the knee joint to minimize shank inertia, the effect on the resultant leg inertia is barely visible. Moreover, because of limited installation space on the shank small-diameter motors with larger stack length must be used to produce the required torques. These motors are normally heavier than larger-diameter motors with shorter stack length at the same power rating. Mechanism A3.2, Figure 2.16*b*, goes one step further. The motors are located on the thigh (1), as close as possible to the hip joint. Power transmission from the motors (6) to the planetary roller screws (9) is accomplished by two synchronous belt drives (7) which connect to angular gears (8). The angular gears (8) are coaxially with the knee joint (4) and redirect the axis of rotation from the knee joint axis to the longitudinal direction of the shank (2). The output of the gearboxes (4) finally drives the screws (9). This design allows to place the heavier transmission components close to the hip joint, reducing their inertial contribution to a minimum. The larger available space in the hip-thigh area allows to use motors with larger diameter and reduced stack length which yields additional weight savings at equal or increased motor performance. The additional transmission components allow for the supplementary adjustment of the reduction ratio, for example by changing the configuration of the belt drive (7) or the angular gear (8). On the other hand, the additional transmission components reduce the overall efficiency. In addition, the angular gear (8) must be designed very carefully to avoid greater backlash on the motor-side. Complexity and part count are considerably higher as opposed to mechanism A3.1. The longer transmission distance between motors (6) and screws (9) is expected to increase the overall mass of the mechanism and goes along with a higher motor-side inertia J_m, which reflects through the gears to the load-side by the square of the reduction ratio. In the final analysis, drive mechanism A3.2 is selected to drive the ankle joint. The advantages of this solution are particularly evident in the effects on global system dynamics due to the minimal inertial contribution.

Using the plantarflexion/dorsiflexion and adduction abduction angles, φ_{fl} and φ_{add}, respectively, the relative Jacobian of rotation for the roller screws is obtained (cf. Figure 2.16*b*). The strokes of the planetary roller screws to adjust a certain posture ($\varphi_{fl}, \varphi_{add}$) are given by:

$$\boldsymbol{l}_{PRS} = \begin{pmatrix} \|\boldsymbol{r}_{OK} + \boldsymbol{A}_{sf}(\varphi_{fl}, \varphi_{add})\boldsymbol{r}_{KB1} - \boldsymbol{r}_{OA1}\| \\ \|\boldsymbol{r}_{OK} + \boldsymbol{A}_{sf}(\varphi_{fl}, \varphi_{add})\boldsymbol{r}_{KB2} - \boldsymbol{r}_{OA2}\| \end{pmatrix}. \tag{2.6}$$

Here $\boldsymbol{r}_{OK}$ denotes the vector from the origin of the shank coordinate system, O_{xyz}, to the ankle joint pivot point, K. $\boldsymbol{A}_{sf}$ is the transformation matrix from the shank into the foot frame, $\boldsymbol{r}_{KB,i}$ are the vectors from the ankle joint to the foot hinging points ($i = 1, 2$) and $\boldsymbol{r}_{OA,i}$ the vectors from the shank origin to the hinging points of the linear carriages. The corresponding screw rotations for given strokes $\boldsymbol{l}_{PRS}$ are

$$\boldsymbol{\varphi}_{PRS} = \frac{2\pi}{P_h}\boldsymbol{l}_{PRS}\,, \tag{2.7}$$

where P_h is the roller screw pitch. The relative Jacobian that relates the angular speed of the screws, $\dot{\boldsymbol{\varphi}}_{PRS}$, to the joint angles, φ_{fl} and φ_{add}, is calculated from Eq. (2.6) in a straightforward manner:

$$\frac{\partial\dot{\boldsymbol{\varphi}}_{PRS}}{\partial\dot{\boldsymbol{q}}} = \frac{\partial\dot{\boldsymbol{\varphi}}_{PRS}}{\partial(\varphi_{fl}, \varphi_{add})^{\mathsf{T}}} = \frac{2\pi}{P_h}\frac{\partial\dot{\boldsymbol{l}}_{\boldsymbol{PRS}}}{\partial(\varphi_{fl}, \varphi_{add})^{\mathsf{T}}}\,. \tag{2.8}$$

Finally, the reduction ratio yields from Eq. (2.8), and the reduction ratios of synchronous belt drive and angular gear, N_{belt} and N_{bevel}, respectively:

$$\boldsymbol{N} = N_{belt} \cdot N_{bevel} \cdot \frac{\partial\dot{\boldsymbol{\varphi}}_{PRS}}{\partial\dot{\boldsymbol{q}}}\,. \tag{2.9}$$

The resulting speed-torque curves of the ankle joint motors are compared in Figure 2.17 to the serial actuation of the ankle joint axes using conventional gear units. Note that, since drive mechanism A32 spans the knee joint, the motor speeds ω_m are also a function of the knee angle, φ_{knee}. Without loss of validity, the knee angle can be assumed constant during the mechanism design, hence the relative Jacobian, $\partial\omega_m/\partial\dot{\boldsymbol{q}}$, is given by Eq. (2.8). For better comparison, the reduction ratios for serial actuation match the mean ratio of the parallel mechanism ($N_{avg} \approx 58$). The motors in the serial configuration show apparently different torque-speed

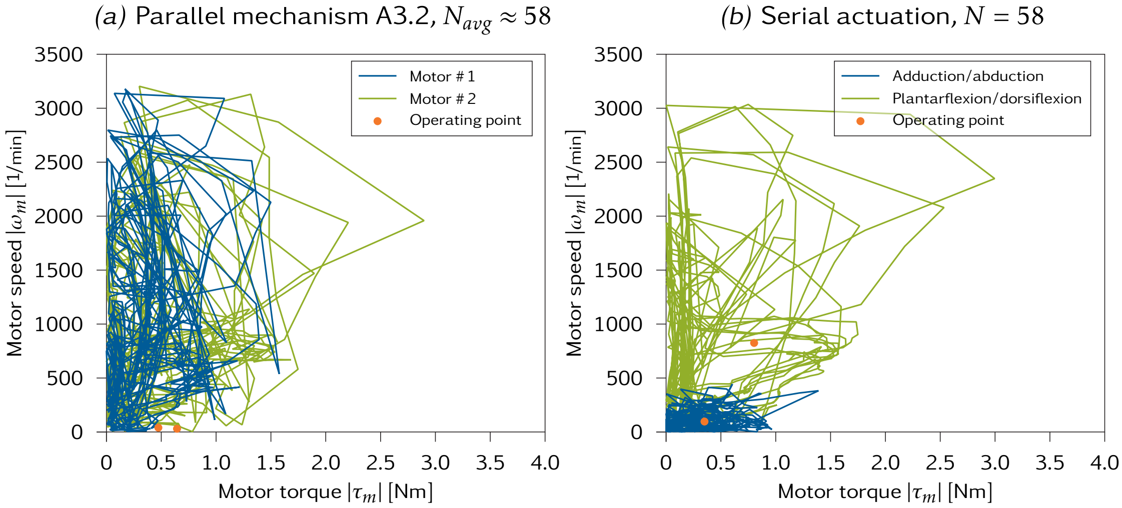

Figure 2.17: Torque-speed diagrams for the ankle joint motors in serial and parallel configuration, cf. [113]

requirements. While the plantarflexion/dorsiflexion axis is subjected to high torques over a wide speed range, the adduction/abduction motor has to deliver rather low torques at considerably lower speeds. Thus, the motors differ clearly in their output power. At a first glance it seems that the motor power increases for the parallel configuration. The speed ranges of both motors are equal while the motor torques remain comparable to the serial setup. However, the continuous operating points, determined by the average speed and torque (cf. Figure 3.2) show a significant reduction of the average motor loads.

2.6.4 Toe Joint Actuation

The toe segment is the end link of the leg. The consistent lightweight design of the toe joint is crucial to keep the resultant leg inertia low. The related work on actuated and passive toe joints is presented in Section 2.2.6.

Figure 2.18 shows four possible actuation principles of the toe joint. Solution idea T1 is the standard design using a Harmonic Drive-based rotary actuator mounted coaxially with the toe joint axis, Figure 2.18*a*. This design is adopted to the robots *H6* and *H7* [128] and, presumably, Toyota's running robot [178]. In order to meet the weight and space restrictions the performance of the rotary actuator must be minimized and exceeding reserve capacities must be avoided. Although simple in design and kinematics, the anthropometric proportions (i. e., the joint position) cannot be fully kept because of the dimensions of the rotary actuator. Solution idea T2 shown in Figure 2.18*b* employs a rotary actuator (5) that is situated close to the knee joint on the shank segment (1) to keep its inertial contribution low. The output torque is transmitted to the toe joint (4) by the coupler link (9), forming a four-bar mechanism. Solution idea T3, Figure 2.18*c*, uses a linear actuator (6) on the shank (1) to drive the toe joint (4) via a coupler link (9). The kinematics are similar to the mechanism proposed by Yoon et al. [208]. Both designs allow to locate all major components of the drive mechanism close to

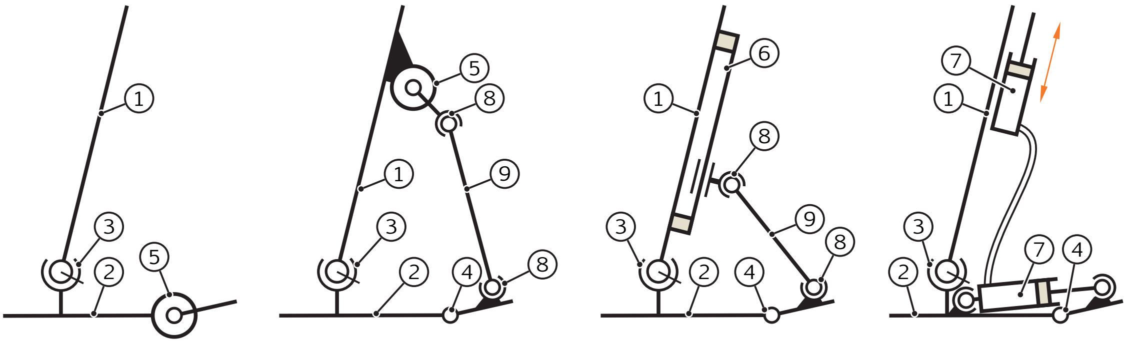

(a) Solution T1 *(b)* Solution T2 *(c)* Solution T3 *(d)* Solution T4

1	Shank	4	Toe joint ($b = 1$)	7	Hydraulic cylinder
2	Foot	5	Rotary actuator ($b = 1$)	8	Spherical joint ($b = 3$)
3	Ankle joint ($b = 2$)	6	Linear carriage ($b = 1$)	9	Coupler link

Figure 2.18: Kinematic actuation principles for the toe joint

the knee joint, reducing leg inertia. Hence the anthropometric joint position is fully kept. However, the actuating force must be transmitted over the two-DoF ankle joint, so that the toe joint actuator must be capable of compensating the ankle joint motion. However, the large angular workspace of the plantarflexion/dorsiflexion axis complicates the realization of solutions T2 and T3. Finally, Figure 2.18*d* illustrates solution T4 which overcomes the difficulties associated with the ankle joint motion. Here, the toe joint is driven by an electro-hydraulic actuator with two linear cylinders in a master-slave configuration. The driving cylinder is located on the shank. It is actuated by an electric motor through a screw drive. The driven cylinder is installed between the forefoot and toe (hallux). Connecting both cylinders by a flexible hose allows to theoretically install the driving cylinder on the pelvis or the upper body, providing the most effective reduction of leg inertia. Despite high power density at compact dimensions, hydraulic systems can develop leakage and the general difficulties with hydraulic systems mentioned in Section 2.5.1 apply, too. The toe joint is therefore designed with a standard rotary actuator, according to solution idea T1. Although other mechanisms may have a smaller impact on leg inertia, the chosen design is advantageous as its kinematics are most simple and there is no interference with other joints.

2.7 Sensor Layout

The sensor system must support the implementation of model-based control algorithms. The variables to be measured are determined from the equations of motion of a rigid multibody system. Further, it is necessary to disambiguate the contact states of the heel and toe segments. Finally, additional variables are required for motor control. Hence the following variables are to be measured for calculating the manipulated variables and controlling the servomechanisms:

1. Vector of generalized coordinates, composed of:
    a) Position and orientation of a frame of reference that is rigidly connected to any of the robot's bodies with respect to an inertial frame. The upper

   body, which is the root link for the kinematic chain in the simulation and control of the robot, is chosen.
   - *b)* Joint angles with respect to the previous link
   - *c)* Joint angular velocities with respect to the previous link
2. External forces, i. e., floor reaction forces and moments
3. Contact state of the feet
4. Additional variables required for field-oriented motor control:
   - *a)* At least two motor phase currents
   - *b)* Angular position of the permanent magnet rotor with respect to the stator windings

The requirements on the inertial measurement system used to estimate the upper body position and orientation are discussed in Section 2.7.1. Sections 2.7.2 and 2.7.3 define the requirements on the joint sensors and the force/torque sensors, respectively.

2.7.1 Upper Body Position and Orientation

The orientation and angular velocities of the upper body are essential control variables for keeping the robot in balance [18]. They are estimated by an inertial measurement system (IMS) which is one of the most important sensors: its accuracy and signal quality considerably affect the performance of the balance controller since the upper body orientation enters into the calculation of the foot positions. At worst, the foot-ground contact occurs too early because of inaccurate and noisy measurements which can easily destabilize the robot.

The IMS works in a closed control loop. The overall bandwidth of the sensor must be 20 to 30 times the bandwidth of the walking gait, so that the closed loop system is not impaired by the sensor dynamics. Assuming a step frequency of approximately 2 Hz, hence the bandwidth of the IMS must be at least 40 Hz to 60 Hz. The dynamics of the robot can be separated into fast and slow subsystems. The fast dynamic corresponds to the motors and the torque-controlled ankle joint. The slow dynamic is due to global system dynamics, represented by the upper body DoFs. Ideally, the IMS should have a data output rate that corresponds to the sampling rate of the balance controller (approximately 1 kHz) but lower rates are acceptable because of the slow upper body dynamic.

Most biped robots employ inertial measurement system that are based on MEMS[12] accelerometers and MEMS gyroscopes, for example [53, 95, 110, 139, 153, 178]. MEMS attitude sensors are widely used in automotive and consumer applications, however, the performance of these sensors is not always sufficient to meet the specifications required in many advanced applications, such as robotics. Notwithstanding, due to the high investment and comparably bulky measurements only few robots employ IMS based on fiber-optic gyroscopes. For example, Honda's robots *P2* and *P3* are equipped with laser gyroscopes [65]. Takahashi et al. [179] develop an inertial measurement system composed of three fiber-optic gyroscopes and three servo accelerometers for a modified version of *HRP-2* at the Digital Human Research Center of AIST. For improved attitude estimation, the

---

[12] Micro-electro-mechanical system

authors propose to take the planned translational acceleration of the robot into account for estimation of the gravity vector. Gienger et al. [48] develop an IMS for the robot *Johnnie* which is composed of three MEMS gyroscopes (measuring range ±150 deg/s) and three MEMS accelerometers (measuring range $\pm 2g$). The orientation of the upper body is estimated using complementary filtering of the gyroscope and accelerometer signals. The IMS transmits the analog sensor signals to the central control unit where the upper body orientation is calculated after digitization. However, the transmission of the analog signals over a longer distance results in rather noisy signals.

In order to define the requirements on the inertial measurement system, the effects of various measurement errors on the walking stability are analyzed using the robot simulation tool (cf. Section 3.3.1):

1. Sensor bandwidth
2. Noisy measurements
3. Data update rate
4. Sensor alignment

First, the overall sensor bandwidth is limited to 80 Hz[13] and 20 Hz. The data output rate of the IMS conforms to the sampling rate of the balance controller of 1 kHz. The robot walks stably in both simulations without visible deviation from the intended path. In the next study analyze the necessary quality of the sensors is analyzed by adding white noise to the accelerometer and gyroscope signals before sensor fusion. Using these noisy signals, the robot walks stably but drifts laterally from its original path. If the noise level is reduced by 5 times oversampling, the lateral drift of the robot is reduced significantly and barely visible. Note that in the case of oversampling the individual sensors are sampled at 1 kHz but the data output rate of the IMS goes down to 200 Hz, hence the upper body orientation and angular velocities are updated every fifth controller cycle. Finally, the influence of alignment errors is analyzed by adding constant angular offsets about the x-axis so that the upper body seems to be tilted sideward. The gait is stable at an alignment error of 0.2° but the robot deviates laterally from the intended path. The stability problems get more emphasized with larger alignment errors. The ground contact occurs unexpectedly at an angular offset of 2.0° which results in a jerky gait and significant lateral drift due to unexpected impacts. After a few steps the robot tips over and falls down. The same behavior is observed during actual experiments with the robot *Johnnie* and leads to the conclusion that the balance controller is very sensitive to alignment errors of the IMS. In summary, the following requirements on the IMS are derived from these results:

- Increase in bandwidth of single sensors is not necessary
- High measurement accuracy
- High signal quality (minimal noise)
- Low offset (long-term bias) is achieved by heading aiding, e. g., by using optical flow
- Reliable adjustment of mounting misalignment, either in hardware or software. Reliable alignment procedure at power-up

---

[13] This configuration corresponds to the *single* bandwidth of the MEMS gyroscopes used in the IMS of *Johnnie*.

– Due to slow global system dynamics, the data update rates of the IMS can be many times higher than the sampling rate of the balance controller

2.7.2 Joint Sensors

The joint sensors acquire the actual position and speed values of the joints. In addition, the motor controller must have an absolute position value of the permanent magnet rotor with respect to the stator windings and at least two motor phase currents available for electrical commutation [166]. The rotary position sensors are important for the control quality since their resolution and accuracy affects the positioning accuracy, speed stability and bandwidth of the servo loop. Instability of the speed control loop can be due to mechanical influence from the drivetrain (e. g., distinct or unmodeled compliance) or low-resolution signals of the position feedback device. Conversely, higher resolution and accuracy reduce disturbances in the motor current, hence the motor operates more quietly with less dissipation. Two architectures for closed-loop motion control systems exist. They differ by the location of the feedback device in the drivetrain which directly affects the quality of the feedback signals.

The indirect measurement of the joint angles and angular velocities relies on an incremental rotary encoder on the motor shaft. The simplicity in system integration and signal processing is supposed to be the main reason why this technique is most prevalent to humanoid robots, examples include [47, 95, 104, 127, 131]. With motor-side position feedback the angular position of the motor shaft is measured and the joint position is inferred through knowledge of the drive mechanism between the encoder and the articulated joint. A repeatable reference point signal within the joint workspace is utilized to obtain the absolute position. The joint velocity is obtained for instance by numerical differentiation of the position signal. The absolute angular position of the motor shaft for commutation is obtained in the same manner and requires a magnetic alignment procedure at power-up. Due to the incremental measuring principle, the zero points of the joints must be determined at every power-up which makes it difficult to start the robot from arbitrary postures. The angular resolution of motor-side feedback depends on the gear ratio which is typically high. On the other hand, the measuring accuracy is affected by mechanical factors such as backlash and transmission errors of the drive mechanism. Furthermore, elastic deformations of the gear and joint under load cannot be detected which severely limits the range of stable loop gains, along with the overall servo performance [197].

Few robots adopt the direct measurement of the joint positions and speeds, for example [7, 188]. Here the actual position and speed values of a joint are obtained by load-side feedback using an absolute angular measurement system. Measuring the joint variables on the output side of the servomechanism avoids drivetrain-induced errors like backlash, hysteresis and other transmission inaccuracies. Also, nonlinearities and compliance in the drivetrain can be compensated within the low-level motor control loops. Using absolute feedback devices, the joint positions must be calibrated once as described in Section 3.11.1, eliminating homing or calibration at power-up. Thus, the robot can (theoretically) start from arbitrary postures, which is vital to real-life scenarios. However, the effect of compliance on the closed-loop performance must as well be considered for load-side feedback. As the controller will encompass unmodeled torsional resonance modes [197], substantial oscillations can arise from different responses of the motor and load side (see Footnote 6).

Unlike most full-size humanoids, each joint of the robot is equipped with an absolute angular sensor for direct measurement of the joint angles. The aforementioned advantages of load-side measurement are particularly evident for the knee and ankle joints which are actuated by complex drive mechanisms with nonlinear transfer behavior, see Sections 2.6.2 and 2.6.3, respectively. An additional incremental rotary encoder is implemented on the motor shaft to provide high-resolution position signals for the electronic commutation of the PMSM. If necessary, this encoder can also serve as a fallback sensor for motor-side position feedback. To improve operational security and to prevent the robot from self-destruction, each absolute angular sensor is complemented by a photoelectric fork sensor to limit the allowed angular workspace. The angular range of each joint is determined by a cam mounted on the output flange. In case of exceeding the allowed workspace, the PWM[14] signals from the motor controller to the inverter are interrupted by the motor controller module with minimal software interaction.

2.7.3 External Forces

The orientation of the upper body is maintained by controlling the contact torques. In addition, active compliance for shock attenuation at initial contact is implemented by force control of the normal contact forces [18]. The precise measurement of the ground reaction forces and moments is therefore essential to the control system of the robot. For most of the implemented control approaches (cf. Section 1.1.2) it is sufficient to determine the vertical force f_z and the lateral moments m_x and m_y by measuring the vertical ground reaction forces at three different points of the contact plane. More sophisticated control strategies, on the other hand, further demand for the tangential forces, f_x and f_y, and the moment about the vertical axis of the contact plane, m_z. For example, these measurements facilitate the compensation of leg tension during double support. Since the robot should provide a high flexibility in the implementation of model-based control strategies, the full contact wrench (forces f_x, f_y, f_z; moments m_x, m_y, m_z) is measured by a six-axis force/torque sensor (F/T sensor) situated within the load path between forefoot and ankle joint.

Most full-size humanoid robots incorporate six-axis F/T sensors in their feet. Most of them use commercial sensors—either off-the-shelf or customized [65, 95, 104, 131] but a few robots employ custom developments. These sensors are designed either as stand-alone devices [46, 99, 140] or as integral parts of the foot structure [44]. The only full-size humanoid without F/T sensors in the feet is Toyota's running robot [178]. While most robot developers rely on well-known design concepts for multi-component force sensors, Nishiwaki et al. [128] adopt different sensor concepts to the robots *H6* and *H7*. The robot *H6* has a three-axis

---

[14] Pulse-width modulation

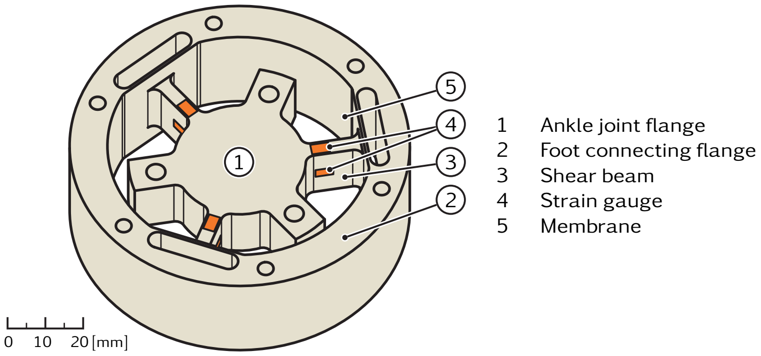

Figure 2.19: Force/torque sensor of the robot *Johnnie* (adapted from [46])

F/T sensor composed of six load cells. Four load cells are located in the toe and two in the forefoot. A six-axis F/T sensor with parallel support structure is developed for the robot *H7* [125]. Using such designs, the force metrology can be tightly integrated to the feet which results in a rather lightweight and compact structure. However, such sensors often suffer from limited accuracy and repeatability due to hysteresis effects caused by backlash and friction in the load cells.

The physics of biped walking yield high vertical ground reaction forces and lateral moments about the ankle joint axes but comparatively small forces and moments in other axes. In addition, high impact transients up to a multiple of the robot's weight occur when the foot hits the ground (cf. Section 2.3). A market survey has shown that commercial six-axis F/T sensors with appropriate measurement range are rather bulky and heavy because of the industrially-ruggedized transducer body made of steel. Moreover, the measurement ranges are equal in all axes which results in a rather low sensitivity of less loaded axes. Most of these sensors require external signal conditioning electronics which are usually too bulky and do not integrate with the electronics architecture. Although the design, manufacturing and calibration of multi-component F/T sensors are very elaborate, the characteristics of the ground reactions suggest the development of a customized solution based on the *Johnnie*-design.

Before actually defining the architecture of the robot's F/T sensors, the custom-made six-axis F/T sensor developed by Gienger [46] is discussed. The monolithic transducer body is made from a high-strength aluminum alloy and holds three shear beams as sensing members. It is shown in Figure 2.19 for reference purposes. Its measurement range is tailored to the ground reaction forces and moments that have been obtained from simulations [109]. The sensor is very compact ($\varnothing 90 \times 30\,\mathrm{mm}^2$) and lightweight, weighing approximately 290 g including signal conditioning electronics. The monolithic transducer body avoids setting and hysteresis effects. Thin membranes reduce cross talk by decoupling the beam deflections to a far extent. Due to narrow tolerances, the transducer body was manufactured by EDM[15] wire cutting. Each shear beam holds four strain gauges which are selected to match the elastic properties of the transducer material. Two opposing strain gauges are series connected, allowing the temperature-compensated

---

[15] Electrical discharge machining

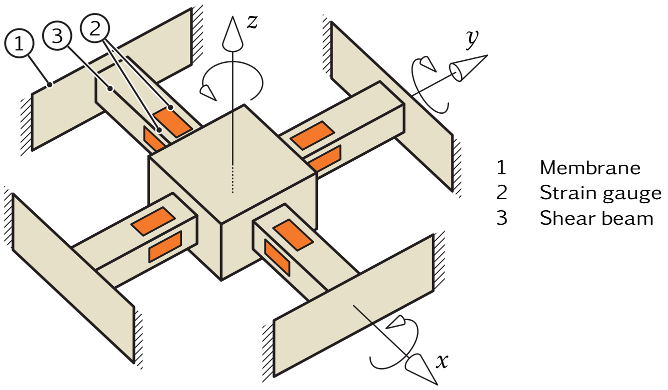

Figure 2.20: Schematic design of a Maltese cross-shaped force/torque sensor

acquisition of biaxial beam bending. The sensor is designed as a stand-alone component with connecting flanges to the ankle joint and foot. Hence modifications of the foot structure are possible without impairing the sensor's function. Since the strain gauges are very sensitive to surface leakage currents, the sensor is isolated from the rest of the robot. However, the low compressive strength of the insulating material caused mechanical failure of the insulating layer after a short operating time. Signal conditioning and offset compensation is contained within the sensor. The analog measuring signals are transferred to the central control unit on the upper body, where the digitization and signal processing are carried out. Hence signal quality and measuring accuracy are impaired by electromagnetic interference. The sensor is calibrated with respect to a reference system located in the middle of the foot support polygon. Although this approach is computationally advantageous to the first implementation of the on-board computer system [46], it complicates changes in the foot geometry.

In the following the fundamental design concept of the F/T sensor is developed, including the measurement principle, the transducer geometry, the integration into the foot structure, and the signal processing.

Because of extensive experience from previous sensor developments metal foil strain gauges are chosen as sensing elements. They have small physical size and low mass and can achieve a very high accuracy in static and dynamic measurements. The resistance change is due to deformation of the surface to which they are attached, which is measured by Wheatstone bridges either in half or full-bridge arrangement. Other physical effects utilized for force measurement are introduced in [187].

Figure 2.20 shows a principal sketch of a F/T sensor in the classic Maltese-cross design. The transducer body holds four equally spaced and crosswise-arranged shear beams as the sensing members. The shear beam geometry is optimized for high sensitivity even of the minor loaded axes without detracting from the sensor stiffness. Hysteresis and setting effects are avoided by the monolithic design of the transducer body. To decouple beam deflection and maximize strain on the beam surfaces, the shear beams connect to the outer sensor frame by thin membranes acting as flexure hinges. For reduced manufacturing effort, the transducer body is manufactured by milling process. Selective sensitivity of certain half bridges for certain forces or moments is achieved by the four-beam design. Moreover, the redundant setup with eight half-bridges can be utilized to improve measurement accuracy. The application of forces beyond the yield point of the gauge pattern is a typical failure mode of strain gauges. Overloading can easily occur during the testing of new control strategies or sudden malfunctions. It may cause permanent damage of the strain gauges and shear beams, finally yielding zero shift, nonlinearity and fatigue of the gauge pattern and transducer. Therefore, the F/T sensor is equipped with an overload protection mechanism.

The F/T sensor is housed on the end link of the legs. A well thought-out lightweight design is therefore essential and affects the measuring accuracy, as well as the integration of the sensor into the foot structure. Significant weight reduction is expected from the tight integration of the sensor into the foot. The sensor frame acts an integral, load-bearing element within the foot structure, eliminating the additional frame structure required for the integration of a self-contained F/T sensor. Hence part count, bolted flange interfaces and, finally, the weight of the entire foot are reduced. To this end, it is necessary to optimize the load-bearing sections of the sensor body for flexural and torsional rigidity. To ensure a high measuring accuracy the deformations of the sensing elements and load-bearing sections must be mechanically decoupled. Further weight savings can be achieved by the intelligent placement of the sensor within the foot structure. In almost all humanoid robots the F/T sensor is situated immediately below the ankle joint. This arbitrary placement results in different moment arms of the forces acting on the heel and toe contact elements and yields a higher moment loading of the sensor. Shifting the sensor towards the center of the foot contact area, the moment loading is reduced while the resolution is increased. Hence the same moment arms account for contact forces acting on the heel and toe, similar to a claim in a patent application by Honda [183].

A/D conversion and signal conditioning are integrated to the sensor electronics, allowing for higher cut-off frequencies of the anti-aliasing filters. In conjunction with oversampling signal quality and bandwidth are improved. The ground reaction forces and moments are then calculated by a microprocessor and transmitted to the central control unit (cf. Section 2.8). The calibration should be independent from the foot geometry to simplify future modifications of the feet. Hence the sensor is calibrated with respect to reference system located at the center of the transducer body.

In summary, the most important requirements on the F/T sensor are:

- Acquisition of the ground contact forces and moments from all three Cartesian coordinates
- Maltese-cross-shaped transducer body with monolithic structure to avoid hysteresis and setting effects
- Shear beam geometry optimized for high sensitivity even of minor loaded axes
- Load-bearing structure designed for tight integration within the forefoot structure
- Sensor placement in the center of the foot contact area
- Integrated signal conditioning and A/D conversion

- Calibration with respect to reference system located at the center of the transducer body

2.7.4 Contact State of the Feet

Due to division of the foot into forefoot and toe, the contact state of the foot contact elements is ambiguous and cannot be determined reliably. However, for stabilization of the robot it is very important to know the contact state of the feet. It can be determined for example by measuring distance of the contact elements to the ground. Kajita and Tani [86] apply ultrasonic distance sensors to the robot *MELTRAN* for real-time detection of the ground profile. Gienger [46] proposes tactile sensors based on potentiometers to determine distance to the ground.

Measuring the distance to ground provides more information and enables more sophisticated control strategies. In a first step, however, it easier to integrate discrete contact sensors to the viscoelastic elements of the heel and toe segments. The contact state is thus measurable and allows, for instance, to implement event-triggered switching of the gait patterns.

2.8 Computer Architecture

This section deals with the conceptual design and fundamental operational structure of the on-board computer system. The performance of the computer architecture is essential to the performance of the walking robot. It has to acquire all sensor data, calculate the trajectories, stabilize the robot, and compute and output the motor control variables. Having a total of 25 actuated joints and numerous sensors for state feedback, the overall system is quite complex. Regarding the modular design of the servo actuators, the implementation of a fully decentralized computer architecture seems obvious. While such architectures have been implemented successfully for many multi-legged walking machines [144], balance control of biped robots requires a central controller instance. Because of highly coupled kinematics and dynamics the control algorithms cannot be reasonably divided into self-contained modules that run on distributed nodes.

In a first approach, a computer system with distributed nodes was implemented to the robot *Johnnie* based on the hardware concept of two previous multi-legged robots [144]. It was composed of a PC-based, external host system and six on-board microcontrollers. All nodes are connected via six CAN bus lines. To achieve a high sampling rate, trajectory planning and stabilizing control run on the host PC, while low-level motor control and data acquisition are handled by the microcontrollers. Using this computer system, a minimum cycle time of 4 ms has been achieved, comprising 2.5 ms for calculation of the controller on the host PC, 0.5 ms for data transmission via CAN, and 1 ms for sensor data acquisition and processing on the microcontrollers. Experiments suggest, however, that the sampling rate of 250 Hz is too slow for the chosen control concept [109], impeding the implementation of faster gait patterns. In the refined version the robot is fully controlled by an on-board PC. An external computer connects to the robot via Ethernet to give basic operating commands and for monitoring purposes.

A customized PCI board interfaces the on-board PC to the sensors and motor electronics. The board is situated in the upper body of the robot and connected to the sensors and electronics with a rather complex and bulky cabling. Thus, the cabling makes about 4.7 % of the overall mass [46]. Many other humanoid robots employ centralized hardware architectures, for example *HRP-2* [95], *Wabian-2* [131] and *H7* [127]. Most of them employ custom-developed interface boards for hardware I/O[16]. Nevertheless, an increasing number of biped robots employs architectures with distributed nodes for low-level data processing and control. In this case a key problem is the communication between the decentralized nodes and the host PC. Most of these robots uses the CAN Bus communication protocol, typically with multiple channels, for example *HUBO* [140], *ARMAR-III* [151] and *iCub* [188]. Few robots employ other communication systems than CAN. The prototype robot *HRP-3P* uses a custom-developed real-time Ethernet system [3, 92] but is migrated to CAN in the robots *HRP-3* [96] and *HRP-4C* [93]. Sarker et al. [161] propose a real-time control system for the robot *MAHRU* which is based on IEEE 1394 (FireWire). DLR's lightweight robots *LWR-II* and *LWR-III* and the two-arm system *Justin* have a modular computer system with one controller module per joint. SERCOS with fiber-optic cables is used as the communication system at a rate of 1 kHz [68]. All electronics are fully integrated to the joint modules [67, 137]. The upper-body humanoid *Robonaut* developed by NASA employs FPGA-based motor controllers and bi-directional host CPU communication using synchronous RS-485 drivers [14].

2.8.1 Design Concept

In order to make the robot computationally autonomous, the computer hardware for trajectory planning, gait stabilization and low-level control is integrated to the robot. As stated above, the highly coupled kinematics and dynamics of biped robots demand a central controller instance. From a technological point of view, however, it is feasible and advantageous to unload the central control unit (CCU) from standard tasks: using a decentralized architecture, low-level motor control and sensor data processing run in parallel on local controllers. Similar to hierarchical structures in biological systems, sensor data is processed locally and only relevant information is forwarded to the CCU. Thus, CCU, local controllers, sensors and servo actuators form an "intelligent sensor-actuator network"[17]. CCU and local controllers are connected by a fast real-time communication system. By unloading the CCU from hardware-related tasks, the local controllers abstract the robot hardware from higher-level control tasks and thus simplify future

---

[16] Input/output

[17] Unfortunately, the term "intelligence" lacks a precise definition. Throughout this thesis, "intelligence" is used in accordance with the definition in the field of sensor technology: an *intelligent sensor* senses and digitizes the input signal and takes some action on it, e. g., amplification, zero error compensation, linearization and scaling. The sensor is also able to execute auxiliary logical functions and instructions and the processed data are communicated digitally to a control unit. Consequently, an *intelligent actuator* receives desired values and configuration commands from a control unit and executes them independently. Again, only actual values and status information are communicated to the control unit.

extensions of the robot. Malfunction of the on-board computer system may cause serious harm to the robot and its environment. The mechanical and electrical robustness of the computer hardware is therefore essential. Furthermore, the complex point-to-point cabling of sensors and actuators is replaced by bus systems for communication and energy supply. Cable harnesses for connecting the servo sensors, actuators and drives to the local controllers can be kept short and mostly do not have to be routed across moving joints. Decentralized architectures are thus expected to reduce the cabling effort and improve electromagnetic interference.

Further decentralization of higher-level control tasks is not considered, so that trajectory planning and control of system dynamics run on the CCU. Nevertheless, this architecture allows for the implementation of different levels of decentralization, ranging from more centralized signal processing concepts to fully decentralized motor control. In the first approach only the current loop is closed in the drive and all other loops are implemented in the CCU. The second approach closes all control loops, including motor position, velocity and current, in the drive. In summary, the functions of the computer components are:

Central control unit (CCU): trajectory planning and stabilizing control; support the implementation of control architectures with different levels of decentralization.

Distributed controllers: low-level motor control, including current, velocity and position control, depending on the control architecture; evaluation of the joint sensors; output control signals to the motor power electronics; parameterization of the motor controllers, e. g., for gain scheduling; data acquisition from the force/torque sensor and inertial measurement system.

Real-time communication system: deterministic connection of CCU and local controllers with low latency; transmission of actual and desired values, and status and diagnostic messages; parameterization of the drives; switching between different operating modes of the motor controller.

2.8.2 Central Control Unit

Using a PC-based platform, the central control unit has the highest possible computing power that can be installed on-board. By using only off-the-shelf components, the CCU can easily be upgraded to the performance requirements of the stabilizing control and trajectory generator. The CCU is built from an industrially ruggedized PC board that is supplemented by an interface board for the communication system.

2.8.3 Decentral Controllers

The decentral controllers must provide all functionality for sensor data acquisition and motor control to reduce the volume for external electronics, as well as the size and number of cable harnesses throughout the system. The proposed system requires the development of custom hardware because there are no commercial controller modules available that provide the combination of interfaces to various sensors and the communication system at compact measurements and low weight. Briefly, the mandatory requirements for the decentral controllers are:

- Interface to the motor shaft encoder, link position sensor, limit switch, current and temperature sensors of each joint
- Suitable to control three PMSM at an intermediate circuit voltage 80 V at up to 25 A (continuous) and 50 A (peak)
- Cycle times of the position control loop as low as 1 ms
- Interface to the force/torque and foot contact sensors
- Interface to the inertial measurement system
- Small outline to allow for positioning close to the servo actuators
- Modular design for reduced development effort
- Low power consumption
- Interface to the real-time communication system

The full integration of the motor controllers and inverters into the servo actuators would consistently follow the idea of a modular hardware design as discussed in Section 3.4. Also, the cabling of the servo actuators would be improved. The huge development effort, however, is beyond the scope of this project. Therefore, it is proposed to integrate the low-level motor control co-located with the actuators.

2.8.4 Communication System

The real-time communication system is the only data interface of the CCU to the robot hardware. It must handle the entire data exchange between the CCU and local controllers. The 25 motor controllers, two force/torque sensors and on IMS are distributed equally among the local controllers. Then the communication system must be able to handle data transfer between a total of nine local controllers within the sampling time of the balance control loop of approximately 1 ms. Multi-axis control applications like biped robots require the synchronicity of all control loops for coordinated motion. Time delay in the control loops is due to the computing time of the control algorithms and the duration of sensor data acquisition, processing, and data transfer. High latency limits the sampling time and can diminish control performance. The communication system should therefore show minimal latency and small protocol overhead. Handling this large data stream with minimal latency is even more difficult due to the small packaging goals that limit overall electronics volume and geometry. For reduced weight and cabling effort the communication system should show bus or ring topology. As the local controllers require custom hardware, implementation effort should be reduced by available driver software and hardware interfaces (ASICs or PCB modules). The requirements on the real-time communication system connecting CCU and local controllers include:

- Real-time capability and a high level of determinism
- Low cycle times
- Guaranteed, high bandwidth for data transfer to all devices within one control cycle
- Synchronicity and minimum of protocol overhead to minimize latency in the control loops

- Synchronization of the local controllers to the CCU time base
- Commercially available driver software and hardware interfaces for simplified system integration
- Small footprint of the hardware interface

2.9 Chapter Summary

This chapter presented the mechatronic design concept of the robot. The following design guidelines for the development of the detailed design of the mechanical and electronic subsystem were derived:

Mechanical configuration: redundant kinematic structure with 25 DoFs, including actuated toe joints; anthropometric proportions of the robot as far as possible; foot dynamics concept with viscoelastic layers and hydraulic damper for effective shock attenuation at initial contact; consistent lightweight design of the mechanical structure with high effective stiffness and natural frequencies; low-inertia design of the leg apparatus for good dynamic performance of the locomotor system.

Joint mechanisms: all joints are driven by servo actuators combining precision gearing with a high-dynamic AC servo motor and sensors in a compact housing; the hip joint is composed of three serial drives, forming a spherical joint with all joint axes intersecting in a single point; for improved mass distribution in the hip-thigh area, the knee joint is driven by a planetary roller screw-based linear actuator acting as length-variable coupler; the ankle joint is driven by a parallel mechanism composed of two spatial slider-crank mechanisms, where the motors are mounted on the thigh, close to the hip joint.

Sensor layout: supports the implementation of model-based control algorithms; upper body orientation with respect to an inertial frame are measured by a high-precision inertial measurement system based on fiber-optic gyroscopes and MEMS accelerometers; joint angles and angular velocities are measured by absolute angular sensors on the gear outputs; additional motor control variables are measured by incremental encoders on the motor shafts; external forces and moments are measured by customized six-axis force/torque sensors in the feet; contact sensors in the heel and toe segments disambiguate the contact state of the divided feet.

Computer architecture: the “intelligent” sensor-actuator network with central control unit (CCU) improves system performance from a technological point of view; the CCU accounts for trajectory planning and global system stabilization; decentral controllers account for low-level motor control and sensor data acquisition and signal processing; a high-bandwidth real-time communication system connects CCU and decentral controllers in order to minimize latency in the control loop.

3 Mechanical Design

Schnell und fein das kann nicht sein.
—My Mother

This chapter presents the design of the mechanical structures. Figure 3.1 shows a photograph of the robot *Lola*, the key data are summarized in Table 3.1. Further dimensions are given in Appendix B.

The development of a complex mechatronic system such as a humanoid walking robot is an iterative and open-ended process of design and simulation. To develop the mechanical system both structured and systematically, the design methodology described in Section 2.1.1 is applied. According to Pahl et al. [138], the design process divides into the four phases of task planning and clarification, conceptual design, embodiment design and detail design. The two last phases, which are subject of this chapter, are based on the requirements and fundamental design concept worked out in the previous chapter. The process of mechanical design and the tools used are introduced briefly in Section 3.1. Additional design rules to achieve a consistent lightweight construction with good dynamic properties are given in Section 3.2. The design calculations, Section 3.3, are based on the dynamics simulation of the full system developed within the sub-project "Simulation and Control." They include the dimensioning of the motors and drive mechanisms and the dimensioning of structural components which are addressed in Sections 3.3.2 and 3.3.3, respectively. To reduce the complexity, the overall system is divided into well-defined sub-assemblies which can be developed consecutively and independently. These are, the

- joint actuators (Section 3.4),
- camera head (Section 3.5),
- trunk and pelvis (Section 3.6),
- arms (Section 3.7),
- legs (Section 3.8), and
- feet (Section 3.9).

Many of these sub-assemblies include the mechanical design of link segments, some prominent examples are described in Section 3.10. After assembly the kinematic and inertial parameters of the robot are identified. The associated procedures are described in Section 3.11. Lastly, Section 3.12 concludes with a discussion of the mechanical design.

3.1 Design Process

The design process comprises the development, evaluation and selection of several design variants and the detailed geometric design of all mechanical components.

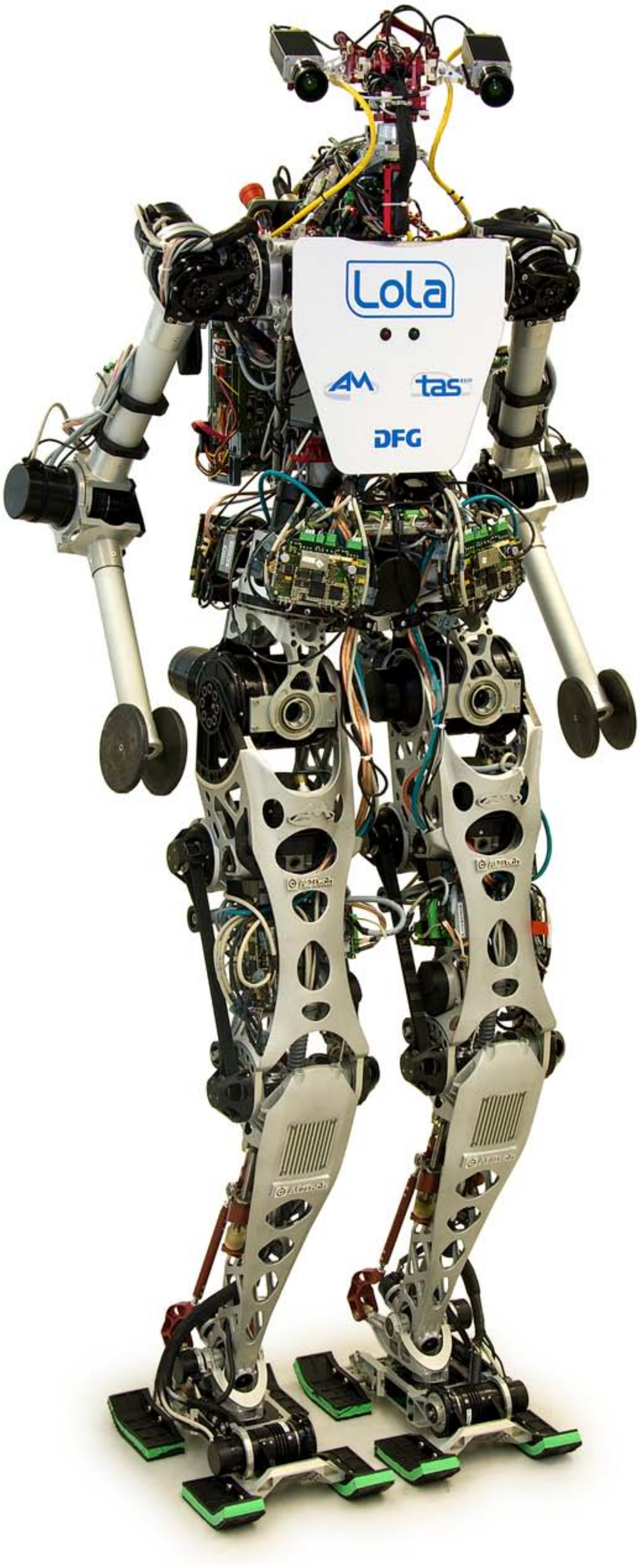

Figure 3.1: 25-DoF humanoid walking robot *Lola*

Table 3.1: Hardware Specifications

General	
Height	180 cm
Mass	60.88 kg
Total DoFs	25
Maximum walking speed (target)	5 km/h
Power supply	external
Legs	
7 DoFs (3 hip, 1 knee, 2 ankle, 1 toe)	
Thigh length	440 mm
Shank length	430 mm
Foot height	105 mm
Distance between hip joints	246 mm

The 3D-CAD system CATIA V5 from Dassault Systèmes[1] is adopted for most of these steps. The robot components are modeled using the CATIA modules *Part Design* (PDG), *Generative Sheetmetal Design* (SMD) and *Generative Shape Design* (GSD). Stress analysis and strength assessment are mainly conducted with the built-in structural analysis modules (GPS/GAS) which provide automatic finite element meshing from native CAD data. CATIA's digital mock-up (DMU) module is applied to confirm the assembly of critical components and identify self-collisions. In particular, the drivetrains of the knee and ankle joints are analyzed thoroughly because the complex kinematics of these mechanisms with several moving parts affect the entire surrounding construction.

The CAD model is organized in the style of the modeling strategies of the guideline VDI 2209 [193] and resembles the tight coupling of mechanical design and dynamics simulation. Each sub-assembly of the CAD model corresponds to a body of the dynamics simulation model (cf. Section 3.3.1). The "root part" of all sub-assemblies does not contain any actual part geometry but a local frame of reference which is defined in accordance with the multibody simulation model. The "root part" further comprises some characteristic elements (reference planes, points, axes, etc.) that are primarily used to define assembly constraints between components. This approach ensures consistency of the CAD and simulation models and simplifies the acquisition of new inertia properties from the CAD model.

3.2 General Design Rules

The fast-moving cantilever links of the legs yield high inertia forces and consequently, high joint torques and bending moments in proximal link sections. Although stresses are normally low, compliance is becoming more pronounced with such link structures. In consequence, unwanted effects on system performance (positioning accuracy, dynamic stability, static and dynamic fatigue strength) arise

---

[1] `http://www.3ds.com/`

from inadequate link and joint stiffnesses. Therefore, the objective of lightweight system construction demands for a methodical procedure, taking lightweight design into account even at the conceptual stage. From the system's perspective, "conceptual lightweight construction" generates savings through functional integration using highly integrated components that combine several functions and parts. Further, the use of lightweight materials such as high-strength aluminum alloys ("lightweight material construction") provides the basis for great weight reductions, cf. Section 3.10. Moreover, the geometrical optimization of single components ("design for lightweight construction," cf. Section 3.3.3) facilitates reduced cross sections with appropriate stiffness.

In the following, a number of general design rules are established in order to achieve a sophisticated mechanical system with appropriate structural dynamic characteristics:

Direct load transfer and distribution: direct load transfer to the main structure; avoid redirection of forces; establish large-area application of loads; design sophisticated load application and distribution structures for thin-walled components; optimized support conditions of areas of load transfer; additional ribbing of flange joints; symmetric design of components; preferably closed instead of open cross sections ("Monocoque-like design"); cambered cross sections for larger load rating.

Preferably filigree structures: prefer thin-walled cross sections with stiffness reinforcing ribs over solid bodies; optimize mass distribution of a component to achieve the largest second moment of area (bending) and/or polar moments of inertia (torsion) for a given mass of the component.

Avoid stress concentrations: avoid weak spots by allowing only smooth changes in cross-sectional shapes.

Systematic stiffening in directions of maximum stress: develop a judicious system of ribs or other reinforcements to achieve anisotropic stiffness wherever appropriate.

Integral part design: reduce part count and assembly complexity; prefer milling from the solid over attaching parts whenever possible; avoid overlap due to bolted or riveted flange connections.

Flange connections: prefer rivets over screws if non-detachable connections are acceptable; arrange flanged joints within the load path (preferably close to the wall or within recesses); design for a direct force flux between the flange members; prefer a larger number of uniformly arranged smaller screws over a lower number of larger screws; prefer longitudinal over transverse stressed bolt connections; use friction enhancement shims [34] for safe load transmission even over smaller flange structures; combine bolted connections with positive locking for high joint stiffness and reduced screw count; reduced offset between the bolt pattern and line of action of the applied forces provides the most effective means of increasing the joint stiffness.

Damping enhancement reduces strain and stress amplitudes: different excitation frequencies act on the robot structure which cannot be determined a priori, depending on the gait pattern, control strategies and other parameters. Thus, a very effective way to reduce structural vibrations is to systematically enhance damping, e. g., by applying viscoelastic elements [155].

Joint stiffness: link connections frequently contribute the dominant structural deformations [154] and should therefore be designed as stiff, backlash-free bearings; prefer adjusted bearing arrangements; prefer thin-section bearings with larger diameter over smaller bearings with equal load rating; use precision bushes with minimal clearance for plain bearings.

Although the goal is to tap the full potential of the design, there are some limitations of this approach. Consistent lightweight design is only achieved if the safety margins for unseizable boundary conditions are reduced. Hence the precise knowledge of all loads acting on the system (in magnitude and direction) is required. In addition, the use of materials with guaranteed specifications and preliminary tests to validate structural details are essential [101]. On the other hand, the robot is planned as a multi-purpose research device. Depending on the speed of locomotion, gait patterns and control strategy, the loads acting on the system can differ significantly. Moreover, the robot must be able to move about in unfamiliar space and/or over obstacles when operated with the autonomous vision and path-planning system. To summarize, task uncertainty obviously goes along with uncertainty of loading and must be taken into account in the design of critical components. Therefore, the prototype investment castings of the link segments (Section 3.10) and some other complex and cost-intensive parts are designed for high-cycle fatigue to avoid failure.

3.3 Design Calculations

This section focuses on the sizing calculations that are carried out within the scope of this work, which include:

1. Sizing of the actuators and their transmissions
2. Structural dimensioning of the links and joints
3. Elastodynamic analysis of the mechanical structure and drive mechanisms

Sections 3.3.2 and 3.3.3 address the dimensioning of the drivetrains and mechanical structures on basis of static and dynamic loads. Static loads include forces and moments under the most demanding operation conditions and correspond to the maximum forces and moments the feet are able to transfer to the ground at a certain robot posture. They represent the worst-case loading that the mechanical system should be able to withstand without damage. Also, static loads are used to determine the actual gear sizes and for worst-case finite element analyses. On the other hand, dynamic loads that occur during normal operation are by far more important and determined with a full dynamics simulation of the robot, Section 3.3.1. These loads are used to determine the dynamic performance of the actuators and gears. Moreover, they serve as constraint forces in the strength analysis of mechanical components.

3.3.1 Calculation of Fundamental Design Data

The mechatronic modeling of the robot is a key tool for hardware and controller design. While the static loads can be determined quite easily by analytical assumptions, the dynamic performance data are obtained from this comprehensive simulation model developed by Buschmann [19]. Considering the major effects on bipedal locomotion, the robot is modeled as three coupled dynamical systems:

- Multibody dynamics (rigid body mechanics, drive friction, gear elasticity, nonlinear kinematics in ankle and knee joints)
- Contact dynamics (unilateral, compliant foot-ground contact)
- Electrical motor dynamics

The stiffness and damping characteristics of the foot-ground contact are adjusted by experiments with the robot *Johnnie*, so that the computed results can be expected to be close to reality [19]. Typical load profiles at a walking speed of 5.55 km/h are given in Appendix D.

The joint loads (torques and velocities), external forces (ground reactions) and the constraint forces and moments of the links are very important data throughout the design process. They are used for the dimensioning of the drive mechanisms and structural components. Moreover, the angular ranges of typical gait patterns are important constraints for the robot topology and link geometry. Conversely, the topology of the kinematic chain, geometric dimensions of all links, motor parameters, gear ratios, and the dynamic properties of the mechanical system serve as input parameters for the robot simulation. After certain milestones of the mechanical design have been completed, the inertia properties of the links and actuators are calculated numerically from the CAD model and imported into the robot simulation. After the balance controller has been adjusted to the new parameters, new design data are calculated to be used in the dimensioning of the mechanical system. In this way both simulation and CAD model are iteratively refined and the final design of the robot is evolved. Finally, the mass parameters of the real robot have been determined during assembly (see Section 3.11.2) to further improve modeling accuracy. Hence the dynamics simulation can be used as a reliable tool for developing and analyzing control system robustness and performance before experimental verification on the real hardware.

3.3.2 Dimensioning of the Drive Mechanisms

Dimensioning the servo drive mechanisms and their components is a demanding task due to constantly reversing motion and the highly variable loading of the joints. The fast link accelerations at higher speeds of locomotion demand for good dynamic performance. The actuators and drive mechanisms are selected, thus, for

- meeting the static and dynamic load requirements, while taking account enough reserve capacity;
- sufficient drivetrain stiffness to avoid oscillations of the leg structure;
- enabling a good tracking and disturbance rejection behavior of the motor controllers;
- good energy efficiency.

The iterative selection procedure for the drive mechanisms is illustrated in Figure 3.2. This section focuses on the highlighted steps. The chosen procedure allows the comparison of different motor-gear combinations with regard to power density, dynamic performance, stiffness and power dissipation. Starting from

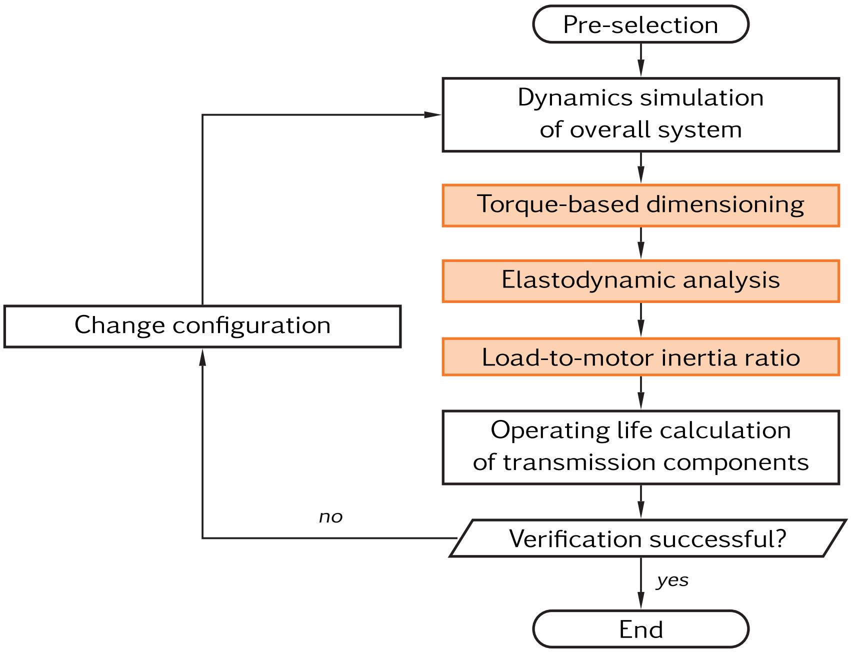

Figure 3.2: Iterative selection procedure for the motors and drive mechanisms. This section deals with the torque-based and elastodynamic dimensioning of the drive mechanisms, and the effects of the load-to-motor inertia ratio on the performance of the servo system.

motor-gear combinations that are expected to be capable of driving the joints, the actual joint loadings are determined by the robot simulation. The static and dynamic load requirements are then analyzed under the assumption of a rigid drive mechanism. The *torque-based dimensioning* must balance the conflicting requirements of minimal weight and overloading capacity: consistent lightweight design implies that the servo actuators should not be oversized, at the same time appropriate reserve capacity must be provided to cope with task uncertainty. However, the finite torsional stiffness of the transmission components introduces compliance in the drive mechanism between the motor and load. Such compliance limits the bandwidth of the mechatronic servo system and can introduce resonant oscillations. Hence the *elastodynamic analysis* of the drivetrain accounts for eliminating or reducing resonances in the drive mechanism. Also, compliant drivetrain components—in particular, the motor-load coupling—greatly affect the tracking and disturbance rejection behavior of the servo system. To achieve good control performance, the *load-to-motor inertia ratio* is considered as an indicator of possible stability problems. Finally, the *operating life* of transmission components is calculated where necessary. If the load rating, operating life or dynamic behavior of the drivetrain does not meet the requirements, the drivetrain configuration is modified and the procedure repeats.

Torque-based Dimensioning

The fundamentals of motor sizing are well-known and beyond the scope of this thesis, so that only a rough overview is given in the following. The reader is referred to the relevant literature, e. g., [165]. Only the continuous and intermittent load ratings of the servo motors are discussed with special regard to thermal capabilities.

In order to dimension the servomechanism, the torques acting on the motor and drive mechanism must be analyzed. Assuming a stiff connection of motor and gear, the motor torque τ_m necessary to follow a given load profile is

$$\tau_m = J_m \underbrace{N\dot{\omega}_l}_{=\dot{\omega}_m} + \frac{\tau_l}{N} + \underbrace{\tau_{f,m}\,\mathrm{sgn}(\omega_m) + \frac{\tau_{f,l}}{N}\,\mathrm{sgn}(\omega_l)}_{=\tau_f} \,. \tag{3.1}$$

In Eq. (3.1) the load-side quantities are calculated to the motor shaft using the gear ratio N, which is constant in the case of a Harmonic Drive gear and posture-dependent for the linear drives of the knee and ankle joints, cf. Eq. (2.9) on page 61. τ_m is composed of the motor shaft acceleration torque resulting from the motor inertia J_m and acceleration $\dot{\omega}_m$. The latter is calculated from the load acceleration, $\dot{\omega}_m = N\dot{\omega}_l$. τ_l is the load torque at the gear output. The friction torque τ_f is composed of the motor and load-side friction, $\tau_{f,m}$ and $\tau_{f,l}$, respectively, and $\mathrm{sgn}(\cdot)$ denotes the sign of the respective value.

Motor Selection Criteria

Motor selection is done on basis of the fundamental design data, Section 3.3.1, and appropriate safety factors f_i to account for task uncertainty[2]. Three main criteria have to be fulfilled:

1. The continuous stall torque rating of the motor has to be greater than or equal the effective torque of the load profile to avoid overheating
2. The peak torque rating of the motor has to be greater than the maximum required torque to avoid demagnetization of the rotor magnets
3. The speed limit of the motor has to be above the maximum speed required by the load profile

The root mean square of the required motor torque during interval T is given by

$$\tau_{m,avg} = \sqrt{\frac{1}{T}\int_T \tau_m^2 \,\mathrm{d}t} \,. \tag{3.2}$$

Using Eq. (3.1) with Eq. (3.2) and the continuous stall torque rating τ_c of the motor, the first criterion is obtained under consideration of the continuous load safety factor f_c:

$$\tau_c \geq f_c \sqrt{\frac{1}{T}\int_T \left(J_m N\dot{\omega}_l + \frac{\tau_l}{N} + \tau_f\right)^2 \mathrm{d}t} \,. \tag{3.3}$$

---

[2] All safety factors f_i for drivetrain dimensioning range from 1.5 to 2.

In order to fulfill the second criterion, the maximum torque during the load cycle must be below the motor peak torque τ_p, including the static load safety factor f_s:

$$\tau_p > f_s \max \left| J_m N \dot{\omega}_l + \frac{\tau_l}{N} + \tau_f \right| . \tag{3.4}$$

Finally, the maximum permissible speed of the motor $\omega_{m,max}$ must be greater than the maximum speed during the load profile, using the speed safety factor f_{ω_m}:

$$\omega_{m,max} > f_{\omega_m} \max |N \omega_l| . \tag{3.5}$$

If several motors match Eqs. (3.3) to (3.5), the motor constant K_m, see Eq. (2.4) on page 41, is used as an indicator for the power-to-torque ratio. In this case, K_m must be considered together with a motor's thermal capability to determine its true efficiency and capacity.

Derivation of the PMSM Speed/Torque Curve

The survey in Eq. (2.4) showed the superior power density of PMSM resulting from the brushless design and thermal capabilities. For proper motor dimensioning with appropriate reserve capacities it is necessary to examine the PMSM speed/torque curve. Assuming identical phase voltages for all motors, the torque-speed characteristic depends on the machine winding and is limited by a voltage-dependent torque-speed boundary and a temperature boundary which depends on the thermal environment of the motor.

For a particular phase voltage U there is a linear relationship between motor speed ω_m and torque τ_m, representing the *torque-speed boundary* of the motor in steady state:

$$\omega_m = \frac{U}{K_\tau} - \frac{R}{K_\tau^2} \tau_m . \tag{3.6}$$

Here K_τ and R are the torque constant and winding resistance, respectively.

Although motor losses are neglected in Eq. (3.6), they must be considered in a second step to determine the continuous operation area of the motor. The two main sources of motor dissipation are electrical losses in the stator windings and magnetic losses in the steel laminations of the stator. Electrical losses are expressed as ohmic dissipation $P_R = I^2 R$. Magnetic losses, or core losses, P_c comprise eddy currents and hysteresis losses. They are typically expressed as an exponential function of the motor speed ω_m and core losses P_{c0} measured at a speed of 1,000 1/min. The core losses of the chosen frameless motor family from Parker Bayside [141] are rated as

$$P_c = P_{c0} \omega_m^{3/2} . \tag{3.7}$$

The maximum allowed dissipation $P_{m,max}$ of the motor is limited by the maximum allowed temperature $\vartheta_{m,max}$ of the winding isolation[3] and the ambient temperature

---

[3] Typically, the stator temperature ϑ_m must not exceed 155 °C.

ϑ_∞ in which the motor is operating:

$$P_{m,max} = \frac{\vartheta_{m,max} - \vartheta_\infty}{R_{th,m}} . \tag{3.8}$$

Here $R_{th,m}$ is the thermal resistance between the windings and the ambient. $R_{th,m}$ depends on the size and mechanical design of the motor and the thermal properties of the surrounding structure, and can be reduced by cooling fins, or forced air or water cooling. Subtracting Eq. (3.7) from Eq. (3.8) yields the maximum allowable electrical losses. Using the torque-current relationship, $\tau_m = K_\tau I$, we finally get the *thermal boundary* of the torque-speed curve:

$$\omega_m = \left[\frac{1}{P_{c0}} \left(\frac{\vartheta_{m,max} - \vartheta_\infty}{R_{th,m}} - \frac{R}{K_\tau^2} \tau_m^2 \right) \right]^{2/3} . \tag{3.9}$$

Obviously, the output is limited by the temperature rise in the stator coils. The load rating is thus greatly enhanced if the motor is tightly integrated into the robot structure which can serve as a high-capacity heat sink. Note that the motor temperature also affects the winding resistance and magnetic characteristic values. As a consequence, the torque-speed curve, Eq. (3.6), becomes steeper and the peak torque τ_p is reduced. Winding resistance increases linearly according to the thermal resistance coefficient α_{Cu} for copper[4], and the winding resistance at motor temperature ϑ_m becomes $R = R_\infty[1 + \alpha_{Cu}(\vartheta_m - \vartheta_\infty)]$. Hence, winding resistance increases up to 1.5 times the nominal value R_∞ for the maximum permissible motor temperature $\vartheta_{m,max}$. Practical experiments with the robot *Johnnie* have shown that the motors reach their thermal steady-state after 20 to 30 minutes of continuous operation [109]. As the dynamics simulation data usually account for less than one minute, the transient heating of the motors is not considered and a constant value for the winding resistance is used instead. It is therefore proposed to create a safety margin by using the value for $\vartheta_{m,max}$ throughout the motor sizing calculations.

Using Eqs. (3.6) and (3.9), the continuous speed/torque curve can be plotted as shown in Figure 3.3. The areas of constant and intermittent operation are shown in ivory and orange, respectively. Since servo motors usually do not operate in continuous duty, the peak torque τ_p during acceleration can be much larger than the continuous stall torque: if the effective dissipation

$$P_{m,avg} = \frac{R}{K_\tau^2} \tau_{m,avg}^2 , \tag{3.10}$$

as calculated from Eq. (3.2), is within the continuous operation limits, the motor can be overloaded intermittently. Typical peak torque multiplication ratios for rare-earth-magnet based motors range from 3 to 5. The limitation is mainly due to saturation effects in the loaded motor which cause a decrease in K_τ to 85 % to 90 % of its nominal value [141].

---

[4] $\alpha_{Cu} = 3.92 \cdot 10^{-3}\ 1/\mathrm{K}$

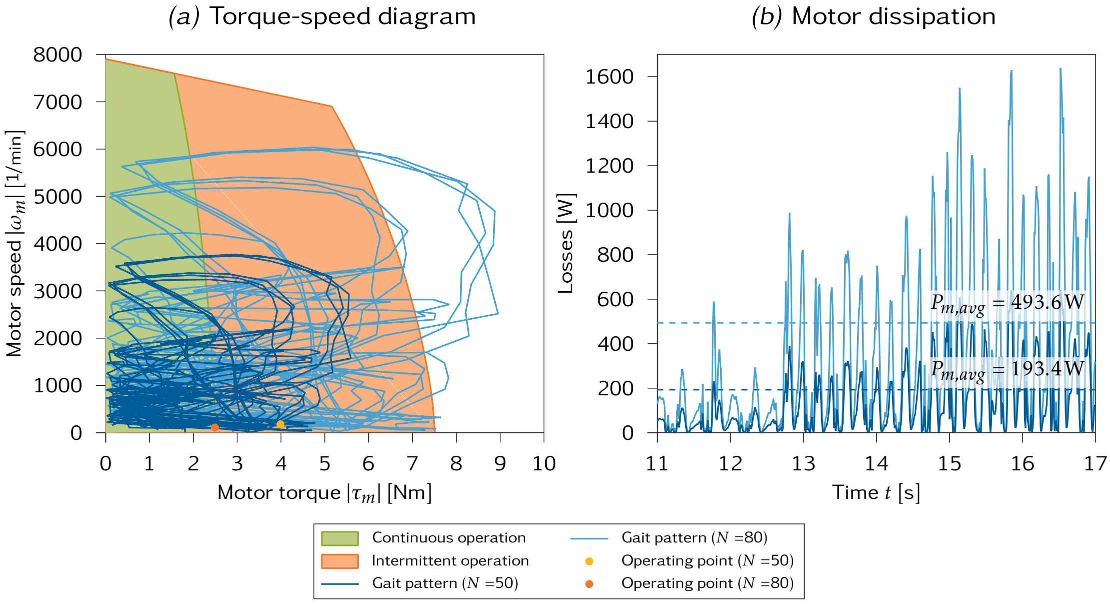

Figure 3.3: *Left,* torque-speed diagram of the hip joint flexion/extension motor for a walking speed of 5.55 km/h; *right,* motor power dissipation for different reduction ratios.

Selection Criteria of Transmission Components

The drive mechanism of a joint is composed of the main transmission which interfaces to the links of the robot and in some cases auxiliary transmissions to connect the electric motor to the main transmission. For the main transmissions, Harmonic Drive gears [59] and planetary roller screws [78] are used. Synchronous belt drives [24], angular gears [55] and coupler links serve as auxiliary transmissions. The dimensioning of other drivetrain components, such as bearings [79] and couplings [159, 160] follows the guidelines of the respective manufacturer. Again, safety factors in the range from 1.5 to 2 account for task uncertainty.

Although the design and working principle of Harmonic Drive gears and planetary roller screws are apparently different, there are some similarities of the selection procedure which are addressed in the following. As the load torque τ_l and speed ω_l are varying, equivalent operating values are determined for both. The average load speed is given by

$$\omega_{l,avg} = \frac{1}{T}\int_T |\omega_l|\,\mathrm{d}t\,. \tag{3.11}$$

The average load torque is calculated as the root mean cube of the load torque τ_l, weighted by the load speed:

$$\tau_{l,avg} = \sqrt[3]{\frac{\int_T |\tau_l(t)^3 \omega_l|\,\mathrm{d}t}{\int_T |\omega_l|\,\mathrm{d}t}}\,. \tag{3.12}$$

The transmission ratio N sets the torque, speed and inertia relationship of the servo drivetrain to the link. Moreover, it affects the motor dissipation. Figure 3.3

illustrates the selection of a suitable motor-gear combination. For example, the hip joint flexion/extension axis[5], shows that the torque-speed characteristics of PMSM allow to decrease the gear reduction ratio N, while the efficiency, denoted by the ratio of the load torque to the motor shaft acceleration torque, increases. Figure 3.3(a) compares the torque-speed requirements for the reference walking pattern for reduction ratios of $N = 50$ and $N = 80$. The shaded areas correspond to Eqs. (3.6) and (3.9) and represent the continuous and intermittent operation area of the motor[6], respectively. For $N = 80$, the higher motor speed increases the acceleration torque of the motor shaft such that a larger motor must be selected. Conversely, for $N = 50$ a less powerful and more lightweight motor can be chosen. Likewise, the operating point for $N = 50$ denoted by the RMS torque, Eq. (3.2), and the mean rotational speed, calculated analogous to Eq. (3.11), is within the continuous operation limits of the motor. Thus, the motor is suitable to drive the joint and can be overloaded intermittently. Conversely, the operating point for $N = 80$ is outside the continuous operation limits and would necessitate a larger motor. The effect of lower reduction ratios can also be seen from the motor dissipation in Figure 3.3(b). The average motor dissipation $P_{m,avg}$, Eq. (3.10), is rated at 193.4 W for $N = 50$, whereas $P_{m,avg}$ increases significantly to 493.6 W (=255 %) for $N = 80$.

Elastodynamic Analysis of the Drive Mechanism

While the entire drive mechanism was considered rigid and free from backlash for the torque-based dimensioning, Eq. (3.1), the finite drivetrain stiffness is a crucial factor in meeting the stiffness requirements of the mechanical structure: because transmission elements, such as gears, belt drives and couplings introduce compliance between the motor and the load, they bring up the problem of mechanical resonance which may limit the bandwidth of the mechatronic servo system and provoke weakly damped oscillations of the link. The aim of the elastodynamic analysis of the drive mechanisms is therefore to

- eliminate or reduce resonances in the drive mechanism caused by the finite stiffness of transmission components;
- achieve a high enough bandwidth and fast response time of the speed control loop;
- minimize power dissipation.

While the stiffness of planetary roller screws is sufficiently high, the distinct compliance of synchronous belt drives and Harmonic Drive gears must be considered in the elastodynamic analysis of the drive mechanism. Backlash also affects the bandwidth of a servo system [10] but can be neglected for Harmonic Drive gears and pre-loaded planetary roller screws.

Although the drivetrains of the robot are rather complex structures, the major effects of the compliant motor-load coupling can be understood by basic analytical considerations. Figure 3.4*a* shows the reduced model of a drivetrain with elastic gearbox. The motor and load inertia, J_m and J_l, are coupled by a backlash-free

---

[5] The complete load profile of the hip joint is given in Appendix D

[6] The relevant technical data of the motors are given in Appendix C

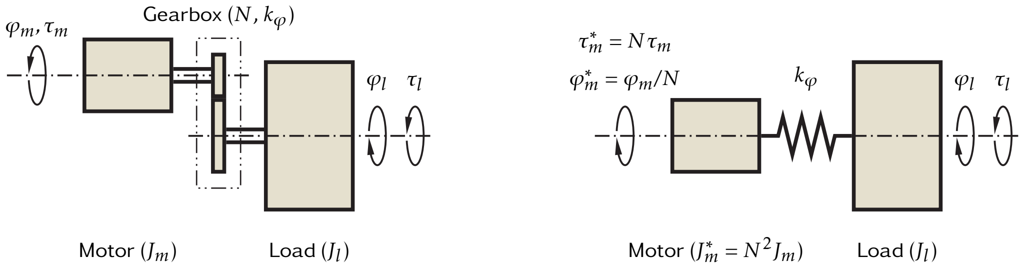

(a) Drivetrain with elastic gearbox *(b)* Two-mass system with flexible coupling

Figure 3.4: Equivalent model of a compliant drive mechanism

gearbox with constant ratio N and torsional stiffness k_φ. The motor and load-side masses of the gearbox are lumped in J_m and J_l, respectively. For the sake of simplicity and because it is a worst case assumption, damping is neglected. The motor torque τ_m and load torque τ_l are active forces acting upon the masses J_m and J_l, respectively. Reducing this model by reflecting the motor quantities to the load side, leads to the unconstrained two-mass system with flexible coupling shown in Figure 3.4*b*. The angle φ_m^* on the motor side differs from the angle φ_l on the load side. The system is described by two ordinary differential equations for the motor and load side, respectively:

$$J_m^* \dot{\omega}_m^* + k_\varphi(\varphi_m^* - \varphi_l) = \tau_m^* \,, \tag{3.13}$$

$$J_l \dot{\omega}_l + k_\varphi(\varphi_l - \varphi_m^*) = \tau_l \,. \tag{3.14}$$

Here $(\cdot)^*$ denotes motor quantities calculated to the load side. Note that the resultant load inertia J_l is composed of several link inertias. Hence J_l is posture-dependent for most drives and the elastodynamic properties must be analyzed for a set of typical postures.

Using Eqs. (3.13) and (3.14), the transfer functions of the motor and load speed are determined. The transfer functions Eqs. (3.15) and (3.16) describe the motor and load response, respectively:

$$\frac{\omega_m^*(s)}{\tau_m^*(s)} = \frac{s^2 + \frac{k_\varphi}{J_l}}{s\left(s^2 + k_\varphi \frac{J_l + J_m^*}{J_l J_m^*}\right)} \tag{3.15}$$

$$\frac{\omega_l(s)}{\tau_m^*(s)} = \frac{\frac{k_\varphi}{J_m^* J_l}}{s\left(s^2 + k_\varphi \frac{J_l + J_m^*}{J_l J_m^*}\right)} \tag{3.16}$$

Here s is the complex variable. The natural frequency and antiresonance of the mechanical system, ω_r and ω_{ar}, correspond to the poles and zeros of the transfer functions, respectively, and are written as

$$\omega_{ar} = \sqrt{\frac{k_\varphi}{J_l}} \,, \qquad \omega_r = \sqrt{\frac{k_\varphi(J_l + J_m^*)}{J_l J_m^*}} = \sqrt{\frac{k_\varphi(J_l + J_m N^2)}{J_l J_m N^2}} \,. \tag{3.17}$$

From Eq. (3.17) it can be seen that ω_{ar} and ω_r are determined by the motor and load inertia, as well as the gear ratio and stiffness. The antiresonance frequency, ω_{ar}, is the frequency where an oscillation node coincides with the point of force application [32] and can be taken as a natural frequency at the load side. A forced torsional oscillation of the load side at ω_{ar} may cause the load side to oscillate at ω_{ar} while the motor remains at standstill or nearly standstill ($\omega_m \approx 0$, $\tau_m \approx 0$), and the servo actuator may fail to respond to desired actions or compensate disturbances. As an empirical value recommended by the gear manufacturer, $f_{ar} = \omega_{ar}/2\pi$ should be above 15 Hz for industrial robots and standard applications in mechanical engineering to avoid such effects [59]. During operation, the resonance speed on the motor side resulting from f_{ar} should be passed rapidly.

Load-to-Motor Inertia Ratio

From the control systems perspective, minimal motor inertia J_m yields faster accelerations and better transient responses due to the high torque-to-inertia ratio. This only holds true for the (unrealistic) assumption of a rigid motor-load coupling. In reality the load response does not correspond with that of the motor because of the finite stiffness of the motor-load coupling, cf. Eqs. (3.13) and (3.14). In this case the load-to-motor inertia ratio is fundamental in limiting the bandwidth of the servo system and, thus, an important parameter for drivetrain sizing and indicator of possible stability problems. The load-to-motor inertia ratio R_j is derived from the ratio of the natural frequencies, Eq. (3.17):

$$\frac{\omega_r}{\omega_{ar}} = \sqrt{1 + R_j}\,, \qquad \text{where} \qquad R_j = \frac{J_l}{J_m^*} = \frac{J_l}{J_m N^2}\,. \tag{3.18}$$

Servo systems with low ratio R_j show good disturbance rejection and response times. In order to prevent overshooting and oscillation at larger ratios ($R_j > 5$), the control gains must be reduced which extends the settling time. Another solution is to use control schemes which take the compliance of the motor-load coupling into account, see for example [29, 166]. According to a closed-loop analysis by Zhang and Furusho [209], the load-to-motor inertia ratio in high-response applications should be $1 \leq R_j \leq 4$. Finally, R_j affects power dissipation of the servo actuator because the motor acceleration torque increases with larger inertia ratios which goes along with higher power dissipation.

Practical Considerations

Rivin [155] addresses fundamental issues that must be considered when analyzing the stiffness and damping of power transmission systems and servomechanisms.

The antiresonance and resonance frequencies, Eq. (3.15), greatly affect the bandwidth of the speed control loop and the response time of the servo actuator [10]. In order to avoid resonance problems and to achieve faster tracking and closed-loop response, it is essential to increase the natural frequencies of the drivetrain without increasing its mass. To this end, the most effective measures to improve or avoid resonance problems are

- reducing the load inertia,
- choosing a higher transmission ratio,
- increasing the torsional stiffness of the drive mechanism, or
- using a motor with higher (peak) torque-to-inertia ratio.

Obviously, consistent lightweight design of the link structure and an improved mass distribution—of individual links and the kinematic chain as a whole—is the best way to reduce the load inertia J_l. If the lightweight design is fully exhausted, higher gear ratio or lower pitch for roller screws can be chosen to adjust the load-to-motor inertia ratio R_j. The coupling stiffness of the motor to the load is another critical issue in the servo drivetrain. Higher torsional stiffness of the motor-load coupling leads to higher natural frequencies of the overall system. As an example, the size of the Harmonic Drive gear unit of the hip joint flexion/extension axis is not only due to the higher torque loading, rather, it increases the stiffness of the motor-load coupling. Motor dynamics should rather be improved by choosing a motor with a higher dynamic factor (i. e., higher peak-torque-to-inertia ratio, cf. Eq. (2.4)) than by increasing the motor inertia. A higher dynamic factor accounts for better acceleration capabilities, thus, the motor can tolerate higher R_j with good response.

3.3.3 Dimensioning of Structural Components

The link structure of *Johnnie* accounts for nearly 43 % of the overall weight [46] which indicates a certain weight saving potential. The primary objective of structural dimensioning is therefore to keep the mass of structural components as low as possible while the static and dynamic stiffness should be high enough to minimize distortion and structural resonances. On the other hand, as discussed in Section 3.2, fully exploiting the weight saving potential is not feasible due to uncertainty of loading.

General Design Approach

Two different development methodologies are employed during the concept design stage:the *empirical design approach* relies on the designer's experience and intuition and is the most appropriate way of developing most part geometries. For major structural components with complex multi-axial stress conditions and/or strict geometric constraints, *topology optimization* is used to generate concept design proposals. Figure 3.5 compares the workflow of both approaches.

The empirical design shown in the left-hand branch is a very efficient trial-and-error approach which allows to develop well thought-out designs for most components, taking into account low mass and ideal force flux. Starting from a logical point, the design of single parts and/or assemblies is iteratively refined using the built-in finite element analysis (FEA) modules of CATIA[7] for structural analysis and strength assessment. Constraints are defined to resemble the actual installation of the component or assembly. Depending on the diversity of load

---

[7] CATIA Generative Part Structural Analysis (GPS) and CATIA Generative Assembly Structural Analysis (GAS) are used for the analysis of single parts and assemblies, respectively. Both GPS and GAS allow the consistent mapping of native CAD models to finite element models and integrate pre-processing, solving and post-processing capabilities.

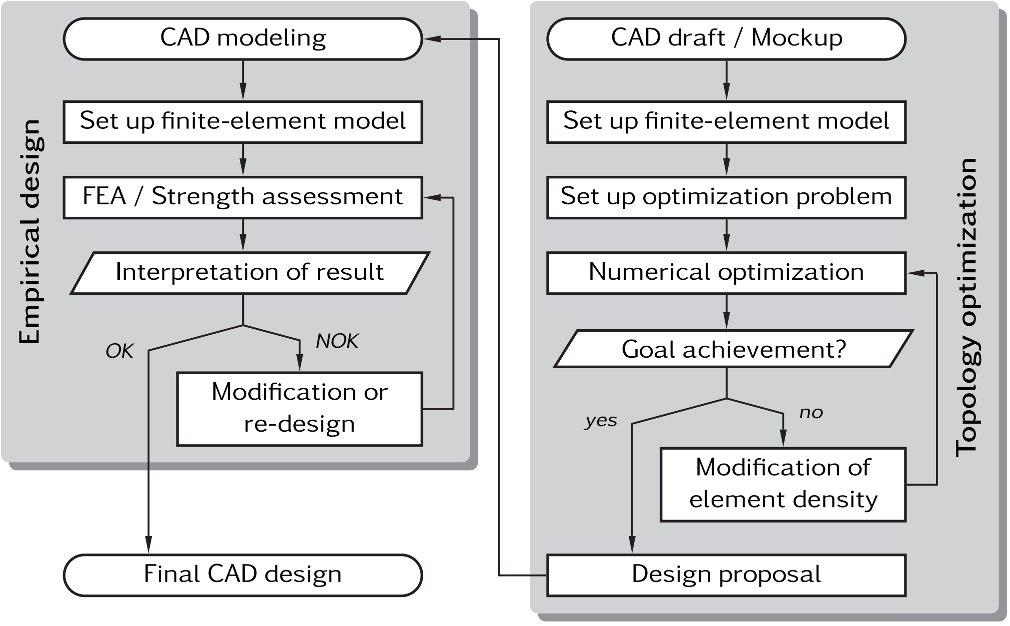

Figure 3.5: Comparison of empirical design to the automated process based on topology optimization

conditions, one or more load cases are analyzed using the constraint forces and moments calculated with the dynamics simulation (Section 3.3.1). This approach is particularly useful for smaller components and/or components where the weight saving potential is mainly limited due to manufacturing constraints and capabilities (e. g., minimum wall thickness or cutter radii).

If a component has various complex load conditions, strict geometric constraints and/or other design limitations, the empirical design approach is not always straightforward. Rather, it is difficult to find a satisfactory solution which meets the requirements. Here the FEM-based topology optimization method [61] aids the designer in achieving an effective lightweight design before modeling the actual part geometry. The additional workflow is shown in the right-hand branch of Figure 3.5. After the allowable designed space has been defined as a solid body or shell structure in CAD, the finite-element model is generated including all loads and constraints required to resemble the installation of the component or assembly as realistic as possible. Then the optimization problem is formulated, using mass or stiffness targets as possible goal functions. Optimization constraints include the maximum allowable deflection, minimum wall thickness, symmetry and manufacturing process parameters. Also, dedicated areas are reserved that must not be modified, e. g., bearing seating surfaces or connecting flanges. The design proposal is then determined iteratively without user interaction by numerical optimization. The result is mathematically optimal and superior to conventional designs, provided that the whole optimization model has been set up properly. Several load cases must be considered for optimization in order to obtain results which apply to typical, realistic scenarios. However, the implementation and verification of an optimization model are very time-consuming tasks. Also, transferring the design proposal into an actual part geometry is very costly

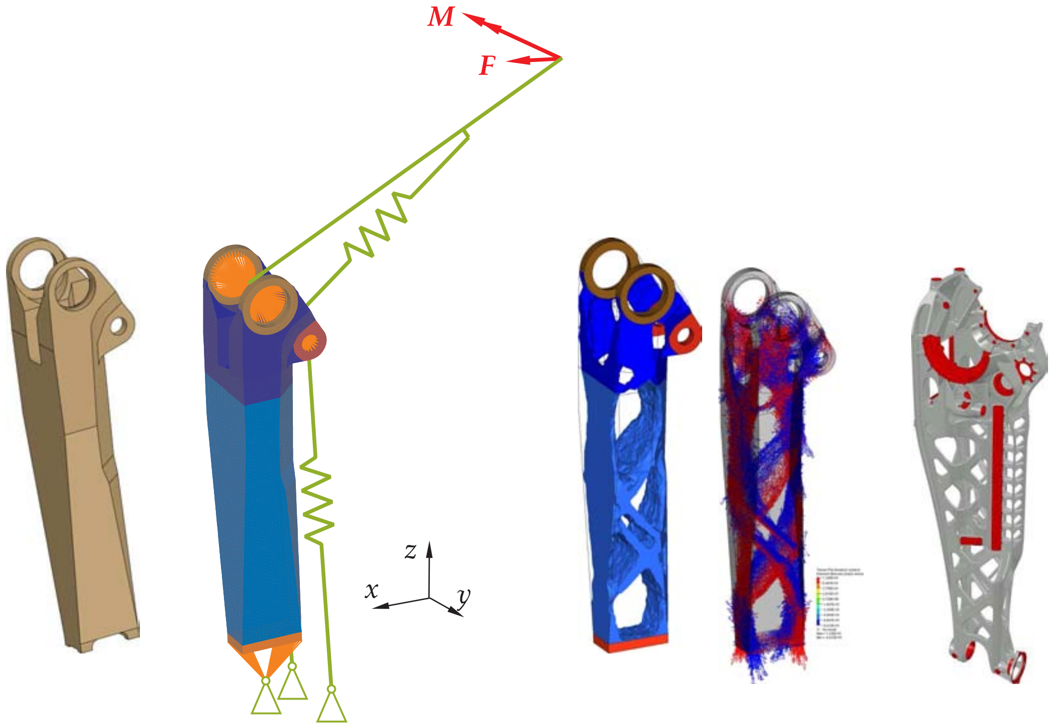

(a) Mockup (b) Optimization model (c) Optimization result (d) Part design

Figure 3.6: Topology optimization of the shank

because special attention has to be paid to manufacturability and assembly. The use of topology optimization must therefore be carefully balanced regarding the cost-benefit ratio and is thus limited to very few and complex parts. Another problem relates to the uncertainty of loading: as the loads can vary significantly when testing different walking patterns and control strategies, appropriate safety margins must be taken into account in the dimensioning of the robot structure. Topology optimization can thus only give an indication for the geometry of the actual part under typical load conditions.

The main bodies of the pelvis [168], thigh and shank segments have a very complex Monocoque-like structure (cf. Section 3.10), suggesting to create design proposals by topology optimization[8]. The optimization process is illustrated in Figure 3.6 using the example of the shank that connects the one-DoF knee joint and the two-DoF ankle joint [112]. Since these joints are actuated by linear mechanisms, the loads are transferred not only at the joint flanges but also at the several hinging points and bearings of the drive mechanisms.

In a first step the CAD mockup is generated which resembles the available designed space of the shank, Figure 3.6*a*. To this end, an interference analysis is conducted between the mockup solid and the operating volumes of moving parts, i. e., the drive mechanisms of knee and ankle joint and the adjacent links. For example, the space reservation for the linear actuator of the knee joint was done through the swept volume of the moving parts created with CATIA's DMU module. The mockup geometry should already consider the intended manufacturing

---

[8] The commercial software HyperWorks/OptiStruct from Altair Engineering was used.

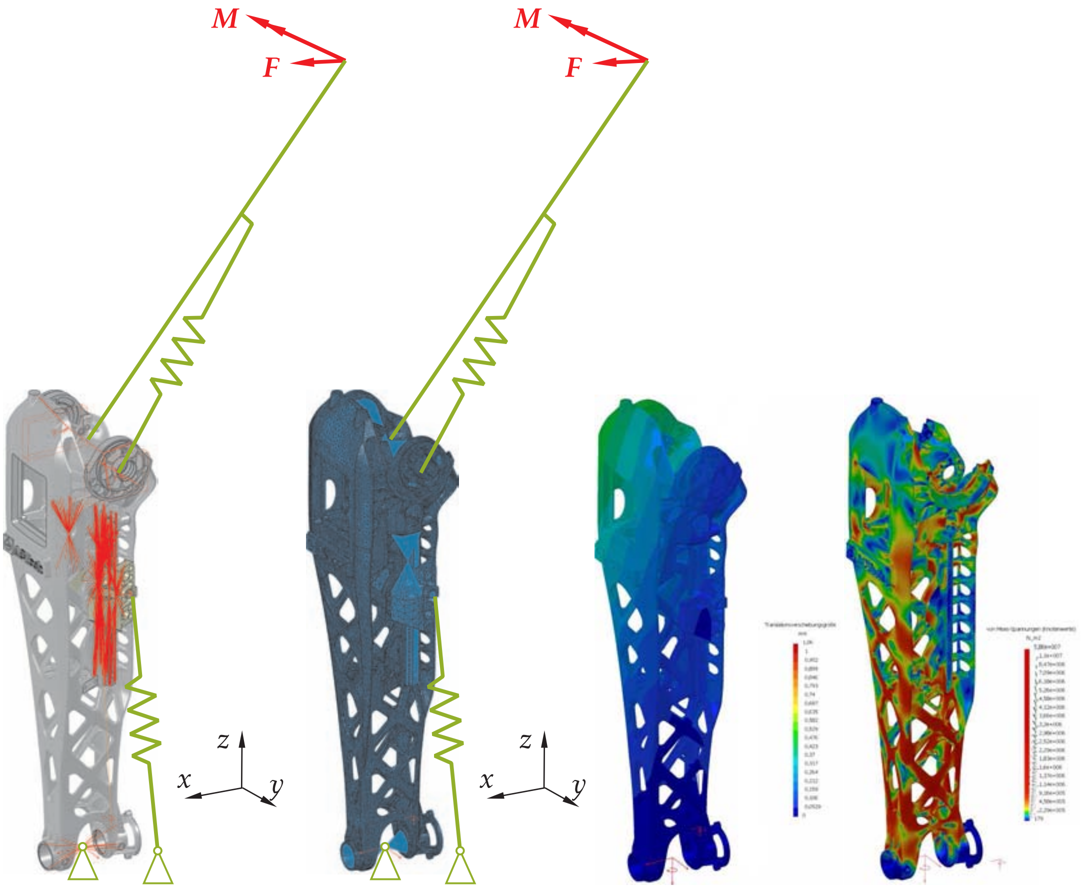

(a) FE model (b) FE mesh (c) Deflection (d) von Mises stress

Figure 3.7: FEM-based strength assessment of the shank

process and capabilities. The optimization model shown in Figure 3.6*b* is built upon the mockup geometry. Since realistic results can only be achieved if the load transfer by the drive mechanisms of the knee and ankle joint is taken into account, the shank and the knee and ankle joint drives are modeled as elastic bending beams. The constraint forces and moments are applied to the hip joint, while the ankle joint and coupler links are cardanically supported to the environment. The visualization of the results allows to locate the load step with the most significant contribution to the maximum load case. After the optimization results have been prepared by calculating an iso-surface of the material distribution, smoothing and data reduction, they are imported in the CAD system. The optimization result is shown in Figure 3.6*c*: the left-hand plot resembles an iso-plot of the element density. The right-hand vector plot shows the principal stresses, indicating the force flux. Finally, the part geometry shown in Figure 3.6*d* is developed based on the optimization result.

Strength assessment

Iterative stress analyses are applied throughout the design process as it allows the rather fast and simple evaluation and comparison of different design approaches, see Figure 3.5. After completion, highly stressed components and sub-assemblies

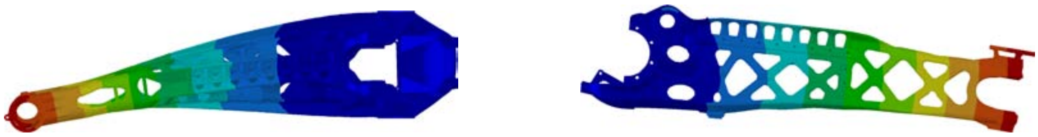

Mode 1 (317 Hz): side-to-side bending

Mode 2 (360 Hz): upward bending

Mode 3 (902 Hz): torsion

Mode 4 (997 Hz):
side-to-side bending & torsion

Mode 5 (1204 Hz): upward bending

Figure 3.8: Natural mode shapes of the shank base body. Scaling is omitted since the calculated deflections are only of qualitative nature. The red and blue areas indicate zero and maximum deflection, respectively.

are assessed by finite element analyses (FEA) for a final strength and fatigue evaluation [54]. The constraint forces and moments are again calculated with the comprehensive robot simulation (see Section 3.3.1). Based on these dynamic load profiles, different load cases are identified, e. g., maximum force, maximum moment and average loading, and safety factors account for load uncertainty. The material data are taken from different sources, such as manufacturer's data sheets or the standard work by Haibach [54]. Because of high manufacturing effort and costs, major link structures and some other critical components are designed conservatively to avoid failure. According to the infinite lifetime concept, stresses are kept below the threshold of fatigue limit.

The FEA of the shank sub-assembly is shown in Figure 3.7 to exemplify the workflow of strength assessment. In order to obtain a realistic and accurate finite element model, Figure 3.7*a*, it is not sufficient to consider solely the main body of the shank. Rather, a sub-assembly must be built consisting of the shank base body, knee joint flanges and linear carriages of the ankle joint drives (cf. Section 3.8.3). Moreover, the surrounding construction, including the thigh, knee joint actuator and coupler links of the ankle joint are modeled as elastic bending beams. The 1-D and 3-D meshes are connected by assembly constraints that resemble fastened, sliding, rigid, or smooth connection properties. Since influence on CATIA's automated meshing algorithms is limited, it is essential to perform iterative mesh refinement to obtain reliable results, Figure 3.7*b*. Lastly, Figure 3.7*c* and *d* illustrate deflection and von Mises stress of the component.

Elastodynamic Analysis

The dynamic stiffness of the leg links determines to a far extent the positioning accuracy of the feet. Structural vibrations can let the foot-ground contact occur too early and may, thus, easily destabilize the robot. Therefore, the resonant behavior of the major leg links is analyzed numerically with the FEM to determine the natural mode shapes and frequencies of the structure during free vibration. Numerical modal analysis supplies information about deflection modes and natural frequencies which are present in the robot structure. The results can help tracing poorly designed elements and structural weak points during the design stage. For example, Figure 3.8 visualizes the natural frequencies and corresponding mode shapes of the shank main body. They are basically characterized as side-to-side bending, upward bending, torsion, and combinations thereof. The figure only depicts the first five frequencies which are typically the most prominent modes at which the shank will vibrate, dominating all the higher frequency modes.

3.4 Modular Joint Design

The detailed weight analysis by Gienger [46] revealed that the servo actuators make the second largest part the total weight—22.7 % account for the motors and another 7.9 % for the gears. Along with the constraints of human dimensions, the weight restrictions exclude the use of off-the-shelf servo actuators. Hence the development of lightweight servo actuators that combine precision gearing with a high-dynamic servo motor and sensors into a compact package is crucial. This section presents the design of the revolute joints based on permanent magnet synchronous motors and Harmonic Drive gears that were discussed in Section 2.5.1.

3.4.1 Motivation for Modularity and its Limitations

Modularity as a design goal has been extensively investigated in the engineering literature [27, 138]. Regarding robotics, modularity is a rather new but suitable approach to designing complex robotic systems. Examples of modular robots built from a set of standard components include research prototypes [67, 120], as well as commercially available systems[9].

Besides well-known design and manufacturing benefits, the principal advantages of modular design include reduced time-to-repair and spares inventory. Moreover, reconfiguration of the robot (to modify certain components according to experimental results, or match different operative requirements), performance upgrades of the actuators, and future extensions (additional DoFs, sensors, etc.) are simplified and have minor effects on the rest of the system. For example, the arms currently have a quite simple structure (cf. Section 2.2.4), tailored to compensate the angular momentum effectively. From a hardware point of view, the replacement by full arms and hands for manipulation is simplified by a modular architecture. The major disadvantages of modular robots are the higher overall

---

[9] For example, the Schunk *PowerCube* system, available at: `http://www.schunk.com/`

mass, lower dynamic performance and reduced stiffness. The overall mass is generally higher because of the larger number of parts and their connections and goes along with lower dynamic performance. Moreover, since all servo actuators are located close to the corresponding joints, the inertia of modular serial-link robots is higher than at comparable non-modular systems. If properly designed, the latter have an improved mass distribution since the spatial separation between the actuators and joints is possible. Finally, the stiffness of modular serial-link robots is reduced due to the higher part count, the presence of numerous connections and, frequently, unfavorable force flux resulting from the standardized flanged connections and joint bearing structures.

Therefore, a fully modular robot architecture, where all functional unit are independent from each other, is not useful for a high-dynamic robot and contradictory to the fundamental design goals developed in Section 2.4. Rather, a limited modular approach with actuators built on the unit construction principle is proposed, while the main structure is non-modular. All rotary drives have the identical structure and comprise a joint, the corresponding actuator (motor and reduction gear) and a servo drive unit that also incorporates a low-level motion controller (see Section 5.2). The sizes of the motors and gears are adapted to the individual power requirements. Many parts are standardized for all drives, only some housings and connecting flanges are customized for optimal force flux. Moreover, the linear actuators of the knee and ankle joints (cf. Sections 3.8.2 and 3.8.3) employ the modular design features to a far extent. This approach turned out to be the most reasonable and economic way of realizing the robot at minimal mass while taking into account ease of manufacturing.

Although the main structure is non-modular, standardized flange connections of many actuators (such as the shoulder and hip joints) and, particularly, the separation of actuators and structural components yield certain modularity on a higher level, allowing to easily exchange the arms and legs, as well as the upper body. Conversely, a rather low level of modularity with joint-specific connections is applied to the legs in order to achieve a particularly advantageous force flux, high stiffness and low mass.

3.4.2 Revolute Joints based on Harmonic Drive Gears

Highly integrated joint units with maximum power density can only be realized, if the latest technologies in the field of electrical drives, gears and sensors are used. As stated in Section 2.5.1, the main reasons to choose frameless PMSM over BDCM are their torque and speed bandwidths, the greater power density and robustness. The fusion of motor, gear and sensors into highly integrated, mechatronic joint units has several advantages for the overall system:

- High velocity range at good dynamic performance
- High power density and efficiency
- Comparatively small designed space per servo actuator
- Reliability due to brushless design of the motors and, in conjunction with decentralized motor control, the ability to self-monitoring and fault diagnosis (cf. Section 5.2)

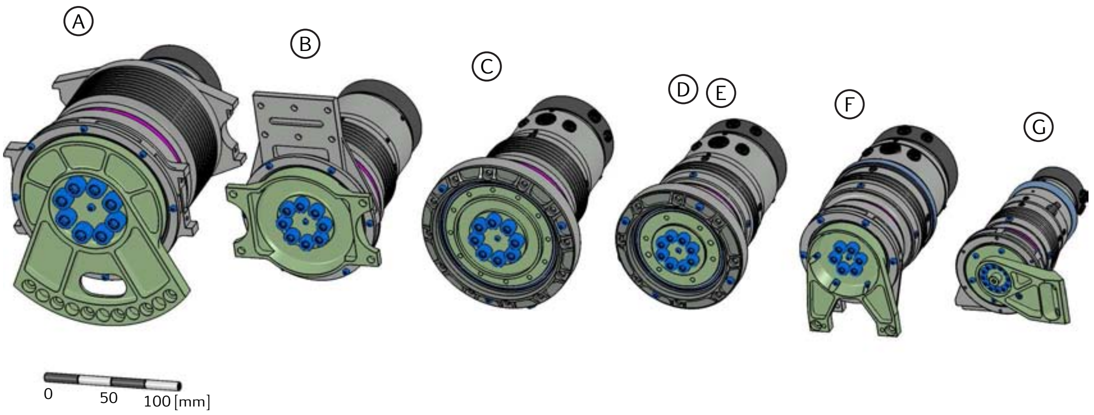

A	Hip joint (flexion/extension)
B	Hip joint (adduction/abduction)
C	Hip joint (internal/external rotation)
D	Pelvis joint (adduction/abduction), Pelvis joint (internal/external rotation)
E	Shoulder joint (flexion/extension)
F	Elbow joint (flexion/extension), Shoulder joint (adduction/abduction)
G	Toe joint (flexion/extension)

Figure 3.9: Modular design of revolute joints based on Harmonic Drive component sets (drawn to scale)

Except for the camera head described in Section 3.5 where the low power requirements allow to use off-the-shelf servo actuators, a total of 16 DoFs are actuated by seven different rotary drives based on Harmonic Drive component sets. All gears are customized lightweight versions with a T-shaped Circular Spline which is, in the author's opinion, the best tradeoff between mass and load rating. The solid Wave Generator plugs are made from either aluminum or steel and modified for low mass and inertia. Most drive units employ HFUC series component sets [59], except for the hip joint flexion/extension axes. Here, CSG series component sets [59] are used as they feature a significant increase in torque capacity in comparison to the HFUC series gears. The toe joint actuators employ off-the-shelf CPL series lightweight component sets [57]. Figure 3.9 gives an overview of the drives, starting from the high-performance drive 'A' used in the hip joint flexion/extension axis, to the lightweight toe joint actuator 'G'. Note that the type 'B' and 'C' actuators share the identical motor housing and differ only in the output bearing. Type 'D' and 'E' differ only in the stack length of the motor, so that drive 'E' is omitted in the figure. The key technical data are listed in Appendix C.

Basically, two joint principles are employed that differ in the output flange bearing. The first type uses a four-point contact ball bearing and an additional support bearing. This type is applied to joints where a single bearing at the output flange would impair the force flux and unacceptably decrease the tilting rigidity of the joint, for instance the hip joint adduction/abduction and flexion/extension axes. The second type employs a thin-ring crossed roller bearing at the output. Although a single bearing is used, tilting rigidity and load rating are maintained, space restrictions can be met easier and the adjacent construction is simplified and more compact.

The design and mode of operation of the servo actuator with four-point contact ball bearing are illustrated by Figure 3.10 which shows the hip joint flexion/extension drive (type 'A'). For optimal heat transfer, the stator (1) of the

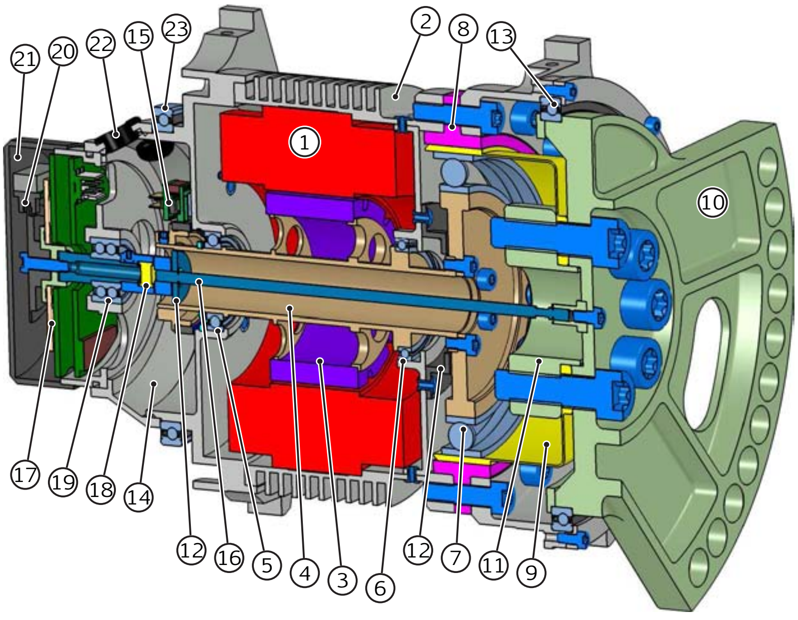

1	Stator
2	Motor housing
3	Permanent magnet rotor
4	Motor shaft
5	Motor shaft bearing A
6	Motor shaft bearing B
7	Wave Generator
8	Circular Spline
9	Flexspline
10	Output flange
11	Clamping ring (Flexspline)
12	Gap seal
13	Four-point bearing
14	Sensor mounting ring
15	Incremental encoder
16	Sensor shaft
17	Absolute angular sensor
18	Elastomer coupling
19	Sensor bearing
20	Limit switch
21	Protective cover
22	Cable grommet
23	Support bearing

Figure 3.10: Harmonic Drive-based revolute joint with four-point contact ball bearing and support bearing, here: hip joint flexion/extension drive (type 'A')

frameless PMSM is bonded into the motor housing (2) with a thermally conductive epoxy. The motor housing (2) has cooling fins for natural convection. The permanent magnet rotor (3) is bonded onto the motor shaft (4) which rotates on two deep groove ball bearings in a locating/non-locating arrangement. The locating bearing (5) is placed next to the sensor area to maintain the axial position of the magnetic ring of incremental encoder (15), ensuring optimal output signals and reducing interpolation errors. The non-locating bearing (6) is placed on the gear side where axial displacement due to thermal expansion is not critical. The Wave Generator (7) is flanged on the motor shaft (4). The Circular Spline (8) is fixed to the motor housing (2), and the Flexspline (9) is attached to the output flange (10), using the clamping ring (11). Hence, turning the motor shaft (4) moves the output flange (10) with respect to the motor housing (2). The *EKagrip* [34] friction shim (not shown), inserted between the Flexspline (9) and the output flange (10), greatly increases the coefficient of friction so that the maximum torques can be safely transmitted. The gap seal (12) keeps the clearance between the gear components and the housing within the specifications for grease lubrication. A four-point contact ball bearing (13) is employed at the output flange (10). It is complemented by the additional support bearing (23), which is a radial contact ball bearing. The inner ring of bearing (23) is clamped in position by the sensor mounting ring (14). The bearings (13) and (23) are sealed thin-section bearings with imperial measurements which are widely used in robotics and aerospace applications. They are characterized by low mass and small cross sections which remain constant as the bore diameter increases. All sensors (cf. Section 4.1) are arranged on the B-side of the motor in a separated dustproof section of the housing, opposite to the gear unit. The incremental encoder (15) is mounted on the motor shaft (4) and provides angular position and velocity of the permanent magnet rotor (3) with

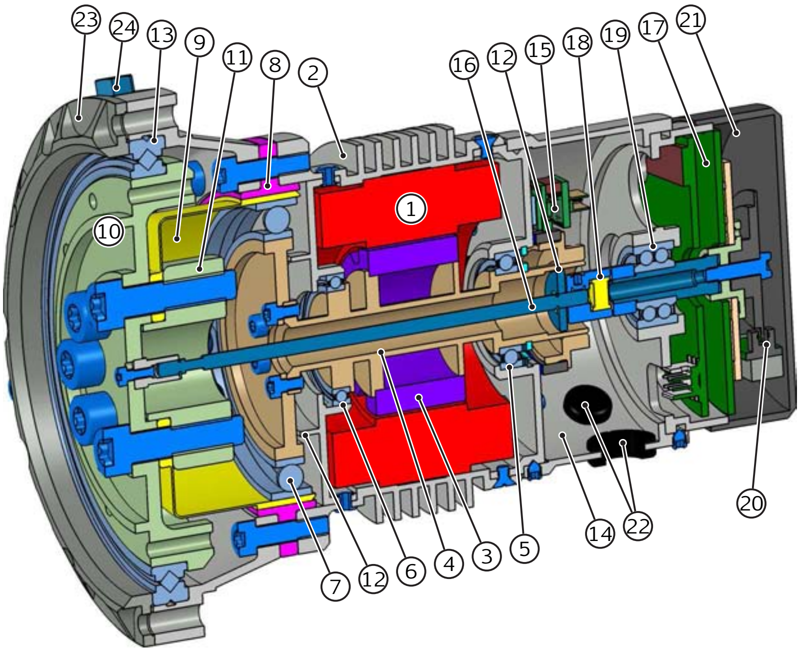

1	Stator
2	Motor housing
3	Permanent magnet rotor
4	Motor shaft
5	Motor shaft bearing A
6	Motor shaft bearing B
7	Wave Generator
8	Circular Spline
9	Flexspline
10	Output flange
11	Clamping ring (Flexspline)
12	Gap seal
13	Crossed roller bearing
14	Sensor mounting ring
15	Incremental encoder
16	Sensor shaft
17	Absolute angular sensor
18	Elastomer coupling
19	Sensor bearing
20	Limit switch
21	Protective cover
22	Cable grommet
23	Clamping ring (bearing)
24	Grease nipple

Figure 3.11: Harmonic Drive-based revolute joint with crossed roller bearing, here: hip joint internal/external rotation drive (type ‘C’)

respect to the stator (1). The flange of the absolute angular sensor (17) is fixed to the gear housing using the mounting ring (14). It is connected to the gear output (10) by the sensor shaft (16), enabling the direct measurement of the output angle without obstructing the connection between the gear output and adjacent construction. The sensor shaft (16) is free from moment and radial loading to ensure an accurate transmission of the output angle. The groove on its output flange side acts as an elastic flexure hinge. In conjunction with the backlash-free miniature elastomer coupling (18), the sensor shaft (16) is angularly flexible to compensate for radial and axial misalignment. The coupling (18) connects to the disk of the angular sensor (17), which is supported by the sensor bearing (19). A double row angular contact ball bearing is used as it takes up less axial space than two single row bearings. The support configuration of the sensor shaft (16) and sensor disk are thus statically determined. The short sensor shaft allows to maintain the correct working distance between the disk and the measuring module of sensor (17). Finally, the photoelectric fork sensor (20) limits the angular workspace of the joint, using a cam fixed to the sensor shaft (16). The housing of the rotary drive is divided into three areas: Harmonic Drive gear, electric motor and sensors are installed in different areas, separated by the bearing flanges. Accordingly, all bearings are equipped with seals, but gap seals are preferred over lip seals due to reduced friction. In addition, the gap seals (12) prevent the grease from ingress into the motor and sensor areas. Protection of the sensors against ingress of solid foreign objects and dust is ensured by the cover (21) and the cable grommets (22).

The second type of rotary servo actuator shown in Figure 3.11 is applied to the internal/external rotation axis of the hip joint. The basic structure is identical to the previous actuator but this type actuator employs a single thin-section

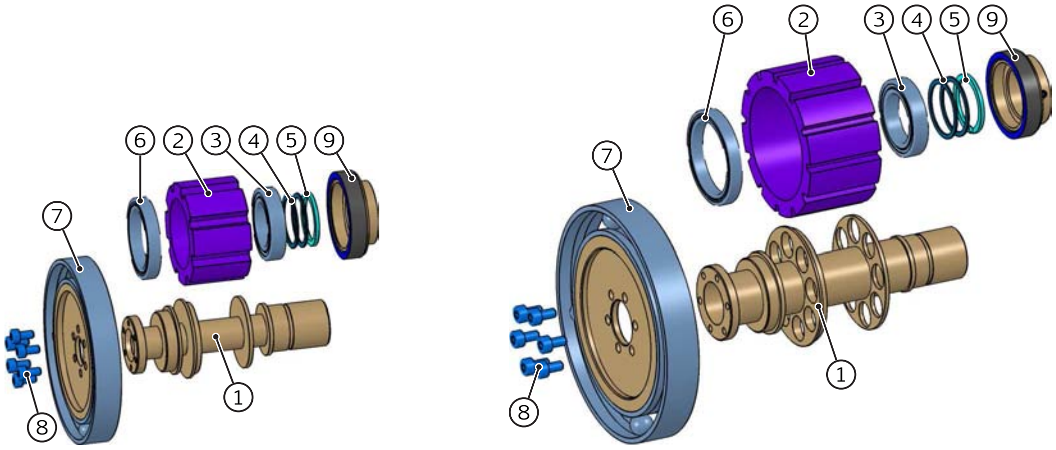

(a) Hip joint internal/external rotation *(b)* Hip joint flexion/extension

1	Motor shaft	4	Adjustment shims	7	Wave generator
2	Permanent magnet rotor	5	Retaining ring	8	Screws
3	Locating bearing	6	Non-locating bearing	9	Magnetic encoder ring

Figure 3.12: Low-inertia design of the motor shafts

crossed roller bearing (13) at its output flange. crossed roller bearings are typically supplied with pre-load and can receive loads in all directions, including radial, axial and moment loads. Due to the line contact between the cylindrical rolling members and the bearing rings, these bearings achieve high tilting rigidity and load ratings, eliminating the need for an additional support bearing. The bearing outer ring is easily fixed to the housing by the clamping ring (23), while the inner ring is fixed by the adjacent construction. During assembly of the drive unit, the clamping ring (23) is fixed only by a few small screws. It is then tightened tension-free and with the prescribed number of screws and tightening torque, when the drive unit is assembled in the adjacent construction. The grease nipple (24) eases maintenance of the crossed roller bearing (13).

Figure 3.12 illustrates the low-inertia design of the motor shafts. Since motor shaft inertia is dominated by the inertias of the permanent magnet rotor (2) and Wave Generator (7), the latter is customized for low inertia and mass. The solid Wave Generator plug is made from aluminum or steel and omits the Oldham coupling of the standard versions. The permanent magnet rotor (2) is bonded onto motor shaft (1) while the Wave Generator (7) is screwed to it. The motor shaft (1) is made from aluminum and shows extremely thin cross sections. It is supported by locating bearing (3), which is fixed in position by adjustment shims (4) and retaining ring (5), and non-locating bearing (6). Both bearings are thin-section ball bearings. The magnetic encoder ring (9) is clamped onto the motor shaft.

3.5 The Stereo Robotic Head

The head of the robot holds a high-resolution stereo camera pair. Its mechanics presented in Figure 3.13 comprise a two-DoF pan-tilt unit whose torque/speed capabilities allows smooth pursuit movements, as well as the generation of human-

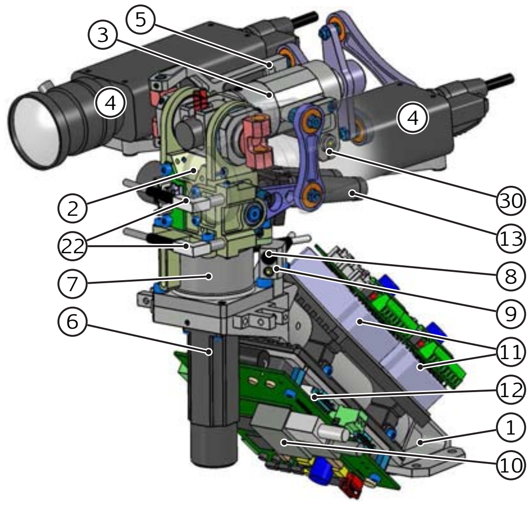

(a) Overview

1	Head mount	17	Support bearing
2	Pan segment	18	Coupler link
3	Tilt segment	19	Spherical plain bearing
4	Camera	20	Tilt bearing
5	Camera receptacle	21	Locknut
6	Pan motor	22	Limit switch
7	Pan gearbox	23	Servo actuator
8	End stop	24	Bellows coupling
9	Limit switch	25	Output bearing
10	DSP module	26	Lever arm
11	Motor controller	27	Coupler link
12	DC/DC converter	28	Vergence axis
13	Cable gland	29	Plain bearing
14	Servo actuator	30	Limit switch
15	Torque limiter	31	Camera spacer
16	Lever arm		

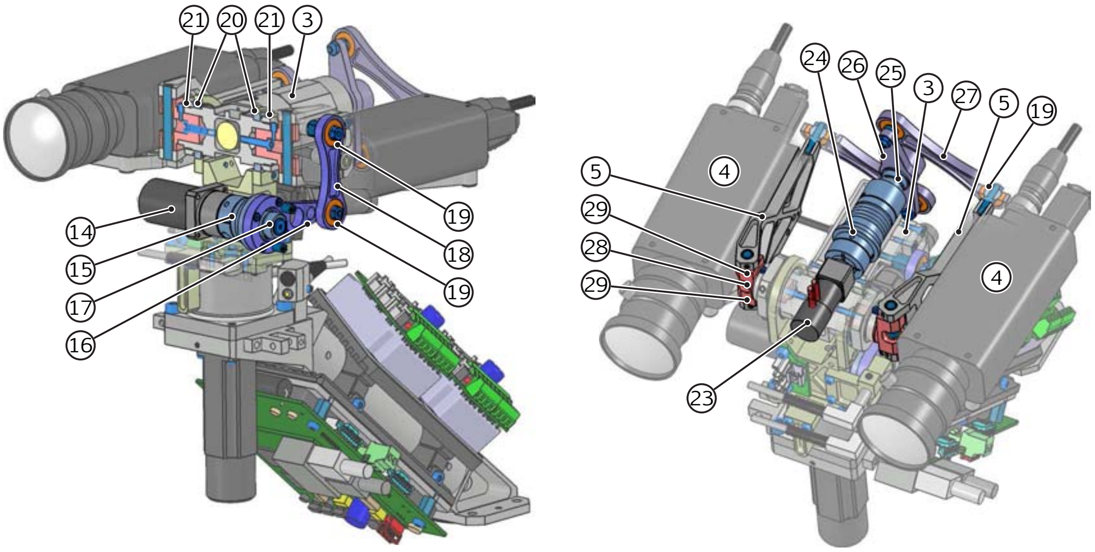

(b) Tilt drive mechanism

(c) Vergence drive mechanism

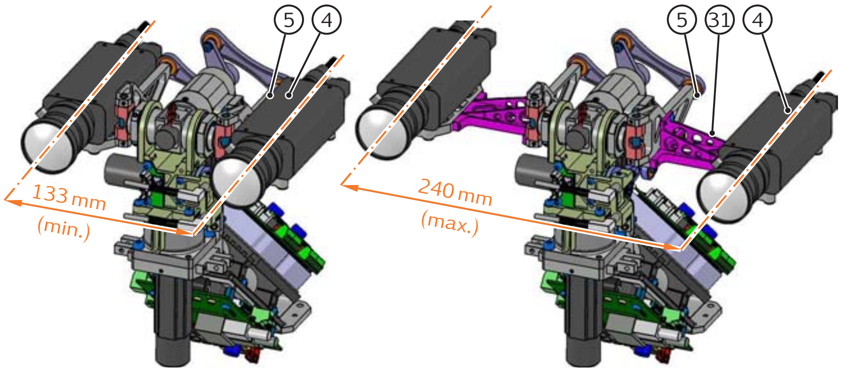

(d) Stereo basis adjustment

Figure 3.13: Mechanical design of the three-DoF camera head

like saccadic camera motions. In addition, a one-DoF mechanism is implemented for camera vergence adjustment, enabling the robot to fixate a visual target with both cameras. The camera stereo basis is manually adjustable within a wide range, and the mechanical camera interface allows to exchange the cameras very easily and precisely. The total mass is 2.4 kg, including the cameras and lenses (0.31 kg each).

The head mount (1) shown in Figure 3.13*a* connects to the upper body. It is composed of two connecting flanges, bonded and riveted to a thin-walled aluminum tube. The upper flange of head mount (1) accepts the pan servo motor (6) and the reduction gear (7). The latter is a very compact and lightweight, off-the-shelf gearbox with integrated output bearing [58]. The angular workspace of the pan segment (2) is limited by two end stops (8). Due to limited space, absolute angular sensors are omitted in the camera head: the switches (9) are precision switches with high repeatability, serving both as limit switches and reference point signals. Likewise, two limit switches (22) for tilt motion are mounted on the pan segment (2), and the limit switch (30) for vergence motion is mounted on the tilt segment (3). The pan segment (2) carries the tilt segment (3) which holds the cameras (4) with the receptacles (5). The mechanical camera interface simplifies experiments with different types of cameras. Each camera (4) is positioned with respect to the receptacle (5) by two locating pins (not shown), ensuring fast and easy replacement with high repeatability. Finally, the head mount (1) holds all the necessary electronics, consisting of DSP module (10), motor controller (11) and DC/DC converter (12) for conversion of the motor voltage. Cable gland (13) guides all cables coming from pan segment (3).

Figure 3.13*b* shows the tilt axis drivetrain. The Harmonic Drive servo actuator (14) [60] is connected to the tilt segment (3) by a parallel-crank mechanism to achieve a compact design: the lever arm (16) is mounted on the output shaft of servo actuator (14), driving the tilt segment (3) via the coupler link (18). The coupler link (18) incorporates spherical plain bearings (19) at its ends. Due to the large distance between the output bearing of servo actuator (14) and lever arm (16), the gear output is supported by bearing (17) for accommodation of tilting moments. The tilt segment bearing (20) is composed of two thin-section ball bearings in an adjusted O-arrangement and secured by the locknuts (21). As the loads during an emergency can easily exceed the collision torque of actuator (14), the output shaft is protected by the torque limiter (15) that provides precise and fast overload protection [160]. If the preset torque limit has been reached, the output of torque limiter (15) is disconnected from the input. The chosen torque limiter is free from backlash in either direction of rotation and provides single-position re-engagement, i. e., it will re-engage automatically 360° from the original position.

Figure 3.13*c* shows the drive mechanism of the vergence axis, which is entirely integrated into tilt segment (3). The mechanism is designed to ensure symmetric adjustment of the camera angle using a single actuator. The camera vergence axes (28) are driven by a Harmonic Drive miniature servo actuator (23) [60] and two four-bar mechanisms that interface to the camera receptacles (5). The mechanisms consist of a double lever arm (26) and two coupler links (27) of equal length. Lever arm (26) is supported by two thin-section ball bearings (25) in an adjusted bearing arrangement, the coupler links (27) employ spherical plain bearings (19). The miniature bellows coupling (24) with integrated torque limiter [160] connects the output of servo actuator (23) and the lever arm axis (26), reducing the risk of damage in an emergency. Both vergence rotational axes (28) are supported by plain bearings (29) with minimal clearance.

Finally, Figure 3.13*d* illustrates the manual adjustment of the camera stereo basis. The stereo basis can be adjusted between 133 mm and 240 mm by interposing camera spacers (31) between the receptacles (5) and the cameras (4).

3.6 The Torso and Pelvis

The upper body is the root segment of the robot multibody system that is used for simulation and control of the robot. The pelvis is a highly loaded segment, interfacing the legs and the upper body. The design of these segments is presented in Figures 3.14*a* and 3.14*b*, showing the front and rear view of the robot, respectively. The figures show the camera head (2), described in the previous section, the arms (3) and the pelvis segment (1). All components are mounted on the trunk support structure which is shown in Figure 3.14*c* and described later in this section. The arms (3) are mounted on the support structure by the shoulder joint flexion drive (4) flange. The upper body also holds the inertial measurement unit (7) which estimates the orientation and angular velocities, see Section 4.4. Mounted on the back of the robot is the PC-based central control unit (8) that is described in Section 5.1. The upper body and the pelvis segment (2) hold several DSP modules and motor electronics (5), cf. Section 5.2, for the upper body and hip joints. The DC/DC converters (6) convert the external small signal voltage to supply all decentral controller modules and the central control unit. The connector panel (9) on the back provides connectors and strain relief for all external cables, i. e., the Ethernet connection, motor and small signal voltage and the emergency stop cable. The panel also includes an emergency stop pushbutton (10) to disable the motor supply in case of failure (cf. Section 5.4). The handles (11) simplify handling of the robot during experiments and transport.

Figure 3.14*c* shows the trunk support structure which is basically designed as a bonded and riveted pipe frame structure. Hence the cavities of the main (13) and shoulder girder (14) could be foamed with polyurethane for improved vibration damping if necessary. All attached parts shown in Figures 3.14*a* and 3.14*b* are mounted on the support structure using pipe clamps or blind nuts. The latter are a very effective solution when load-bearing threads are required in thin-walled parts. The support structure is flanged on the pelvis internal/external rotation joint (not shown) by the connecting flange (12). The main girder (13) extends from the pelvis joint flange (12) up to the shoulder joint level where it merges into the shoulder girder (14) and the shoulder joint flanges (16). The shoulder transverse tubes (15) and struts (19) provide additional load-moment support and reinforce the connection of the shoulder joint flanges (16). The support structure provides a connecting flange to the head mount (17) on its top face which is supported by

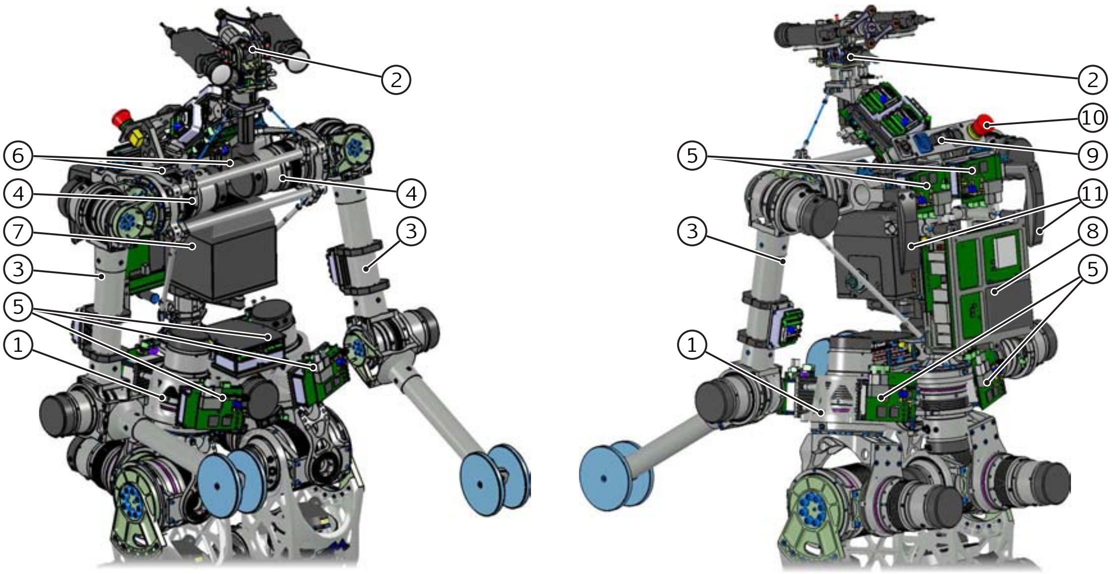

(a) Front view

(b) Rear view

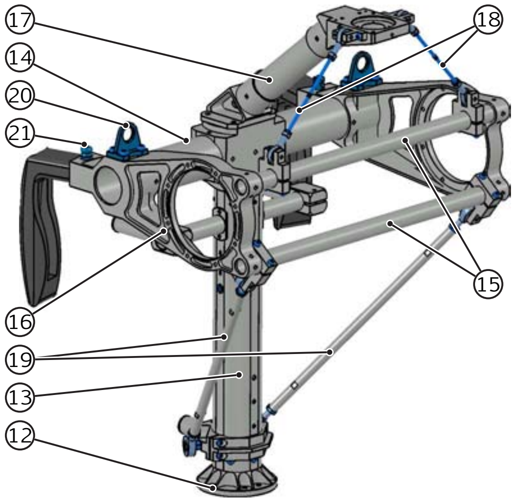

(c) Trunk support structure

1	Pelvis segment
2	Camera head
3	Arm
4	Shoulder joint flexion drive
5	Motor electronics
6	DC/DC converter
7	Inertial measurement system
8	Central control unit
9	Connector panel
10	Emergency stop pushbutton
11	Handle
12	Pelvis joint connecting flange
13	Main girder
14	Shoulder girder
15	Shoulder transverse tube
16	Shoulder joint flange
17	Head mount
18	Strut (head)
19	Strut (shoulder)
20	Fastening eye
21	Locating pin

Figure 3.14: Mechanical design of the upper body

head strut (18) for increased tilting stiffness. In order to avoid damage of the robot during experiments, it is secured by a safety rope. The rope is attached to the robot by the fastening eyes (20). Lastly, two locating pins (21) are used to fixate the upper body in the calibration jig (cf. Section 3.11.1).

The pelvis interfaces to the internal/external rotation joints of the legs and to the upper body via the two-DoF pelvis joint. Using the pelvis joint, upper body orientation is independent from leg motion except for flexion/extension. Pelvic rotation can be utilized to increase the step lengths and provides an additional means of compensation the total body angular momentum, as discussed in Section 2.2.5. Leg swing induces high torsional moments into the pelvis structure. The main body shown in Figure 3.14(a) must therefore show high stiffness to

(a) Pelvis base body

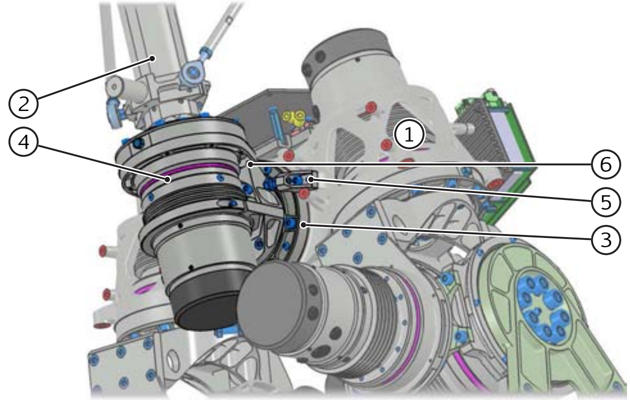

1	Pelvis segment
2	Upper body support structure
3	Adduction/abduction joint
4	Internal/external rotation joint
5	End stop
6	Pelvis joint connecting member

(b) Pelvis joint

Figure 3.15: Mechanical design of the pelvis segment and joint

ensure accurate foot placement with low distortion. The compact and lightweight pelvis segment is manufactured from aluminum by investment casting[10]. The two-DoF pelvis joint is shown in Figure 3.15(b). The adduction/abduction (3) and internal/external rotation joints (4) connect to the pelvis segment (1) and the upper body support structure (2), respectively. The mechanical end stops (5) limit the angular motion of the adduction/abduction axis and avoid collisions with electronics components and cable overstretching.

3.7 The Arms

The arms of the robot have a rather minimalist design with three DoFs each. Since manipulation tasks are not considered, they are used only for compensating total body momentum to avoid slippage. Figure 3.16 shows the design of the right arm. The housing of the shoulder flexion/extension drive (2) is flanged on the support structure of the upper body (1). The shoulder drive (2) is a type ‘E’ servo actuator (Figure 3.9) with a single crossed roller bearing at its output. The shoulder adduction/abduction joint (3) and the elbow flexion/extension joint (4)

---

[10] See Section 3.10 for details on the design and manufacturing of the investment castings.

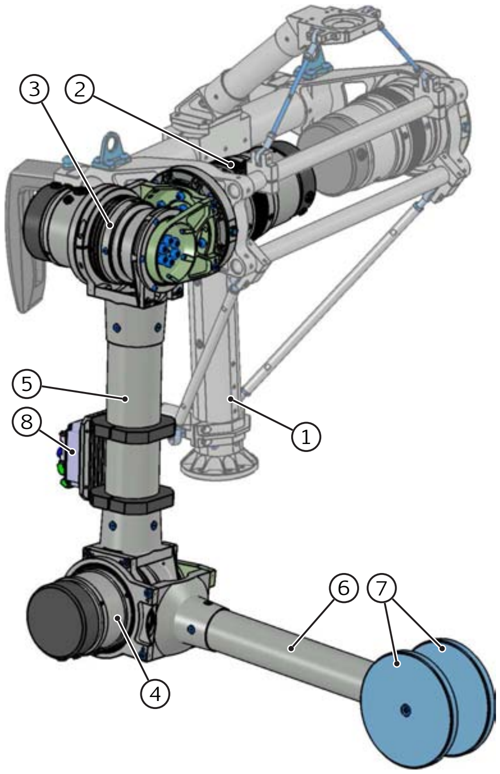

1	Upper body support structure
2	Shoulder joint flexion/extension
3	Shoulder joint adduction/abduction
4	Elbow joint flexion/extension
5	Upper arm
6	Lower arm
7	Balance weight
8	Motor controller

Figure 3.16: Mechanical design of the arms

are driven by a type ‘F’ servo actuators with four-point contact ball bearings and additional support bearings. The upper arm (5) and lower arm (6) are made of thin-walled aluminum tubes. The connecting flanges to the servo actuators are mounted with blind rivets and polyurethane adhesive bond. The lower arms (6) are equipped with balance weights (7) at their ends. The upper arm holds the motor controller (8) of the elbow joint.

3.8 The Legs

This section introduces the leg design which is considered the core component of the mechanical structure. Section 3.8.1 introduces the hip joint, a spherical joint composed of three serial drives. Sections 3.8.2 and 3.8.3 elaborate on the novel drive mechanisms for the knee and ankle joint, respectively. Both designs reduce the resultant leg inertia significantly, as discussed in Section 2.4. Section 3.12 concludes with a discussion of the mechanical design and compares different drive mechanisms of the knee and ankle joints.

3.8.1 The Hip Joint

As stated in Section 2.6.1, the three-DoF hip joint is composed of serial drives, forming a spherical joint with common intersection point. Particular care is necessary in the conception and design of the hip joint. Besides sufficient actuator performance, the static and dynamic stiffness of the connecting joint between the leg and the pelvis is fundamental for the walking performance of the robot. Figure 3.17 shows the mechanical design of the hip joint. The internal/external rotation axis (2) is inclined 10° to the vertical axis to achieve a better power distribution among the drives [46].

The hip joint drives are among the highest loaded joints of the robot. The integration of these drives in a very narrow installation space is most challenging. In addition, the hip joint structure and bearings must show high tilting rigidity which is complicated by the large workspace of the flexion/extension axis. Therefore, several design approaches were designed and compared in terms of their static and dynamic properties. The chosen design shown in Figure 3.17*a* comprises the internal/external rotation drive (2) with crossed roller bearing (type 'B', Figure 3.9) which is screwed to the pelvis segment (1). It is followed by the adduction/abduction drive (3) and the flexion/extension drive (4) which are of type 'C' and 'A', respectively. For high tilting rigidity and direct force flux, drives (3) and (4) comprise four-point contact ball bearings at the output flanges and additional support bearings (7). Both bearings (7) are thin-section deep groove ball bearings in a non-locating arrangement. The fork-shaped rotation segment (8) holds the adduction/abduction drive (3) and support bearing (7), surrounding the hip joint adduction/abduction segment (9). Despite its slender shape, bending and torsional stiffness of segment (8) are high enough.

Figure 3.17*b* explains the fixation of the hip joint in the pelvis segment. The connecting flange of the internal/external rotation drive (2) is screwed on the pelvis segment (1) together with the outer ring of crossed roller bearing (5). For direct force transmission into the pelvis segment, motor housing (2) is additionally supported by the polyurethane ring (6) inserted between the motor housing (2) and bearing surface of pelvis segment (1). The viscoelastic properties of polyurethane ring (6) enhance damping and provide an effective way to reduce structural vibrations and oscillations of the swing foot.

3.8.2 The Knee Joint

As pointed out in Section 2.6.2, a linear drive acting as length-variable coupler improves the mass distribution in the hip-thigh area, opposite to a conventional design with Harmonic Drive gears. Hence thigh inertia is only marginally larger compared to *Johnnie* but knee joint performance is increased significantly. In addition, using planetary roller screws instead of ballscrews leads to additional weight savings due to the considerably higher load rating of these machine elements.

Figure 3.18*a* gives an overview of the one-DoF knee joint (1), located between the thigh (2) and shank (4) segments. The servomechanism comprises the linear actuator (5) and the absolute angular sensor (8) that enables the direct measurement of the knee angle. The driving side of linear actuator (5) is attached to the thigh segment (2) by the universal joint (6). The output side of actuator (5) is connected to the shank (4) by the universal joint (7). Because of limited space and moving parts in the knee joint area, all cables coming from the shank (4) are guided by the protective cable conduit (9) to avoid cable jamming.

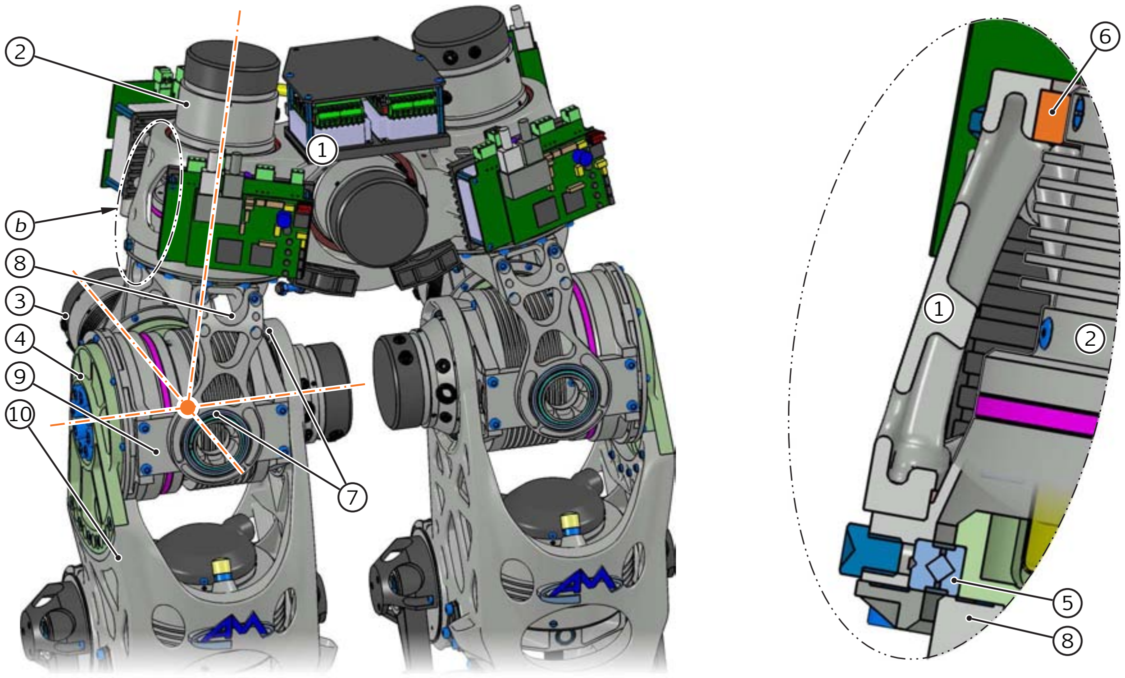

(a) Overview

(b) Hip joint rotation axis

1	Pelvis segment	5	Crossed roller bearing	8	Hip joint rotation segment
2	Internal/external rotation drive	6	Polyurethane ring	9	Hip joint adduction segment
3	Adduction/abduction drive	7	Support bearing	10	Thigh segment
4	Flexion/extension drive				

Figure 3.17: Mechanical design of the hip joint composed of three serial drives with intersecting axes

Because of limited available space in the knee joint axis, the absolute angular sensor (8) is shifted towards the thigh (2) using a parallel-crank mechanism. Figure 3.18*b* explains the sensor arrangement. The four-bar mechanism is composed of the lever arm (11) mounted on the shaft of the sensor (8) and the coupler (12) which connects the shank segment (4) and the lever arm (11) using spherical plain bearings. The length of lever arm (11) equals the distance from the knee joint (1) axis to the shank articulation point of coupler (12), while the length of coupler (12) corresponds to the distance between the knee joint (1) axis and the shaft of the absolute angular sensor (8). Figure 3.18*b* shows the two extreme positions of the shank segment (4) for knee angles of -120° and 5°. The positions of lever arm (13) and coupler (14) at a knee angle of -120° show that coupler (14) must be cranked to avoid collisions with the angular gear (10) which is coaxially with the knee joint.

Figure 3.18*c* shows the compact design of universal joint (7) which connects the output link of knee joint actuator (5) to the shank segment (4). The spider (15) is made from high-tension steel in order to keep its dimensions to a minimum. Precision plain bearings (16) with adjusted clearance are used in the one axis of the spider (15), where only minimal rotation due to elastic deformation of the leg structure occurs. Since the main axis of rotation is subject to higher rotational speeds, it is supported by the needle roller bearing (17) which can

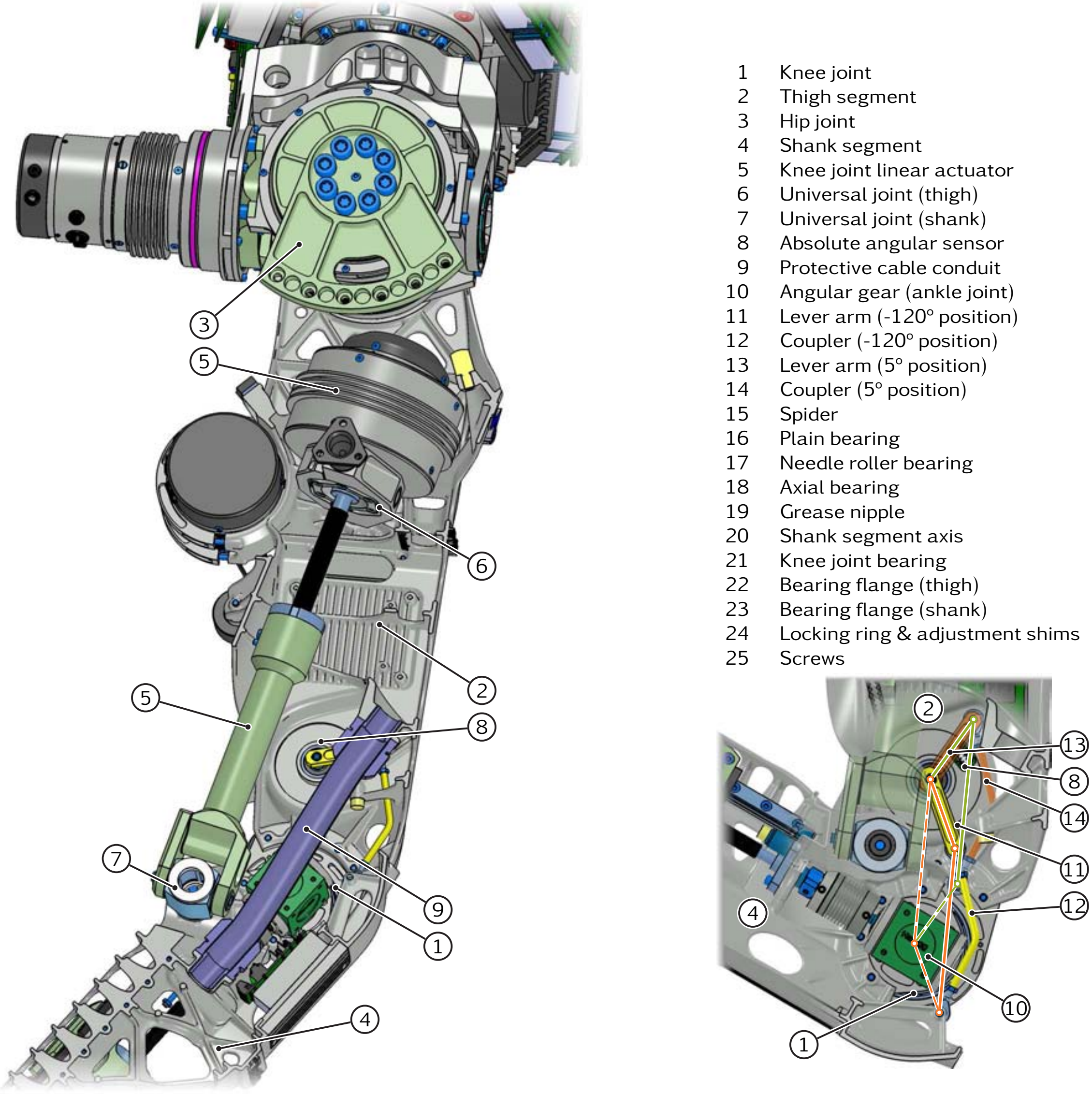

1	Knee joint
2	Thigh segment
3	Hip joint
4	Shank segment
5	Knee joint linear actuator
6	Universal joint (thigh)
7	Universal joint (shank)
8	Absolute angular sensor
9	Protective cable conduit
10	Angular gear (ankle joint)
11	Lever arm (-120° position)
12	Coupler (-120° position)
13	Lever arm (5° position)
14	Coupler (5° position)
15	Spider
16	Plain bearing
17	Needle roller bearing
18	Axial bearing
19	Grease nipple
20	Shank segment axis
21	Knee joint bearing
22	Bearing flange (thigh)
23	Bearing flange (shank)
24	Locking ring & adjustment shims
25	Screws

(a) Overview *(b)* Absolute angular sensor

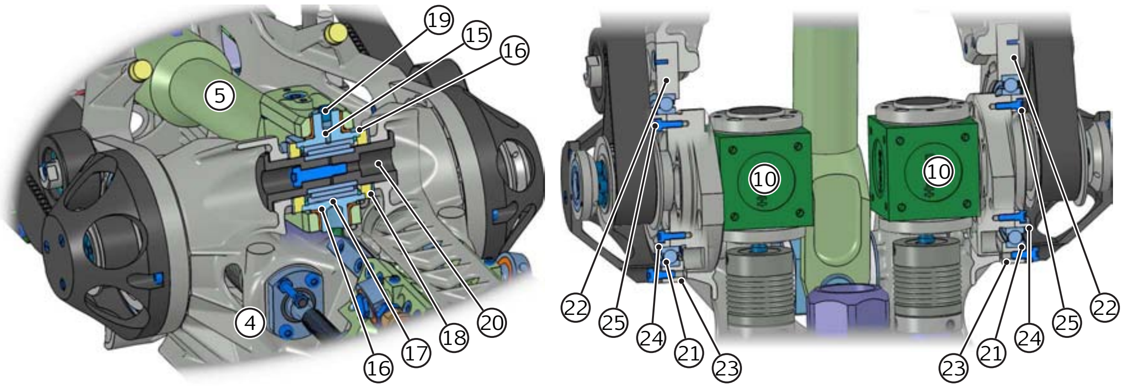

(c) Universal joint (shank segment) *(d)* Knee joint bearing structure

Figure 3.18: Mechanical design of the knee joint

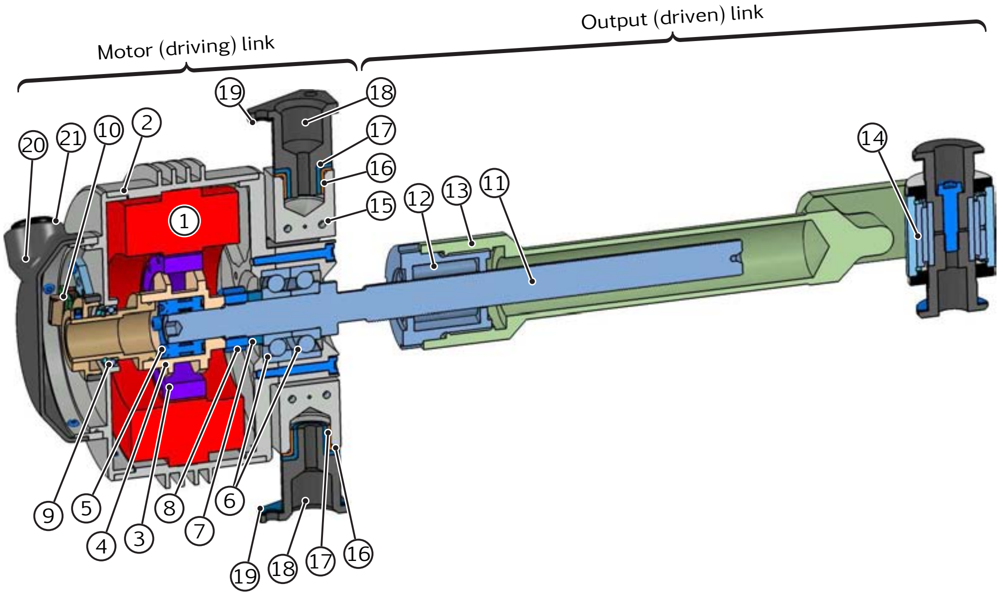

1	Stator	8	Locknut	15	Spider (thigh)
2	Motor housing	9	Roller screw bearing B	16	Plain bearing
3	Permanent magnet rotor	10	Incremental encoder	17	Steel raceway
4	Rotor receptacle	11	Roller screw shaft	18	Cantilever axis (thigh)
5	Cone clamping	12	Roller screw nut	19	Adjustment shim
6	Roller screw bearing A	13	Immersion tube	20	Protective cover
7	Bearing spacer	14	Universal joint (shank)	21	Cable grommet

Figure 3.19: Mechanical design of the knee joint actuator

accommodate high radial forces at very compact dimensions. It is complemented by two axial bearings (18) which prevent the universal joint (7) from floating. Each axial bearing (18) is composed of a bearing washer that is bonded onto the shank segment (4), and a plastic thrust washer mounted on spider (15). The grease nipple (19) simplifies maintenance of needle roller bearing (17). The universal joint (7) is located in the shank segment (4) using the shank axis (20) which is divided for assembly. It is inserted into the fitting bores from both sides of shank segment (4) and fastened by a screw. Since the axis (20) also axially locates the inner ring of bearing (17), its axial fixation in the shank is adjusted with shims (not shown).

Finally, Figure 3.18*d* shows the bearing arrangement of the knee joint: it is composed of two thin-section deep groove ball bearings (21) in an adjusted O-arrangement. The outer ring of bearing (21) is press-fit into the bearing flange (22) of the thigh segment. The inner ring is mounted on the bearing flange (23) of the shank segment. Bearing flange (23) is designed as an integral part of the angular gear (10), cf. Section 3.8.3. Bearing clearance is adjusted with shims (not shown). The inner ring of bearing (21) is axially located by the locking ring (24) and screws (25).

The mechanical design of the knee joint actuator is presented in Figure 3.19. It is composed of the motor (driving) link which connects to the thigh segment and the output (driven) link, connecting to the shank segment. In the driving link, PMSM stator (1) is bonded into the motor housing (2) using a thermally conductive epoxy. The motor housing (2) has cooling fins for natural convection.

The permanent magnet rotor (3) is bonded onto the motor receptacle (4). For assembly convenience, the receptacle (4) is divided into two parts which are clamped together using radially arranged set screws that engage into a V-groove. The cone clamping (5) fastens the receptacle (4) on the roller screw shaft (11). The rotating part of the driving link which consists of the roller screw shaft (11) and motor receptacle (4), rotates on two angular contact ball bearings (6) and a thin-section deep groove ball bearing (9) in a locating/non-locating arrangement. Unlike the Harmonic Drive-based revolute joints, cf. Section 3.4.2, where the locating bearing is placed next to the incremental encoder, locating bearing (6) of the the roller screw shaft (11) resides on the opposite side of motor housing (2), providing ideal force flux to the thigh segment. Locating bearing (6) is composed of two matched single row angular contact ball bearings with internal pre-load. This arrangement allows to accommodate high axial loads acting in both directions. Bearings (6) are mounted immediately adjacent to each other and axially located by bearing spacer (7) and locknut (8). The non-locating bearing (9) provides additional radial support and ensures reliable working distance between the magnetic ring and the scanning head of incremental encoder (10). Cover (20) and cable grommet (21) protect the encoder (10) against ingress of solid foreign objects and dust. The motor link is cardanically supported in the thigh segment by the spider (15). Oil-free precision plain bearings (16) with minimal clearance are used in both axes of the universal joint, as they are better suited for oscillating bearing motions with small angles of oscillation than rolling bearings. They run on steel raceways (17) which are bonded onto the bearing journals of the motor housing (2, not shown) and spider (15). The spider (15) is located in the thigh segment by the cantilever axes (18). To prevent the motor link from floating, axial clearance of the bearings (16) is adjusted with shims (19) during assembly. The output (driven) link consists of the roller screw nut (12), which is flanged on the immersion tube (13). The figure shows the working principle of the drive. The roller screw shaft (11) plunges into the immersion tube (13), changing the distance between the upper and lower hinging points of the actuator. The output link connects to the shank segment by universal joint (14), see Figure 3.18*c*.

3.8.3 The Ankle Joint

As shown in Section 2.6.3, the ankle joint axes differ clearly in their torque-speed characteristics. Despite the higher development effort, the main reason to implement a parallel mechanism is the significant reduction of the average loads that are distributed almost equally among the motors. The low-inertia design of this new drive mechanism places heavier component parts near the hip joint. The mechanism is stiff, singularity-free throughout the working range, it is back-drivable and shows only minimal backlash. The overall reduction ratio of the mechanism ranges from 30 to 70. Due to the high complexity, the explanation of the mechanism is split into two figures. Figure 3.20 gives an overview of the entire drive mechanism and describes the transmission components on the thigh segment, Figure 3.21 shows the spatial slider-crank mechanism and all other transmission components located on the shank.

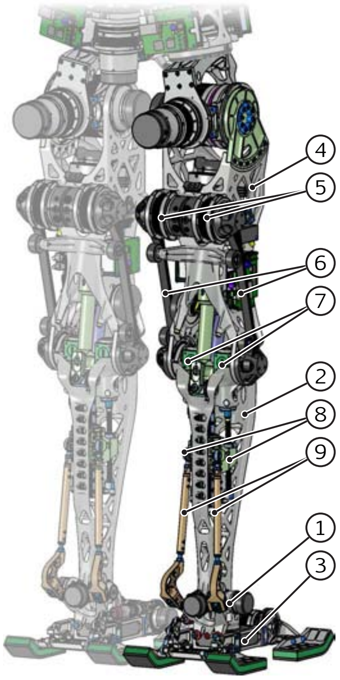

1	Ankle joint	14	Motor shaft bearing A
2	Shank segment	15	Motor shaft bearing B
3	Foot segment	16	Support bearing
4	Thigh segment	17	Support bearing housing
5	Ankle joint motor	18	Pulley (driving)
6	Synchronous belt drive	19	Pulley (driven)
7	Angular gear	20	Cone clamping
8	Linear carriage	21	Incremental encoder
9	Coupler link	22	Protective cover
10	Stator	23	Cable grommet
11	Motor housing	24	Synchronous belt
12	Permanent magnet rotor	25	Idler (fixed)
13	Motor shaft	26	Idler (adjustable)

(a) Overview

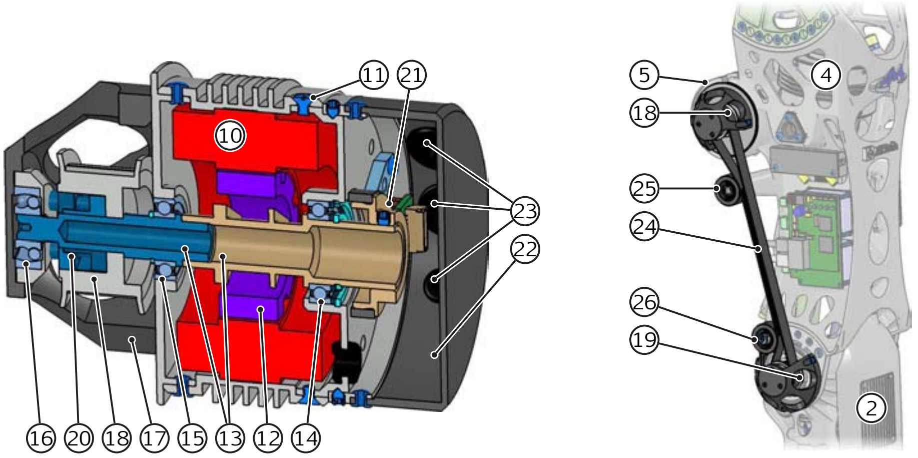

(b) Ankle joint motor

(c) Synchronous belt drive

Figure 3.20: Mechanical design of the ankle joint, part 1

Figure 3.20*a* shows the overall structure of the mechanism. The two-DoF ankle joint (1) connects the shank (2) to the foot segment (3). It is actuated by two spatial slider-crank mechanisms (8–9) with one DoF each. The motors (5) are mounted on the thigh segment (4), close to the hip joint. Each slider-crank mechanism is basically composed of the linear carriage (8) which translates along the longitudinal axis of shank (2). The coupler link (9) connects carriage (8) and the foot segment (3). Moving the linear carriages (8) on both sides of the shank (2) in equal directions results in a flexion/extension movement of the ankle joint (1), moving them in opposite direction yields an adduction/abduction movement. The linear carriages (8) are driven by the motors (5) which connect to the slider-crank mechanisms (8–9) via synchronous belt drives (6) and angular gears (7).

Figure 3.20*b* explains the design of the ankle joint motor. The structure is almost identical to the Harmonic Drive-based revolute joints, cf. Section 3.4.2. The PMSM stator (10) is bonded into the motor housing (11). The permanent magnet rotor (12) is bonded onto motor shaft (13) which is supported by bearings (14) and (15) in a locating/non-locating arrangement. Thin-section deep groove ball bearings are employed for both locating (14) and non-locating bearing (15). For better accommodation of the radial forces resulting from the synchronous belt drive (6), the motor shaft (13) is additionally supported by the self-aligning ball bearing (16). The ability of this arrangement to compensate dynamic angular errors as well as axial misalignment avoids internal forces in the bearing system of the motor shaft. Accordingly, a high-strength yet lightweight design of motor shaft (13) is achieved by a two-part design: the inner part which holds the permanent magnet rotor (12) is made from aluminum. Since the output part of the motor shaft is subject to considerable rotating bending resulting from the radial forces of the synchronous belt drive, it is made from high-tension steel. The driving pulley (18) of synchronous belt drive (6) is fastened onto motor shaft (13) using cone clamping (20). The support bearing housing (17) holds the bearing (16) and provides protection against accidental contact of the pulley (18). The incremental encoder (21) is mounted on the opposite side of the motor shaft (13) and protected by the cover (22) and cable grommets (23).

Figure 3.20*c* shows the synchronous belt drive that connects the motor (5) to the input shaft of the angular gear (not shown). The driving pulley (18) is fastened onto the motor shaft (5). The driven pulley (19) resides on the input shaft of the angular gear, coaxially with the knee joint. The pulleys are connected by the synchronous belt (24). The fixed idler (25) increases the wrap angle of the driving pulley (18). Accordingly, the adjustable idler (26) increases the wrap angle of the driven pulley (19) and allows to set belt tension and compensate the tolerances of synchronous belt (24).

Figure 3.21 illustrates all drivetrain components situated on the shank. Figure 3.21*a* shows the spatial slider-crank mechanism (8–9), located on both sides of shank (2). The main components are the linear carriage (8), which moves in longitudinal direction of shank (2), and coupler link (9) which connects carriage (8) to the foot (3). The linear carriage (8) is guided by a pre-loaded linear recirculating ball bearing and guideway assembly (32), which can accommodate loads from all directions—except for the direction of motion—and moments about all axes. The linear bearing unit comprises a single guideway (32) and two ball bearing carriages which are screwed to carriage (8). Using two smaller instead of one larger carriage reduces the mass and increases rating life. In addition, guideway (32) is inclined by 20° to the sagittal plane to achieve a better loading condition. The linear carriage (8) is driven by a planetary roller screw. The screw shaft (27) and nut (28) are attached to the shank (2) and carriage (8), respectively. The screw shaft (27) is supported by the axial angular contact ball bearing (29) and needle roller bearing (30) in a locating/non-locating arrangement. Coupler link (9) connects to the linear carriage (8) by a heavy-duty rod end (33) with reduced clearance ($5 - 10\,\mu\text{m}$) that can support high alternating loads and shock loads. The

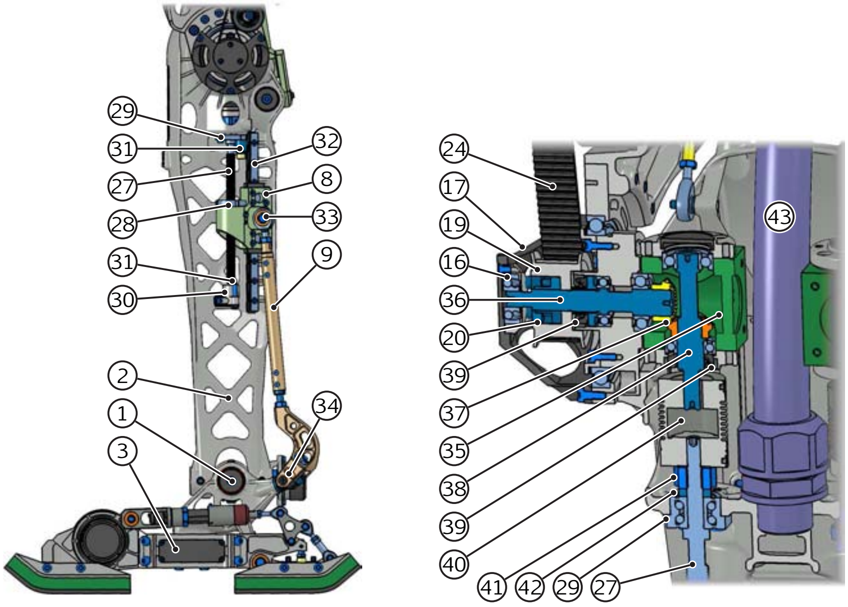

(a) Slider-crank mechanism *(b)* Angular gear

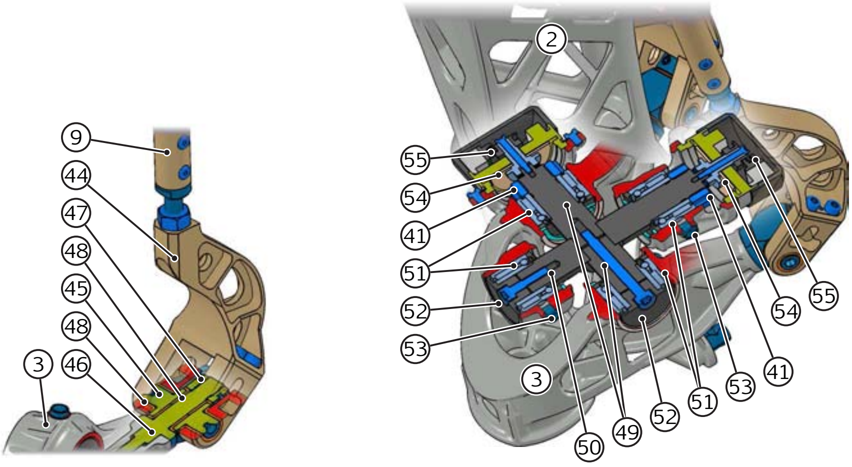

(c) Universal joint (coupler link) *(d)* Ankle joint

1	Ankle joint
2	Shank segment
3	Foot segment
8	Linear carriage
9	Coupler link
16	Support bearing
17	Support bearing housing
19	Pulley (driven)
20	Cone clamping
24	Synchronous belt
27	Roller screw shaft
28	Roller screw nut
29	Roller screw bearing A
30	Roller screw bearing B
31	End stop
32	Guideway
33	Rod end
34	Universal joint (coupler link)
35	Angular gear housing
36	Angular gear input shaft
37	Bevel gear assembly
38	Angular gear output shaft
39	Sealing ring
40	Bellows coupling
41	Locknut
42	Bearing spacer
43	Protective cable conduit
44	Universal joint adapter
45	Spider
46	Cantilever axis
47	Set collar
48	Plain bearing
49	Flexion/extension axis
50	Adduction/abduction axis
51	Ankle joint bearing
52	Locking plate
53	Grease nipple
54	Absolute angular sensor
55	Limit switch

Figure 3.21: Mechanical design of the ankle joint, part 2

other end of link (9) connects to the foot segment (3) by universal joint (34).

The slider-crank mechanisms (8–9) are arranged in the longitudinal direction of the shank, perpendicular to the knee joint axis. It is therefore necessary to redirect the axes of rotation of the motors (5) by angular gear units which are shown in Figure 3.21*b*. Minimal backlash of these gears is crucial for servo performance and accuracy, but can only be achieved by experience and very precise assembly. Therefore, a commercial bevel gear (35–39) is employed in a customized version. The precision gear unit is optimized for position servo applications and features a lightweight aluminum housing (35) for good heat dissipation. The internal gear design provides high efficiency ranging from 94 % to 97 % and minimal angular backlash of less than 8 arc min [55]. The bevel gear unit is fitted with hardened bevel gears (37) with spiral toothing, allowing for higher speed and load rating and less vibration and noise. Moreover, the angular gears have amply dimensioned ball bearings for a high degree of transmission accuracy. As the speed range requires oil splash lubrication, the gear box is sealed with sealing rings (39). Synchronous belt (24) connects the motor shaft (not shown) to the input shaft (36) of the angular gear which is coaxially with the knee joint. The driven pulley (19) of the synchronous belt drive is fastened onto the input shaft (36) using the cone clamping (20). The self-aligning ball bearing (16) accommodates the radial forces resulting from the synchronous belt drive and reduces the loading of input shaft (36). Bearing (16) is mounted on the knee joint bearing flange using the support bearing housing (17). The miniature bellows coupling (40) connects the output shaft (38) of the angular gear to the roller screw shaft (27). It is characterized by zero backlash, high torsional stiffness, low inertia and the ability to compensate for axial, lateral and angular shaft misalignments. The coupling incorporates a blind mate press-fit connection for assembly convenience. The roller screw shaft (27) is axially located by the axial angular contact ball bearing (29), which is fastened by the bearing spacer (42) and the locknut (41). The axial angular contact ball bearing (29) is a double row unit with internal pre-load to accommodate radial forces as well as high axial forces acting in both directions. It is optimized for screw drives and characterized by high accuracy, high load carrying capacity, high rigidity and low friction. The protective cable conduit (43) guides all cables in the knee joint area and avoids cable jamming.

The large required workspace in the dorsiflexion/plantarflexion axis inhibits the use of standard spherical plain bearings to connect the the coupler link (9) and foot segment (3). Hence the universal joint (34) is developed as shown in Figure 3.21*c*. The fork-shaped universal joint adapter (44) at the end of coupler (9) clasps around the spider (45). The cranked shape of (44) is due to limited space in the shank-foot area and avoids collisions with the foot (3) and shank. The cantilever axis (46) is bolted into the foot segment (3) and holds the spider (45). Both spider (45) and cantilever axis (46) are made from high-tension steel to achieve extremely compact dimensions and the required mating material hardness for the plain bearings (48). All axes of the universal joint run on oil-free bronze bushings (48) which are assembled with minimal clearance ($5 - 10\,\mu\text{m}$). Plain bearings with solid lubrication are superior in abrasion resistance compared to composite bushings. They can withstand heavy and shock loads and are suitable for low-speed oscillating motions at small angles of oscillation. Axial clearance of the bearings running on cantilever axis (46) are adjusted with set collar (47).

Finally, Figure 3.21*d* concludes with the ankle joint that is designed as Cardan joint with intersecting axes. The shank segment (2) holds the adduction/abduction axis (50), the flexion/extension axis (49) is assigned to the foot segment (3). The bearing arrangement is identical for both axes and comprises combined needle roller/angular contact ball bearings (51) in an adjusted bearing arrangement, thus the ankle joint is free from backlash. The bearings (51) are able to accommodate radial and axial loads and allow to realize an adjusted bearing arrangement with high radial load carrying capacity at limited radial space. The outer rings of the bearings (51) rest against retaining rings, the inner rings are fixed with locking plates (52) and locknuts (41), respectively. The latter are also used to adjust bearing clearance. Grease nipples (53) at all bearings simplify bearing maintenance. The absolute angular sensors (54) allow the direct measurement and control of the joint angles, and are complemented by the limit switches (55). However, the allowed angular range must be monitored by software, since the operating range of the ankle joint is non-rectangular due to collisions between the shank (2) and foot segments (3).

3.9 The Feet

As stated in Section 2.3, the main requirements on the foot structure include:

- High grip on different surfaces to ensure proper ground contact
- Passively compliant elements with good damping characteristics for shock attenuation at initial contact and progressive spring characteristics at ground contact to ensure effectiveness of stabilizing control
- Rigid mechanical structure to transmit the propulsive forces at a bandwidth sufficient for system stabilization
- Compensate smaller unevenness
- Minimal mass

From these requirements, the design of the robotic foot shown in Figure 3.22*a* is derived. The foot segment is connected to the shank (1) by the two-DoF ankle joint (2) and actuated by the coupler links (3) via the universal joints (4). The foot receptacle (5) holds the flexion/extension bearings of the ankle joint and interfaces to the inner sensor flange of force/torque sensor (6), which is an integral, load-bearing element within the forefoot. Details on the sensor design and function are given in Section 4.2. The sensor (6) is shifted 40 mm towards the center of the support polygon in order to achieve equal loading conditions in either direction. Every corner of the sensor frame has a connecting flange (7), accepting the toe joint actuator (8) at its front and the heel segment at its back. The toe joint (8) divides the foot into forefoot and hallux.

Several mechanisms account for effective shock attenuation. Viscoelastic contact elements (9) with good damping characteristic are used in analogy to the fat pads in the human heel and toe for damping the impact transients and compensating small unevenness. The design of the contact elements is described below in more

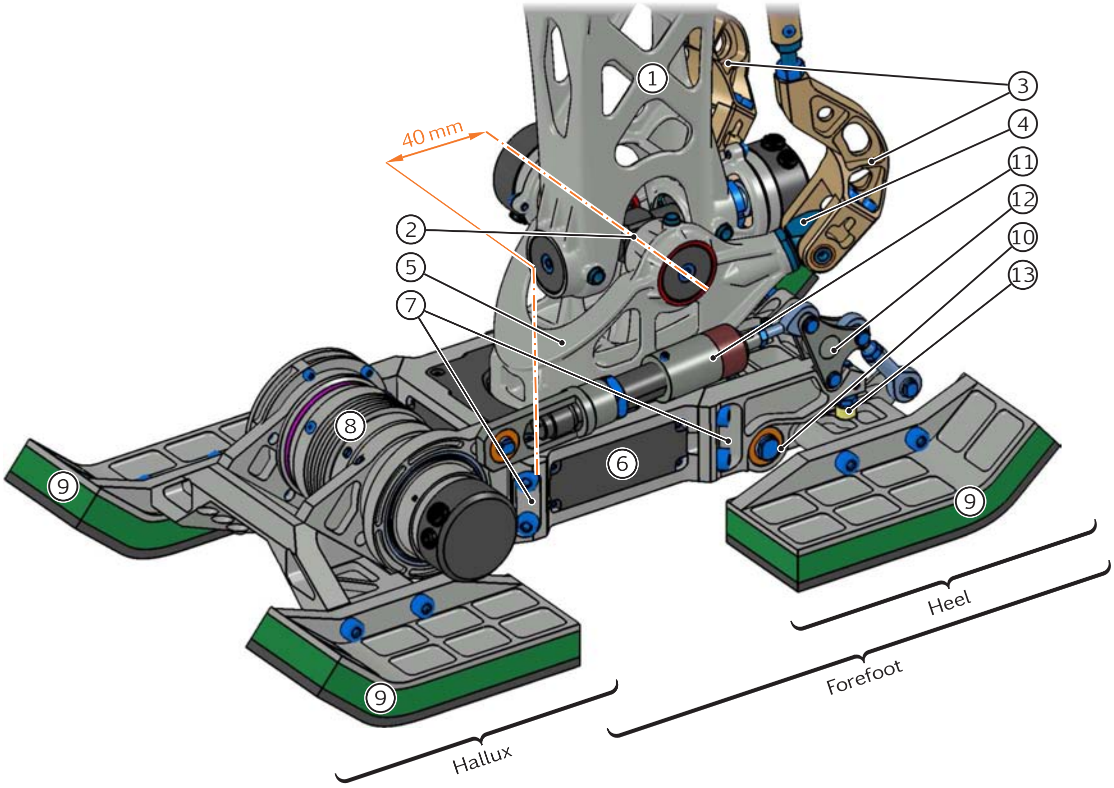

(a) Overview

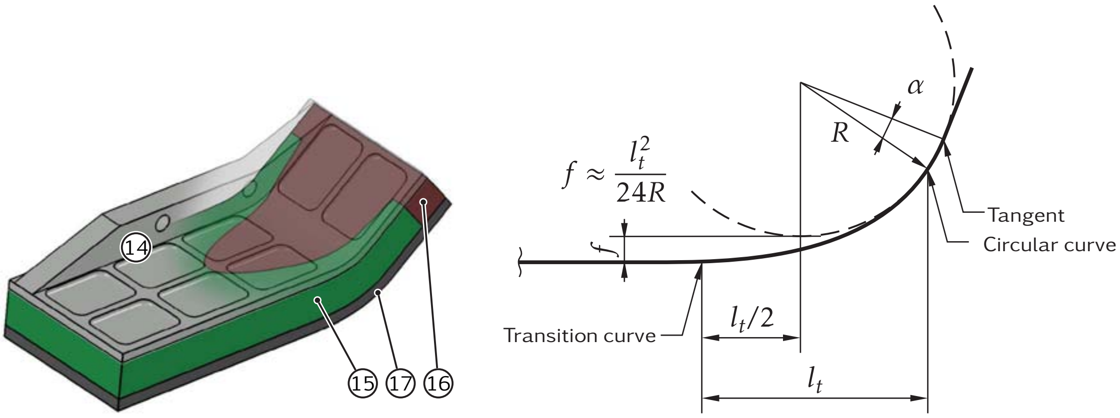

(b) Contact element *(c)* Contact element geometry

1	Shank	7	Foot connecting flange	13	End stop
2	Ankle joint	8	Toe joint (actuator)	14	Contact element base body
3	Coupler link (ankle joint)	9	Contact element	15	Viscoelastic layer A
4	Universal joint	10	Heel bearing	16	Viscoelastic layer B
5	Foot receptacle	11	Hydraulic shock absorber	17	Outsole
6	Force/torque sensor	12	Four-bar linkage		

Figure 3.22: Mechanical design of the feet

detail. In addition, a passive heel segment is proposed for improved energy dissipation during initial contact: similar to the human hindfoot, the passive heel contributes to energy dissipation during initial contact by increasing the time over which the foot is decelerated and energy is dissipated. For that reason, it incorporates a hydraulic shock absorber (11) with adjustable damping. The four-bar linkage (12) adjusts the strokes of heel and damper. The heel bearing (10) consists of two spherical plain bearings in a locating/non-locating arrangement and corresponds to the subtalar joint of the human foot. The mechanical end stop (13) ensures proper transmission of the propulsive forces and stabilizing moments while in ground contact. The feasibility of this new design has been proved in preliminary tests with the robot *Johnnie* [164].

Figure 3.22*c* illustrates the multi-layered structure of these elements. The rigid aluminum base body (14) interfaces to the heel and toe segments by a combined parallel key and screw connection. Bonded onto contact element (14) are viscoelastic layers (15,16) with different material properties, adjusted for better impact attenuation. The viscoelastic layers (15) and (16) consist of *Sylomer*, a volume-compressible PUR elastomer that is widely used in vibration isolation [45]. Layer A (15) covers the major part of the contact area and is mainly relevant during mid and terminal stance. An elastomer with comparatively low modulus of elasticity is chosen due to the large contact area, where the loads are distributed among the four contact elements. The material properties are adjusted experimentally to the bandwidth of the ankle joint torque controller. Conversely, layer B is mainly active during initial contact. The specific loads acting on this layer are significantly higher due to the high landing impacts and the small contact area. Thus, an elastomer with higher modulus of elasticity is used. The outsole (17) is bonded onto the viscoelastic layer. It is made from wear-resistant, high-friction rubber from orthopedic supplies.

The geometric shape of the heel contact elements permits a smooth rolling motion of the feet. At initial contact the heel contacts ground and rolls on the circular section of the contact element. If the straight section is tangent to the circular section, the hallux touches down abruptly as the curvature at the transition point jumps from zero to the reciprocal of radius R. Therefore, in order to prevent abrupt forces during the loading response phase, a transition curve is fitted between the circular and straight section of the contact element. The transition curve is a clothoid, which is widely used to connect a straight and a circular section of a rail track or highway. As illustrated in Figure 3.22*c*, its curvature begins at zero at the straight section, increases linearly with its curve length and ends at the curvature of the circular curve, $1/R$. The vertical offset f between the straight section and the circular curve can be calculated approximately from the radius R and the transition length l_t.

The functionality of the foot during the gait phases is illustrated in Figure 3.23. At initial contact, Figure 3.23*a*, the heel segment protrudes from the foot sole. Its passive motion increases the time over which the foot is decelerated and during which energy is dissipated by the hydraulic damper. At loading response, Figure 3.23*b*, the heel segment is retracted and more impact energy is dissipated by deformation of the viscoelastic layers. The foot rolls from heel to toe and

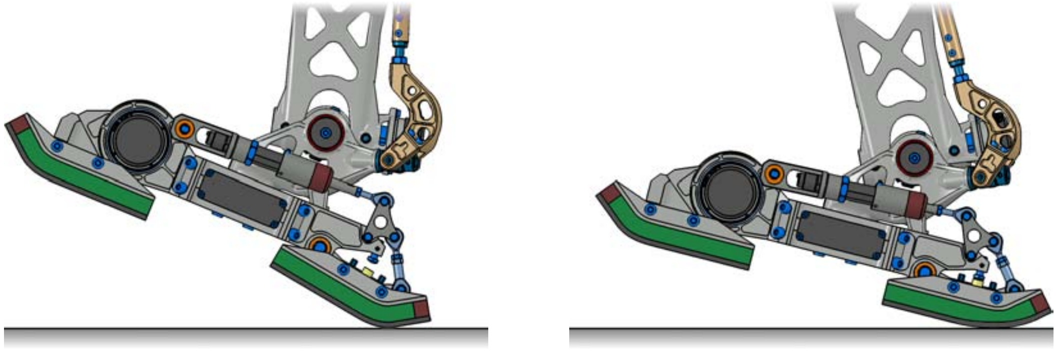

(a) Initial contact *(b)* Loading response

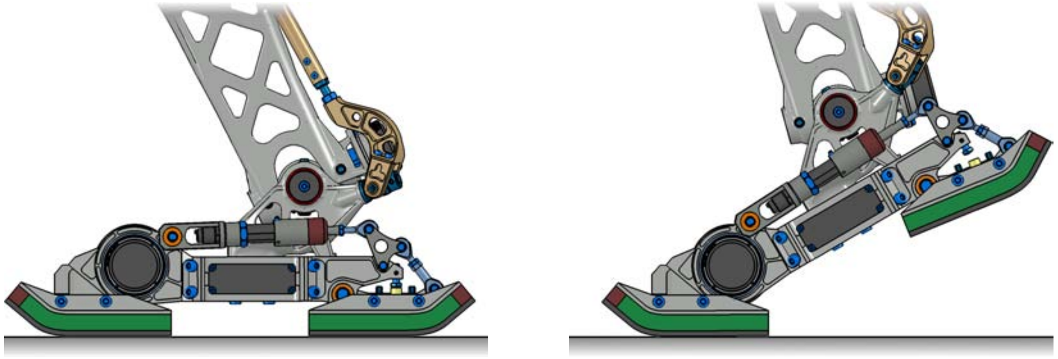

(c) Mid stance *(d)* Terminal stance

Figure 3.23: Function of the heel and toe segments during one gait cycle. Besides viscoelastic members, the passive heel segment with hydraulic damper contributes to shock attenuation.

the hallux touches down. Ground contact during mid stance, Figure 3.23*c*, is ensured by the heel and hallux. Then the robot's weight is transferred to the hallux and, finally, the heel lifts in terminal stance, Figure 3.23*d*. However, these passive mechanisms of shock absorption are limited by the required bandwidth for stabilizing the upper body orientation, see Section 2.3.

The modular mechanical configuration of the feet enables modifications of the foot geometry (contact area size and shape, geometry of contact elements) by simply replacing the contact elements. Moreover, it facilitates experiments with different foot configurations. Figure 3.24*a* shows the default configuration of *Lola*'s feet with active toe joints (8), using the lightweight rotary actuators type 'G', cf. Figure 3.9. Figure 3.24*b* shows a configuration with passive toe joint. Because the passive toe joint is more compact, the anthropometric position of the toe joint can be fully kept. The toe joint bearings are designed in a locating/non-locating arrangement. Due to the high radial loads, locating bearing (18) is a combined needle roller/angular contact ball bearing which can accommodate axial loads in both directions. Bearing (18) is fixed with locknut (19). A needle roller bearing is used as non-locating bearing (20). A torsional spring (21) is employed that supplies torque to restore the joint to its zero position. The absolute angular sensor (22) acquires the toe joint angle, providing it for the trajectory planning

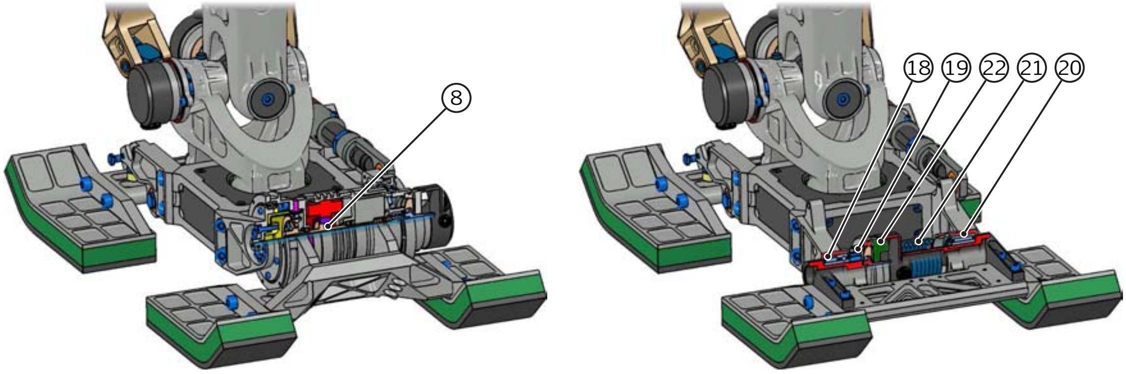

(a) Active toe joint *(b)* Passive toe joint

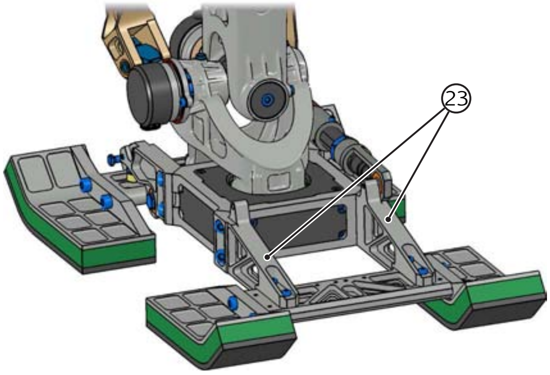

8	Toe joint (actuator)
18	Toe joint bearing A
19	Locknut
20	Toe joint bearing B
21	Torsional spring
22	Absolute angular sensor
23	Hallux receptacle

(c) Monolithic foot

Figure 3.24: Modular structure of the feet, enabling experimental evaluation of different configurations

algorithms. The simplest hallux configuration, the monolithic foot, is depicted in Figure 3.24*c*. Here, the hallux contact elements are mounted on the receptacles (23), providing a rigid connection to the forefoot.

3.10 The Link Segments

The component-related selection of construction materials and joining techniques offers great potential for weight savings in many cases. Manufacturing major structural components from fiber-reinforced polymer, e. g., carbon-fiber reinforced plastic (CFRP), is quite obvious because—if properly designed—CFRP components have a higher specific strength and stiffness than Aluminum. On the other hand, CFRP components are more elaborate in design and production. Moreover, missing facilities for in-house manufacturing make CFRP components rather costly. Instead, combining semi-finished CFRP tubes and attachment parts made from aluminum are a more economical solution for simpler parts such as the arm segments. But such multi-layered CFRP tubes seem to be available only in larger customized batches. Magnesium, as the metal with the lowest density ($1{,}8\,\mathrm{g/cm^3}$) of all construction metals, is excellently suited for use in lightweight constructions. Despite good machinability, Magnesium and its alloys are mainly cast materials due to limited cold forming properties. Complex-shaped single copy Magnesium components can be manufactured by investment casting as described below. But again, very high manufacturing costs are against Magnesium castings. The robot *Johnnie* was made solely from various standard and high-tensile Aluminum alloys. These materials have been proven successful during the lab work, where accidental tipping over of the robot never caused serious damage to components. Furthermore, subsequent modifications are possible and can be conducted promptly in the in-house workshop. Consequently, using CFRP or Magnesium alloys for the robot structure is abandoned but the tried and tested aluminum alloys are used instead for most components. Less loaded parts and covers are made from plastic (e. g., POM, ABS).

As stated in Section 3.2, lightweight design also affects the selection of joining techniques, i. e., screwing, bolting, riveting and/or bonding. The weight analysis of the robot *Johnnie* has revealed that screws make 4,7 % of the robot's weight [46], suggesting to reduce bolted flange connections to a minimum. In particular, other joining techniques should be preferred for connections that need not to be loosened for maintenance. Although bolted flange joints provide assembly convenience, they contribute certain compliance to the robot structure. Thus, increasing the stiffness of a flanged joint without increasing its mass is a worthwhile design objective. More reliable transmission of forces and torques is achieved by *EKagrip* shims [34]. These friction-enhancing shims provide microscale interlocking with the joint surfaces, increasing the static friction coefficient by up to 300 %. *EKagrip* shims are utilized in the highly loaded flange connections of the Harmonic Drive Flexspline and the output flange, Section 3.4.2, as well as in the hip, knee and ankle joint flanges (cf. Sections 3.8.1 to 3.8.3). On the other hand, joining aluminum parts by bonding and/or riveting provides reliable force and/or material-locking connections. Opposite to welding, the main benefits include the maintaining of original material strength, no distortion and the possibility to connect non-weldable, high-tensile Aluminum alloys or steel parts. As blind rivets are made from Aluminum, they allow joining connections with virtually no increase in weight. For adhesive connections of aluminum, polyurethanes are preferred over epoxies due to their tough-elastic properties and good impact and peel resistance. In addition, combined bonding and riveting connections have higher strength and stiffness.

Generally speaking, prototype investment castings made from Aluminum are a more economical solution than Magnesium castings. Nevertheless, this technology enables the manufacture of very sophisticated, complex-shaped and thin-walled parts with indentations, openings of any kind and complex rib structures. Since there are almost no limitations in component shape, investment casting allows the integration of various functions into a single part and the design of one-piece link segments. It is possible to integrate attaching parts to reduce assembly complexity. Thus, overlap due to bolted or riveted flange connections is avoided. Other than "conventional" manufacturing techniques such as milling from the solid, prototype investment casting allows for designing one-piece shell structures. Hence mainly the part exterior is utilized to support the structural load [163], opposite to frame

(a) Hip joint adduction segment (two parts, milling from the solid)

(b) Leg components (investment casting). *Left to right:* thigh base body, shank base body, ankle joint connecting flange.

Figure 3.25: Examples of link segments, manufactured by milling from the solid or investment casting

or truss structures. The main objectives of this construction technique, which is also referred to as *Monocoque design*, are spreading the structural load evenly over the part and reducing the overall workload, finally leading to additional weight savings.

The prototype investment casting process starts with the manufacturing of the investment casting model using the native 3D-CAD data of the finished part, considering allowances, shrinkage and mounting links for follow-up machining. The models are manufactured by laser-sintering of plastic. The plastic master is then embedded into molding material and molten out. After casting and cooling, the casting blank part is cleaned and ready for after-treatment and inspection. This includes heat treatment to adjust the mechanical characteristics, blank measurement to check distortion and shrinkage, and X-ray imaging to check for internal defects. The final CNC machining of the casting blank is essential as the castings only become fully usable by the machining of all functional surfaces.

Figure 3.25 shows examples of link segments, manufactured either by milling from the solid or prototype investment casting. Figure 3.25*a* depicts the fork-shaped hip joint adduction/abduction segment which surrounds the hip joint flexion/extension drive, cf. Figure 3.17. It is composed of two parts which are manufactured by milling from the solid and joined using dowel pins and screws. The left side of the assembly interfaces to the adduction/abduction drive by a parallel key and screws. Figure 3.25*b* shows three components manufactured by investment casting with machined functional surfaces: the main bodies of the thigh and shank, and the ankle joint connecting flange. The castings incorporate several functions: for example, the thigh base body has connecting flanges to the hip and knee joints, bearing seats for the knee joint actuator, the flange for the knee joint angular sensor, and two mounting surfaces for motor controllers with cooling fins on their back. The shank base body comprises the connecting flange to the knee joint, bearing seats for the ankle joint, and all mounting surfaces and bearing seats for the ankle joint drive mechanism. The one-piece design allows to combine all corresponding surfaces in a single component, which are machined in a single setting in order to keep the geometric tolerances. This design and manufacturing approach further ensures accuracy of kinematic parameters (e. g., location and orientation of neighboring links) which is necessary for precise and robust trajectory planning and balance control.

3.11 Parameter Identification

This section deals with the identification of the kinematic and inertial parameters of the robot after assembly. Determining the angular offsets of the link position sensors is the main objective of kinematic calibration procedure described in Section 3.11.1. The identification of the rigid-body inertial parameters, Section 3.11.2, aims at obtaining an accurate model for multibody simulation and stabilizing control.

3.11.1 Kinematic Calibration

The kinematic parameters of the robot include geometric parameters, such as the location of the local coordinate systems of neighboring links, the location of the stereo cameras relative to the upper body coordinate system, as well as angular offsets of the link position sensors. For the robot geometry, it can be assumed that all significant dimensions are within the respective tolerances for linear and angular dimensions: particularly, the one-piece design of the leg segments and the machining of all corresponding surfaces in a single setting ensures high geometric accuracy and tight tolerances within few tenths of a millimeter, see Section 3.10. On the other hand, the accurate identification of the angular offsets of the absolute link position sensors is fundamental to the control performance. The absolute angular sensors are mounted in arbitrary angular positions, thus

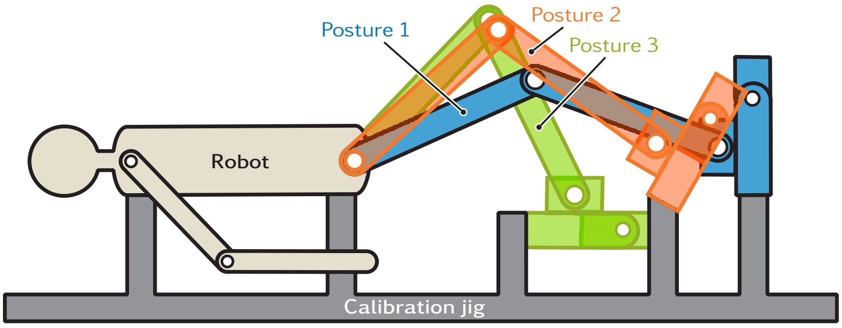

Figure 3.26: Schematic diagram of the calibration procedure for closed-loop calibration of the joint angles

calibration for offset determination is required. The procedures of kinematic calibration of robotic manipulators can be categorized in two general methods [71]:

Open-loop calibration relies on external metrology to measure the posture of a link chain, for example a camera-based motion capture system or a high-precision inertial measurement unit mounted on the end link.

Closed-loop calibration physically constrains the end link in all degrees of freedom in predefined positions and orientations, substituting actual measurements of the end link postures.

Due to lack of a motion capture system, a closed-loop calibration procedure is chosen, using a calibration jig[11] for accurate closed-loop calibration of the joint-based parameters.

Figure 3.26 illustrates the method to identify the angular offsets of the encoders. The calibration jig fixes the pelvis segment as the root link of the cantilever serial leg structure. The upper body is positioned using the locating pins on the upper body support structure (item (21) in Figure 3.14*c*). The feet can be mounted in three different positions, utilizing the locating pins on the foot receptacle (item (5) in Figure 3.22*a*). Hence the calibration jig enables the joint angle measurement in three different leg postures to increase the calibration accuracy. The toe joint is calibrated by another jig. Since it is not considered in the leg posture, the joint angles of the remaining six-DoF serial link chain can be calculated by inverse kinematics from the known position and orientation of the forefoot.

3.11.2 Link Inertial Parameter Estimation

The rigid-body inertial parameters are necessary for the multibody system used for off-line simulation of the robot, and online trajectory planning. Moreover, the inertial parameters enter the derivation of simplified models used for stabilizing the robot. Thus, accurate knowledge of the inertial parameters is crucial for walking performance and stability.

While the joint angles can be calibrated as described in the previous section, the experimental identification of the inertial parameters is more involved. For

---

[11] The calibration jig was designed by Markus Schwienbacher

Table 3.2: Mass distribution of the robot and percentage of the overall weight. The amount of correction mass per segment was determined by weighing the robot. The total masses per segment are the basis for the CAD-based approach for estimating the full inertial parameters.

	Correction mass [kg]		Total mass [kg]		Percentage [%]	
Segment	Left	Right	Left	Right	Left	Right
Arms						
Shoulder	0.0	0.0	0.561	0.561	0.92	0.92
Upper arm	0.205	0.198	1.900	1.891	3.12	3.11
Lower arm	0.0	0.0	1.486	1.486	2.44	2.44
Subtotal	0.205	0.198	3.947	3.938	6.48	6.47
Legs						
Hip rotation	0.0	0.0	1.844	1.844	3.03	3.03
Hip adduction	0.0	0.0	2.838	2.838	4.66	4.66
Thigh	0.309	0.393	6.419	6.503	10.54	10.68
Shank	0.125	0.125	3.403	3.403	5.59	5.59
Ankle	0.0	0.0	0.138	0.138	0.23	0.23
Forefoot	0.027	0.032	1.643	1.648	2.70	2.71
Toe (active)	0.013	0.013	0.797	0.797	1.31	1.31
Subtotal	0.473	0.563	17.082	17.171	28.06	28.20
Upper body						
Head tilt	0.0		1.013		1.66	
Head pan	0.0		0.249		0.41	
Torso	0.597		9.884		16.23	
Subtotal	0.597		11.146		18.31	
Pelvis						
Pelvis rotation	0.166		1.316		2.16	
Pelvis adduction	0.411		6.281		10.32	
Subtotal	0.577		7.597		12.48	
Full body total	2.612		60.881		100.0	

example, using the feet as proof masses, the masses, centers of mass and inertia tensors relative to the link coordinate systems can be estimated by measuring the joint torques, velocities and accelerations for given leg trajectories. Because of limited mobility and the lack of accurate joint torque sensing, it is impossible to estimate all inertial data [71]. Although the incomplete data may be sufficient for fixed-base manipulators, all inertial parameters are required to calculate whole-body dynamics of a humanoid robot with unilateral foot-ground contact. Therefore, a CAD-based approach is proposed for estimating the full inertial parameters. Accurate modeling of all purchased components is accomplished by weighing the parts and adjusting the material properties of the CAD model. Still, the calculated mass of the link segments can only be a rough estimate as long as cable harnesses are not considered. Therefore, all components, including the cables, are weighed during assembly. While the mass of components manufactured by milling and/or turning can be determined reliably from the native CAD data, the castings are weighed and the material density is adjusted in the CAD model. A large portion of the robot's mass is due to the joint servo actuators. To take account for an accurate mass distribution, all drives are weighed after assembly. For the output side of the drives, the numerically obtained mass from CAD data is sufficient. The link masses are adjusted in the CAD model by adding solids with adjusted material density, thus, the inertial parameters can be assumed to be close to reality. Finally, the new inertial parameters are determined for the multibody simulation model of the robot (Section 3.3.1).

Table 3.2 shows the mass of each segment, the percentage of the total mass and the amount of correction masses. The total amount of correction masses is 2.612 kg, corresponding to an initial modeling error of 4.3 %. The largest correction masses are applied to the thighs, pelvis and upper body, where most of the electronics and cable harnesses are situated.

3.12 Discussion

This section discusses some of the most relevant design features of the mechanical structure. Section 3.12.1 treats the mass distribution of the robot. The chosen designs of some leg joints are compared against other approaches in Section 3.12.2 regarding their effect on the dynamic performance of the overall system.

3.12.1 Mass Distribution

The total mass of the robot is 60.88 kg. The contribution of the individual links given in Table 3.2 resembles the typical mass distribution of a biped walking robot. Contrary to humans, where most of the mass resides in the upper part of the body, the legs make the largest portion of the robot's mass. Weighing 17.082 kg and 17.171 kg, the legs account for approximately 56 % of the total mass. Note that the portion of the highly accelerated segments (thigh, shank, ankle, forefoot, toe) is approximately 12.45 kg per leg, or 20.4 % of the total mass.

3.12.2 Analysis of Dynamic Performance

Consistent lightweight design of the mechanical structure with high effective stiffness and natural frequencies obviously contributes to better dynamic properties of the robot. As discussed in Section 2.4, greater acceleration capability of the locomotor system is further achieved by systematically minimizing the inertia of the individual links, as well as the resultant inertia of the whole kinematic chain. These measures go along with lower nonlinear effects due to varying inertia, which is expected to support the performance and robustness of balance control.

In order to asses the effectiveness of this approach, meaningful criteria are necessary. Numerous dynamic performance criteria have been established for fixed-base robotic manipulators [6], but few address legged robots. For example, Bowling [15] proposes a measure of how well a legged robot uses the contact forces to accelerate itself under consideration of the kinematic constraints associated with unilateral ground contact. All these indices are suggesting that the acceleration capability of the robot's locomotor system is, to a large extent, a function of the resultant leg moment of inertia.

Static and dynamic stiffness of the hip joint assembly is analyzed with special consideration of the gear stiffness. Furthermore, the contribution of the implemented drive mechanisms of the knee, ankle and toe joints to the resultant leg moment of inertia is compared to other designs that have been realized in actual robots or proposed in the literature. For a more reliable comparison, only components of the drive mechanisms are considered. The effect of varying inertia due to knee motion is analyzed for the ankle and toe joints. The mass and inertia data are obtained numerically from CAD data throughout the analysis. Note that actual mass and inertia data are only available for the implemented designs. Due to lack of available reference data, they are estimated for all other design variants. Since the estimation is done on basis of the available CAD data and experience, the data can nevertheless assumed to be realistic.

Hip Joint Stiffness

Static and dynamic stiffness of the hip joint considerably affect accuracy of foot placement. Even small (static) forces applied to the feet yield high torque loadings of the hip joint due to the long lever arm of the foot contact points ($\approx 1{,}000\,\mathrm{mm}$). The torsional stiffnesses of the gear units in the adduction/abduction (Harmonic Drive HFUC 25-100) and flexion/extension axes (Harmonic Drive CSG 32-50) are $k_1 = 3.1 \cdot 10^4\,{}^{\mathrm{Nm}}\!/\!_{\mathrm{rad}}$ and $k_1 = 5.4 \cdot 10^4\,{}^{\mathrm{Nm}}\!/\!_{\mathrm{rad}}$, respectively [59]. For example, a load torque of $100\,\mathrm{Nm}$ causes a torsional distortion of the Flexspline of $3.226 \cdot 10^{-3}\,\mathrm{rad}$ and $1.852 \cdot 10^{-3}\,\mathrm{rad}$ in the adduction/abduction and flexion/extension axes, respectively, resulting in a foot displacement of $3.226\,\mathrm{mm}$ in the lateral, and $1.852\,\mathrm{mm}$ in the fore-aft direction. For comparison, *Johnnie* incorporates Harmonic Drive HFUC 25-80 gears in the flexion/extension joints, resulting in a foot displacement of $3.226\,\mathrm{mm}$ in the fore-aft direction under the same loading conditions.

As a result of the considerations in Section 2.4 and Footnote 6, lower link inertias advance the natural frequency and antiresonance of the drive mechanisms. In the following, the antiresonance frequency of the adduction/abduction and flexion/extension drives are analyzed using the resultant inertia of the stretched leg as a worst case assumption. For the adduction/abduction the resultant inertia amounts to $3.62\,\mathrm{kgm}^2$, and $3.631\,\mathrm{kgm}^2$ for the flexion/extension axis. Using the torsional stiffnesses of the gear units in Eq. (3.17) on page 89, the antiresonances of the adduction/abduction and flexion/extension drives are $f_{n,add} = 14.73\,\mathrm{Hz}$ and $f_{n,fl} = 19.41\,\mathrm{Hz}$, respectively. Thus, antiresonance of the adduction/abduction gear is marginally smaller than the manufacturer's recommendation, see Footnote 6, but the antiresonance of the flexion/extension gear is well above this value. In conclusion, it was the right decision to choose the larger gear for the flexion/extension drive. The high torsional stiffness significantly contributes to the accuracy of foot placement even under high loading. Note, however, that these calculations only consider the gear stiffness. The actual foot displacements are affected by the stiffnesses of the link structure and its bearings and thus considerably higher.

Table 3.3: Evaluation of different knee joint mechanisms

Design	Thigh inertia* [kg m^2]	Mass† [kg]
K1.1	0.585	3.009
K1.2	0.360	3.450
K2	0.150	3.560
K4	0.085	1.931

* For better comparison, only the drive mechanisms are considered, any structural components are neglected.

† Estimation (except design K4)

Knee Joint Mechanism

Table 3.3 compares the mass and thigh moment of inertia of four knee joint mechanisms. Design variant K1.1 corresponds to solution K1, Figure 2.12*a*. The mechanism consists of a Harmonic Drive-based servo actuator (type 'A', Figure 3.9) that is mounted coaxially with the knee joint axis. This design obviously has the largest moment of inertia because both motor and gear unit are located in the knee joint. Design variant K1.2 is similar to the previous design but the motor is shifted close to the hip joint. The Harmonic Drive-based gear unit is coaxially with the knee joint axis and connected to the motor by a synchronous belt drive. The thigh inertia decreases by 38.5 % but additional components (auxiliary transmissions, shafts, bearings, housings) increases the mass of the mechanism by 14.7 %. Design variant K2 corresponds to a patent application by Honda [51] and is shown schematically in Figure 2.12*b*. It employs the same Harmonic Drive-based servo actuator as variant K1.1 but the entire actuator is located close to the hip joint. The knee joint is actuated by a coupler link, forming a parallel crank mechanism. The thigh inertia reduces significantly by 74.4 % compared to design K1.1. On the other hand, the estimated mass increases because of additional transmission components such as heavy-duty bearings of the gear unit output flange and coupler link. Finally, design variant K4 represents the implemented mechanism, cf. Sections 2.6.2 and 3.8.2. The four-bar mechanism with length-variable linear drive complies Figure 2.12*d*. The thigh inertia and the mass are reduced by 85.5 % and 35.8 %, respectively.

In summary, the chosen knee joint mechanism K4 has shown advantageous for the dynamic performance of the leg apparatus because it provides by far the largest reduction in inertia and mass compared to well-established designs, such as K1.1 and K1.2.

Ankle Joint Mechanism

Table 3.3 compares the mass and posture-dependent shank inertia of different mechanisms for ankle joint actuation. The ankle joint in design variant A0 is actuated in a serial arrangement. The considered drive mechanism is characterized by reduced shank inertia compared to similar designs (cf. Section 2.6.3) and covered by two patents by Honda [50, 119]. Harmonic Drive-based gear units are mounted coaxially with the flexion/extension and adduction/abduction axes of the ankle joint. The motors are located near the knee joint and connect to

Table 3.4: Evaluation of different ankle joint mechanisms

Design	Thigh inertia*	Shank inertia w.r.t. hip joint*, dependent on knee angle [kg m^2]				Mass†
	[kg m^2]	0°	30°	60°	90°	[kg]
A0	—	1.743	1.635	1.341	0.939	3.12
A2	—	1.032	0.930	0.740	0.510	2.42
A3.1	—	0.932	0.898	0.770	0.592	2.44
A3.2	0.058	0.654	0.614	0.520	0.408	3.14

* For better comparison, only the drive mechanisms are considered, any structural components are neglected.

† Estimation (except design A3.2)

the gear units via synchronous belt drives. An additional bevel gear redirects the motor axis of the adduction/abduction axis. Despite its simple kinematic structure, this drive mechanism is unfavorable with regard to leg dynamics. The long transmission distance between the motors and gear units leads to a rather high mass and shank inertia is very high due to the large perpendicular distance of the gear units to the hip joint. The mass distribution also results in a high posture dependence. At a knee angle of 90° the shank inertia decreases by 23 % compared to the stretched leg configuration. Design variant A2 corresponds to Figure 2.15*b*, a detailed description is given in [113]. The ankle joint is actuated by a parallel mechanism composed of two linear actuators acting as length-variable couplers. The actuators are connected to the shank and feet by universal joints. Design A2 has the lowest mass of all considered mechanisms because its structure is very simple and requires only a small number of components. Compared to design variant A0, the shank inertia reduces to 59.2 % in the stretched leg configuration. The variation of shank inertia over the knee joint workspace is 22.3 %.

The structure of design variant A3.1 is shown in Figure 2.16*a*. Two spatial slider-crank mechanisms mounted on the shank drive the ankle joint in a parallel arrangement. The motors are placed close to the knee joint and drive the linear carriage through synchronous belt drives. Hence the entire drivetrain is mounted on the shank, similar to the *Johnnie* design [47]. The mass of the mechanism is comparable to design variant A2. The shank inertia is 53.5 % in the stretched leg configuration compared to design variant A0, and varies by 19.1 % over the relevant knee angles. Finally, design variant A3.2 is the mechanism that is adopted to the ankle joint of *Lola*, cf. Section 3.8.3 and Figure 3.20. The kinematic structure (Figure 2.16*b*) is identical to design A3.1 but the motors are placed on the thigh, close to the hip joint. Power transmission from the motors to the planetary roller screws occurs by synchronous belt drives and angular gears that are coaxial with the knee joint. The higher mass compared to design A3.1 results from the longer transmission distance between the motors and screws. Although the mass is similar, the contribution to the resultant leg inertia reduces to 40.8 % of the serial arrangement A0 (stretched leg configuration). The shank inertia varies by only 17.1 % over the knee angle.

The analysis shows that drive mechanism A3.2 drastically improves the acceleration capability if the legs. Although the mass is comparable to the serial

Table 3.5: Evaluation of different toe joint configurations

Design	Foot inertia w.r.t. hip joint*, dependent on knee angle [kg m^2]				Mass*
	0°	30°	60°	90°	[kg]
monolithic foot	0.367	0.369	0.323	0.242	0.389
passive toe joint	0.503	0.505	0.441	0.328	0.537
active toe joint	0.830	0.833	0.727	0.542	0.912

* For better comparison, only the hallux is considered, the remaining foot structure is neglected.

arrangement, which is found in most humanoid robots, it has by far the lowest moment of inertia with respect to the hip joint. Also, the effects of varying shank inertia are lower than in the other designs.

Toe Joint Mechanism

Table 3.5 compares the contribution of different foot configurations to the resultant leg inertia. The mechanical design of the monolithic foot structure, passive and active toe joint are shown in Figure 3.24.

Unsurprisingly, the monolithic foot structure, Figure 3.24*c*, has the lowest inertia and mass. The inertia variation over the knee workspace is 34 %. The mass of the passive toe joint illustrated in Figure 3.24*b* is 138 % of the monolithic foot, likewise, the inertia increases to 137 % in the stretched leg configuration. With 34.8 %, the inertia variation is comparable. For the active toe joint, Figure 3.24*a*, the mass and resultant inertia for the stretched leg configuration increase to 234 % and 226 % of the monolithic foot, respectively. The inertia variation accounts for 34.7 % over the knee workspace.

Although a comparison between the different foot concepts is quite limited, the analysis shows that the effort for improving the acceleration capability of the locomotor system is little counteracted by the active toe joint. However, the advantage of more flexible and natural gait generation and the potential to unload other leg joints (see Section 2.2.6) outweigh the disadvantages.

3.13 Chapter Summary

This chapter detailed on the mechanical design of the robot. Distinguishing characteristics are the redundant kinematic structure with seven-DoF legs, consistent lightweight construction and a modular joint design with high power density. Furthermore, mass distribution of the legs is improved to achieve good dynamic performance:

Design calculations: fundamental design data are obtained from a multibody simulation model and form a basis for dimensioning the mechanical structure and servomechanisms. Torque-based selection of the servomechanisms and their components aims at meeting the static and dynamic load requirements. It is complemented by the elastodynamic analysis of the drive mechanisms to ensure high dynamic performance of the locomotor system. Most structural components are designed using an empirical design approach.

Topology optimization is applied to components subject to complex loading. Since structural vibrations can easily destabilize the robot, dynamic stiffness of the leg links is analyzed by numerical modal analysis.

Modular joint design: the constraints of human dimensions and mass demand for the development of very compact and lightweight servo actuators. The rotary drives integrate permanent magnet synchronous motor, Harmonic Drive gear, sensors and other components in very compact units with high power density. For minimal mass and better mass distribution, the main structure of the robot is non-modular. But the drives are built on the unit construction principle, simplifying design and manufacturing.

High-dynamic leg structure: special emphasis was put on an improved mass distribution of the leg apparatus to achieve good dynamic performance. Mass distribution in the hip-thigh area is improved significantly by employing a roller screw-based linear actuator in the knee joint. The ankle joint is actuated by a parallel mechanism of two linear actuators whose motors are mounted on the thigh. Thus, a large part of the actuator mass is be shifted close to the hip joint rotational axis, resulting in high-dynamic behavior of the legs. In addition, the base bodies of pelvis, thigh, shank and foot are designed as investment castings. Prototype investment casting allows for one-piece shell structures that result in very sophisticated, complex-shaped and lightweight parts with high effective stiffness.

The feet: the toe joint divides the foot into forefoot and hallux. Despite the lightweight design, the feet have a rigid mechanical structure to reliably transmit the propulsive forces for system stabilization. The modular mechanical configuration allows replacement of the heel and toe segments and/or other components. Several mechanisms are implemented for impact attenuation: viscoelastic contact elements with good damping characteristic are used in analogy to the human fat pads. Similar to the human hindfoot, a passive heel segment with hydraulic shock absorber contributes to energy dissipation during initial contact. Proper ground contact is ensured by an outsole made from wear-resistant, high-friction rubber.

Parameter identification: a calibration jig is used to determine angular offsets of the link position sensors in a closed-loop calibration procedure. In order to realistically represent the mass distribution in the multibody simulation model, all components including cable harnesses are weighed during assembly. The link masses are adjusted in the CAD model and corrected inertial parameters are adopted into the robot simulation.

Evaluation of dynamic performance: compared to other design variants, the drive mechanisms of the knee and ankle joints by far have the lowest contribution to resultant leg moment of inertia. Thus, acceleration capability of the legs is improved significantly. Although the active toe joints little counteract the low-inertia design of the legs, these disadvantages are outweighed by the ability to generate more versatile gait patterns and the potential to unload other leg joints.

4 Sensor System

> *The machine has no feelings, it feels no fear and no hope […] it operates according to the pure logic of probability. For this reason I assert that the robot perceives more accurately than man.*
>
> —Max Frisch, Homo Faber

This chapter introduces the sensor system of the robot. The joint sensors for motor control and link position sensing are explained in Section 4.1. The custom-developed force/torque sensor for measuring the ground reactions is presented in Section 4.2. Finally, the motivation for employing a high-precision inertial measurement system is given in Section 4.4.

4.1 Joint Sensors

Each joint is equipped with an incremental rotary encoder, an absolute angular sensor for direct link position sensing and a limit switch. For the rotary servo actuators, all sensors are placed inside the housing, assembled as space-saving as possible. The arrangement is exemplified in Figure 3.10.

Typical accuracy requirements on the encoder technology used are sufficient for this application. However, the range of suitable sensors is severely limited by the tight packaging goals and weight restrictions. Standard housed shaft-end encoders come with integral bearing, hence the measuring accuracy is insusceptible to alignment errors. Although easy to install and robust against dirt and vibrations, the industrially ruggedized design makes such encoders too heavy and bulky. Instead, kit encoders without integral bearing and housing must be used. In this case the precision of the encoder mechanical assembly (concentricity of the disk and scanning head, etc.) is crucial to measurement accuracy. Hence encoder installation and alignment are very elaborate and require sophisticated measurement equipment.

The incremental rotary encoder on the motor shaft utilizes the giant magnetoresistive effect to measure rotation by detecting the magnetic field and its changes. Figure 4.1*a* shows the scanning head and scale graduation of this sensor. Magnetoresistive encoders are characterized by a high resolution, robustness, resistance against humidity, dust and oil, and a high-dynamic response. The scanning head is a very compact PCB[1] module with integrated signal conditioning electronics, enabling simple assembly and adjustment without further calibration. The scale graduation of an incremental magnetic encoder is a multi-pole magnetic ring.

In addition to software-based monitoring, each joint incorporates a limit switch to avoid problems like self-collisions and cable wind-up. The sensor shown in

---

[1] Printed circuit board

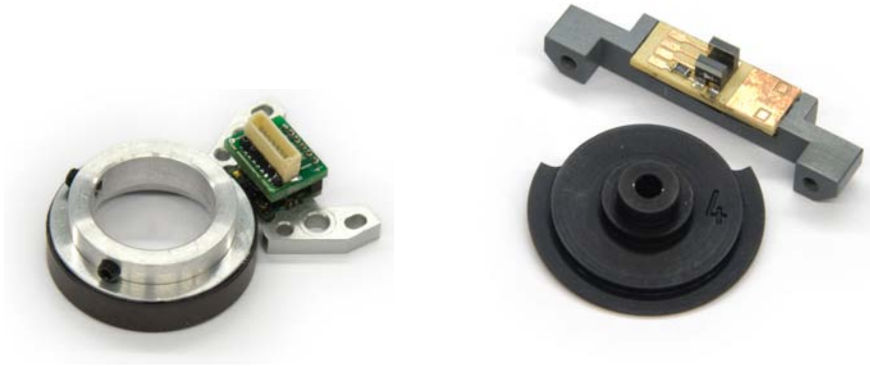

(a) Incremental rotary encoder *(b)* Limit switch with cam

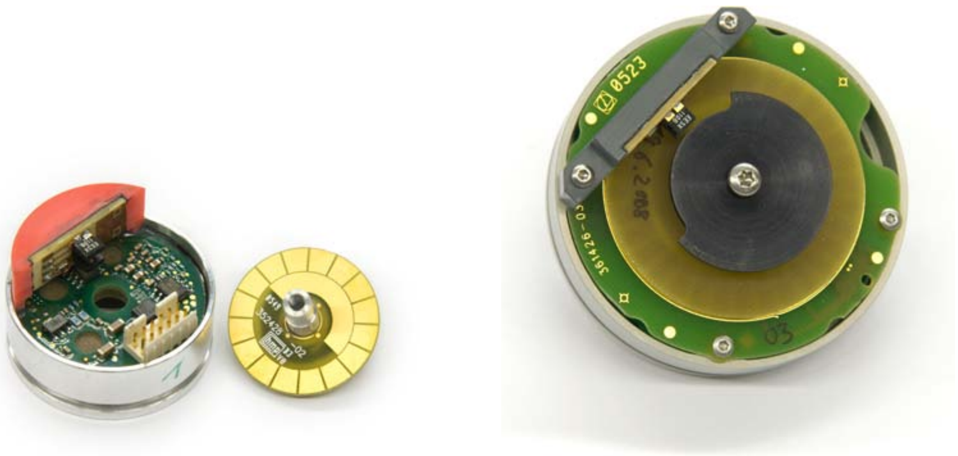

(c) Absolute angular sensor, type 1 *(d)* Absolute angular sensor, type 2

Figure 4.1: Joint sensors

Figure 4.1*b* is composed of a photoelectric fork sensor and a cam that is connected to the gear output. The allowed angular range is determined by the cam which is different for each degree of freedom. When a limit is encountered motor voltage is interrupted inside the motor controller module with minimum software overhead before reaching the joint's mechanical end stops.

Figures 4.1*c* and 4.1*d* show the angular sensors for load-side feedback. Both sensor determine the absolute joint angle within a single revolution. The rotary encoders of type ECI are manufactured by Heidenhain and typically used as resolver replacement in industrial motor control. The sensors of type 1 and 2 differ in the size and resolution. Type 1 shown in Figure 4.1*c* has a diameter of 37 mm and a resolution of 16 bit per revolution and is used in the ankle and toe joints. The other joints employ sensor 2, Figure 4.1*d*, which has a diameter of 65 mm and a resolution of 17 bit. Both sensors have a measurement accuracy of 0.1°, a cutoff frequency 6 kHz and a latency for continuous sampling of position values of 5 µs. Hence the delay in position feedback is minimal and velocity measurement can be done by numerical differentiation. Position values and configuration data are transmitted via the digital, bidirectional EnDat interface. ECI encoders utilize the inductive measuring principle and come without integrated bearing. The

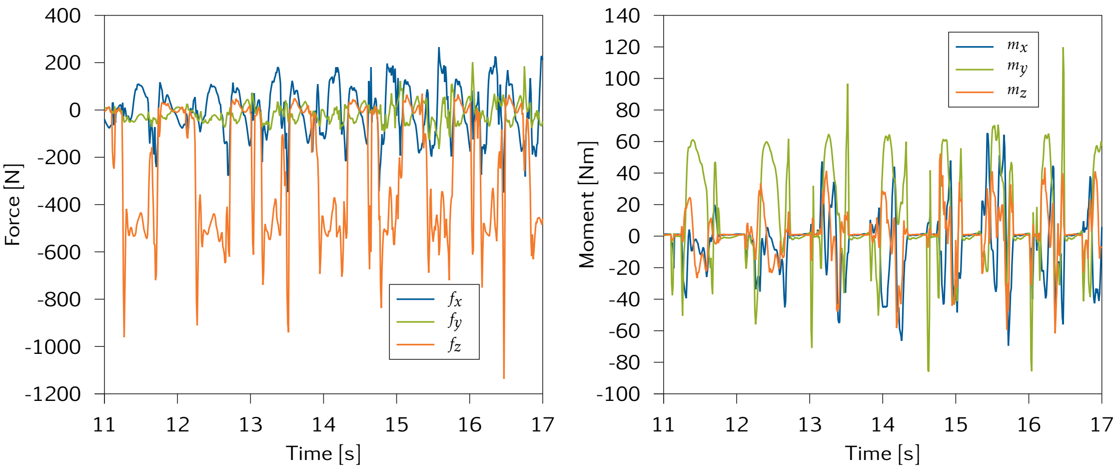
(a) Ground reaction forces

(b) Ground reaction moments

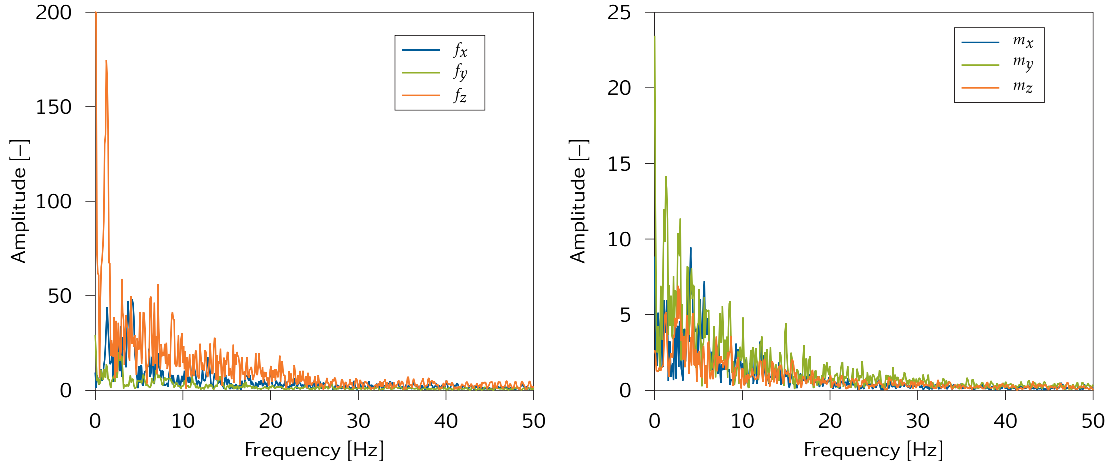
(c) FFT ground reaction forces

(d) FFT ground reaction moments

Figure 4.2: *Above,* ground reaction forces and moments for a walking speed of 5.55 km/h obtained from simulation; *below,* frequency spectrum of the contact wrench.

encoder shaft is fixed to the output flange using an elastomer coupling, as shown in Figure 3.10, and the encoder flange is fixed to the motor housing. Besides rotational speed, the attainable accuracy depends on the air gap between rotor and stator and the mounting conditions. The air gap between the scanning PCBs is adjusted with shims during assembly. As changes in the air gap, e. g., due to thermal expansion of the sensor shaft, or wobbling of the rotor PCB, affect signal quality. These errors are minimized by the short distance between encoder shaft bearing and the rotor PCB.

4.2 Force/Torque Sensors

This section presents the design of the six-axis force/torque sensor based on the fundamental design concept developed in Section 2.7.3. Figure 4.2 shows the ground reaction forces and moments for walking at a speed of 5.55 km/h obtained

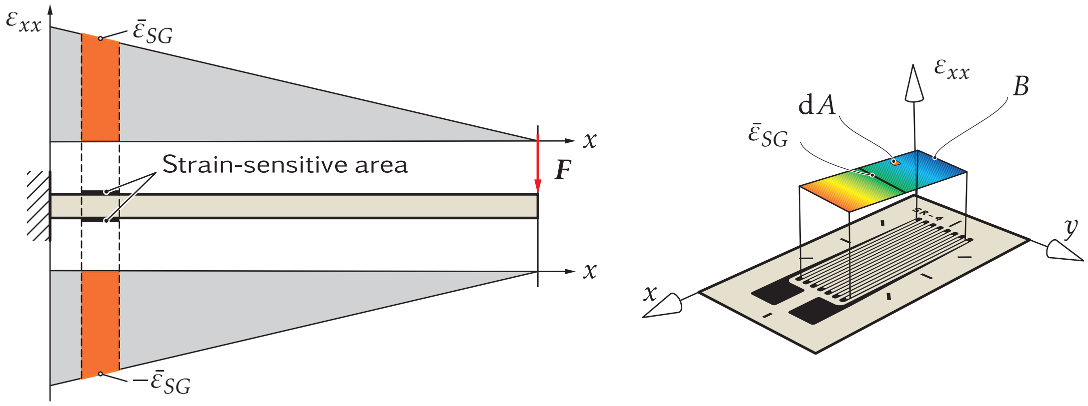

Figure 4.3: Cantilever beam as basic transducer geometry. *Left,* high sensitivity is achieved by applying the strain gauges close to the clamping; *right,* the strain gauge averages strain over the area covered by the grid.

from the multibody simulation model by Buschmann, cf. Section 3.3.1. Using these data, the measurement range of the force/torque sensor is derived:

$$\boldsymbol{F} = \pm \begin{pmatrix} 500 \\ 100 \\ 1200 \end{pmatrix} [\mathrm{N}]; \qquad \boldsymbol{M} = \pm \begin{pmatrix} 100 \\ 120 \\ 50 \end{pmatrix} [\mathrm{Nm}]. \tag{4.1}$$

Uchiyama et al. [189] propose a systematic procedure for the structural design of a robotic force/torque sensor: the condition number of the strain-compliance matrix serves as a measure for the maximum possible error in the measured forces and moments. It is an indicator for the isotropy of structural compliance of the transducer body with respect to sensor strain, and is equal to one in the case of perfect isotropy. But the sensor performance is also affected by the relationship of beam length l and sensor size $L = r + l$ (cf. Figure 4.4) and other factors such as stiffness, eigenfrequencies, decoupling, linearity, and hysteresis [52]. Lastly, in order to obtain a wide enough bandwidth, the natural frequencies of the transducer body should be higher than the frequencies of motion. To this end, a fast Fourier transform (FFT) is conducted on the ground reaction forces to provide an estimation of the frequency range of a typical gait pattern. The FFT of the ground reaction forces and moments are shown in Figure 4.2(c) and (d), respectively. These results indicate that the frequency spectrum of the reference walking pattern ranges up to 25 Hz.

The following sections describe the mechanical design, sensor electronics and the calibration and verification procedure. Most of these results are lifted from the Diploma thesis by Schwienbacher [167].

4.2.1 Optimized Shear Beam Geometry for High Sensitivity

The most fundamental force transducer shown on the left of Figure 4.3 is the cantilevered beam with strain gauges applied to its surface. The force $\boldsymbol{F}$ induces surface strain ε that increases arithmetically towards the clamping. Hence the

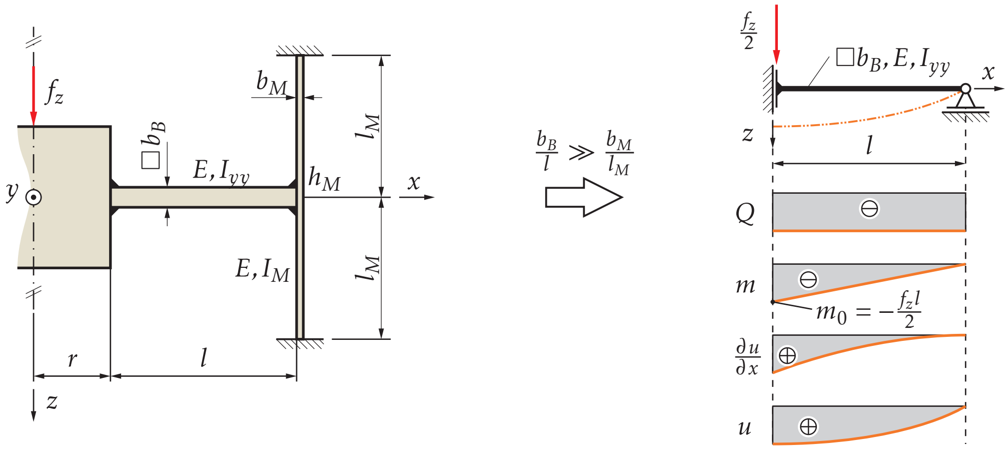

Figure 4.4: *Left,* mechanical model of a shear beam (index B) supported by a membrane (index M); *right,* reduced planar model of the shear beam. The elastic relations (shear Q, moment m, slope $\frac{\partial u}{\partial x}$, deflection u) are shown qualitatively.

strain gauges are placed close to the clamping to achieve high sensitivity. The transducer sensitivity β_T obviously corresponds to the indicated strain $\bar{\varepsilon}_{SG}$ and can thus only be increased at the expense of reduced transducer stiffness k_T:

$$\beta_T \propto \bar{\varepsilon}_{SG} \propto \frac{1}{k_T} \tag{4.2}$$

On the other hand, the strain is typically not distributed uniformly over the active area of a strain gauge. As a result, the averaging over the strain-sensitive area A causes a loss of sensitivity as indicated on the right of Figure 4.3:

$$\bar{\varepsilon}_{SG} = \frac{1}{A} \int_B \varepsilon_{xx} \, \mathrm{d}A \, . \tag{4.3}$$

All current Maltese cross sensors have shear beams with constant cross sections. As shown by the following analysis, this design is not optimized for sensitivity but mainly motivated by ease of design and manufacturing. The beam geometry is therefore modified for high sensitivity by maximizing stress and achieving constant strain in the active area of strain gauge installation. The "ideal" beam geometry is examined using analytical beam theory and then verified numerically by finite element analysis.

For a simplified analysis the Maltese cross-shaped transducer (cf. Figure 2.20) is treated as a 2-D elastostatic mechanical system using shear beam theory. The simplified model is shown on the left of Figure 4.4. Due to symmetry, the model can be reduced to a single beam that extends along the x-axis. Without loss of generality, we assume a square beam cross section of side b_B. The beam is supported by a prismatic bearing at its root ($x = 0$), allowing only rectilinear translation along the z-axis: $\left.\frac{\partial u}{\partial x}\right|_{x=0} = 0$. At $x = l$ the beam is supported by a membrane of thickness b_M, height h_M and length $2 \cdot l_M$, which restrains the beam end from rotation and transversal displacement. Provided that the membrane is thin compared to the beam, $\frac{b_B}{l} \gg \frac{b_M}{l_M}$, the resisting moment caused by the membrane is negligible. The membrane joint reduces to a pin connection with deflection and moment fixed to zero: $u|_{x=l} = \left.\frac{\partial^2 u}{\partial x^2}\right|_{x=l} = 0$. The external force f_z is applied to the sensor hub in center of the transducer. Only the two beams perpendicular to the load axis are deformed, hence the beams along the z-axis are neglected in the reduced planar model. Then f_z is equally spread on the x-axis beams: $Q = -EI_{yy} \left.\frac{\partial^3 u}{\partial x^3}\right|_{x=0} = -f_z/2$. These assumptions finally lead to the simply supported Euler-Bernoulli beam shown on the right of Figure 4.4. The surface strain is given by

$$\varepsilon = \frac{b_B\, m}{2EI_{yy}}\,. \tag{4.4}$$

Here E is the Young's modulus and m the moment

$$m = m_0\left(1 - \frac{x}{l}\right), \qquad \text{with} \quad m_0 = \tfrac{1}{2} f_z l\,. \tag{4.5}$$

Using this model, four different beam geometries with varying cross sections $b_B(x)$, Figure 4.5, are compared in terms of their stiffness-sensitivity relationship:

1. Rectangular cross section
2. Cross section with constant surface strain
3. Trapezoidal cross section
4. Double-trapezoidal cross section

Rectangular Shaped Beam

The standard rectangular shaped beam ($b_B = \text{const.}$) illustrated in Figure 4.5*a* is considered for reference purposes. Assuming a square cross section of side b_B, the second moment of area is

$$I_{yy} = \frac{b_B^4}{12}\,. \tag{4.6}$$

Using Eqs. (4.5) and (4.6), the surface strain becomes

$$\varepsilon_{(a)} = \frac{6m_0(1 - \frac{x}{l})}{Eb_B^3}\,. \tag{4.7}$$

The elastic relations are normalized for better comparison of the different models. For instance, Eq. (4.5) is being normalized to

$$m' = \frac{m}{m_0} = 1 - x', \qquad \text{with} \quad x' = \frac{x}{l} \in [0, 1]\,. \tag{4.8}$$

Here the prime $(\cdot)'$ denotes unitless parameters. Normalizing Eq. (4.7) with Eq. (4.8), $E = 6$ and $b_B = 1$, we get the surface strain for the rectangular beam:

$$\varepsilon'_{(a)} = 1 - x'\,. \tag{4.9}$$

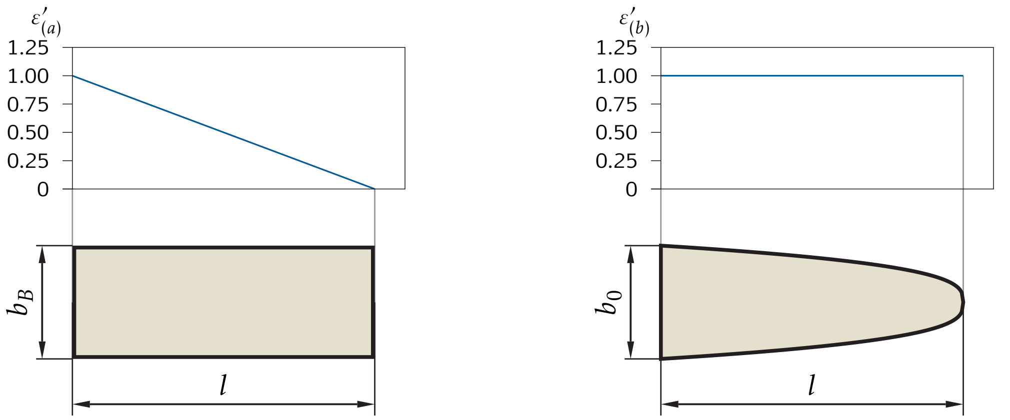

(a) Rectangular cross section *(b)* Constant strain cross section

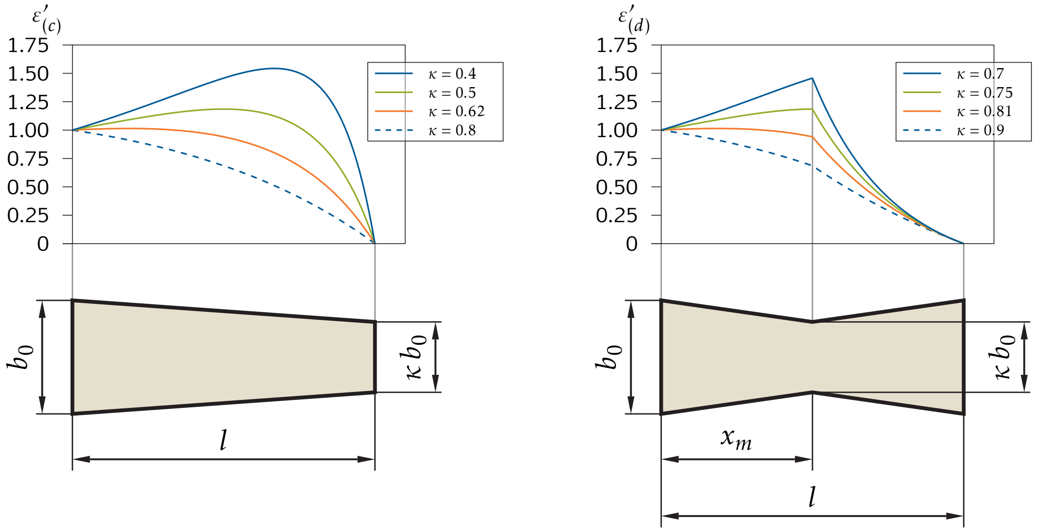

(c) Trapezoidal cross section *(d)* Double-trapezoidal cross section

Figure 4.5: Influence of shear beam geometry on surface strain and sensitivity

Cross Section with Constant Surface Strain

The averaging behavior of the strain gauges is eliminated if the beam cross section is designed to satisfy the condition of constant surface strain along the beam length as shown in Figure 4.5*b*. Solving Eq. (4.7) for b_B results in the beam width

$$b_B = \sqrt[3]{\frac{6m_0(1-\frac{x}{l})}{E\varepsilon_{(b)}}}, \qquad \text{where} \quad b_0 = b_B|_{x=0} = \sqrt[3]{\frac{3\max(f_z)l}{E\varepsilon_{(b)}}}. \tag{4.10}$$

Here the indicated strain $\varepsilon_{(b)}$ is constant and chosen to match the properties of the strain gauges. Furthermore, the initial beam width b_0 is given by the maximum load, $\max(f_z)$, and the beam length l and cannot be chosen arbitrarily. Normalizing this equation using Eq. (4.8), $E = 6$ and $\varepsilon_{(b)} = 1$ yields

$$b'_B = \sqrt[3]{1-x'}. \tag{4.11}$$

While this approach is advantageous to sensitivity, the curved surfaces resulting from Eq. (4.11) are unfavorable for milling and strain gauge installation.

Trapezoidal Cross Section

The third approach is therefore based on a first-degree polynomial function. The trapezoidal-shaped cross section shown in Figure 4.5*c* is a modification of the rectangular beam. The beam width and height reduce arithmetically over the beam length:

$$b_B = b_0 \cdot \left[(\kappa - 1)\tfrac{x}{l} + 1 \right] . \tag{4.12}$$

Here $b_0 = b_B|_{x=0}$ is the initial beam width and $\kappa = \frac{b_B|_{x=l}}{b_0}$ the slope ratio. Using this equation in Eq. (4.4), we obtain

$$\varepsilon_{(c)} = \frac{6m_0(1 - \frac{x}{l})}{Eb_o^3[(\kappa - 1)\frac{x}{l} + 1]^3} . \tag{4.13}$$

Normalized with Eq. (4.8), $b_0 = 1$ and $E = 6$, the above equation reduces to

$$\varepsilon'_{(c)} = \frac{1 - x'}{[(\kappa - 1)x' + 1]^3} . \tag{4.14}$$

The plot in Figure 4.5*c* shows the surface strain $\varepsilon'_{(c)}$ for different slope ratios κ. The sensitivity increases with decreasing κ but goes along with a significant reduction in stiffness. A suitable trade-off between stiffness and sensitivity is found for $\kappa = 0.62$: here $\varepsilon'_{(c)}$ is flattened in the area of strain gauge installation $(0.1 \leq x' \leq 0.3)$.

Double-Trapezoidal Cross Section

The main disadvantage of the previous design is the considerable loss of stiffness over the beam length. The cross section is therefore modified in the fourth design to achieve (almost) constant strain in the active area, while the loss of stiffness is reduced. The idea is to introduce a weak spot in the area of strain gauge installation. As in the previous design, the beam width b_B reduces arithmetically but increases immediately after the area of strain gauge installation. As a result, the beam is composed of two pyramidal frustums with rectangular bases, adjoined at their top bases. Figure 4.5*d* shows the double-trapezoidal cross section which is defined by the piecewise function

$$b_B = \begin{cases} b_0 \cdot \left(\dfrac{\kappa - 1}{x_m} \cdot x + 1 \right) , & 0 \leq x \leq x_m ; \\ b_0 \cdot \left(\dfrac{1 - \kappa}{l - x_m} \cdot x + \dfrac{\kappa l - x_m}{l - x_m} \right) , & x_m < x \leq l . \end{cases} \tag{4.15}$$

Here $b_m = b_B|_{x=x_m} = \kappa \cdot b_0$ is the minimal beam width at $x = x_m$ and κ the slope ratio. Assuming that b_m is located in the middle of the beam $(x_m = 0.5)$, and using

Eq. (4.15) in Eq. (4.7), the surface strain becomes

$$\varepsilon_{(d)} = \begin{cases} \dfrac{6m_0(1-\frac{x}{l})}{Eb_0^3\left(2(\kappa-1)\frac{x}{l}+1\right)^3}, & 0 \leq x \leq \frac{l}{2}; \\ \dfrac{6m_0(1-\frac{x}{l})}{Eb_0^3\left(2(1-\kappa)\frac{x}{l}+2\kappa-1\right)^3}, & \frac{l}{2} < x \leq . \end{cases} \tag{4.16}$$

Normalizing this equation with $x' = \frac{x}{l}$, $E = 6$ and $b_0 = M_0 = 1$ finally yields

$$\varepsilon'_{(d)} = \begin{cases} \dfrac{1-x'}{[2(\kappa-1)x'+1]^3}; & 0 \leq x' \leq 0.5 \\ \dfrac{1-x'}{[2(1-\kappa)x'+2\kappa-1]^3}; & 0.5 < x' \leq 1 \end{cases} \tag{4.17}$$

The plot in Figure 4.5*d* shows the surface strain $\varepsilon'_{(d)}$ at different slope ratios κ. As in the previous design, strain is increased by the diminished cross section for $x \leq x_m$. Conversely, the extending cross section for $x > x_m$ limits stiffness losses. A suitable trade-off between stiffness and sensitivity is found for $\kappa = 0.81$ where $\varepsilon'_{(d)}$ is flattened in the area of strain gauge installation ($0.1 \leq x' \leq 0.3$). From the manufacturing point of view, the double-trapezoidal cross section is noncritical.

In summary, the stiffness-sensitivity relationship is improved by using the double-trapezoidal beam geometry. The tapered cross section acts as a notch that causes a stress raise and consequently increases the strain level in the strain gauge active area. Moreover, an almost uniform strain distribution in the area of strain gauge installation is achieved by choosing an appropriate slope rate κ.

Verification by FEA

In the following the analytical results are verified numerically by using a detailed finite element model in order to overcome idealized assumptions about the analytical model and principal limitations of beam theory. The beam with double-trapezoidal cross section is compared to the beam with rectangular shape, Figures 4.5*a* and 4.5*d*, in terms of the stiffness-sensitivity relationship. Each model comprises a single shear beam with its end supported by a membrane, and parts of the inner sensor hub. Different load cases are applied to the sensor hub using a compound of rigid elements. The model results are presented in Figure 4.6. Each load case *a*–*d* corresponds to a single-axis force or moment loading. The isosurfaces show the strain distribution for both models. In addition, the strain $|\varepsilon|$ along the normalized node path ξ' is plotted in the area of strain gauge installation, and the integral strains $|\bar{\varepsilon}_{SG}|$ indicated by the strain gauges are labeled. Due to the qualitative nature of the results scaling is omitted for all variables but all isosurfaces share the same color mapping. The results obtained from FEA qualitatively correspond well with the analytical models. The strain levels, $\varepsilon'_{(a)}$ and $\varepsilon'_{(d)}$, Figure 4.5, are comparable to $|\varepsilon|$ along node path ξ'. For the double-trapezoidal beam a more "flattened" strain distribution in the strain gauge active area is achieved by parameter modification. A good tradeoff is found for a slope rate of $\kappa = 0.85$ (analytical result: $\kappa = 0.81$), as the notch stress concentration

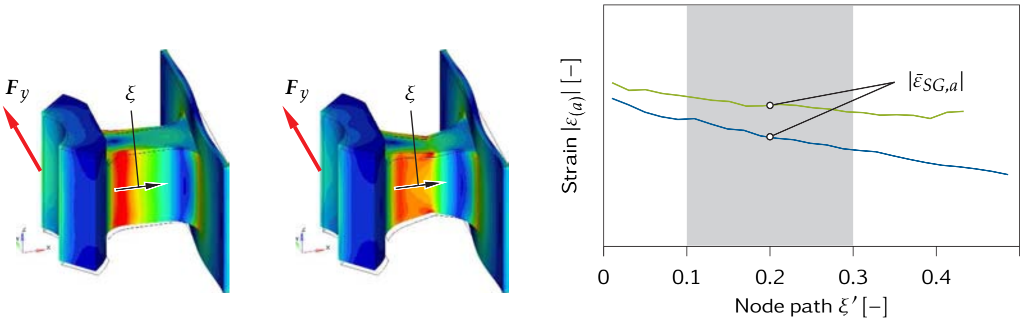

(a) Load case 1: F_y

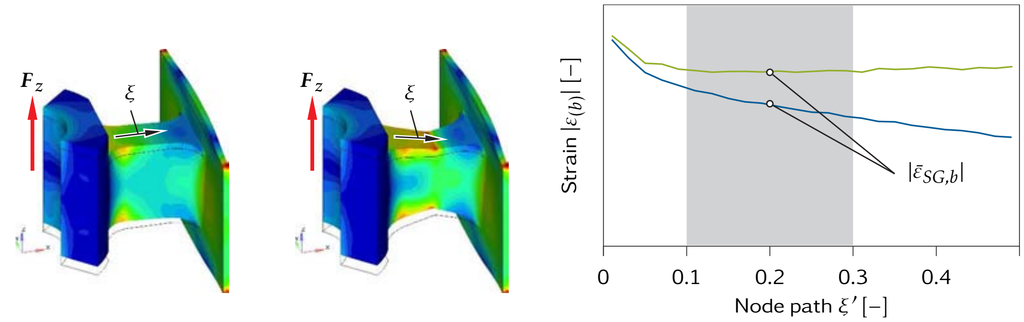

(b) Load case 2: F_z

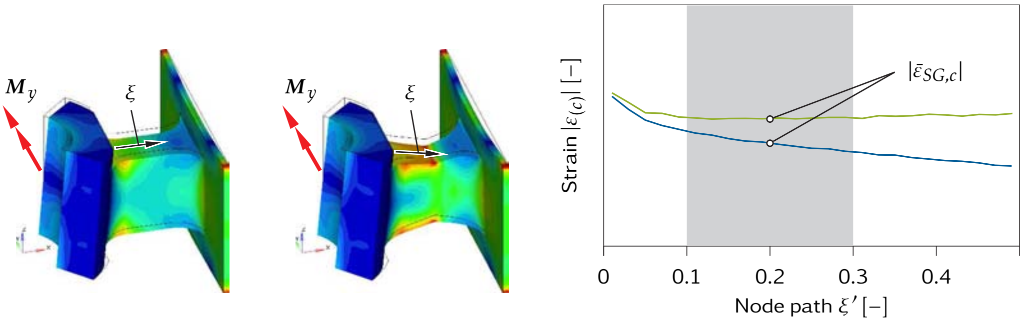

(c) Load case 3: M_y

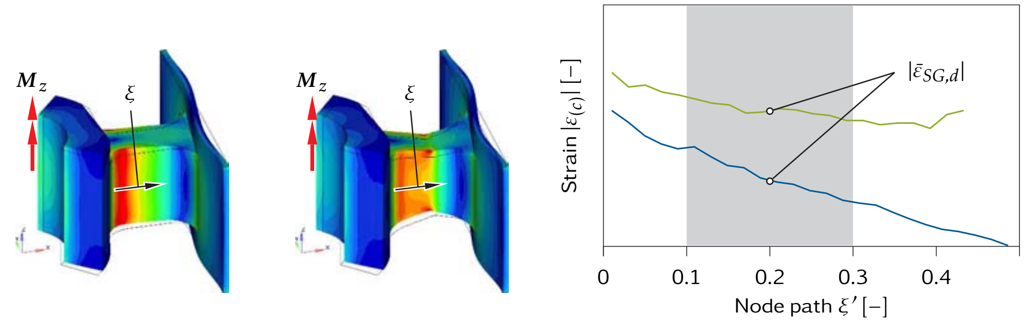

(d) Load case 4: M_z

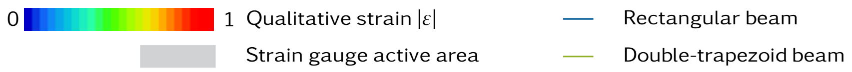

Figure 4.6: Numerical verification by FEA. The results for the rectangular and double-trapezoid beams are shown qualitatively.

Table 4.1: Comparison of rectangular and double-trapezoidal beam geometry in terms of stiffness and sensitivity

Criterion		Load case (a) f_y	 (b) f_z	 (c) m_y	 (d) m_z
Stiffness	$\mathcal{K}$ [–]	0.85	0.88	0.88	0.84
Sensitivity	$\mathcal{E}$ [–]	1.38	1.44	1.44	1.40
Stiffness-sensitivity relationship	$\mathcal{S}$ [–]	1.17	1.26	1.26	1.18

increases significantly for smaller κ.

Using the FEA results, Table 4.1 compares the stiffness of the rectangular and double-trapezoid beam geometries by the ratio of axial displacement, u, and the angle of twist, φ, for force and moment loading, respectively:

$$\mathcal{K} := \frac{k_{(d)}}{k_{(a)}} = \begin{cases} \dfrac{u_{(a)}}{u_{(d)}}, & \text{force loading;} \\ \dfrac{\varphi_{(a)}}{\varphi_{(d)}}, & \text{moment loading.} \end{cases} \tag{4.18}$$

Here, u and φ are calculated with respect to the point of force application. The sensitivity of both designs is compared by the ratio of indicated strains:

$$\mathcal{E} := \frac{|\bar{\varepsilon}_{SG,d}|}{|\bar{\varepsilon}_{SG,a}|}. \tag{4.19}$$

Finally, the stiffness-sensitivity relationship is introduced for better comparison of the overall effect:

$$\mathcal{S} := \mathcal{K} \cdot \mathcal{E}. \tag{4.20}$$

The indices given in Table 4.1 emphasize the superior performance of the novel double-trapezoid beam geometry: although transducer stiffness is reduced by 12 to 16 %, sensitivity increases significantly by 38 to 44 %. Although the manufacturing of the double-trapezoid shear beams is more involved, it is noncritical if a modern CNC milling machine is used.

4.2.2 Mechanical Design

Based on the general requirements stated in Section 2.7.3 the mechanical system of the sensor is developed. In this section, the overall design and assembly is introduced, followed by a more detailed presentation of the transducer body. The detailed FEA provides information on the strain level, stiffness and elastodynamic properties.

Figure 4.7 shows photographs of the assembled F/T sensor. The top and bottom covers are removed to reveal the strain gauges and sensor electronics. The sensor has rather compact measurements ($100 \times 40 \times 100\,\mathrm{mm}^3$). Weighing a total of 395 g, the sensor is heavier than the one developed for the robot *Johnnie* (approximate

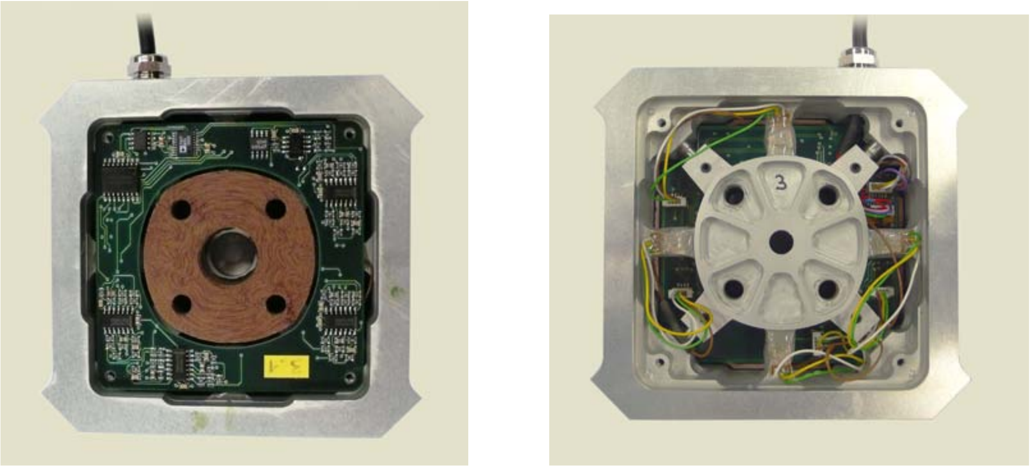
(a) Top view *(b)* Bottom view

Figure 4.7: Photographs of the six-axis force/torque sensor

weight 290 g). Still, the integration of the sensor as a load-bearing element within the forefoot structure eliminates most of the surrounding foot structure and finally reduces the overall weight of the foot segment.

The cross-sectional view in Figure 4.8*a* gives an overview of the sensor assembly. The monolithic transducer body (1) is the key component of the sensor and is described below in full detail. The bushes (2) are bonded to the inner flange of the transducer and insulate the sensor from the rest of the robot. They are made from phenolic cotton fabric laminate (HGW 2088) which shows high compressive strength and superior insulation properties. The contact pressure under the bolt heads (10) is spread over the lower insulation bush (2) by the load-spreading disk (3). The screws (10) connect the sensor and ankle joint (not shown). Four overload protection pins (4a) are mounted to the inner flange by press-fitting and secured by set screws (4b). The functional principle of the overload protection mechanism is described below. The transducer body provides seating surfaces for the sensor electronics (5). The sensor cable (not shown) supplies electric energy and is used for transmission of sensor data and configuration commands. It is secured by a cable gland (not shown) to ensure reliable connections. Covers are integrated on the top (7), bottom (8) and membranes (9) to protect the sensor against damage and ingress of solid foreign objects and dust. The bottom cover (8) is made from aluminum for higher flexural rigidity of the sensor assembly, whereas the top and membrane covers (7,9) are made from plastic. The inside of the plastic covers is coated with a copper-based, highly conductive coating to shield from electromagnetic waves. Figure 4.8*b* shows the monolithic transducer body in a standard Maltese-cross design with four equally spaced and crosswise-arranged shear beams (3). The transducer is made from the high-strength aluminum alloy EN AW-7075 T651 which offers high dimensional stability and typically very low residual stress. The inner flange (1) connects to the ankle joint. Four bolted flange connections (2) situated at the corners of the sensor frame interface to the forefoot. The four shear beams (3) have the double-trapezoid shear beam cross section developed in Section 4.2.1. The novel geometry of the sensing members signifi-

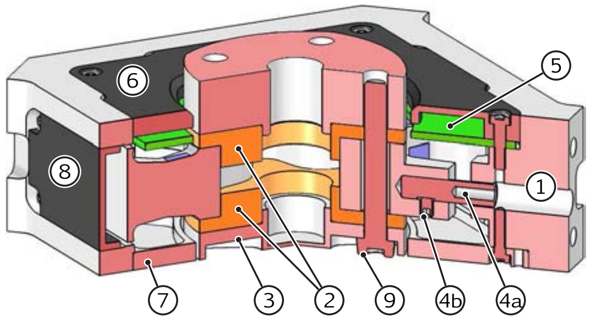

1	Transducer body
2	Insulation bush
3	Load-spreading disk
4a	Overload protection pin
4b	Set screw
5	Sensor electronics
6	Top cover
7	Bottom cover
8	Membrane cover
9	Ankle joint screw

(a) Cross-sectional view of sensor assembly

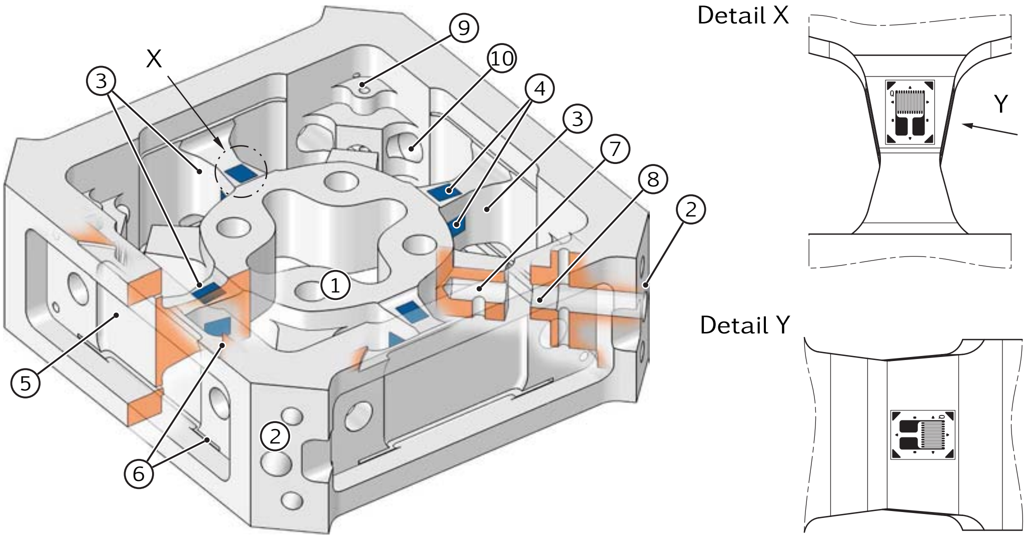

1	Ankle joint (inner) flange	4	Strain gauge	7, 8	Overload protection (bores)
2	Forefoot flange	5	Membrane	9	PCB seating surface
3	Double-trapezoid shear beam	6	Membrane slot	10	Cable bushing

(b) Design of transducer body and strain gauge placement

Figure 4.8: Mechanical design of the six-axis force/torque sensor

cantly improves the overall sensitivity, while the reduction of transducer stiffness remains acceptable. Details X and Y in Figure 4.8*b* illustrate the orientation of the strain gauges (4) on the shear beams (3). The meander-shaped measuring grid is aligned with the beam longitudinal axis. The strain gauges (4) are bonded to the center of the locating face using a hot-curing adhesive. Silicone rubber coating provides mechanical protection of the gauges and soldering terminals. The membranes (5) have a thickness of 1.3 mm and are cut from the transducer body by thin slots (6) on the top and bottom side. The ends of the membrane slots are radiused and the greater wall thickness reduces notch effects. The ankle joint connects to the inner flange (1) at the center of the sensor. The bolted flange connection is electrically isolated by bushes which are bonded to the transducer body and isolate both flange and screws (see below). The outer sensor frame has four bolted connections (2) with inclined flange faces to connect to the forefoot: two flanges connect to the heel segment and the toe joint, respectively. Because of space and weight restrictions the forefoot interface has a comparatively small flange area and reduced screw count. To provide additional safety margin when transmitting the high ground reaction forces *EKagrip* friction shims (cf. Section 3.2) are placed between the connecting members to safely transmit the high loads over the comparatively small flanges. The transducer body comprises a mechanical overload protection of the sensing members. Overload pins (not shown) are fixed to the inner flange bore (7) and extend into a bore (8) of slightly larger diameter in the outer sensor frame: the gap between the overload pin and the bore (8) determines the permissible beam deflection. The gap size has been determined by FEA so that the protection mechanism engages at a vertical load corresponding three times the weight of the robot. If the predetermined load limit is exceeded, the overload pins engage into the sensor load path and the additional "overload bypass" protects strain gauges and sensor geometry. The complex geometry was machined from the solid on a 5-axis CNC milling machine, removing more than 75 % of the total volume of metal. Precision and tight tolerances were ensured by manufacturing the beam and membrane geometry in only two settings from the top and bottom side.

CATIA's built-in FEA tool is used to iteratively refine the shear beam geometry (dimensions, slope ratio, membrane shape, etc.). For a more thorough analysis and fine tuning, a high-resolution finite element model is implemented in Altair HyperWorks. The model setup shown in Figure 4.9 considers all components within the sensor load path, including the transducer body, insulating bushes and load-spreading disk. A hybrid mesh comprising tetrahedron and hexahedron elements is created based on the CAD data. Good-quality hexahedral mesh is chosen for the shear beams, while unstructured tetrahedral meshing is chosen for other regions. This approach allows an accurate analysis of the sensor behavior while the effort of mesh generation is kept manageable. Detail view X in Figure 4.9 illustrates the adaptive mesh refinement of the hexahedral mesh and the transition to the unstructured mesh. The model is simply supported using appropriate displacement boundary conditions for the forefoot flange surfaces. To ensure homogenous and realistic load transmission to the sensor flange, the loads are applied using a rigid body element and a reduced model of the ankle joint.

Figure 4.9 shows the results for different load cases that correspond to the maximum measurement range given in Eq. (4.1). Load case 3 ($|m_y| = 120\,\mathrm{Nm}$) yields the highest stress: the maximum von Mises effective stress of approximately $140\,\mathrm{N/mm^2}$ occurs in the area of strain gauge installation and is below the threshold of fatigue limit of the transducer material[2]. Also, with $|\bar{\varepsilon}_{SG,m_y}| = 1.424 \cdot 10^{-3}$ the indicated strain in this region is below the fatigue characteristics of the installed strain gauges[3]. From Figure 4.9 it can be seen that achieving high sensitivity both for force and moment measurement are conflicting requirements: the sensor geometry is dimensioned for the lateral moments, m_x and m_y, which finally reduces the sensitivity of force measurement.

Table 4.2 specifies the translational and torsional stiffnesses of the transducer body as calculated from the FEA results.

---

[2] The dynamic fatigue strength of aluminum alloy EN AW-7075 T651 is rated at $\sigma_{FL} = 150\,\mathrm{N/mm^2}$ [54].

[3] The estimated fatigue life of the chosen strain gauges is rated at 10^7 cycles and a strain level of $\bar{\varepsilon}_{SG} = \pm 2.2 \cdot 10^{-3}$ [194]

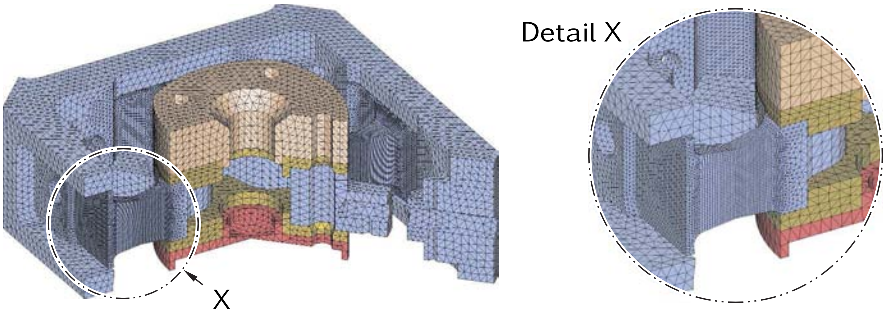

(a) Model setup

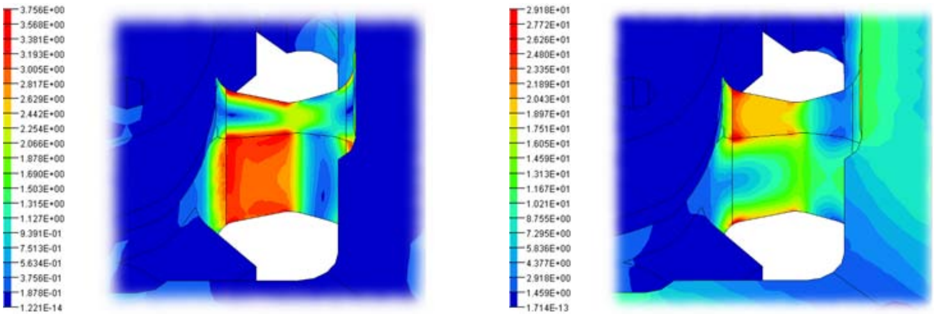

(b) Load case 1: $|f_y| = 500\,\mathrm{N}$

(c) Load case 2: $|f_z| = 1200\,\mathrm{N}$

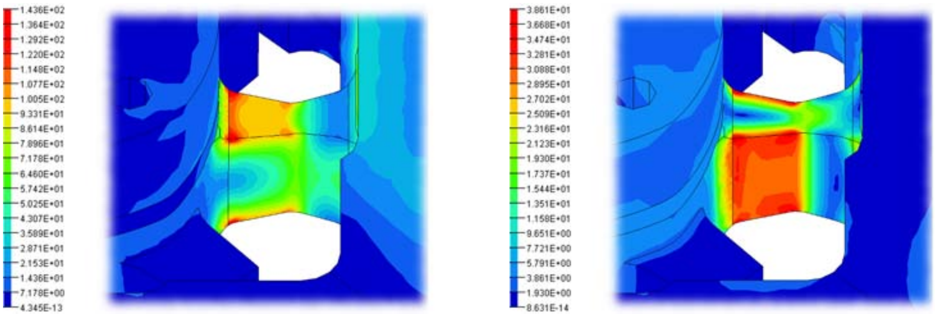

(d) Load case 3: $|m_y| = 120\,\mathrm{Nm}$

(e) Load case 4: $|m_z| = 50\,\mathrm{Nm}$

Figure 4.9: FE analysis of the transducer body

Table 4.2: Calculated translational and torsional stiffnesses

Translational [N/m]		Torsional [Nm/rad]	
k_x	$3.675 \cdot 10^7$	$k_{\varphi,x}$	$4.965 \cdot 10^4$
k_y	$3.650 \cdot 10^7$	$k_{\varphi,y}$	$4.890 \cdot 10^4$
k_z	$5.089 \cdot 10^7$	$k_{\varphi,z}$	$7.339 \cdot 10^4$

4.2.3 Sensor Electronics

The sensor employs metal foil strain gauges as sensing elements. They are chosen to match the elastic properties of the transducer material to provide good self-correction of temperature-dependent changes in the transducer sensitivity. Two strain gauges are installed at opposing surfaces of each shear beam and connected to half bridges for effective temperature compensation. The strain gauge placement is shown in Figure 4.8*b*. An exact application was ensured by aligning the strain gauges by a mechanical positioning jig. During setting of the adhesive, a tailor-made clamping tool was used, providing constant pressure for constant glue line thickness. The heat-curing adhesive required a two-stage curing process. At any time the curing temperature was kept below the structural transformation temperature of the precipitation hardening alloy EN AW-7075 T651. All these measures finally lead to a high zero point stability of the sensor signals.

The half bridges are connected to the integrated sensor electronics. A simplified circuit schematic is shown in Figure 4.10. The sensor electronics, Figure 4.10*a*, comprise the signal conditioning and filtering circuits and A/D conversion for eight strain gauge bridges. To ensure measurement accuracy and stability, a precision voltage source supplies the Wheatstone bridges illustrated in Figure 4.10*b* and all other analog circuits. The bridge voltages are low-level and subject to noise and offset errors. Before digitization, the signals are amplified and the offsets are adjusted to match the available dynamic range of the A/D converter. Each channel offset is adjusted individually by applying a programmable DC voltage from the D/A converter to the reference pin of the instrumentation amplifier. The signals are low-pass filtered to prevent aliasing effects in the digital signals and digitized sequentially by the A/D converter. At a sampling rate of ≥8 kHz the A/D converter has a resolution of ≥12 bit. The circuit contains a serial EEPROM for sensor identification and storage of the calibration matrix to simplify sensor replacement and make the signal processing software more portable. Signal processing runs on an external DSP module, cf. Section 5.2. A serial interface (SPI) is used for data exchange with the DSP module.

4.2.4 Force Sensor Calibration

The F/T sensor is designed for operation within the elastic range of the transducer material. Hence there is a linear relationship between external forces and moments and internal strains:

$$\boldsymbol{C}_S \, \boldsymbol{z} = {}_T\boldsymbol{l}_S \, . \tag{4.21}$$

Here ${}_T\boldsymbol{l}_S = ({}_T\boldsymbol{F}^\mathsf{T}, {}_T\boldsymbol{M}^\mathsf{T})^\mathsf{T} \in \mathbb{R}^6$ is composed of the forces and moments acting on the sensor with respect to sensor frame T, whose origin is in the center of the ankle joint flange. $\boldsymbol{z} \in \mathbb{R}^8$ is the vector of measured strains, and $\boldsymbol{C}_S \in \mathbb{R}^{6\times 8}$ the strain compliance matrix to be identified. The design of the transducer body with four equally-spaced, crosswise-arranged shear beams results in the selective sensitivity of certain half bridges for certain forces or moments. Assuming the strain gauge bridges are labeled from A to H, the theoretical configuration of the calibration

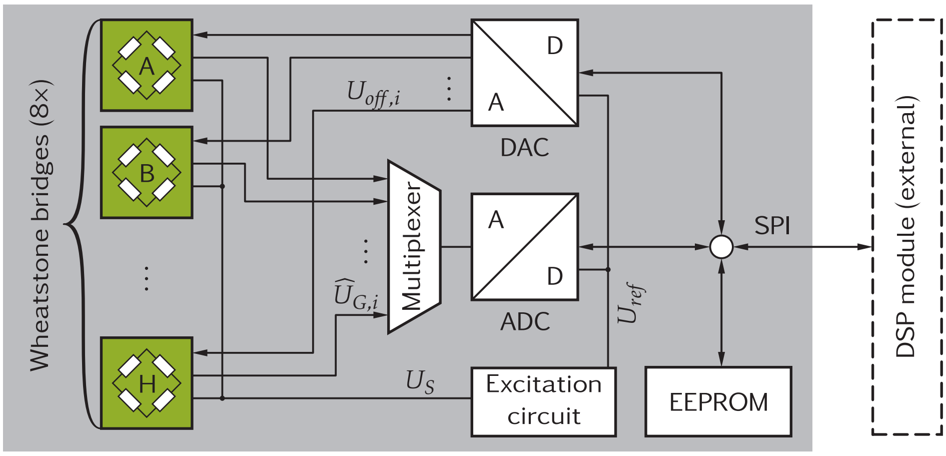

(a) Schematic of sensor electronics

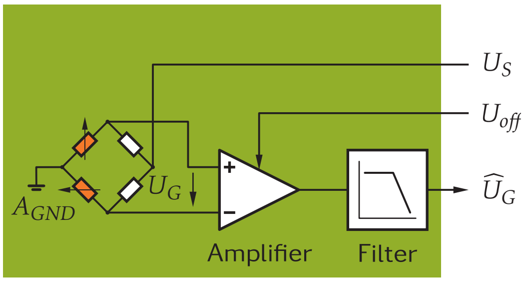

(b) Single Wheatstone bridge

Figure 4.10: Simplified circuit schematic of the sensor electronics

matrix $\boldsymbol{C}_S$ can be derived:

$$\boldsymbol{C}_S = \left(\begin{array}{ccccccccc} & \mathrm{A} & \mathrm{B} & \mathrm{C} & \mathrm{D} & \mathrm{E} & \mathrm{F} & \mathrm{G} & \mathrm{H} \\ f_x & 0 & 0 & c_1 & 0 & 0 & 0 & -c_1 & 0 \\ f_y & c_2 & 0 & 0 & 0 & -c_2 & 0 & 0 & 0 \\ f_z & 0 & c_3 & 0 & c_3 & 0 & c_3 & 0 & c_3 \\ m_x & 0 & 0 & 0 & -c_4 & 0 & 0 & 0 & c_4 \\ m_y & 0 & -c_5 & 0 & 0 & 0 & c_5 & 0 & 0 \\ m_z & c_6 & 0 & c_6 & 0 & c_6 & 0 & c_6 & 0 \end{array}\right) \tag{4.22}$$

The coefficients c_i $(1 \leq i \leq 6)$ relate external loading with internal strains and bridge voltages, respectively. Each line of the matrix shows the sensitivity of each of the eight bridges to different basic loading conditions: for instance, moment loading ${}_T\boldsymbol{M}_x$ causes a bending of the beams along the ${}_Ty$-axis, which is detected by the bridges D and H. The quasi-symmetric design of the transducer yields $c_1 \approx c_2$ and $c_4 \approx c_5$. In practice, the configuration of the calibration matrix can deviate for several reasons, including strain gauge misalignment errors, signal noise and numerical errors during calibration.

Several methods have been proposed in the literature for the calibration of multi-component force sensors. The most common ones are based on the *least squares method* and perform with high accuracy, provided that the applied forces are exactly known in magnitude and direction [42, 171, 198]. The set of forces must be selected carefully, in particular,

- the number of applied forces k must at least equal the number of sensor channels m; typically a redundant set is required (i. e., $k \gg m$) to minimize errors;
- the loads should be linearly independent;
- the loads should be of increasing magnitude, spanning the measurement range in order to ensure accuracy over the entire working range.

Using Eq. (4.21), the series of measurement can be written in matrix notation as:

$$C_S \cdot \begin{pmatrix} z_1^\mathrm{T} \\ z_2^\mathrm{T} \\ \vdots \\ z_k^\mathrm{T} \end{pmatrix} = \begin{pmatrix} l_1^\mathrm{T} \\ l_2^\mathrm{T} \\ \vdots \\ l_k^\mathrm{T} \end{pmatrix} \tag{4.23}$$

Each line of the load matrix $L \in \mathbb{R}^{6\times k}$ and the measurement matrix $Z \in \mathbb{R}^{8\times k}$ holds the applied loads $l_i \in \mathbb{R}^6$ and the associated strain gauge values $z_i \in \mathbb{R}^8$ of load case i, respectively. The total number of load cases is k. Using Eq. (4.23), the calibration matrix C_S is computed using the MOORE-PENROSE generalized inverse (pseudoinverse) of the measurement matrix Z:

$$C_S = Z^+ L\,. \tag{4.24}$$

The pseudoinverse Z^+ is then obtained accurately by singular value decomposition. Although mathematically simple and effective, least squares data fitting is very sensitive to random noise such as errors in load magnitude and orientation, measurement noise and numerical errors. On the other hand, it is well known that calibration accuracy depends on the number of different loads that are applied. Moreover, an accurate calibration requires the redundant measurement data to achieve a better signal-to-noise ratio. The whole calibration procedure is thus very time-consuming and costly, yet limited in accuracy.

The *shape from motion* approach proposed by VOYLES et al. [195] originates from machine vision. Calibration accuracy is comparable to least-squares methods, yet this method reduces the effort of load application. As the above methods, it relies on a high number of measurements but explicit knowledge of the applied loads is not necessary. The raw data are continuously gathered while a proof-mass is randomly moved by a manipulator. Only a small number of precisely known loads are required to establish the sensor reference frame and to relate the raw data. The calibration matrix is then recovered by singular value decomposition.

Load Application Procedure

The error of least squares calibration can only be minimized by exercising extreme care during load application, thus, incorporating a redundant set of loads is essential but very time-consuming. It is obvious to rationalize load application by employing a systematic procedure and specialized calibration equipment. SHIMANO and ROTH [171] installed a force sensor on the wrist of an industrial robot for in-situ calibration. The robot wrist was reoriented in various poses

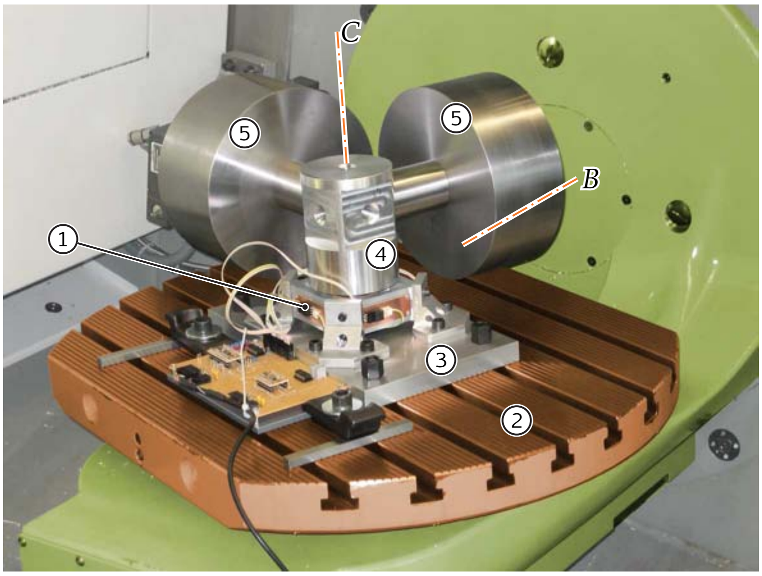

1	Force/torque sensor
2	Swivel rotary table
3	Loading fixture
4	Adapter
5	Proof-mass

(a) Calibration setup

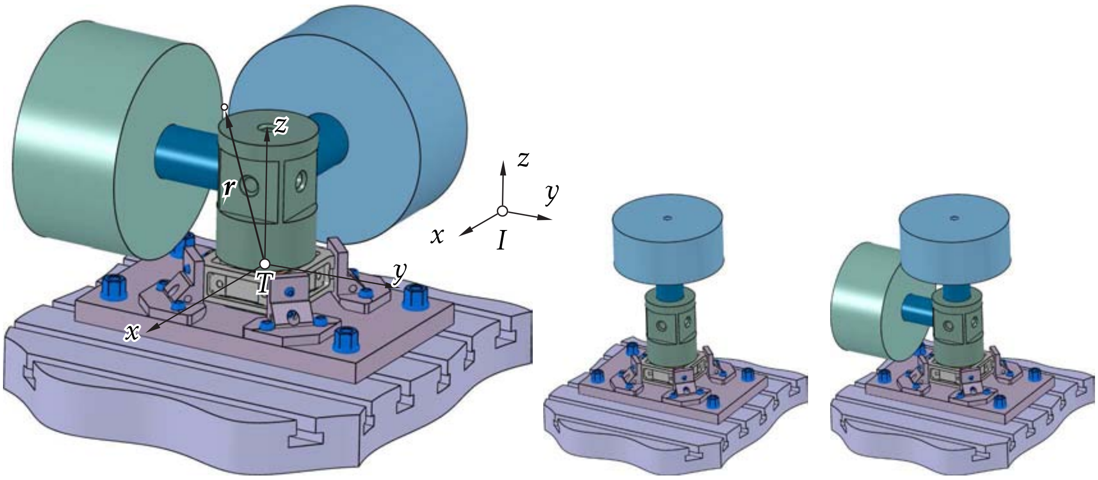

Configuration 1 Configuration 2 Configuration 3

(b) Proof-mass configurations

Figure 4.11: Setup for sensor calibration. *Above,* the loading fixture mounted on the swivel rotary table of a 5-axis milling machine allows the precise application of a highly redundant set of loads in a very efficient way; *below,* three different proof-mass configurations are used to span the working range of the sensor.

with known proof-masses attached to the sensor, so that the loads could be easily estimated. The accuracy of this procedure, however, was limited by the kinematic and positioning accuracy of the robot arm. Uchiyama et al. [189] applied various forces and moments by hanging known weights on a lever arm in different configurations.

The load application procedure proposed here aims at applying and recording a highly redundant set of load cases which should span the entire sensor working range in a very accurate and time-effective way. Load application was conducted in a semi-automated procedure on a 5-axis milling machine. High positioning accuracy of the CNC machine enables precise and efficient application of a highly redundant set of loads. Figure 4.11*a* shows the calibration setup. The F/T sensor (1) is mounted on the swivel rotary table (2) of the milling machine by loading fixture (3). Adapter (4) is bolted to the inner sensor flange. It provides five mounting surfaces for the proof-masses (5) so that different load configurations can be realized.

The procedure uses varying loads to determine the calibration matrix: three different proof-mass configurations (Figure 4.11*b*) that differ in their CoM positions with respect to the sensor frame, span almost the entire sensor working range. CoM positions are obtained from CAD data. For maximum accuracy all components of the calibration setup were weighed and adjusted in the CAD model. Depending on the proof-mass configuration, forces of approximately 500 N and moments up to 80 Nm can be applied. The orientation of the force vector is modified incrementally by rotating the loading fixture about the ${}_Tx$ and the ${}_Tz$ axis using the B-axis and C-axis of the swivel rotary table, respectively. Each sensor was calibrated using 162 measured values per configuration, making a total of 486 load cases. The recording took approximately 3 hours per sensor.

Calibration and Verification

The high positioning accuracy of the CNC swivel rotary table and the knowledge of all proof-mass CoMs allow the precise reconstruction of all load cases. Hence the calibration matrix $\boldsymbol{C}_S$ is obtained reliably from the least squares method. The position vector ${}_T\boldsymbol{r} = (r_x, r_y, r_z)^{\mathsf{T}}$ from the sensor frame origin to the proof-mass CoM is obtained from the validated CAD model (Figure 4.11 bottom). Using ${}_T\boldsymbol{r}$, each line of the load matrix $\boldsymbol{L}$ in Eq. (4.23) can be written as

$$\boldsymbol{l}_i = \begin{pmatrix} {}_T\boldsymbol{F}_i \\ {}_T\boldsymbol{M}_i \end{pmatrix}^{\mathsf{T}} = \begin{pmatrix} {}_T\boldsymbol{F}_i \\ {}_T\boldsymbol{r} \times {}_T\boldsymbol{F}_i \end{pmatrix}^{\mathsf{T}} = {}_T\boldsymbol{F}_i^{\mathsf{T}} \cdot \begin{pmatrix} 1 & 0 & 0 & 0 & r_z & -r_y \\ 0 & 1 & 0 & -r_z & 0 & r_x \\ 0 & 0 & 1 & r_y & -r_x & 0 \end{pmatrix} . \tag{4.25}$$

The force ${}_T\boldsymbol{F}_i$ acting on the sensor is obtained from the proof-mass weight m_l:

$${}_T\boldsymbol{F}_i = m_l \cdot \boldsymbol{A}_{TI} \cdot {}_I\boldsymbol{g} \, . \tag{4.26}$$

Here ${}_I\boldsymbol{g} = (0, 0, -g)^{\mathsf{T}}$ is the gravity vector with respect to the inertial frame I, $\boldsymbol{A}_{TI}$ the transformation matrix from the inertial into the sensor frame. $\boldsymbol{A}_{TI}$ depends on the spatial orientation of the CNC swivel rotary table which was recorded automatically during the load application procedure. Using the so obtained load matrix $\boldsymbol{L}$ and the measurement data matrix $\boldsymbol{Z}$, the calibration matrix is obtained from Eq. (4.24). Figure 4.12 shows the deviations of the measured values $\boldsymbol{l}_i^{\mathsf{T}} = (\boldsymbol{F}_i^{\mathsf{T}}, \boldsymbol{M}_i^{\mathsf{T}})$ from the actual loads $\hat{\boldsymbol{l}}_i^{\mathsf{T}} = (\widehat{\boldsymbol{F}}_i^{\mathsf{T}}, \widehat{\boldsymbol{M}}_i^{\mathsf{T}})$. $\boldsymbol{l}_i$ is calculated from Eq. (4.21), while the actual loads $\hat{\boldsymbol{l}}_i$ are obtained from Eq. (4.25). The errors of force and moment measurement are defined as:

$$\frac{\Delta \boldsymbol{F}_i}{\widehat{\boldsymbol{F}}_i} = \frac{\|\boldsymbol{F}_i - \widehat{\boldsymbol{F}}_i\|}{\|\widehat{\boldsymbol{F}}_i\|} \, ; \qquad \frac{\Delta \boldsymbol{M}_i}{\widehat{\boldsymbol{M}}_i} = \frac{\|\boldsymbol{M}_i - \widehat{\boldsymbol{M}}_i\|}{\|\widehat{\boldsymbol{M}}_i\|} \, . \tag{4.27}$$

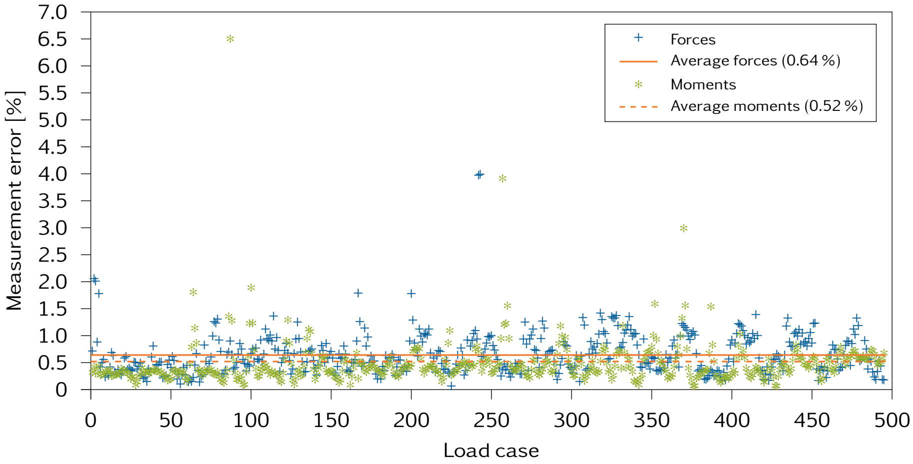

Figure 4.12: Verification of the least squares calibration

Deviations are calculated from the norm of vectorial difference between the calculated load and the theoretical wrench. In addition, the mean deviations provide information on the calibration accuracy of the proposed method. The achieved accuracy is 0.64 % and 0.52 % for force and moment measurement, respectively.

4.3 Contact Sensors

The segmentation of the foot into forefoot and hallux (cf. Section 3.9) yields an ambiguous contact state of the foot segments. In order to detect and disambiguate the contact state, four force-sensitive resistors are integrated into the contact elements of each foot. The signals are digitized using Schmitt triggers and transmitted to a local DSP module (see Section 5.2).

Knowledge of the contact state is necessary to calculate the ground reaction forces: during terminal stance and the swing phase, only the toe segment has ground contact but the force/torque sensor is located in the forefoot. Therefore, in addition to the toe joint angle, measuring the contact state helps to reliably determine the ground reactions. Moreover, contact sensors enable the implementation of event-triggered gait patterns.

4.4 Inertial Measurement System

The simulative study in Section 2.7.1 has shown that balance control is very sensitive to measurement errors of the upper body orientation. The IMS is thus one of the most critical components of the stabilizing system. It must show high accuracy and signal quality and long-term stability. The *overall* bandwidth of the sensor must be at least 40 Hz to 60 Hz.

Inertial measurement systems determine the orientation and angular velocity of a rigid body from its rotational and translational movements. Today's implementation of inertial measurement systems is in so-called *strapdown systems* where three mutually orthogonal arranged gyroscopes and accelerometers, respectively,

Table 4.3: Technical data of high-accuracy inertial measurement systems

Criterion	Unit	iMAR iVRU-FC-C167	Crossbow VG700CB	Crossbow IMU700CB
General				
Update rate	[Hz]	200	100	125
Weight	[kg]	0.8	1.6	1.6
Angular rate				
Sensor range	[deg/s]	±200	±200	±200
Short-term bias	[deg/s]	±0.003	±0.03	±0.03
Long-term bias	[deg/h]	±36	±20	±20
Scale error	[%]	<0.2	<2	<2
Linearity	[%]	<0.2	<1	<1
Resolution	[deg/s]	<0.001	<0.0025	<0.025
Bandwidth	[Hz]	200	>100	>100
Random walk	$[\mathrm{deg}/\sqrt{\mathrm{h}}]$	<0.02	<0.4	0.4
Linear acceleration				
Sensor range	[g]	±2	±4	±4
Short-term bias	[mg]	0.5	n/a	n/a
Long-term bias	[mg]	2.5	<12	<12
Scale error	[%]	<0.3	<1	<1
Linearity	[%]	<0.3	<1	<1
Resolution	[mg]	<0.1	<0.5	<0.5
Bandwidth	[Hz]	>200	>10	>75
Random walk	$[\mathrm{m}/\mathrm{s}\sqrt{\mathrm{h}}]$	<0.02	<0.1	<0.1

are fixed to that rigid body. Due to accelerometer and gyro errors, the measured angular rates and accelerations show an offset (bias) that results in integration drift. Even small errors in measurement are integrated into progressively larger errors in velocity and orientation. Integration drift can be compensated by measuring other states of the system. Any sensor can be used that provides speed or position information, such as a GPS receiver or magnetometer [56]. Similar to human beings that utilize the eyes to supporting the sense of balance, the stereo vision system of the robot can be utilized to provide the IMS with heading aiding information [108, 152]. The inertial measurement system for the robot can be realized by revising the customized IMS of the robot *Johnnie* [46] or by applying a commercial system.

The revision of the *Johnnie*-IMS includes the redesign of all signal processing electronics using simultaneous sampling of all sensors and oversampling. The sensor fusion algorithms are extended by, e. g., error models, heading aiding from optical flow. However, accelerometers and, particularly, gyroscopes with better performance are barely available. Only a few systems for aerospace and military applications were found. But these sensors are too expensive, compared to off-the-shelf IMS. In summary, revising the *Johnnie*-IMS is a very elaborate task. The high complexity and the tight project schedule implies that only existing technologies could be applied without any new scientific results.

On the other hand, an extensive market survey has revealed that several com-

Figure 4.13: Open-frame inertial measurement system iVRU-FC-C167 from iMAR Navigation

mercial IMS math the requirements of a humanoid robot. The technical data and accuracy of inertial measurement systems of similar performance are listed in Table 4.3. The most relevant criteria for comparison are:

Update rate: because the IMS is used within a closed control loop (sampling rate approximately 1 kHz), the update rate should be as high as possible.

Accuracy (bias, linearity, random walk): the long-term stability (bias) of the first system is lower than the other systems. However, comparing the other accuracy data, the iVRU system is expected to be of better performance.

Weight: the weight of the sensor is another decisive criterion. The weight of the first system is about 50 % of the other systems which is mainly due to the customized open-frame design.

The high-precision inertial measurement system iVRU-FC-C167 from iMAR Navigation [77] is built from fiber-optic gyroscopes and MEMS accelerometers. Fiber-optic gyroscopes are distinguished from other gyros (like MEMS) in very low noise, insensitivity against vibrations, high bandwidth, high zero-point stability, and the absence of g-dependent drift. For example, the noise of a fiber-optic gyro is one order of magnitude below the noise of a MEMS gyro. At an update rate of 200 Hz the system comprises the sensor fusion algorithms and internal error models. Also, it provides an open interface for heading aiding, e. g., by a GPS receiver, magnetometer, or optic flow. The IMS comes in a customized lightweight version weighing approximately 0.8 kg. A plastic cover protects the system mechanically. Figure 4.13 shows a photograph of the open-frame inertial measurement system *iVRU-FC-C167* from iMAR Navigation.

Figure 4.14 shows the mounting arrangement for the inertial measurement

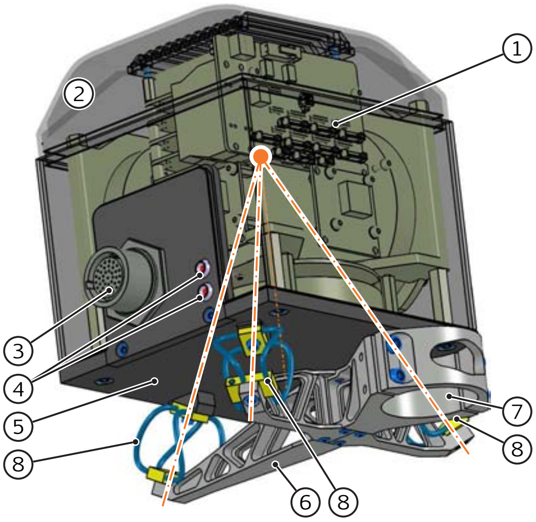

1	Inertial measurement system
2	Protective cover
3	Connector
4	Status LEDs
5	Sensor carrier
6	IMS support structure
7	Trunk connection
8	Shock absorber
●	CoM

Figure 4.14: Mounting arrangement for the inertial measurement system on the torso

system. The IMS (1) is mounted to the carrier (5) and protected by cover (2). The connector (3) provides all the necessary interfaces for data output and configuration. Two LEDs (4) indicate the status of the IMS. The support structure (6) which holds the entire IMS assembly is mounted on the upper body using the clamping (7). In the current setup, carrier (5) and support structure (6) are connected by three pillars (not shown). The IMS is exposed to a rather high dynamic environment. In order to account for possible measurement errors, the support structure is prepared for the installation of shock absorbers. A preliminary analysis of walking on the spot showed peaks at 46 Hz, 55 Hz and above in the frequency spectrum of the accelerometer and gyroscope signals. Since sensor fusion operates at a sampling frequency of 100 Hz, a low-pass filtering of the raw sensor data with a cutoff frequency of 50 Hz would be necessary to fulfill the sampling theorem. According to signal processing theory, however, the accelerometer and gyroscope signals cannot be filtered electronically. Therefore, it is be desirable to provide a mechanism for vibration isolation that attenuates shock and vibrational energy above 50 Hz. To this end, an isolation system can be interposed between the sensor carrier (5) and the support structure (6). The system consists of three wire rope isolators (8) that are capable of simultaneous shock and vibration attenuation in all axes, have good damping properties and a fail-safe construction. The shock absorbers (8) are arranged symmetrically with respect to the CoM of the sensor assembly. The resultant force of each element passes through the sensor CoM to avoid coupling modes. As a result of the external forces and torques, only translational motion (x, y, z) of the IMS occurs, but rotation (from equilibrium) about the coordinate axes $(\theta_x, \theta_y, \theta_z)$ is omitted.

4.5 Chapter Summary

This chapter introduced the sensor system. It is able to acquire the complete system state, except for the joint torques, and allows the implementation of model-based control schemes:

Joint sensors: each joint contains an incremental rotary encoder, an absolute angular sensor for link position sensing and a limit switch. The incremental rotary encoder is mounted on the motor shaft and mainly used for motor control. The absolute angular sensors on the output flanges allow direct measurement of the joint angles, compensating elasticity and nonlinearity. Furthermore, they enable the robot to start from arbitrary positions. For operational security and to prevent the robot from self-destruction each joint incorporates a limit switch.

Force/torque sensors: Each foot holds a custom-made six-axis force/torque sensor that is tightly integrated to the foot structure. The sensor comprises a monolithic transducer with four shear beams in a Maltese-cross arrangement. Thin membranes mechanically decouple beam deflections and reduce cross talk. The novel double-trapezoid beam geometry results in a uniform strain distribution over the sensing area and increases overall sensitivity significantly without reducing the transducer stiffness. An overload protection is integrated to protect the sensor from damage: mechanical end-stops engage into the force flux when exceeding a certain load and unload the sensitive measurement beams.

Contact sensors: to detect and disambiguate the contact state of the feet, four force-sensitive resistors are integrated to the contact elements of each foot.

Inertial measurement system: a high-precision inertial measurement system that is built from fiber-optic gyroscopes and MEMS accelerometers is employed to estimate the upper body orientation and velocity with respect to an inertial frame. The system is characterized by very low noise, insensitivity against vibrations, high bandwidth, high zero-point stability, and the absence of g-dependent drift.

5 Electronics Architecture

> *I'm completely operational and all my circuits are functioning normally.*
> —HAL *(2001, A Space Odyssey)*

A robust and high-performance computer system is crucial to the performance of the overall mechatronic system. This chapter briefly introduces the electronics architecture and its essential components. Based on the considerations and requirements developed in Section 2.8, the central control unit, local controllers and the real-time communication system are presented. The chapter concludes with an overview of the hardware security functions.

Electronics hardware development and programming are not part of this work: the DSP board was developed by Mathias Bachmayer, all other electronics by Georg Mayr. The hardware was tested and programmed by Valerio Favot.

As discussed in Section 2.8, the informational structure of the robot as an "intelligent sensor-actuator network" accounts for reducing the overall complexity.

Figure 5.1 gives a schematic overview of the electronics architecture. Although purely technologically motivated, similar hierarchical structures are found in biological systems, though of incomparably higher complexity. *Lola* is controlled by a central control unit mounted on the upper body and nine local controllers that are distributed over the robot. Fully decentralized control architectures are not suitable because of the highly coupled kinematics and dynamics: stabilization of global dynamics is therefore carried out by the central control unit. But low-level control of the link positions and velocities is shifted into local controllers. Concerning the electronics and control effort PMSM are considerably more elaborate than BDCM. Thus, closing the low-level motor control loops co-located with the actuators reduces the cabling effort and is expected to improve electromagnetic compatibility. Each local controller can handle up to three servo systems. Actual motor control is done on dedicated servo controller modules that are commanded by the local controllers using the CANopen protocol. The local controllers also account for sensor data acquisition and processing. In a sense of informational pre-filtering only relevant data are transmitted to the higher-ranking control layer. Gait generation and stabilization run fully autonomously on the on-board computer system without any support from outside. An external PC is used only for monitoring purposes and to give basic operating commands if the robot is not connected to the vision system. Due to high computing power requirements, vision processing is done on an external PC cluster.

Lola is mostly operated in the laboratory environment, so that energy is supplied from an external source for convenience. There are separate power supplies for the motors and electronics. The electronics power supply delivers a voltage of 48 V to the robot which is converted on-board into the voltages required for the CCU and peripheral components. The motors are rated at 80 V, except for the

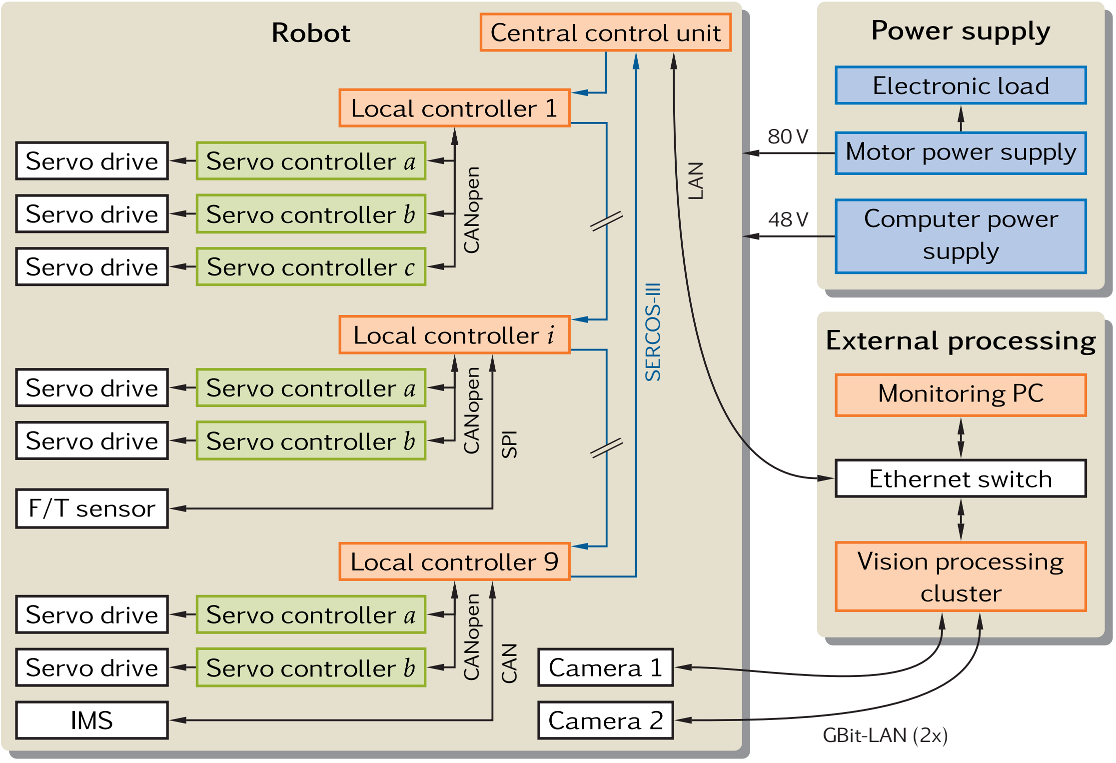

Figure 5.1: Overview of the electronics architecture

miniature head actuators that are supplied with 24 V. Head motor supply voltage is converted from the motor power supply. The motor controllers allow for operating the motors in four quadrants. Thus, decelerating a motor can induce current into the intermediate circuit, causing overvoltage. Therefore the motor power supply consists of a power supply and an electronic load, acting as current source and sink, respectively.

5.1 Central Control Unit

Trajectory generation and control of global system dynamics run on the CCU. A PC-based platform is chosen because of the standardized hardware, convenient programming and debugging, and high performance. It is based on an embedded Mini-ITX mainboard with Intel Core 2 Duo Mobile processor (T7600, 2.33 GHz), running the QNX real-time operating system. The concept of the "intelligent" sensor-actuator network requires only an interface board to the real-time communication system (Section 5.3) which is commercially available. An Ethernet connection handles data exchange with the external monitoring PC.

5.2 Local Controllers

Nine local controllers carry out data acquisition, signal processing and low-level motor control, unloading the CCU from these standard tasks. Off-the-shelf em-

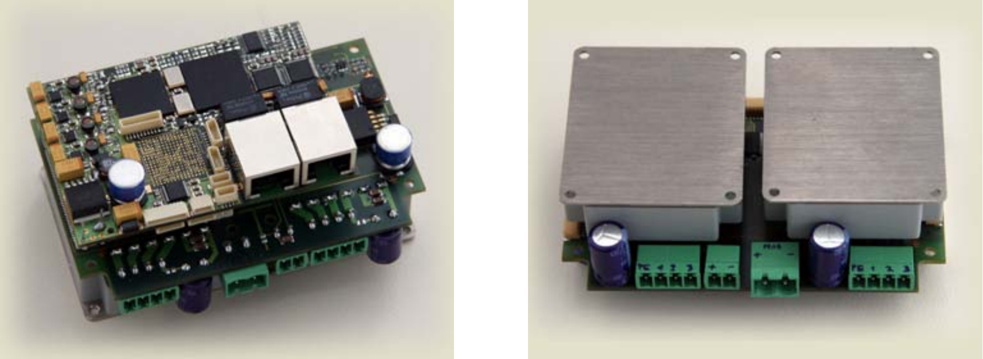

(a) Top view

(b) Bottom view

Figure 5.2: Decentral control electronics composed of the DSP board, interface board and two PCB-mounted Elmo servo controller modules

bedded systems in a small package that provide all necessary interfaces and functionality are not available, thus, a proprietary development is necessary. The small packaging goals and thus high integration density of the local controllers requires to design multi-layer PCBs, using SMD-technologies with tiny chips like ball grid arrays.

The design of the local controller modules follows a modular concept: the decentral electronics are divided into a universal DSP board with an interface to the real-time communication system. The DSP board is always used in combination with an application-specific interface board that provides all the necessary interfaces and connectors to sensors, motor controllers, etc. Actual motor control is done on dedicated servo controller modules by Elmo Motion Control [33] that are commanded using the CANopen protocol. The Elmo modules are distinguished by an extremely space-saving design and high power density due to the highly efficient inverter. They comprise a fully digital motion controller that features current, velocity and position loops, commutation alignment, gain scheduling modes and built-in error protection. For most motors the PCB-mounted *Whistle* module [33] is employed that weighs only 50 g and can support up to 20 A continuous and 40 A peak current. The maximum continuous power output is rated at 1.6 kW. The hip joint flexion/extension and knee motors are driven by *Guitar* servo controllers [33] that can deliver up to 25 A of continuous current and 50 A of peak current. Weighing only 165 g, the maximum continuous power output is 2 kW.

Figure 5.2 shows a photograph of the local controller, the key features are listed in Table 5.1. The DSP board is on top of the PCB stack and mounted piggyback to the interface board. One local controller can connect up to three motor controllers: two servo controllers are PCB-mounted to the bottom of the interface board and fixed to the robot structure with their base plates for optimal heat transfer. The third “satellite module” allows for tight integration of the controllers into the robot structure and near the servo actuators. For example, the toe joint is controlled by a satellite module housed on the shank, while the local controller is situated on the thigh. Handling up to three motors by one controller is particularly useful for multi-DoF joints because the inverse kinematics of the drive mechanism can

Table 5.1: Key features of the local controller hardware

DSP board	
CPU	DSP Freescale MC 56F8367
Communication interface	SERCON 100S core on Xilinx FPGA XC3S400
Quadrature Decoder	2 channels
PWM	2×6 channels
Data bus	16 bit parallel bus (address range up to 16 MB)
CAN	2 ports
RS 232	2 ports
SPI	1 port for up to 5 slaves
Analog input	4 analog low pass filters up to fourth order
RAM	Up to 8 MB SRAM mountable
Dimensions	80×55 mm^2
Mounting	Piggyback design
Interface board	
Motor controllers	2 Elmo Whistle modules (PCB-mounted), 1 CAN port (satellite module)
RS 232	2 ports
Absolute angular sensors	3 EnDat IP cores on Xilinx FPGA XC3S400
F/T sensor	1 port (SPI)
Electronics power supply	12 V DC (plus on-board regulators)
Motor power supply	80 V DC
Dimensions	100×64.5 mm^2
Mounting	Piggyback design

be calculated locally, making the kinematic structure of the robot transparent to higher control layers. For instance, the knee and ankle joints are handled by the same local controller which allows to compensate knee motion in the ankle joint mechanism (Section 2.6.3) without any cross-communication between the local controllers.

5.3 Communication System

The real-time communication system handles the entire data exchange between central controller running on the CCU and the local controllers. Being the only data interface to the robot hardware, it must support the cyclic exchange of actual and desired values, status and diagnostic messages, as well as the non-cyclic parameterization of sensors and drives. Besides the mandatory real-time capability, the communication system must operate in a deterministic manner. The bandwidth must be high enough to exchange all data throughout the system within one communication cycle, corresponding to the sampling time of the CCU of approximately 1 ms. The communication system should enable the testing of different controller structures, ranging from more centralized to fully decentralized signal processing concepts. In the first case only the current or velocity loop is closed in the drive. All other loops are implemented in the CCU, thus the required communication system bandwidth is considerably higher. The communication system should use ring, line or bus topology to reduced the cabling effort; systems using point-to-point cabling are not considered. For reasonable hardware development effort a commercial interface board must be available for the CCU. The physical interface of the local controllers should be available as ASICs or integrated into the microprocessor.

A number of different real-time communication systems [12] were evaluated, including CAN, FireWire, SERCOS and other proprietary implementations of real-time Ethernet. As a result, a communication system based on SERCOS turned out to be the most suitable solution.

Originating from the automotive sector, CAN-based communication systems are widely used in industrial applications, including motion control. Advantages of CAN are the easy setup and configuration of the bus structure and numerous standard CAN-devices (sensors, controls and drives), PC interface cards and diagnostic tools. The purely event-triggered communication in one major drawback of CAN, besides the rather low bandwidth of 1 Mbit/s. Hence peak loads can occur in cases of multiple simultaneous message transfer requests. However, such requests occur frequently in multi-axis control applications. The mechanism of bus arbitration ensures the priority-based transfer of all messages. But message transfer is generally non-deterministic because it cannot be guaranteed within a certain cycle. Using CAN in multi-axis control applications is therefore problematic. Many controls overcome these shortcomings by reducing the communication effort and longer cycle times. The trajectory generation is shared between the CAN host and the servo nodes. However, such approaches are insufficient for the impedance controlled ankle joints [18]. In this case long cycle times and trajectory interpolation by the servo nodes is not applicable. Rather, updating the desired position values within every cycle of the central control loop (approximately 1 ms) is important to achieve stability.

Originally targeted at consumer-electronic applications, IEEE 1394 (FireWire) is a serial bus with tree-like topology that connects nodes at data rates up to 800 Mbit/s. It supports asynchronous and isochronous transactions. Isochronous data transfer is used for data that require fixed, guaranteed bandwidth and deterministic submission. IEEE 1394 can handle up to 63 isochronous channels. Isochronous data are split into packets that are sent every 125 µs. *Cycle Start Packets* synchronize the clock cycles of all nodes to this 8 kHz clock. Because isochronous transfer does not retransmit lost or corrupted packets but delivers data at a constant rate, it is well suited for time-triggered communication in distributed control systems [38]. Moreover, the entire communication system can be built from cheap standard hardware and a variety of ASICs for interfacing the local controllers. Hardware drivers, however, for connecting the local controllers are currently not available. The in-house development is beyond the scope of this research.

The *SERCOS interface* [75] is an internationally standardized real-time communication system, targeting specifically at distributed motion control applications. It supports cyclic exchange of actual and desired values with a high bandwidth. Industrial applications include robotics, and tooling, paper and printing machines. SERCOS uses ASICs as bus controllers and fiber optics as the transmission medium.

Synchronization between the central control unit and the drives is realized by hardware with minimal jitter for accurate coordination of all drives. Likewise, all actual values are acquired simultaneously and the desired values become valid simultaneously. SERCOS communications uses Master Synchronization Telegrams (MST), Master Data Telegrams (MDT), and Amplifier Telegrams (AT) to send real-time information. For cyclic master-slave communication each drive (slave) has its own time slot assigned to transfer data to the central controller (master). SERCOS also supports configurations where multiple motors are assigned to a single slave. Such setups are particularly useful for the parallel mechanisms of the ankle joints. SERCOS includes a non-cyclic channel (service channel) to transfer communication data, parameters and diagnostic data. The service channel allows the parameterization of the drives, gain scheduling and switching between different operating modes.

The current standard *SERCOS-III* [76] combines the communication and synchronization mechanisms described before with Ethernet physics and twisted-pair copper cable. In addition to the cyclic real-time and the non-cyclic service channel, an IP channel can be added for transfer of non-real-time data without affecting the real-time data exchange. Both real-time telegrams and IP channel telegrams are embedded into standard Ethernet frames. SERCOS-III does not add a new protocol to the standard Ethernet stack but puts Ethernet under control of the motion bus in order to achieve a high level of determinism. Typical standard Ethernet networks use the star topology with all devices connected to a central switching device. As many other real-time Ethernet solutions SERCOS-III has line or ring topology to reduce cabling. To permit these bus topologies with switched Ethernet, a switch is needed in every connected node [36]. Due to the greater bandwidth of Ethernet, SERCOS-III can connect a large number of slaves at cycle times down to 31.25 μs. Thus, it is possible to implement both decentralized drive concepts where all control loops are closed in the drive, and centralized signal processing concepts where only the current loop is closed in the drive and all other loops are implemented in the central controller. The open standard allows to add data types for connecting the force/torque sensor and the inertial measurement system to the communication system. To summarize, SERCOS-III provides the following advantages:

- Time-slot mechanism for collision-free real-time communication
- High efficiency of the communication protocol
- Transfer of real-time and non-real-time data
- Identical topology, telegram structure and synchronization as former SERCOS implementations
- Capable of cross-communication between the slaves
- Connects to proprietary devices by adding SERCOS data fields (force/torque sensors, inertial measurement system)

At the time of writing (March 2010), the implementation of the SERCOS-III communication system on the robot not finished yet. Instead, a CAN-based system with eight parallel buses enabling point-to-point connections to the local controllers, was used in order to speed up the first-time operation of *Lola*.

5.4 Security System

Regarding actuator performance and body size, the robot is a very dangerous machine and can cause severe injury. In order to protect the operators, environment and robot, several security functions are implemented. Effectiveness, reliability and reaction time of software-based security functions is limited compared to hardware-based systems. On the other hand, software-based solutions can be triggered by certain states throughout the program flow. Moreover, certain functionality cannot be implemented in hardware: for example, the allowed angular workspace of the two-DoF ankle joint mechanism (Section 2.6.3) is non-rectangular. Thus, is cannot be limited by limit switches in the two rotational axes but must rely on monitoring of the actual and desired values by software. In conclusion, the combination of both software and hardware-based security systems is the most reasonable approach. Possible hardware-triggered events include:

- Motor overcurrent
- Over and undervoltage of the motor intermediate circuit voltage
- Motor and inverter over-temperature
- Angular range of the joints

In addition, there is an emergency stop circuit with several switches. In case of failure, the operator can disable the motor power supply. CCU and local controllers are supplied independently for simplified debugging.

6 Lessons Learned

> *To regret one's own experiences is to arrest one's own development. To deny one's own experiences is to put a lie into the lips of one's life. It is no less than a denial of the soul.*
>
> —Oscar Wilde

In this chapter a series of recommendations for work related either specifically to the humanoid robot *Lola* or other bipeds is given based on the author's experiences in the course of completing the research contained in this thesis.

6.1 Conceptual Issues

Body Size

Due to the tight schedule, it was not possible to investigate the influence of body size on the walking performance. The proportions of *Lola* are thus equal to the robot *Johnnie*. In order to make the robot more human-friendly, the author proposes to consider a reduction in body size. Moreover, smaller robots are easier to handle and less dangerous to the operators and experiments are simplified. On the other hand, the stride length reduces with the leg length and leads to lower walking speeds or higher joint velocities due to increased step frequencies.

Arm Movement

Leg advancement yields high moments about the contact normals which must be compensated to avoid slippage. An effective counterforce is created by moving other body parts opposed to leg advancement. Possible approaches are the upper body rotation or arm swing. Arm movement is thus essential for fast locomotion. The shoulder adduction/abduction joints and the newly introduced elbow joints greatly improve the effectiveness of arm swing. In this configuration, however, the movements of the arm endpoints are not fully decoupled from the upper body orientation. The elbow joints permit translational movement of the arm endpoints in the sagittal plane. In the transverse plane, however, mainly rotation about the pelvis joint occurs, again yielding moments about the contact normals. Therefore, an additional internal/external rotation joint in the upper arms is proposed to enable translational arm movement in the transverse plane.

Knee Kinematics

Flexion/extension of the human knee is not a simple hinge movement, rather, it performs a rotary-gliding motion: the instantaneous center of rotation moves upward and backward during flexion. Prosthetic knee mechanisms try to resemble human knee kinematics, for example by four-bar linkage mechanisms. Such mechanisms are designed for minimal energy consumption during stance [148].

The angular range of the knee joint is sufficient for walking and running. For other movements such as kneeling down, getting up or passing through narrow spaces larger flexion angles would be useful. One approach to extend the motion range would be to apply such a four-bar linkage mechanism to the knee joint. Moreover, such a mechanism can further reduce actuator performance if designed for the load profiles typical gait patterns. However, this mechanism cannot be combined with the ankle joint drive mechanism developed in Section 3.8.3.

6.2 Mechanical System

The redundant kinematic structure with seven-DoF legs, the consistent lightweight construction, a modular joint design with high power density and improved mass distribution of the legs are the distinguishing characteristics of *Lola*'s mechanical system.

Lightweight Design

Lightweight design and high effective stiffness of the mechanical structure obviously contribute to better robot performance. To this end, manufacturing major structural components by investment casting has proven advantageous for achieving sophisticated designs with good dynamic characteristics and low weight. Due to high manufacturing effort and cost, it is advisable to design these components for high-cycle fatigue to avoid failure. Thus, the only way of reducing the weight would be to reduce the loads that act on the robot, for instance by reducing the body size or further reducing the moving masses. Alternatively, other materials with higher specific stiffness could be used, e. g., fiber-reinforced polymers.

Actuator Performance

These considerations go along with lower actuator performance: lighter mechanical structures yield smaller motors and transmissions and, thus, additional weight savings. The servo actuators of *Lola* provide enough reserve capacity for implementing various walking patterns. On the other hand, the performance of the servo actuators is strictly constrained by the general weight restrictions. The robot *Lola* provides a reliable platform for evaluating performance and overloading capacity of the PMSM. The experimental results can help tailoring motor performance to the actual needs of a next-generation robot.

Foot Dynamics

In the author's opinion, refining on the mass distribution of the legs is by far more significant. The evaluation of dynamic performance in Section 3.12.2 suggests that actuator relocation is a suitable strategy to improve dynamic performance of the system. The analysis also shows that the active toe joint contributes substantially to resultant leg inertia. Despite the difficulties to finding suitable drive mechanisms, actuator relocation of the active toe joint would considerably reduce leg inertia. It is further proposed to compare active and passive toe joints regarding their functionality in typical gait patterns. Passive toe joints should be chosen over active ones if they are equal in effectiveness due to the obviously lower weight and complexity.

Unfortunately, there is almost no relevant literature on the design of robotic feet. Developing an ultra-lightweight foot concept that enables the robot to walk on uneven terrain notwithstanding offers great potential for improving the walking performance and further reduction of the resultant leg inertia.

6.3 Sensor System

With more than 50 sensors, the sensor layout of the robot *Lola* is rather complex. For example, light barriers were applied to the robot *Johnnie* for angular referencing of the joints. For *Lola*, they are replaced by absolute angular sensors, enabling direct measurement and control of the joint angles. Although the sensor count remains constant, complexity of the electronics increases due to the proprietary sensor interface. In summary, these sensors are nonetheless useful, especially with regard to future applications in the human environment.

Joint Torque Measurement

The sensor layout of *Lola* is capable of acquiring the complete system state, except for the joint torques. Integrating torque sensors to the leg joints—at least the sagittal plane joints—would enable active compliant control and establish a basis for evaluating more sophisticated, model-based control schemes. Thus, the robot could be operated in position, velocity and torque mode. Active servo compliance could help to attenuate the landing impacts more effectively. Moreover, active control of the leg stiffness would allow the evaluation of biomechanical models on a fully actuated humanoid robot. Another aspect of joint-level torque sensing is related to safety. *Lola* is able to exert very high forces that can lead to severe injuries. While the risk is controllable within the laboratory environment, additional measures are required when the robot is to interact with humans, sharing the same workspace: for example, a collision detection based on joint-level torque measurement would lead to much lower risk of injuries.

Various approaches to joint-level torque measurement for the different joint types exist that differ in the modification effort. Rather simple solutions apply to the knee and ankle joints: torque measurement in the knee joint is enabled by applying strain gauges to the immersion tube (output link, see Figure 3.19) to measure the tension and compression forces. Similarly, direct torque control of the ankle joint is possible by integrating load cells into the coupler links (cf. Figure 3.21). For example, calibrated off-the-shelf piezoelectric force links could be applied. They are lightweight and compact, and very sensitive to tension and compression forces. Applying torque sensors to the flexion/extension joint of the hip and other Harmonic Drive-based rotary joints is more involved: it can be accomplished by integrating force transducers into the output flange, or measuring torsion of the gear housing.

Better Signal Quality and Accuracy

Local digitization of the force/torque sensor has reduced the measurement noise significantly. To further improve signal quality and accuracy it is proposed to use simultaneous sampling A/D converters for proper data synchronization. High resolution sigma-delta (Σ-Δ) converters should be used as they provide better dynamic accuracy and eliminate phase errors. Σ-Δ converters allow the direct digitization of the strain gauge bridges without the need for additional external signal conditioning circuits.

6.4 Electronics Architecture

The main intention in the design of the electronics architecture was to unload the central controller from hardware-related tasks such as data acquisition and motor control. Moreover, less and smaller cable harnesses throughout the system were expected by replacing the complex point-to-point cabling of sensors and actuators by bus systems for communication and energy supply.

Cabling

All joint sensors are incorporated in the rotary servo actuators (Section 3.4.2). Since the local controllers are co-located with the actuators a single cable harness is needed to connect servo actuator and controller. For assembly convenience, however, individual cables were used for the sensors and motor. In consequence, the cabling of the robot more complex than expected due to the high number of different sensors. It is therefore proposed to reduce the cable harnesses by using one composite cable per joint. For instance, single strands could be combined with a heat shrinkable tubing. This measure not only improves the appearance of the robot, rather, it leads to weight savings and higher reliability. Furthermore, all cables should be fitted with strain relief clamps as the miniature wire-to-board connectors may easily loose contact due to vibrations and cable bending.

Local Controllers

Different interfaces for sensors and the real-time communication system made the development of custom hardware necessary. The strict packaging goals involved a substantial development effort to implement the decentral electronics. For future developments, it is proposed to use off-the-shelf electronics hardware whenever possible in order to achieve robust, EMI-resistant[1] designs at reduced development effort. In the meantime, several compact bus nodes for connecting to real-time Ethernet became commercially available. Combined with a powerful microprocessor module that incorporates all essential circuitry such as RAM, Flash memory and standard communication interfaces, only an interface board comprising application-specific peripherals must be developed.

---

[1] Electromagnetic interference

7 Conclusions and Future Work

> *Wer am Ende ist, kann von vorn anfangen, denn das*
> *Ende ist der Anfang von der anderen Seite.*
> —Karl Valentin

Humanoid robots are a new and promising application area for robotics. Bipedal locomotion is considered one of the core technologies. All current full-size humanoids are capable of stable dynamic walking but few are able to walk—or even run—at speeds comparable to humans. Moreover, flexible motion generation in realistic environments still remains challenging. Aiming at fast and autonomous bipedal locomotion, the development of the humanoid walking robot *Lola* wishes to make an important step towards this goal. Besides the challenging control problems, fast bipedal locomotion puts high demands on the robot hardware—an aspect which is often neglected or de-emphasized.

This thesis deals with the design and realization of the robot's mechatronic system. The issues covered include the mechatronic design concept, electrical drive systems, design and analysis of the mechanical structure, sensor technology, and contributions to the computer and electronics architecture.

The mechatronic system "humanoid walking robot" is characterized by a high complexity. Here the systematic procedure adopted throughout the development has proved to be successful. It is based on the virtual development of the complete system prior to manufacturing actual hardware, using 3D-CAD and validation by finite element analysis. The load profiles of the mechanical structure and actuators are calculated with the comprehensive robot simulation model developed within the sub-project "Simulation and Control."

The robot has a kinematic structure with 25 actuated degrees of freedom in a redundant configuration which allows more natural and flexible gait patterns. In particular, actuated toe joints enable rolling the feet from heel to toe and reduce the loads of other leg joints, compared to the standard leg configuration.

The mechanical structure is characterized by the consistent lightweight design with high effective stiffness and natural frequencies. To this end, design proposals for some components are created by topology optimization and the major links are designed as aluminum investment castings in a Monocoque-like structure. Numerical modal analysis is adopted to assess the dynamic properties of the mechanical structure. The elastodynamic behavior of the drive mechanisms is analyzed to avoid resonance oscillations and achieve high enough bandwidths and fast response times of the speed control loops.

The joint drives form a basis for high dynamic performance and acceleration behavior of the robot. The powerful yet lightweight servo actuators combine a high-dynamic brushless servo motor with precision gearing and sensors into a compact package. While most joints are driven through Harmonic Drive gears, the knee and ankle joints employ linear actuators using planetary roller screws.

Special attention is paid to the dynamic capabilities of the locomotor system. The drive mechanisms of the knee and ankle joints place the actuators in the hip-thigh area to minimize inertial contribution. Driving the ankle joint in a parallel arrangement results in a more uniform load distribution among the actuators and reduces the average motor loads significantly. As a result, superior acceleration behavior and reduced effects of varying inertia are achieved, compared to other leg architectures. In addition, the center of mass height is increased which reduces the angular momentum about the fore-aft axis and, ultimately, enlarges the stability margins available for balance control.

The dynamic performance is further affected by the kinematic constraints associated with unilateral foot-ground contact. The foot dynamics concept therefore ensures reliable contact on different surfaces. The feet further incorporate viscoelastic contact layers and passive heel segments with hydraulic shock absorbers for effective impact attenuation at initial contact.

The sensor layout supports the implementation of model-based control algorithms. Absolute angular sensors are employed for direct measurement of the joint angles, compensating compliance and nonlinearity in the drive mechanisms. The high-precision inertial measurement unit with fiber-optic gyroscopes and MEMS accelerometers estimates the orientation and angular velocity of the upper body. Furthermore, the ground reaction forces and moments are measured by customized six-axis force/torque sensors.

The "intelligent" sensor-actuator network with central control unit improves system performance from a technological point of view. The central control unit accounts for trajectory planning and balance control. Low-level motor control and sensor data acquisition and signal processing are done on nine decentral controllers. The Ethernet-based real-time communication system SERCOS-III handles the data exchange between all controllers with minimal latency.

Unfortunately, the early stage of experimental evaluation does not allow the final assessment of the robot's capabilities. First results nevertheless look very promising. At the time of writing, *Lola* is able to walk at a maximum of 3.34 km/h, which makes it the fastest anthropomorphic humanoid walking robot. According to publicly available data, *Asimo* achieves a walking (not running!) speed of 2.7 km/h, all other bipeds are slower. Only *PETMAN* can walk as fast as 7.08 km/h, however, this robot does not have anthropomorphic leg kinematics (cf. Section 1.1.1). Up to now the locomotor system has proven to be extremely dynamic and seems to have excellent acceleration behavior. These preliminary results support the hypothesis that the proposed approach of low-inertia leg design provides significantly improved agility, compared to traditional designs. Furthermore, the high quality of the sensor signals is noteworthy. In particular, the balance controller benefits from the very low noise and high accuracy of the inertial measurement system and force/torque sensors. It is not easy to quantitatively assess the notion of "human-like" or "natural" gait. In the author's opinion, the redundant kinematic structure with toe joints allows for a more human-like or natural looking gait. It is left to the reader to view the videos of walking that are available on the project website[1] for an independent assessment.

---

[1] `http://www.amm.mw.tum.de/`

The robot provides a reliable basis for the evaluation of different control approaches. In particular, the combination of vision system, mechatronics and balance control give the robot a high degree of autonomy. At the *HANNOVER MESSE 2010*, *Lola* was presented with a vision and path planning system developed by the Institute of Autonomous Systems Technology[2], University of the Bundeswehr, München. The robot worked well and without considerable failure during more than 25 demonstrations of vision-guided autonomous locomotion and obstacle avoidance.

Future Work

Regarding the robot's bipedal walking capabilities, the following recommendations for future work can be made.

The author believes that the further development of the foot dynamics concept, Section 2.3, can make a significant contribution towards the goal of human-like versatile locomotion.

Despite their importance for gait generation, the analysis in Section 3.12.2 has shown that the active toe joints counteract the low-inertia design of the legs. Aiming at the development of ultra-lightweight feet, it is proposed to compare active and passive toe joints with regard to their functionality in typical gait patterns. Different concepts of passive toe joints should be evaluated, and passive toe joints should be preferred if they are equal in effectivity to active toe joints. The viscoelastic contact elements are crucial to the performance of ankle joint torque control. Therefore, the systematic analysis and comparison of different materials for shock attenuation and contact geometries is proposed. Finally, the feet should be equipped with mechanisms for walking on uneven terrain.

Although reliable bipedal and autonomous locomotion are fundamental skills, humanoid robots must have extended capabilities in order to be useful and commercially successful. Possible extensions of the robot involve, for instance:

- The integration of manipulation capabilities (i. e., full arms and hands)
- Energy autarky
- Autonomous locomotion in more complex and realistic scenarios
- The implementation of safety features for human-robot interaction

---

[2] `http://www.unibw.de/lrt8/`

Appendix A

Anatomic and Biomechanical Fundamentals of Human Locomotion

Three basic reference planes are used in human anatomy that are shown on the left of Figure A.1. Note that the same notation is used for planes that belong to the total body or are fixed to a single link. The *sagittal plane* is the longitudinal plane of symmetry (xz-plane) which extends from the front to the back of the body or single link, dividing it into left and right portions. The sagittal plane runs through the total or link CoM. The *coronal plane* is orthogonal to the sagittal plane and runs through the CoM and divides the body or single link into anterior and posterior sections (yz-plane). The *transverse plane* is orthogonal to the sagittal and coronal plane and, running through the CoM, separates the body or a single link into superior and inferior parts (xy-plane). The relative movement of body structures is described with respect to these reference planes as shown on the right of Figure A.1. The rotation of a link about an axis perpendicular to the coronal plane is called *flexion/extension*. Flexion decreases the angle between two parts, and extension increases it. For the ankle joint, these movements are called *dorsiflexion* and *plantarflexion*; using the common notation for camera movement, these rotations of the camera head are called *tilt*. *Adduction* and *abduction* describe the rotation of a link about an axis that is orthogonal to the coronal plane. Adduction pulls a link away from the midline, abduction pulls a structure or part towards the midline of the body. *Internal/external rotation* describes the rotation of a link about an axis perpendicular to the transverse plane. Internal and external rotation turn a link inwards or outwards, respectively. For the camera head, this movement is called *pan*.

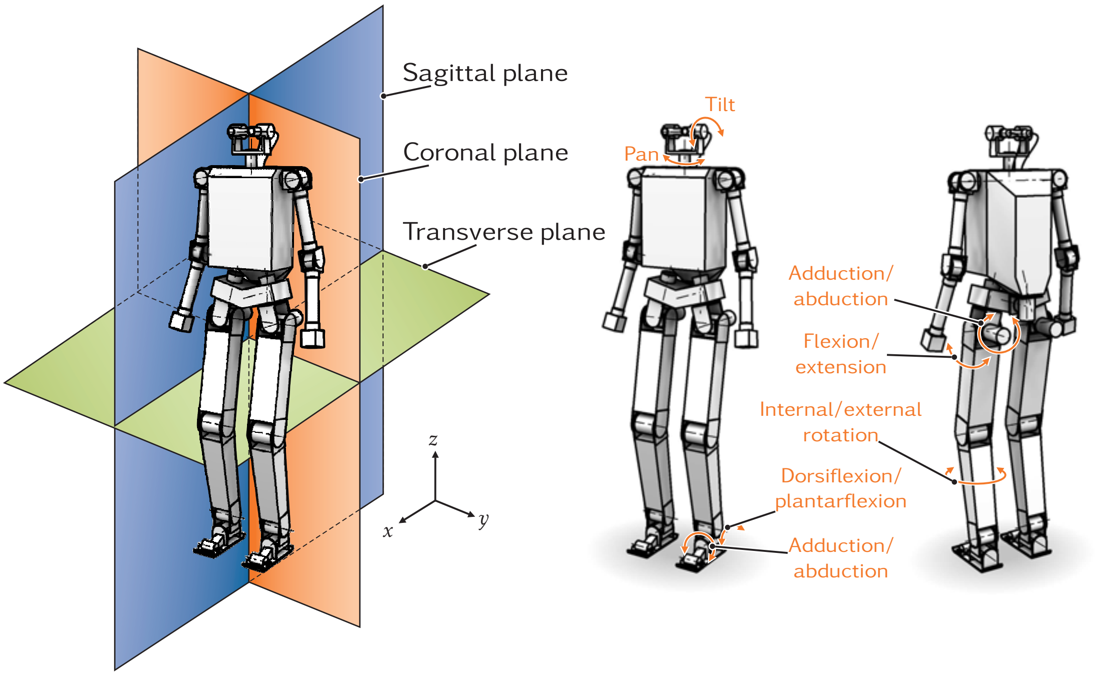

Figure A.1: Reference planes in human anatomy (left) and movement of body structures (right)

Appendix B

Main Dimensions

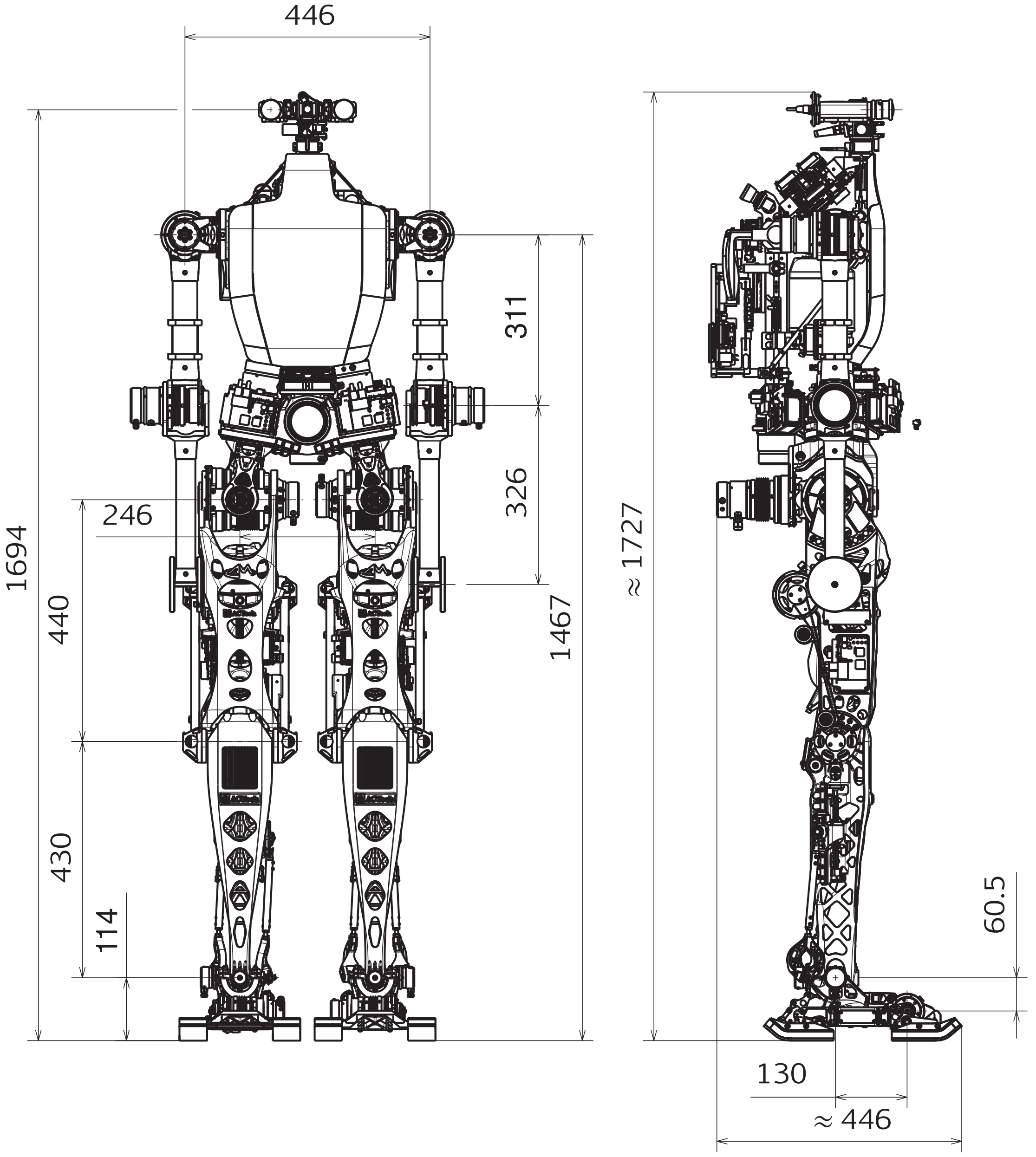

Appendix C

Technical Data of the Joint Actuators

C.1 Mechanical

				Load rating		Gear	
Drive	Mass $m\,[\mathrm{kg}]$	Motor inertia $J_m\,[\mathrm{kgm}^2]$	Top speed $\dot{\varphi}_{l,max}\,[\mathrm{rad/s}]$	Continuous $\tau_{l,avg}\,[\mathrm{Nm}]$	Peak $\tau_{l,max}\,[\mathrm{Nm}]$	Type	Ratio $N\,[-]$
Rotary actuators based on harmonic drive gears (cf. Section 3.4)							
A	3.010	$1.814{\cdot}10^{-4}$	12.06	122^{*}	243^{*}	CSG-32	50
B	1.438	$4.598{\cdot}10^{-5}$	8.16	$108^{\dagger}$	$284^{\dagger}$	HFUC-25	100
C	1.522	$4.598{\cdot}10^{-5}$	8.16	$108^{\dagger}$	$284^{\dagger}$	HFUC-25	100
D	0.933	$1.960{\cdot}10^{-5}$	8.16	78^{*}	$147^{\dagger}$	HFUC-20	100
E	1.082	$2.375{\cdot}10^{-5}$	8.16	78^{*}	$147^{\dagger}$	HFUC-20	100
F	0.973	$1.385{\cdot}10^{-5}$	9.17	$54^{\dagger}$	$110^{\dagger}$	HFUC-17	100
G	0.531	$3.809{\cdot}10^{-6}$	10.68	24^{*}	48^{*}	CPL-14	100
Linear actuators based on planetary roller screws (cf. Sections 3.8.2 and 3.8.3)							
Knee	1.931	$5.544{\cdot}10^{-5}$	10.68	$\leq 189^{*}$	$\leq 378^{*}$	RGTF-12×5	≤ 72
Ankle	0.516	$1.544{\cdot}10^{-5\ddagger}$	10.68	$\leq 115^{*}$	$\leq 230^{*}$	RGTF-8×5	≤ 70
Stereo camera head actuators (cf. Section 3.5)							
Pan	0.237	5.00·10–7	8.90	0.90	7.50	CSF-11	100
Tilt	0.066	$7.310{\cdot}10^{-8}$	10.47	0.44	$1.40^{\dagger}$	RSF-5A	100
Vergence	0.031	$1.170{\cdot}10^{-8}$	10.47	0.11	$0.30^{\dagger}$	RSF-3B	100

* Limited by inverter current

† Limited by gear rating

‡ Only motor, motor-side transmission components are not considered

C.2 Electrical

		Torque rating		Constants		
Drive	Motor type*	Continuous $\tau_{m,c}$ [Nm]	Peak $\tau_{m,p}$ [Nm]	Torque K_τ [Nm/A]	Motor K_m [Nm/$\sqrt{\text{W}}$]	Time T_{el} [ms]
Rotary actuators based on harmonic drive gears (cf. Section 3.4)						
A	PB K375100-4D	3.0	4.85†	0.097	0.267	1.53
B	PB K064075-7Y	0.85	2.56	0.130	0.122	1.60
C	PB K064075-7Y	0.85	2.56	0.130	0.122	1.60
D	PB K064050-9D	0.62	1.56†	0.078	0.087	0.96
E	PB K064025-GD	0.31	0.93	0.080	0.048	0.58
F	PB K064025-GD	0.31	0.93	0.080	0.048	0.58
G	PB K044025-JY	0.12	0.48	0.095	0.020	0.39
Linear actuators based on planetary roller screws (cf. Sections 3.8.2 and 3.8.3)						
Knee	PB K375050-5Y	1.72	5.14	0.105	0.153	1.45
Ankle	PB K064050-8Y	0.62	1.87	0.109	0.087	1.15
Stereo camera head actuators (cf. Section 3.5)						
Pan	WI MSSI 022H-017C	0.025	0.09†	0.009	0.075	0.10
Tilt	HD RSF-5A	0.004	0.014	0.011	0.008	0.32
Vergence	HD RSF-3B	0.001	0.003	0.038	0.023	0.13

* PB = Parker Bayside [141]; HD = Harmonic Drive [60]; WI = Wittenstein [202].

† Limited by inverter current

Appendix D

Load Profiles

The reference gait pattern for the dimensioning of the mechanical system has been determined by BUSCHMANN using his multibody simulation model of the robot (Section 3.3.1). The following gait parameters were used:

Walking speed	5.55	km/h
Step length	0.54	m
Step frequency	2.86	Hz
Double support phase	15.0	%
CoM (upper body) height	1.15	m

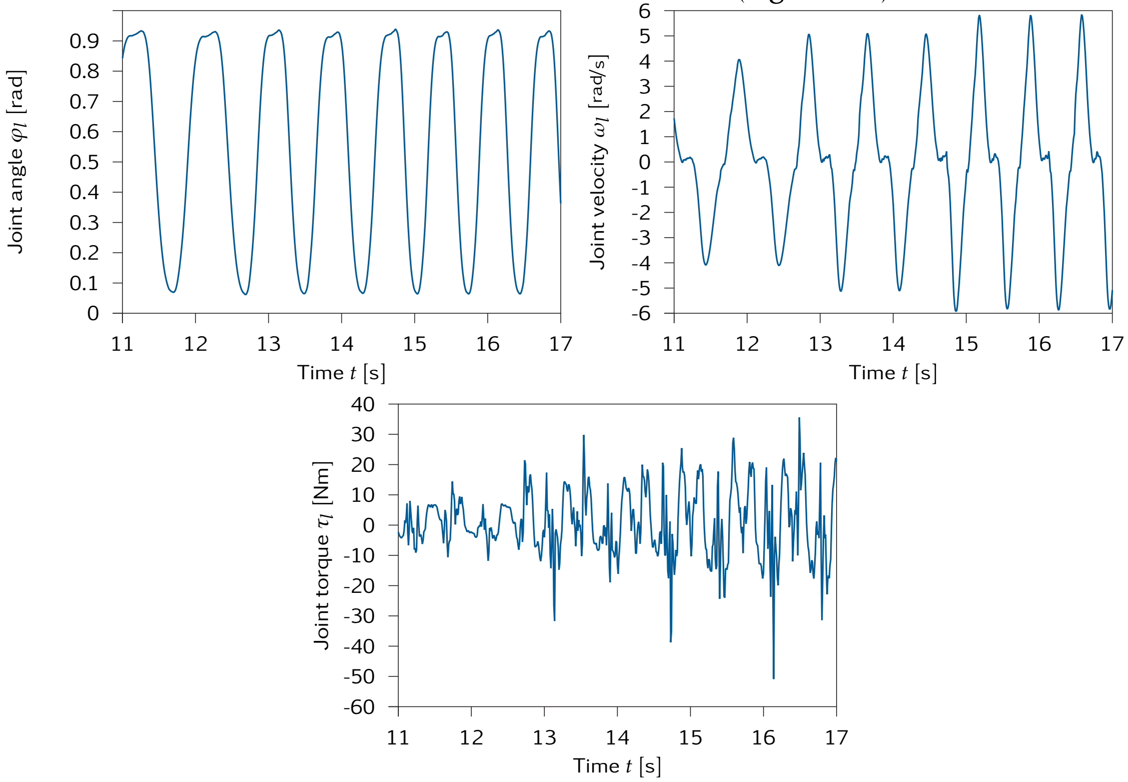
Shoulder flexion/extension (right arm)

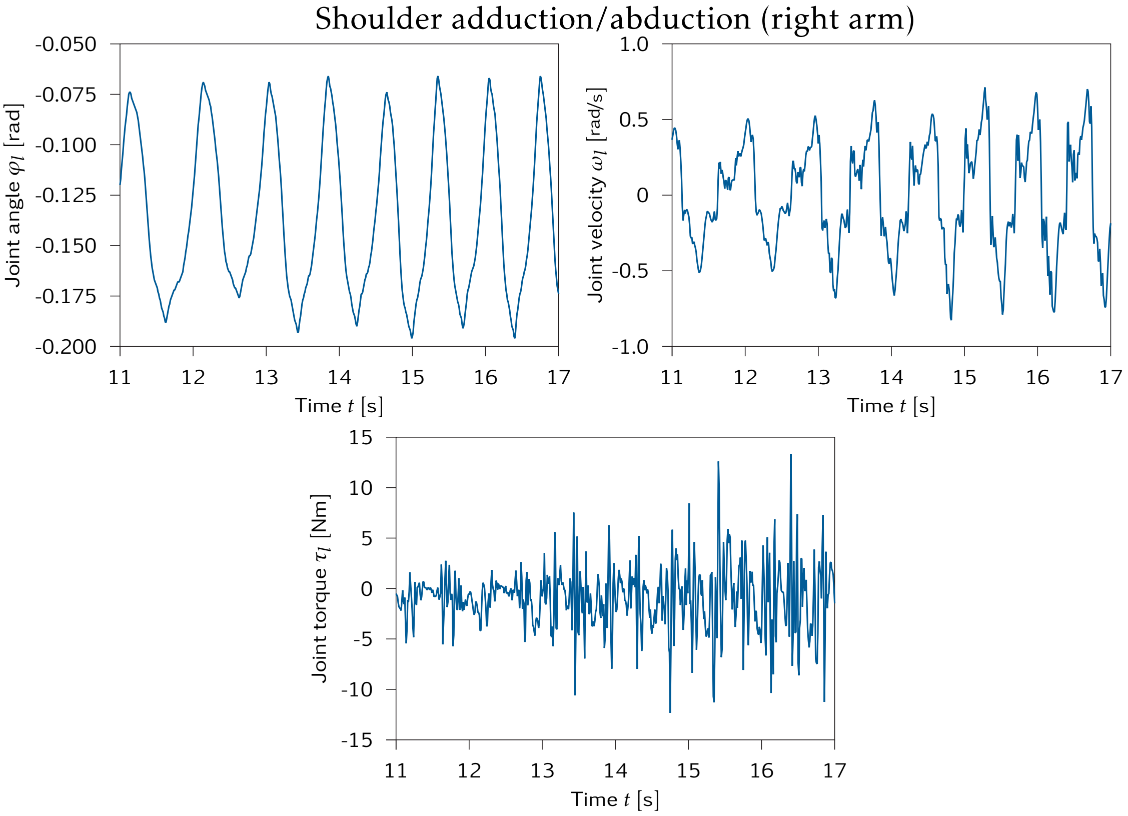
Shoulder adduction/abduction (right arm)

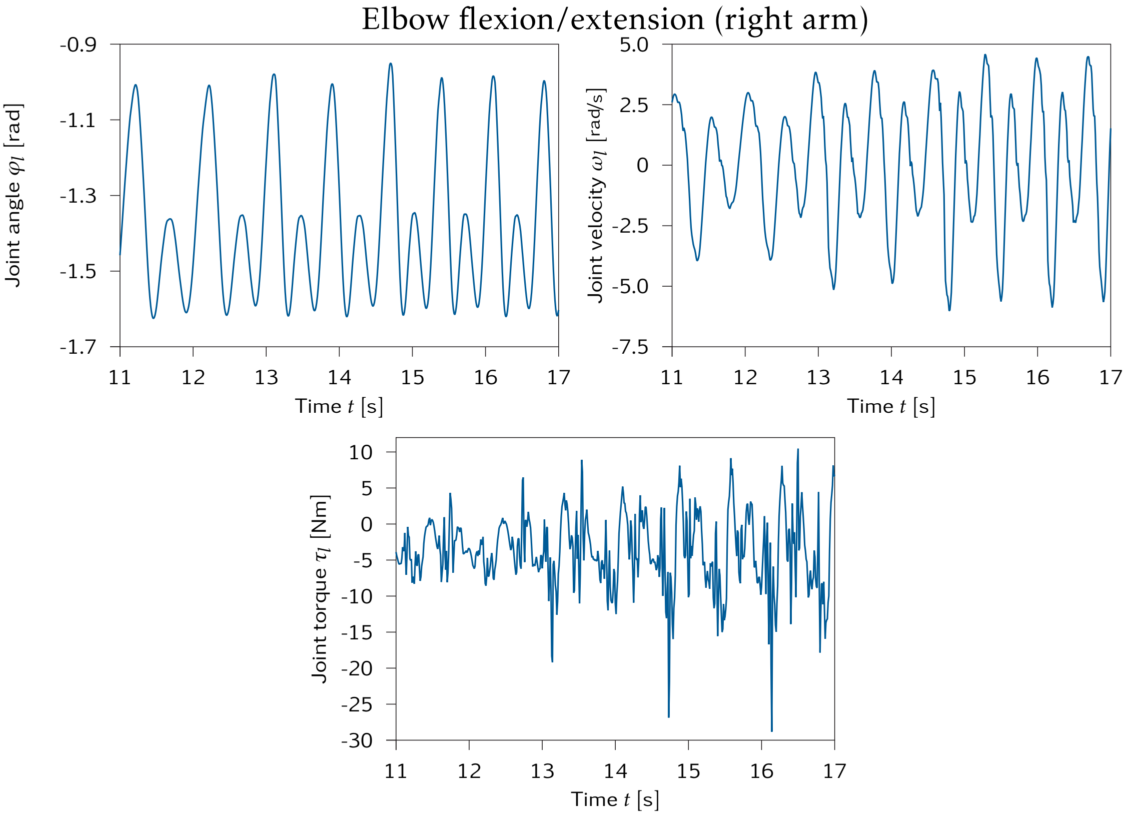
Elbow flexion/extension (right arm)

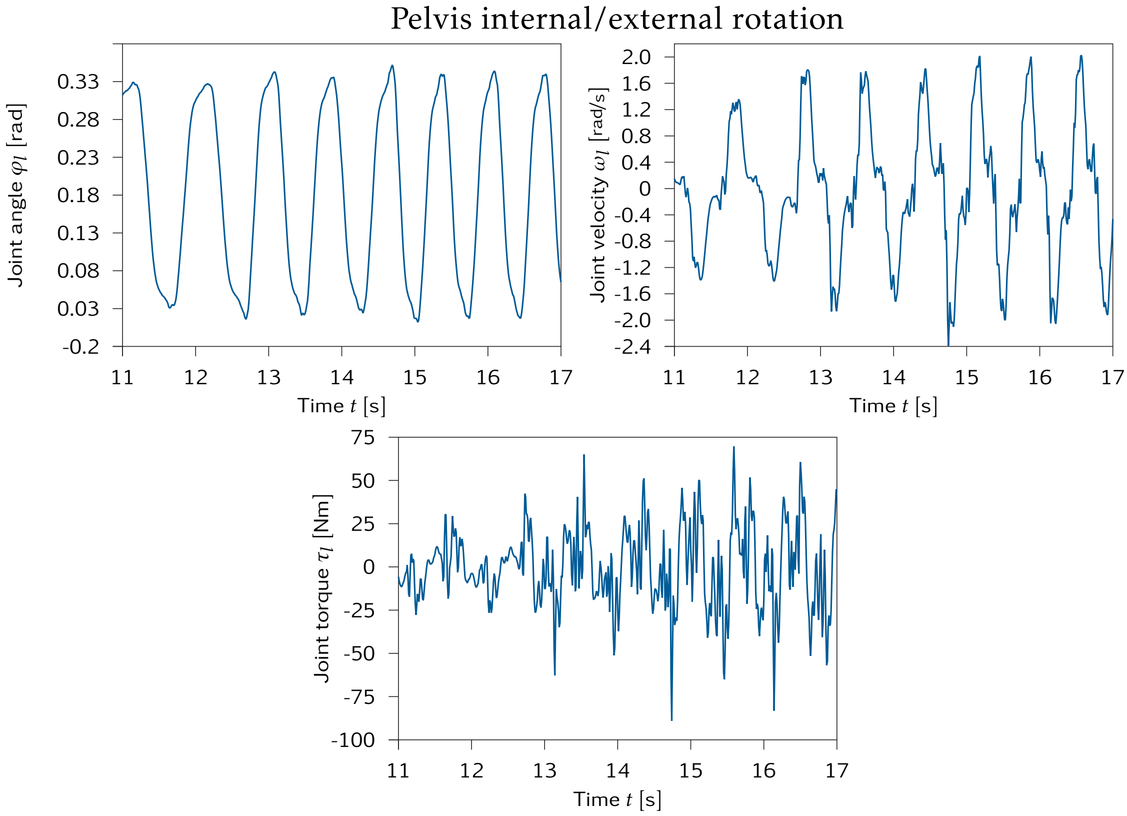
Pelvis internal/external rotation
Joint angle φ_l [rad]
0.33
0.28
0.23
0.18
0.13
0.08
0.03
-0.2
11
12
13
14
15
16
17
Time t [s]
Joint velocity ω_l [rad/s]
2.0
1.6
1.2
0.8
0.4
0
-0.4
-0.8
-1.2
-1.6
-2.0
-2.4
11
12
13
14
15
16
17
Time t [s]
Joint torque τ_l [Nm]
75
50
25
0
-25
-50
-75
-100
11
12
13
14
15
16
17
Time t [s]

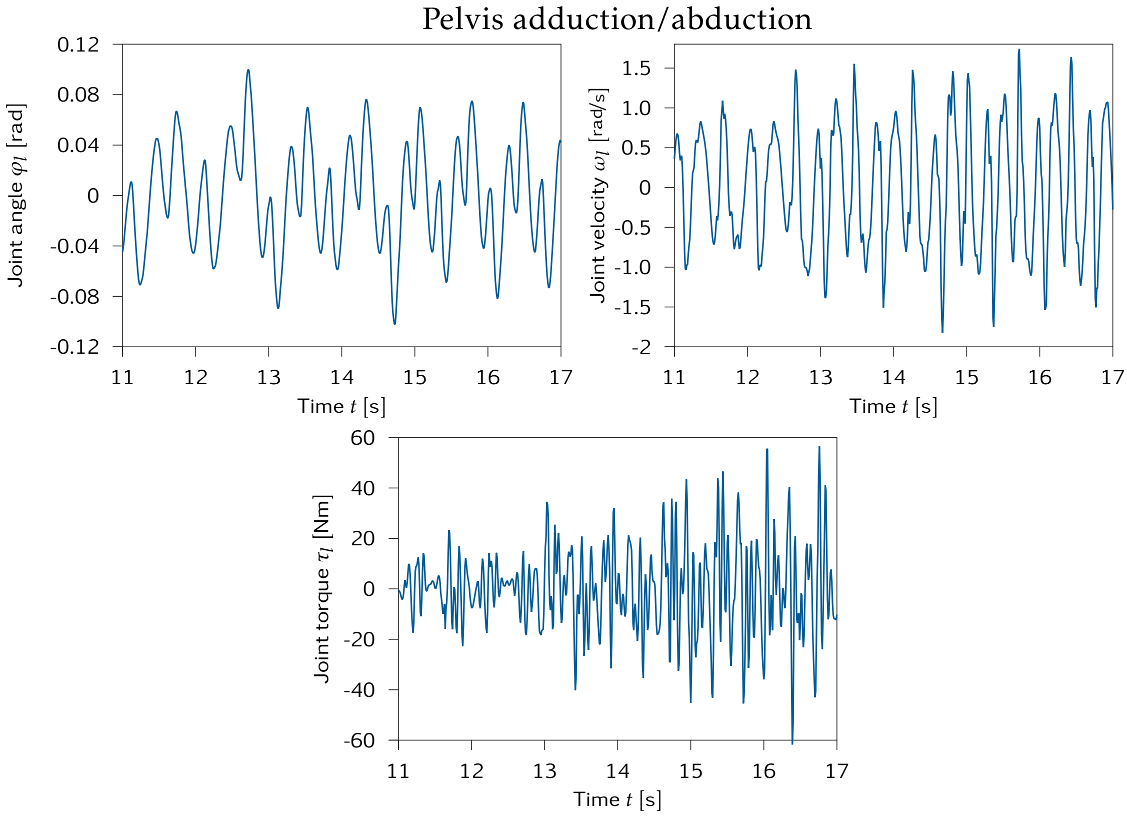
Pelvis adduction/abduction
Joint angle φ_l [rad]
0.12
0.08
0.04
0
-0.04
-0.08
-0.12
11
12
13
14
15
16
17
Time t [s]
Joint velocity ω_l [rad/s]
1.5
1.0
0.5
0
-0.5
-1.0
-1.5
-2
11
12
13
14
15
16
17
Time t [s]
Joint torque τ_l [Nm]
60
40
20
0
-20
-40
-60
11
12
13
14
15
16
17
Time t [s]

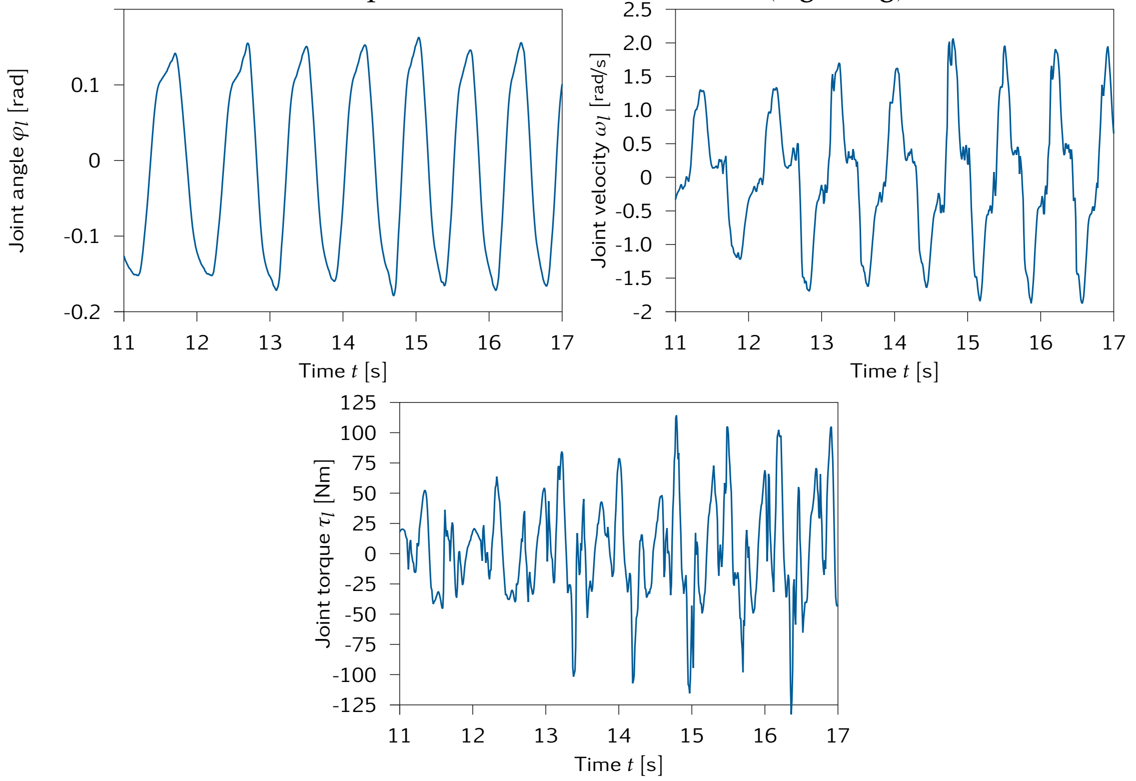

Hip internal/external rotation (right leg)

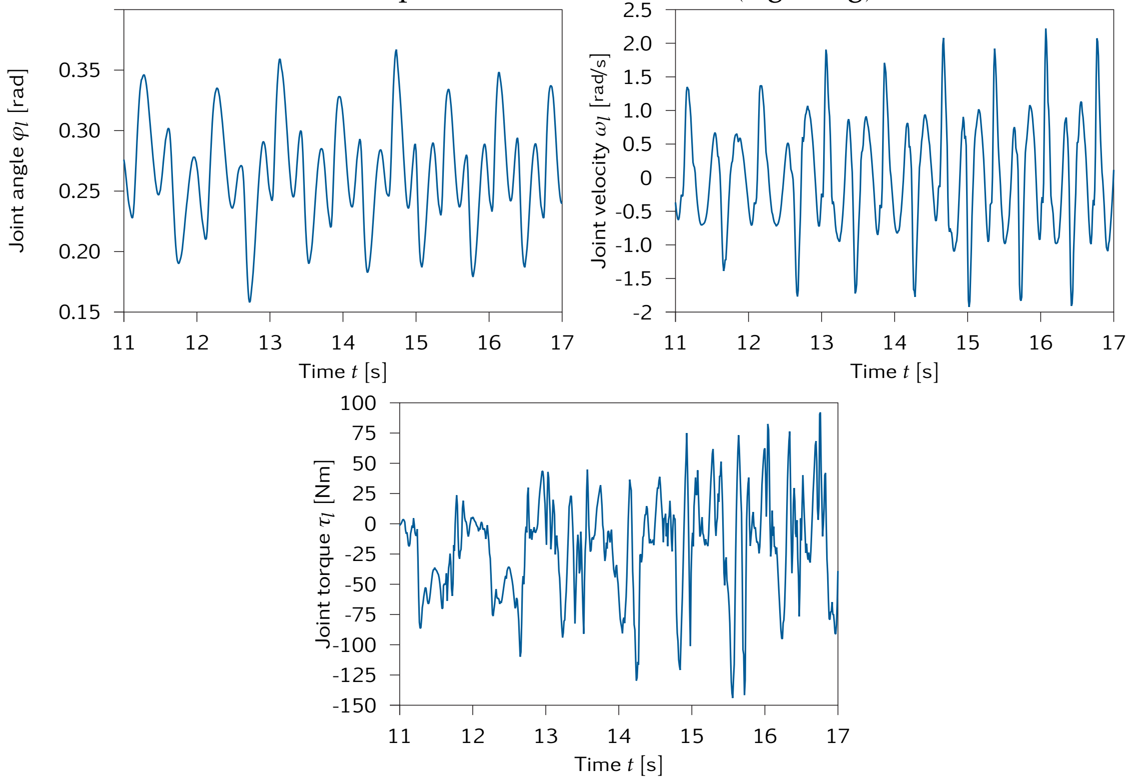

Hip adduction/abduction (right leg)

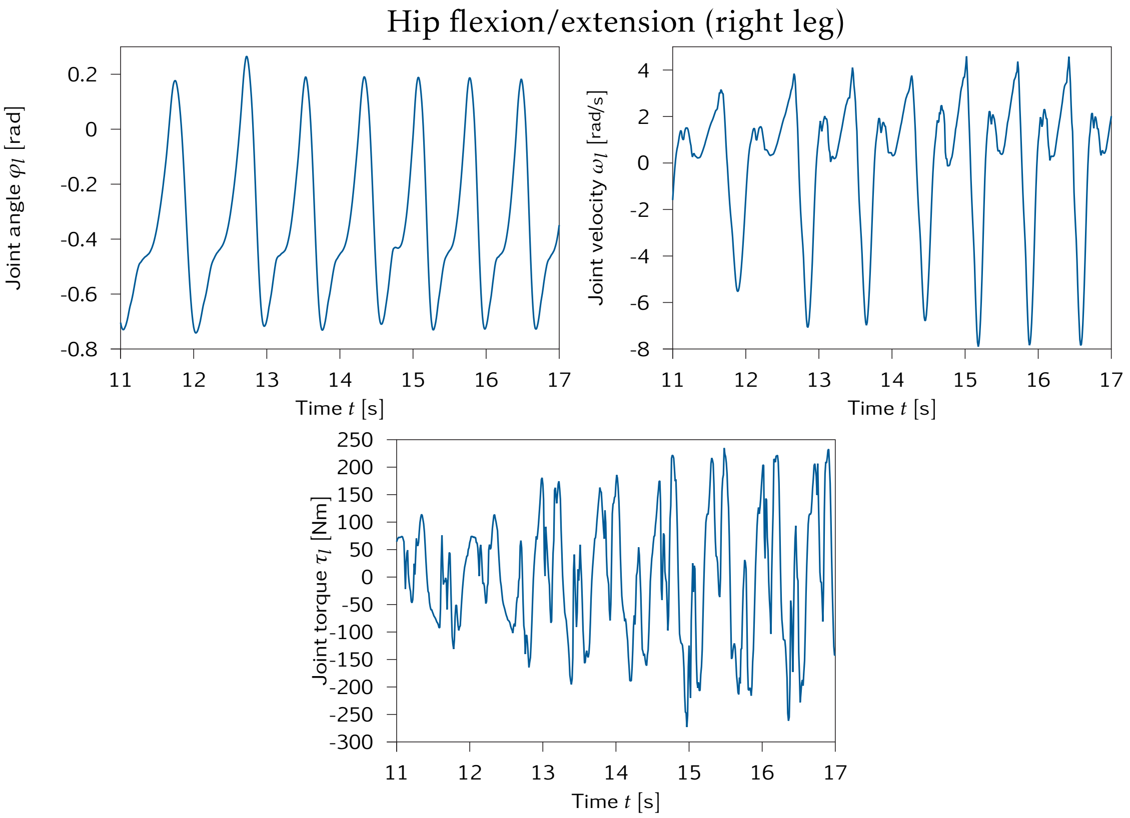
Hip flexion/extension (right leg)
Joint angle φ_l [rad]
0.2
0
-0.2
-0.4
-0.6
-0.8
Joint velocity ω_l [rad/s]
4
2
0
-2
-4
-6
-8
Joint torque τ_l [Nm]
250
200
150
100
50
0
-50
-100
-150
-200
-250
-300
11
12
13
14
15
16
17
Time t [s]

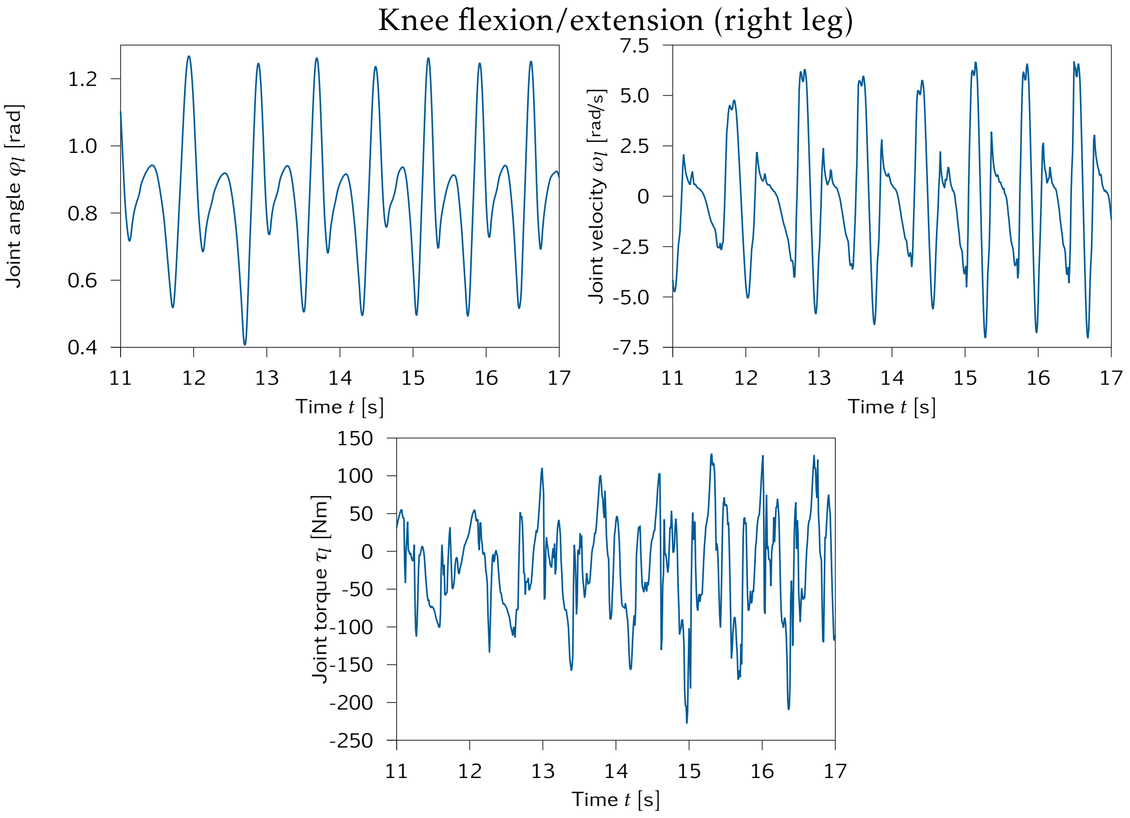
Knee flexion/extension (right leg)
Joint angle φ_l [rad]
1.2
1.0
0.8
0.6
0.4
Joint velocity ω_l [rad/s]
7.5
5.0
2.5
0
-2.5
-5.0
-7.5
Joint torque τ_l [Nm]
150
100
50
0
-50
-100
-150
-200
-250
11
12
13
14
15
16
17
Time t [s]

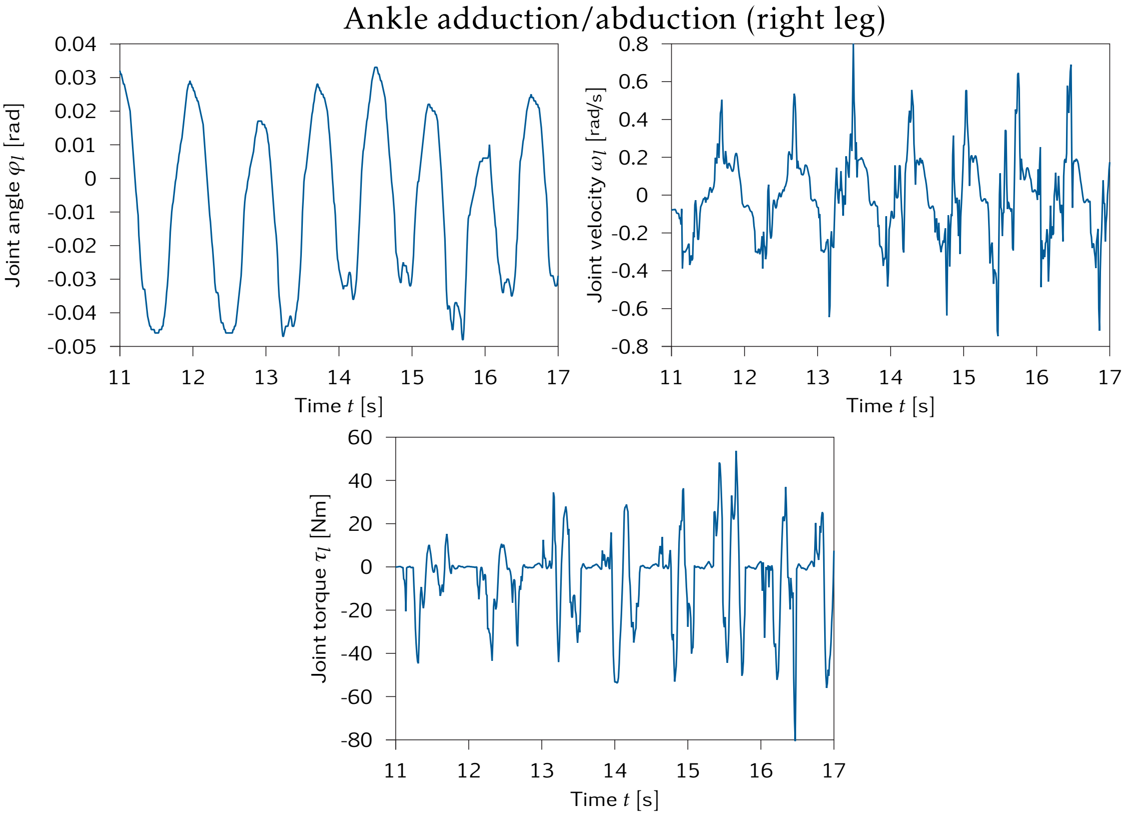

Ankle adduction/abduction (right leg)

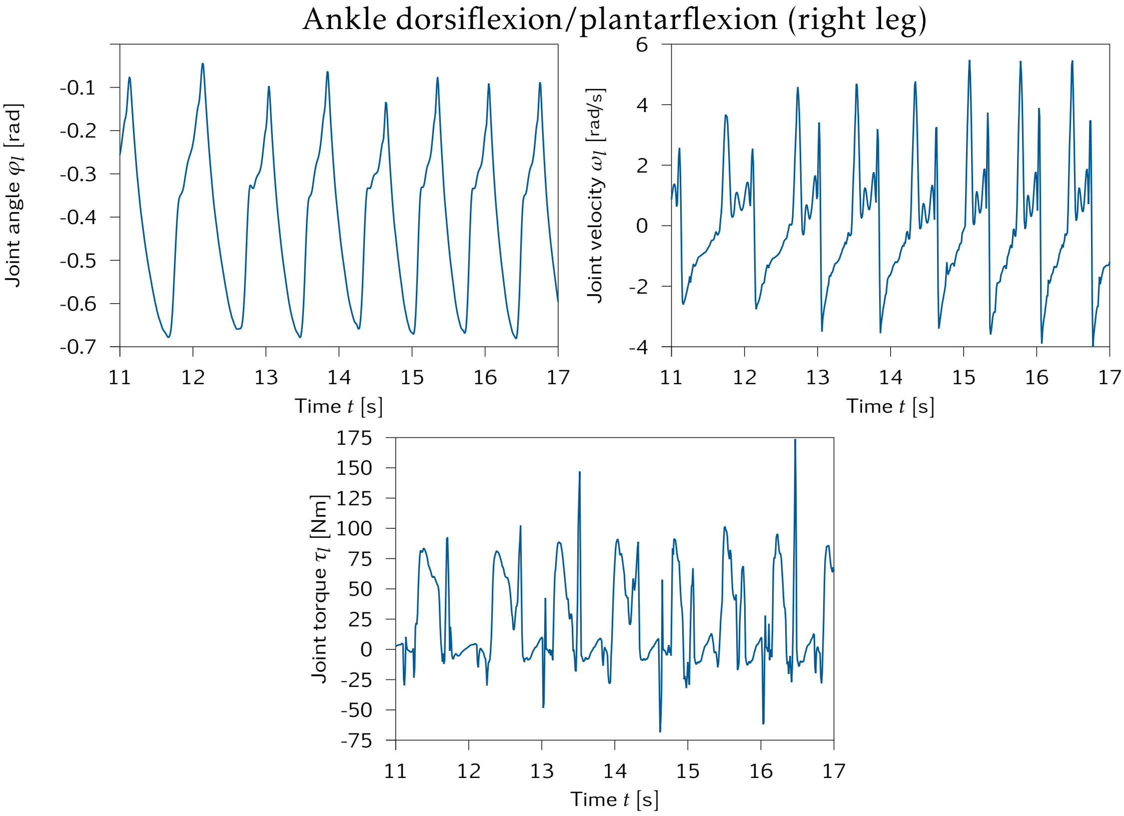

Ankle dorsiflexion/plantarflexion (right leg)

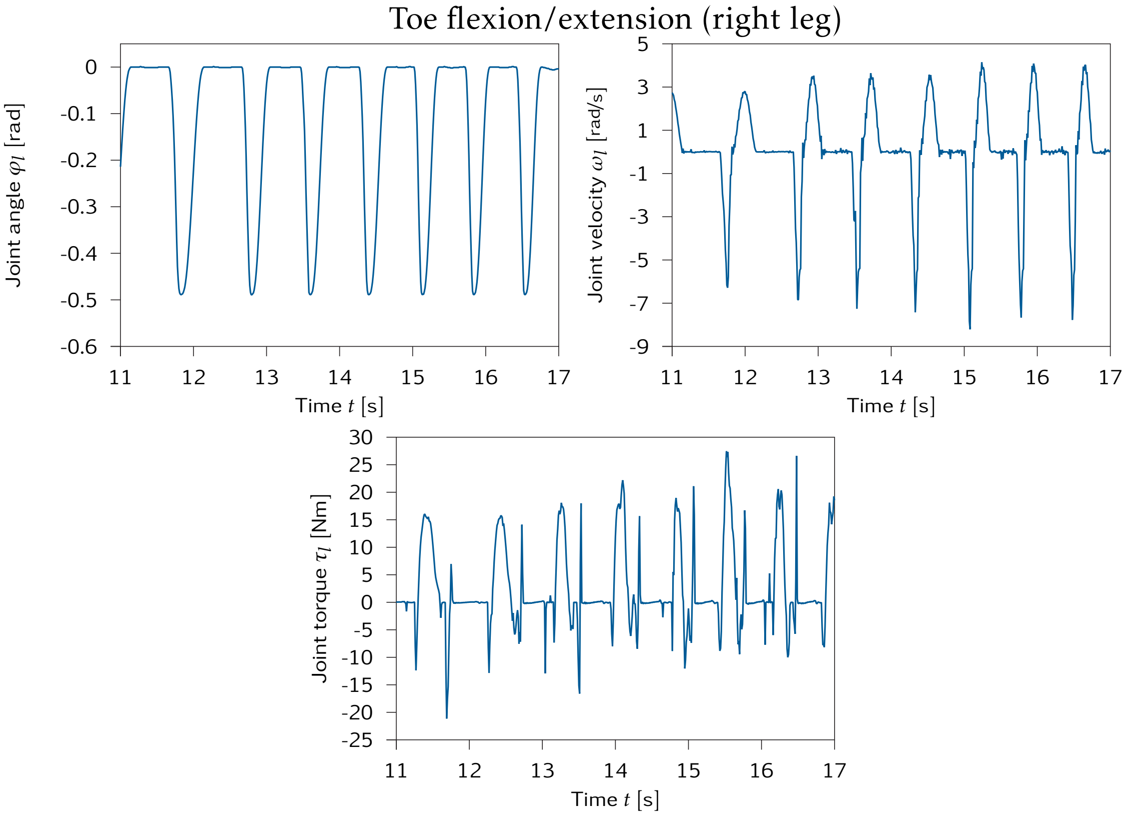
Toe flexion/extension (right leg)

Bibliography

[1] Aerotech, Inc. *1000 Series Brush, Rotary DC Servomotors*. Product catalog. 2007. url: `http://www.aerotech.com/`.

[2] Aerotech, Inc. *S-Series Brushless, Frameless Torque Motors*. Product catalog. 2007. url: `http://www.aerotech.com/`.

[3] Akachi, K., Kaneko, K., Kanehira, N., Ota S. Miyamori, G., Hirata, M., Kajita, S., and Kanehiro, F. "Development of Humanoid Robot HRP-3P". In: *Proc. IEEE-RAS Int. Conf. Humanoid Robot. (Humanoids)*. 2005, pp. 50–55. doi: 10.1109/ICHR.2005.1573544.

[4] Albers, A., Brudniok, S., Ottnad, J., Sauter, Ch., and Sedchaicharn, K. "ARMAR III - Design of the upper body". In: *Proc. Workshop Human-Centered Robotic Systems (HCRS)*. 2006.

[5] Albert, A., Hofschulte, J., and Schermeier, O. "Entwicklung des zweibeinigen, autonomen Laufroboters BARt-UH". In: *Proc. ROBOTIK*. (in German). VDI-Verlag, 2000, pp. 509–14.

[6] Angeles, J. and Park, F.C. "Performance Evaluation and Design Criteria". In: *Springer Handbook of Robotics*. Chap. 10, pp. 229–44.

[7] Asfour, T., Regenstein, K., Azad, P., Schröder, J., Bierbaum A. Vahrenkamp, N., and Dillmann, R. "ARMAR-III: An Integrated Humanoid Platform for Sensory-Motor Control". In: *Proc. IEEE-RAS Int. Conf. Humanoid Robot. (Humanoids)*. 2006, pp. 169–75. doi: 10.1109/ICHR.2006.321380.

[8] Axsys Technologies, Inc. *Brush Type DC Motors Handbook*. San Diego CA, USA, 2005. url: `http://www.axsys.com/`.

[9] Axsys Technologies, Inc. *Brushless DC Motors Handbook*. San Diego CA, USA, 2005. url: `http://www.axsys.com/`.

[10] Baek, J.H., Kwak, Y.K., and Kim, S.H. "On the frequency bandwidth change of a servo system with a gear reducer due to backlash and motor input voltage". In: *Arch. Appl. Mech.* **73**, 5-6 (2003), pp. 367–76. doi: 10.1007/s00419-003-0293-6.

[11] Beira, R., Lopes, M., Praca, M., Santos-Victor, J., Bernardino, A., Metta, G., Becchi, F., and Saltaren, R. "Design of the robot-cub (iCub) head". In: *Proc. IEEE Int. Conf. Robot. Autom. (ICRA)*. 2006, pp. 94–100.

[12] Benzi, F., Buja, G.S., and Felser, M. "Communication architectures for electrical drives". In: *IEEE Trans. Ind. Inf.* **1**, 1 (2005), pp. 47–53. doi: 10.1109/TII.2005.844428.

[13] Bevans, J.S. "Biomechanics: a review of foot function in gait". In: *The Foot* **2**, 2 (1992), pp. 79–82. doi: 10.1016/0958-2592(92)90022-H.

[14] Bluethmann, W., Ambrose, R., Diftler, M., Askew, S., Huber, E., Goza, M., Rehnmark, F., C., Lovchik, and Magruder, D. "Robonaut: A Robot Designed to Work with Humans in Space". In: *Auton. Robot.* **14** (2003), pp. 179–97. doi: 10.1023/A:1022231703061.

[15] Bowling, A. "Mobility and Dynamic Performance of Legged Robots". In: *Proc. IEEE Int. Conf. Robot. Autom. (ICRA)*. 2005, pp. 4100–7.

[16] Bruijn, S.M., Meijer O.G. van Dieën, J.H., Kingma, I., and Lamoth, C.J.C. "Coordination of leg swing, thorax rotations, and pelvis rotations during gait: The organisation of total body angular momentum". In: *Gait Posture* **27**, 3 (2008), pp. 455–62. doi: 10.1016/j.gaitpost.2007.05.017.

[17] Buschmann, T., Lohmeier, S., Bachmayer, M., Ulbrich, H., and Pfeiffer, F. "A Collocation Method for Real-Time Walking Pattern Generation". In: *Proc. IEEE-RAS Int. Conf. Humanoid Robot. (Humanoids)*. 2007.

[18] Buschmann, T., Lohmeier, S., and Ulbrich, H. "Biped Walking Control Based on Hybrid Position/Force Control". In: *Proc. IEEE/RSJ Int. Conf. Intell. Robots Syst. (IROS)*. 2009, pp. 3019–24. doi: `10.1109/IROS.2009.5354643`.

[19] Buschmann, T., Lohmeier, S., Ulbrich, H., and Pfeiffer, F. "Dynamics Simulation for a Biped Robot: Modeling and Experimental Verification". In: *Proc. IEEE Int. Conf. Robot. Autom. (ICRA)*. 2006, pp. 2673–78.

[20] Buschmann, T., Lohmeier, S., Ulbrich, H., and Pfeiffer, F. "Optimization Based Gait Pattern Generation for a Biped Robot". In: *Proc. IEEE-RAS Int. Conf. Humanoid Robot. (Humanoids)*. 2005, pp. 98–103. doi: `10.1109/ICHR.2005.1573552`.

[21] Carbone, G., Lim, H., Takanishi, A., and Ceccarelli, M. "Stiffness analysis of biped humanoid robot WABIAN-RIV". In: *Mech. Mach. Theor.* **41**, 1 (2006), pp. 17–40. doi: `10.1016/j.mechmachtheory.2005.05.001`.

[22] Carson, M.C., Harrington, M.E., Thompson, N., O'Connor, J.J., and Theologis, T.N. "Kinematic analysis of a multi-segment foot model for research and clinical applications: a repeatability analysis". In: *J. Biomech.* **34**, 10 (2001), pp. 1299–307. doi: `10.1016/S0021-9290(01)00101-4`.

[23] Cheng, G., Hyon, Sang-Ho, Morimoto, J., Ude, A., Colvin, G., Scroggin, W., and Jacobsen, S.C. "CB: A Humanoid Research Platform for Exploring NeuroScience". In: *Proc. IEEE-RAS Int. Conf. Humanoid Robot. (Humanoids)*. 2006, pp. 182–87. doi: `10.1109/ICHR.2006.321382`.

[24] ContiTech Antriebssysteme GmbH. *CONTI SYNCHROBELT HTD Synchronous Drive Belts*. Product catalog. Hannover/Germany, 2002. url: `http://www.contitech.de/`.

[25] Croce, U.D., Riley, P.O., Lelas, J.L., and Kerrigan, D.C. "A refined view of the determinants of gait". In: *Gait Posture* **14**, 2 (2001), pp. 79–84. doi: `10.1016/S0966-6362(01)00128-X`.

[26] Cupec, R., Lorch, O., and Schmidt, G. "Vision-Guided Humanoid Walking – Concepts and Experiments". In: *Proc. Int. Workshop Robotics in Alpe-Adria-Danube Region (RAAD)*. 2003.

[27] Dahmus, J.B., Gonzalez-Zugasti, J.P., and Otto, K.N. "Modular product architecture". In: *Design Studies* 22, 5 (2001), pp. 409–24. doi: `10.1016/S0142-694X(01)00004-7`.

[28] Danaher Corp. *Kollmorgen RBE(H) Series Motors*. Wood Dale IL, USA, 2003. url: `http://www.danahermotion.com/`.

[29] De Luca, A. and Book, W. "Robots with Flexible Elements". In: *Springer Handbook of Robotics*. Chap. 13, pp. 287–319.

[30] DIN 33402-1. *Körpermaße des Menschen - Teil 1: Begriffe, Meßverfahren*. (in German). Jan. 1978.

[31] DIN 33402-2. *Ergonomie - Körpermaße des Menschen - Teil 2: Werte*. (in German). Dec. 2005.

[32] Dresig, H. and Holzweissig, F. *Maschinendynamik*. 7th ed. (in German). Springer, 2006. isbn: 3-540-22546-3.

[33] Elmo Motion Control, Ltd. *SimplIQ Superior Servo Technology Products*. Rev. 10. Product catalog. Nov. 2009.

[34] ESK Ceramics GmbH & Co. KG. *EKagrip Friction Shims. Technical data.* Kempten/Germany, 2008. url: `http://www.esk.com/fileadmin/esk/medien/pdf/TDS_ekagrip_e.pdf`.

[35] Espiau, B. and Sardain, P. “The Anthropomorphic Biped Robot BIP2000”. In: *Proc. IEEE Int. Conf. Robot. Autom. (ICRA)*. 2000, pp. 3997–4002. doi: `10.1109/ROBOT.2000.845354`.

[36] Felser, M. “Real-Time Ethernet – Industry Prospective”. In: *Proc. IEEE* **93**, 6 (2005), pp. 1118–29.

[37] Förg, D. and Ulbrich, H. “Simulation of a Biologically Inspired, Partly-Actuated Robot Model with Passive Elements”. In: *Proc. ECCOMAS Conf. Multibody Dynamics*. 2009.

[38] Frommhagen, K., Nauber, P., Schelinski, U., and Scholles, M. “1394AP: a protocol for deterministic industrial communication via IEEE 1394”. In: *Proc. IEEE Conf. Emerging Technologies and Factory Automation*. 2005, pp. 933–40. doi: `10.1109/ETFA.2005.1612772`.

[39] Fujiwara, K., Kanehiro, F., Kajita, S., Yokoi, K., Saito, H., Harada, K., Kaneko, K., and Hirukawa, H. “The first human-size humanoid that can fall over safely and stand-up again”. In: *Proc. IEEE/RSJ Int. Conf. Intell. Robots Syst. (IROS)*. 2003, pp. 1920–6.

[40] Fukaushima, T., Kuroki, Y., and Ishida, T. “Development of a new actuator for a small biped walking entertainment robot”. In: *Proc. Int. Conf. Power Electronics, Machines and Drives (PEMD)*. 2004, pp. 126–31.

[41] Fukumoto, Y., Nishiwaki, K., Inaba, M., and Inoue, H.; “Hand-centered whole-body motion control for a humanoid robot”. In: *Proc. IEEE/RSJ Int. Conf. Intell. Robots Syst. (IROS)*. 2004, pp. 1186–91. doi: `10.1109/IROS.2004.1389557`.

[42] Galway, R.D. *A Comparison of Methods for Calibration and Use of Multi-component Strain Gauge Wind Tunnel Balances*. NRC/NAE Aeronautical Report LR-600. National Research Council Of Canada Ottawa, Mar. 1980.

[43] Gard, S.A. and Childress, D.S. “The influence of stance-phase knee flexion on the vertical displacement of the trunk during normal walking”. In: *Arch. Phys. Med. Rehabil.* **80**, 1 (1999), pp. 26–32. doi: `10.1016/S0003-9993(99)90303-9`.

[44] Gerecke, M., Hofschulte, J., and W., Gerth. “Realization of a Lightweight Sensory Foot for a Bipedal Robot”. In: *Proc. Int. Conf. Climbing and Walking Robots (CLAWAR)*. 2003, pp. 895–902.

[45] Getzner Werkstoffe GmbH. *Sylomer — cutting-edge material*. 2009. url: `http://www.getzner.com/en/solutions/materials/sylomer/` (visited on 11/03/2009).

[46] Gienger, M. *Entwurf und Realisierung einer zweibeinigen Laufmaschine*. Fortschrittberichte VDI, Reihe 1 378. (in German). Düsseldorf: VDI-Verlag, 2005. isbn: 3-18-337801-9.

[47] Gienger, M., Löffler, K., and Pfeiffer, F. “Towards the Design of a Biped Jogging Robot”. In: *Proc. IEEE Int. Conf. Robot. Autom. (ICRA)*. 2001, pp. 4140–45. doi: `10.1109/ROBOT.2001.933265`.

[48] Gienger, M., Löffler, K., and Pfeiffer, F. “Walking Control of a Biped Robot based on Inertial Measurement”. In: *Proc. Int. Workshop Humanoid Human Friendly Robot. (IARP)*. 2002, pp. 22–29.

[49] Gomi, H. and Hamaya, K. “Legged Walking Robot”. Pat. EP 1 097 860 (B1). Honda Motor Co., Ltd. Oct. 12, 2003.

[50] Gomi, H., T., Kumagai, Hirose, M., and M., Nishikawa. “Articulated Structure for Legged Walking Robot”. Pat. EP 0 433 096 (B1). Honda Motor Co., Ltd. Oct. 22, 1997.

[51] Gomi, H., Hamaya, K., Toyoda, H., and Takemura, Y. “Legged mobile robot”. Pat. EP 1 535 705 (A1). Honda Motor Co., Ltd. Aug. 7, 2003.

[52] Gorinevski, D. M., Formalsky, A. M., and Schneider, A. Yu. *Force Control of Robotics Systems*. CRC Press, 1997. isbn: 0-8493-2671-0.

[53] Gouaillier, D., Hugel, V., Blazevic, P., Kilner, C., Monceaux, J., Lafourcade, P., Marnier, B., Serre, J., and Maisonnier, B. "Mechatronic design of NAO humanoid". In: *Proc. IEEE Int. Conf. Robot. Autom. (ICRA)*. 2009, pp. 769–74.

[54] Haibach, E. *Betriebsfestigkeit*. 2. Aufl. (in German). Berlin ; Heidelberg [u.a.]: Springer, 2002. isbn: 3-540-43142-X.

[55] Hans Haugg Antriebstechnik GmbH & Co. KG. *"Hermetic K-Series" bevel gear boxes*. Product catalog. Hiltenfingen/Germany, 2007.

[56] Harada, T., Sato, T., and Mori, T. "Development of Tiny Orientation Estimation Device under Motion and Magnetic Disturbance". In: *Int. J. Robot. Res.* **26**, 5 (2007), pp. 547–59. doi: 10.1177/0278364907079272.

[57] Harmonic Drive AG. *CPL-2A Series Lightweight Component Sets*. Product information. Limburg/Lahn, 2007. url: http://www.harmonicdrive.de/.

[58] Harmonic Drive AG. *CSF Mini Series Gearboxes*. Product information. Limburg/Lahn, 2007. url: http://www.harmonicdrive.de/.

[59] Harmonic Drive AG. *Precision in Motion*. Full-line catalog. Limburg/Lahn, 2007/08. url: http://www.harmonicdrive.de/.

[60] Harmonic Drive AG. *RSF-Supermini AC Servo Actuator*. Product information. Limburg/Lahn, 2007. url: http://www.harmonicdrive.de/.

[61] Harzheim, L. *Strukturoptimierung*. 1. Aufl. (in German). Frankfurt am Main: Verlag Harri Deutsch, 2008. isbn: 978-3-8171-1809-0.

[62] Hashimoto, K., Sugahara, Y., Hayashi, A., Kawase, M., Sawato, T., Endo, N., Ohta, A., Tanaka, C., and Takanishi, A. "New Foot System Adaptable to Convex and Concave Surface". In: *Proc. IEEE Int. Conf. Robot. Autom. (ICRA)*. 2007, pp. 1869–74. doi: 10.1109/ROBOT.2007.363594.

[63] Henze, A. "Dreidimensionale biomechanische Modellierung und die Entwicklung eines Reglers zur Simulation zweibeinigen Gehens". (in German). Ph.D. thesis. Tübingen: Eberhard-Karls-Universität, 2002.

[64] Hirai, K., Hirose, M., and Takenaka, T. "The Development of Honda Humanoid Robot". In: *Proc. IEEE Int. Conf. Robot. Autom. (ICRA)*. 1998, pp. 1321–26. doi: 10.1109/ROBOT.1998.677288.

[65] Hirose, M. and Ogawa, K. "Honda humanoid robots development". In: *Phil. Trans. R. Soc. A* **365** (2007), pp. 11–19. doi: 10.1098/rsta.2006.1917.

[66] Hirzinger, G., Butterfass, J., Fischer, M., Grebenstein, M., Hahnle, M., Liu, H., Schaefer, I., and Sporer, N. "A mechatronics approach to the design of light-weight arms and multifingered hands". In: *Proc. IEEE Int. Conf. Robot. Autom. (ICRA)*. 2000, pp. 46–54. doi: 10.1109/ROBOT.2000.844038.

[67] Hirzinger, G., Sporer, N., Albu-Schäffer, A., Hähnle, M., Krenn, R., Pascucci, A., and Schedl, M. "DLR's torque-controlled light weight robot III – are we reaching the technological limits now?" In: *Proc. IEEE Int. Conf. Robot. Autom. (ICRA)*. 2002, pp. 1710–6. doi: 10.1109/ROBOT.2002.1014788.

[68] Hirzinger, G., Albu-Schäffer, A., Hähnle, M., Schaefer, I., and Sporer, N. "On a New Generation of Torque Controlled Light-Weight Robots". In: *Proc. IEEE Int. Conf. Robot. Autom. (ICRA)*. Vol. 4. Seoul, Korea, 2001, pp. 3356–3363. doi: 10.1109/ROBOT.2001.933136.

[69] Hobbelen, D., de Boer, T., and Wisse, M. "System overview of bipedal robots Flame and TUlip: tailor-made for Limit Cycle Walking". In: *Proc. IEEE/RSJ Int. Conf. Intell. Robots Syst. (IROS)*. 2008, pp. 2486–91. doi: 10.1109/IROS.2008.4650728.

[70] Hofschulte, J., Gerth, W., and Seebode, M. “Parallel Manipulator Hip Joint for a Bipedal Robot”. In: *Proc. Int. Conf. Climbing and Walking Robots (CLAWAR)*. 2004, pp. 601–9. doi: `10.1007/3-540-29461-9_60`.

[71] Hollerbach, J., Khalil, W., and Gautier, M. “Model Identification”. In: *Springer Handbook of Robotics*. Chap. 14, pp. 321–44.

[72] Horakova, J. “The (Short) Robot Chronicle (On the 20th Century Cultural History of Robots)”. In: *Proc. Int. Workshop Robotics in the Alpe-Adria-Danube Region (RAAD)*. 2006.

[73] Hughes, J., Clark, P., and Klenerman, L. “The importance of the toes in walking”. In: *J. Bone Joint Surg. Br.* 72, 2 (1990), pp. 245–51.

[74] Hurst, J.W., Chestnutt, J., and Rizzi, A. “Design and Philosophy of the BiMASC, a Highly Dynamic Biped”. In: *Proc. IEEE Int. Conf. Robot. Autom. (ICRA)*. 2007, pp. 1863–8. doi: `10.1109/ROBOT.2007.363593`.

[75] IEC/EN 61491. *Electrical equipment of industrial machines – Serial data link for real-time communication between controls and drives*. Oct. 2002.

[76] IEC/PAS 62410. *Real-time Ethernet SERCOS III*. Aug. 2005.

[77] iMAR GmbH. *iVRU-FC: Vertical Reference Unit with Fiber Optic Gyros, MEMS Accelerometers and integrated Strapdown Processor*. Technical Datasheet. St. Ingbert/Germany, 2007.

[78] INA Schaeffler KG. *Planetary roller screws and bearing components (RGT)*. Product catalog. Homburg/Germany, 2000. url: `http://www.ina.com/`.

[79] INA Schaeffler KG. *Wälzlager*. Product catalog (in German). Herzogenaurach/Germany, 2006. url: `http://www.ina.com`.

[80] International Federation of Robotics (IFR), ed. *World Robotics 2008*. VDMA Verlag, 2008.

[81] Isermann, R. *Mechatronische Systeme – Grundlagen*. (in German). Springer, 1999. isbn: 3-540-64725-2.

[82] Ishida, T. and Takanishi, A. “A Robot Actuator Development With High Backdrivability”. In: *Proc. IEEE Conf. Robotics, Automation and Mechatronics*. 2006, pp. 1–6. doi: `10.1109/RAMECH.2006.252631`.

[83] Ishida, T., Kurokoi, Y., Nagasaka, K., and Yamaguchi, J. “A Small Biped Entertainment Robot and its Attractive Applications”. In: *Proc. Int. Workshop Humanoid Human Friendly Robot. (IARP)*. 2002, pp. 116–9.

[84] Ishida, T., Kuroki, Y., and Yamaguchi, J. “Mechanical system of a small biped entertainment robot”. In: *Proc. IEEE/RSJ Int. Conf. Intell. Robots Syst. (IROS)*. 2003, pp. 1129–34. doi: `10.1109/IROS.2003.1248796`.

[85] Kajita, S. and Espiau, B. “Legged Robots”. In: *Springer Handbook of Robotics*. Chap. 16, pp. 361–89.

[86] Kajita, S. and Tani, K. “Adaptive Gait Control of a Biped Robot Based on Realtime Sensing of the Ground Profile”. In: *Auton. Robot.* 4, 3 (1997), pp. 297–305. doi: `10.1023/A:1008848227206`.

[87] Kajita, S., Nagasaki, T., Kaneko, K., Yokoi, K., and Tanie, K. “A hop towards running humanoid biped”. In: *Proc. IEEE Int. Conf. Robot. Autom. (ICRA)*. 2004, pp. 629–35. doi: `10.1109/ROBOT.2004.1307219`.

[88] Kajita, S., Kanehiro, F., Kaneko, K., Fujiwara, K., Yokoi, K., and Hirukawa, H. “A Realtime Pattern Generator for Biped Walking”. In: *Proc. IEEE Int. Conf. Robot. Autom. (ICRA)*. 2002, pp. 31–7. doi: `10.1109/ROBOT.2002.1013335`.

[89] Kajita, S., Nagasaki, T., Kaneko, K., Yokoi, K., and Tanie, K. “A Running Controller of Humanoid Biped HRP-2LR”. In: *Proc. IEEE Int. Conf. Robot. Autom. (ICRA)*. 2005, pp. 616–22.

[90] Kajita, S., Kaneko, K., Morisawa, M., Nakaoka, S., and Hirukawa, H. "ZMP-based Biped Running Enhanced by Toe Springs". In: *Proc. IEEE Int. Conf. Robot. Autom. (ICRA)*. 2007, pp. 3963–9. doi: `10.1109/ROBOT.2007.364087`.

[91] Kaminaga, H., Ono, J., Nakashima, A., and Nakamura, Y. "Development of Backdrivable Hydraulic Joint Mechanism for Knee Joint of Humanoid Robots". In: *Proc. IEEE Int. Conf. Robot. Autom. (ICRA)*. 2009, pp. 1577–82.

[92] Kanehiro, F., Ishiwata, Y., Saito, H., Akachi, K., Miyamori, G., Isozumi, T., Kaneko, K., and Hirukawa, H. "Distributed Control System of Humanoid Robots based on Real-time Ethernet". In: *Proc. IEEE/RSJ Int. Conf. Intell. Robots Syst. (IROS)*. 2006, pp. 2471–77. doi: `10.1109/IROS.2006.281691`.

[93] Kaneko, K., Kanehiro, F., Morisawa, M., Miura, K., Nakaoka, S., and Kajita, S. "Cybernetic Human HRP-4C". In: *Proc. IEEE-RAS Int. Conf. Humanoid Robot. (Humanoids)*. 2009, pp. 7–14. doi: `10.1109/ICHR.2009.5379537`.

[94] Kaneko, K., Kajita, S., Kanehiro, F., Yokoi, K., Fujiwara, K., Hirukawa, H., Kawasaki, T., Hirata, M., and Isozumi, T. "Design of Advanced Leg Module for Humanoid Robotics Project of METI". In: *Proc. IEEE Int. Conf. Robot. Autom. (ICRA)*. 2002, pp. 38–45. doi: `10.1109/ROBOT.2002.1013336`.

[95] Kaneko, K., Kanehiro, F., Kajita, S., Hirukawa, H., Kawasaki, T., Hirata, M., Akachi, K., and Isozumi, T. "Humanoid Robot HRP-2". In: *Proc. IEEE Int. Conf. Robot. Autom. (ICRA)*. 2004, pp. 1083–90. doi: `10.1109/ROBOT.2004.1307969`.

[96] Kaneko, K., Harada, K., Kanehiro, F., Miyamori, G., and Akachi, K. "Humanoid robot HRP-3". In: *Proc. IEEE/RSJ Int. Conf. Intell. Robots Syst. (IROS)*. 2008, pp. 2471–78. doi: `10.1109/IROS.2008.4650604`.

[97] Kemp, C.C., Fitzpatrick, P., Hirukawa, H., Yokoi, K., Harada, K., and Matsumoto, Y. "Humanoids". In: *Springer Handbook of Robotics*. Chap. 56, pp. 1307–33.

[98] Kerrigan, D.C., Croce, U.D., Marciello, M., and Riley, P.O. "A refined view of the determinants of gait: significance of heel rise". In: *Arch. Phys. Med. Rehabil.* **81** (2000), pp. 1077–80. doi: `10.1053/apmr.2000.6306`.

[99] Kim, G., Shin, H., and Yoon, J. "Development of 6-axis force/moment sensor for a humanoid robot's intelligent foot". In: *Sensor Actuator Phys.* **141**, 2 (2008), pp. 46–53. doi: `j.sna.2007.08.011`.

[100] Kim, J., Park, I., Lee, J., Kim, M., Cho, B., and Oh, J. "System Design And Dynamic Walking Of Humanoid Robot KHR-2". In: *Proc. IEEE Int. Conf. Robot. Autom. (ICRA)*. 2005, pp. 1443–48.

[101] Klein, B. *Leichtbau-Konstruktion*. 4th ed. (in German). Vieweg, 2000. isbn: 3-528-34115-7.

[102] Konno, A., Sellaouti, R., Amar, F.B., and Ouezdou, F.B. "Design and development of the biped prototype ROBIAN". In: *Proc. IEEE Int. Conf. Robot. Autom. (ICRA)*. 2002, pp. 1384–9. doi: `10.1109/ROBOT.2002.1014736`.

[103] Krishnan, R. "Selection Criteria for Servo Motor Drives". In: *IEEE Trans. Ind. Applicat.* **23**, 2 (1987), pp. 270–5. doi: `10.1109/TIA.1987.4504902`.

[104] Kwon, W., Kim, H.K., Park, J.K., Roh, C.H., Lee, J., Park, J., Kim, W., and Roh, K. "Biped Humanoid Robot Mahru III". In: *Proc. IEEE-RAS Int. Conf. Humanoid Robot. (Humanoids)*. 2007.

[105] Li, J., Huang, Q., Zhang, W., Yu, Z., and Li, K. "Flexible foot design for a humanoid robot". In: *Proc. IEEE Int. Conf. Automation and Logistics (ICAL)*. 2008, pp. 1414–9. doi: `10.1109/ICAL.2008.4636375`.

[106] Lim, H. and Takanishi, A. "Biped walking robots created at Waseda University: WL and WABIAN family". In: *Phil. Trans. R. Soc. A* **365**, 1850 (2007), pp. 49–64. doi: `10.1098/rsta.2006.1920`.

[107] Lindemann, U. *Methodische Entwicklung technischer Produkte*. 2nd ed. (in German). Springer, 2007. isbn: 978-3-540-37435-0.

[108] Lobo, J. and Dias, J. "Vision and inertial sensor cooperation using gravity as a vertical reference". In: *IEEE Trans. Pattern Anal. Machine Intell.* **25**, 12 (2003), pp. 1597–1608. doi: `10.1109/TPAMI.2003.1251152`.

[109] Löffler, K. *Dynamik und Regelung einer zweibeinigen Laufmaschine*. Fortschrittberichte VDI, Reihe 8 1094. (in German). Düsseldorf: VDI-Verlag, 2006. isbn: 3-18-509408-5.

[110] Löffler, K., Gienger, M., Pfeiffer, F., and Ulbrich, H. "Sensors and control concept of a biped robot". In: *IEEE Trans. Ind. Electron.* **51**, 5 (2004), pp. 972–80. doi: `10.1109/TIE.2004.834948`.

[111] Lohmeier, S., Buschmann, T., Ulbrich, H., and Pfeiffer, F. "Design Concept of Humanoid Robot LOLA". In: *Proc. CISM-IFToMM Symposium on Robot Design, Dynamics, and Control (RoManSy)*. 2008.

[112] Lohmeier, S., Buschmann, T., Ulbrich, H., and Pfeiffer, F. "Humanoid Robot LOLA — Research Platform for High-speed Walking". In: *Motion and Vibration Control — Selected Papers from MOVIC 2008*. Ed. by Ulbrich, H. and Ginzinger, L. Springer, 2008, pp. 221–30. isbn: 978-1-4020-9437-8.

[113] Lohmeier, S., Buschmann, T., Schwienbacher, M., Ulbrich, H., and Pfeiffer, F. "Leg Design for a Humanoid Walking Robot". In: *Proc. IEEE-RAS Int. Conf. Humanoid Robot. (Humanoids)*. 2006, pp. 536–41. doi: `10.1109/ICHR.2006.321325`.

[114] Lohmeier, S., Buschmann, T., and Ulbrich, H. "System Design and Control of Anthropomorphic Walking Robot LOLA". In: *IEEE/ASME Trans. Mechatron.* **14**, 6 (2009). Focused Section on Anthropomorphism in Mechatronic Systems, pp. 658–66. doi: `10.1109/TMECH.2009.2032079`.

[115] Maxon Motor AG. *Full-line Catalog*. Sachseln (Switzerland), 2008. url: `http://www.maxonmotor.com/`.

[116] McGeer, T. "Passive Dynamic Walking". In: *Int. J. Robot. Res.* **9**, 2 (1990), pp. 62–82. doi: `10.1177/027836499000900206`.

[117] Miyachi Systems Corp. *Miniature Humanoid Robots*. (in Japanese). 2010. url: `http://www.miyachi-sys.com/services/robot/index.html` (visited on 02/15/2010).

[118] Miyazaki, S. and Otani, T. "Leg Type Movable Robot". Pat. EP 1 609 567 (A1). Honda Motor Co., Ltd. Dec. 28, 2005.

[119] Miyazaki, S. and Takahashi, H. "Leg Structure of Legged Robot". Pat. EP 1 344 614 (A1). Honda Motor Co., Ltd. Sept. 17, 2003.

[120] Murata, S., Yoshida, E., Tomita, K., Kurokawa, H., Kamimura, A., and Kokaji, S. "Hardware design of modular robotic system". In: *Proc. IEEE/RSJ Int. Conf. Intell. Robots Syst. (IROS)*. 2000, pp. 2210–7. doi: `10.1109/IROS.2000.895297`.

[121] Nagakubo, A., Kuniyoshi, Y., and Cheng, G. "Development of a high-performance upper-body humanoid system". In: *Proc. IEEE/RSJ Int. Conf. Intell. Robots Syst. (IROS)*. 2000, pp. 1577–1583. doi: `10.1109/IROS.2000.895198`.

[122] Nagakubo, A., Kuniyoshi, Y., and Cheng, G. "ETL-Humanoid – A high-performance full body humanoid system for versatile actions". In: *Proc. IEEE/RSJ Int. Conf. Intell. Robots Syst. (IROS)*. 2001, pp. 1087–92. doi: `10.1109/IROS.2001.976313`.

[123] Nakamura, Y., Okada, M., Shinohara, T., and Goto, T. "Mechanical Challenges for Further Humanoid Robot Evolution". In: *Proc. Third IARP International Workshop on Humanoid and Human Friendly Robotics*. 2002.

[124] Nakanishi, Y., Namiki, Y., Hongo, K., Urata, J., Mizuuchi, I., and Inaba, M. "Design of the musculoskeletal trunk and realization of powerful motions using spines". In: *Proc. IEEE-RAS Int. Conf. Humanoid Robot. (Humanoids)*. 2007, pp. 96–101. doi: `10.1109/ICHR.2007.4813854`.

[125] Nishiwaki, K., Murakami, Y., Kagami, S., Kuniyoshi, Y., Inaba, M., and Inoue, H. "A Six-axis Force Sensor with Parallel Support Mechanism to Measure the Ground Reaction Force of Humanoid Robot". In: *Proc. IEEE Int. Conf. Robot. Autom. (ICRA)*. 2002, pp. 2277–82. doi: 10.1109/ROBOT.2002.1013571.

[126] Nishiwaki, K., Kagami, S., Kuffner, J., Inaba, M., and Inoue, H. "Humanoid 'JSK-H7': Research Platform for Autonomous Behavior and Whole Body Motion". In: *Proc. Int. Workshop Humanoid Human Friendly Robot. (IARP)*. 2002, pp. 2–9.

[127] Nishiwaki, K., Kuffner, J., Kagami, S., Inaba, M., and Inoue, H. "The experimental humanoid robot H7: a research platform for autonomous behaviour". In: *Phil. Trans. R. Soc. A* **365**, 1850 (2007), pp. 79–107. doi: 10.1098/rsta.2006.1921.

[128] Nishiwaki, K., Kagami, S., Kuniyoshi, Y., Inaba, M., and Inoue, H. "Toe Joints that Enhance Bipedal and Fullbody Motion of Humanoid Robots". In: *Proc. IEEE Int. Conf. Robot. Autom. (ICRA)*. 2002, pp. 3105–10. doi: 10.1109/ROBOT.2002.1013704.

[129] Novacheck, T.F. "The biomechanics of running". In: *Gait Posture* **7** (1998), pp. 77–95. doi: 10.1016/S0966-6362(97)00038-6.

[130] Ogura, Y., Aikawa, H., Lim, H.-O., and Takanishi, A. "Development of a human-like walking robot having two 7-DOF legs and a 2-DOF waist". In: *Proc. IEEE Int. Conf. Robot. Autom. (ICRA)*. 2004, pp. 134–39. doi: 10.1109/ROBOT.2004.1307141.

[131] Ogura, Y., Aikawa, H., Shimomura, K., Kondo, H., Morishima, A., Lim, H., and Takanishi, A. "Development of A Humanoid Robot WABIAN-2". In: *Proc. IEEE Int. Conf. Robot. Autom. (ICRA)*. 2006, pp. 76–81.

[132] Ogura, Y., Shimomura, K., Kondo, H., Morishima, A., Okubo, T., Momoki, S., Lim, H., and Takanishi, A. "Human-like Walking with Knee Stretched, Heel-contact and Toe-off Motion by a Humanoid Robot". In: *Proc. IEEE/RSJ Int. Conf. Intell. Robots Syst. (IROS)*. 2006, pp. 3976–81. doi: 10.1109/IROS.2006.281834.

[133] Okada, M. and Nakamura, J. "Development of a Cybernetic Shoulder – A Three-DOF Mechanism That Imitates Biological Shoulder Motion". In: *IEEE Trans. Robot.* **21**, 3 (2005), pp. 438–43. doi: 10.1109/TRO.2004.838006.

[134] Okada, M., Shinohara, T., Gotoh, T., Ban, S., and Nakamura, Y. "Double Spherical Joint and Backlash Clutch for Lower Limbs of Humanoids". In: *Proc. IEEE Int. Conf. Robot. Autom. (ICRA)*. 2003, pp. 491–6.

[135] Omer, A.M., Ogura, Y., Kondo, H., Morishima, A., Carbone, G., Ceccarelli, M., Lim, H., and Takanishi, A. "Development of A Humanoid Robot Having 2-DOF Waist and 2-DOF Trunk". In: *Proc. IEEE-RAS Int. Conf. Humanoid Robot. (Humanoids)*. 2005, pp. 333–8. doi: 10.1109/ICHR.2005.1573589.

[136] Oota, N., Kawasaki, T., and Isozumi, T. "Impact Absorbing Mechanism of Walking Robot". Pat. EP 1 550 533 (A1). Kawada Industries, Inc. July 6, 2005.

[137] Ott, Ch., Eiberger, O., Friedl, W., Bäuml, B., et al. "A Humanoid Two-Arm System for Dexterous Manipulation". In: *Proc. IEEE-RAS Int. Conf. Humanoid Robot. (Humanoids)*. 2006, pp. 276–83. doi: 10.1109/ICHR.2006.321397.

[138] Pahl, G., Beitz, W., Feldhusen, J., and Grote, K.H. *Konstruktionslehre: Grundlagen erfolgreicher Produktentwicklung. Methoden und Anwendung*. 6th ed. (in German). Springer, 2005. isbn: 3-540-22048-8.

[139] Park, I.-W., Kim, J.-Y., Lee, J., and Oh, J.-H. "Mechanical Design of Humanoid Robot Platform KHR-3 (KAIST Humanoid Robot - 3: HUBO)". In: *Proc. Int. Conf. Humanoid Robots (Humanoids)*. 2005, pp. 321–26. doi: 10.1109/ICHR.2005.1573587.

[140] Park, I.-W., Kim, J.-Y., Lee, J., and Oh, J.-H. "Mechanical Design of the Humanoid Robot Platform, HUBO". In: *Adv. Robotics* **21**, 11 (2007), pp. 1305–22. doi: 10.1163/156855307781503781.

[141] Parker Hannifin Corp. *Frameless Motor & Gearmotors*. Port Washington, NY USA, 2007. url: `http://www.parkermotion.com/`.

[142] Perry, J. *Gait Analysis – Normal and Pathological Function*. 3rd ed. Slack, 1992. isbn: 1-55642-192-3.

[143] Peterka, R.J. "Sensorimotor Integration in Human Postural Control". In: *J. Neurophysiol.* **88**, 3 (2002), pp. 1097–1118. url: `http://jn.physiology.org/cgi/content/full/88/3/1097?ijkey=0a502c131800afcfadf15766c60f25289f11994a`.

[144] Pfeiffer, F. "The TUM walking machines". In: *Phil. Trans. R. Soc. A* **365** (2007), pp. 109–31. doi: `10.1098/rsta.2006.1922`.

[145] Pfeiffer, F. and Cruse, H., eds. *Autonomes Laufen*. (in German). Berlin, Heidelberg, New York: Springer, 2004. isbn: 3-540-25044-1.

[146] Pratt, D.J. "Mechanisms of shock attenuation via the lower extremity during running". In: *Clin. Biomech.* **4**, 1 (1989), pp. 51–7. doi: `10.1016/0268-0033(89)90068-5`.

[147] Pratt, J. and Krupp, B. "Design of a bipedal walking robot". In: *Proc. SPIE*. Vol. 6962. 2008. doi: `10.1117/12.777973`.

[148] Radcliffe, C.W. "Four-bar linkage prosthetic knee mechanisms: kinematics, alignment and prescription criteria". In: *Prosthet. Orthot. Int.* **18** (1994), pp. 159–73.

[149] Rautscher, G. "Modellierung und Simulation einer geregelten PM-Synchronmaschine mir Matlab/Simulink". (in German). Bachelor's thesis. Lehrstuhl für Angewandte Mechanik, TU München, 2004.

[150] Regele, R., Levi, P., and Bott, W. "ProRobot – Predicting the Future of Humanoid Robots". In: *RoboCup 2003: Robot Soccer World Cup VII*. Lecture Notes in Computer Science. Springer, 2004, pp. 366–73. doi: `10.1007/b98623`.

[151] Regenstein, K., Kerscher, T., Birkenhofer, C., Asfour, T., Zöllner, M., and Dillmann, R. "Universal Controller Module (UCoM) – component of a modular concept in robotic systems". In: *Proc. IEEE Int. Symposium Industrial Electronics (ISIE)*. 2007, pp. 2089–94. doi: `10.1109/ISIE.2007.4374930`.

[152] Rehbinder, H. and Ghosh, B.K. "Pose estimation using line-based dynamic vision and inertial sensors". In: *IEEE Trans. Automat. Contr.* **48**, 2 (2003), pp. 186–99. doi: `10.1109/TAC.2002.808464`.

[153] Resetov, D., Pietsch, B., and Gerth, W. "Aufbau des humanoiden Roboters BART III". In: *Autonome Mobile Systeme 2009*. Ed. by Dillmann, R., Beyerer, J., Stiller, C., Zöllner, M., and Gindele, T. (in German). Springer, 2009, pp. 209–16. isbn: 978-3-642-10283-7. url: `http://www.springer.com/computer/artificial/book/978-3-642-10283-7`.

[154] Rivin, E.I. *Mechanical Design of Robots*. McGraw-Hill, 1988. isbn: 0-07-052992-2.

[155] Rivin, E.I. *Stiffness and Damping in Mechanical Design*. Marcel Dekker, 1999. isbn: 0-8247-1722-8.

[156] RoboDrive GmbH. *Robodrive: Products*. available online: `http://www.robodrive.de/index.php`. Seefeld/Germany, Oct. 2008. url: `http://www.robodrive.de/`.

[157] Rome, K. "Mechanical properties of the heel pad: current theory and review of the literature". In: *Foot* **8**, 4 (1998), pp. 179–85. doi: `10.1016/S0958-2592(98)90026-8`.

[158] Rosheim, M.E. *Robot Wrist Actuators*. John Wiley & Sons, Inc., 1989. isbn: 0-471-61595-1.

[159] R+W Antriebselemente GmbH. *Miniatur-Metallbalgkupplungen: Modellreihe MK*. (in German). Klingenberg/Germany, 2007. url: `http://www.rw-kupplungen.de/`.

[160] R+W Antriebselemente GmbH. *Sicherheitskupplungen: Modellreihe SK*. (in German). Klingenberg/Germany, 2007. url: `http://www.rw-kupplungen.de/`.

[161] Sarker, M.O.F., Kim, C.H., Back, S., and You, B.-J. “An IEEE-1394 Based Real-time Robot Control System for Efficient Controlling of Humanoids”. In: *Proc. IEEE/RSJ Int. Conf. Intell. Robots Syst. (IROS)*. 2006, pp. 1416–21. doi: `10.1109/IROS.2006.281933`.

[162] Saunders, J.B., Inman, V.T., and Eberhart, H.D. “The major determinants in normal and pathological gait”. In: *J. Bone Joint Surg.* **35**, A (1953), pp. 543–58.

[163] Scheinman, V. and McCarthy, L.M. “Mechanisms and Actuation”. In: *Springer Handbook of Robotics*. Chap. 3, pp. 67–86.

[164] Schmidt, N. “Konstruktion des Fußes für einen humanoiden Roboter”. (in German). Term project. Lehrstuhl für Angewandte Mechanik, TU München, 2006.

[165] Schröder, D. *Elektrische Antriebe – Grundlagen*. 3rd ed. (in German). Berlin, Heidelberg, New York: Springer, 2007. isbn: 978-3-540-72764-4.

[166] Schröder, D. *Elektrische Antriebe – Regelung von Antriebssystemen*. 2nd ed. (in German). Berlin, Heidelberg, New York: Springer, 2001. isbn: 3-540-41994-2.

[167] Schwienbacher, M. “Entwicklung eines Kraft-Momentensensors für einen Humanoiden Roboter”. (in German). Diploma thesis. Lehrstuhl für Angewandte Mechanik, TU München, 2007.

[168] Schwienbacher, M. “Entwicklung und Konstruktion des Beckens für einen humanoiden Roboter mit Hilfe der Topologieoptimierung”. (in German). Term project. Lehrstuhl für Angewandte Mechanik, TU München, 2006.

[169] Seara, J.F., Schmidt, G., and Lorch, O. “ViGWaM Active Vision System – Gaze Control for Goal-Oriented Walking”. In: *Proc. Int. Conf. Climbing and Walking Robots (CLAWAR)*. 2001, pp. 265–72.

[170] Sellaouti, R., Stasse, O., Kajita, S., Yokoi, K., and Kheddar, A. “Faster and Smoother Walking of Humanoid HRP-2 with Passive Toe Joints”. In: *Proc. IEEE/RSJ Int. Conf. Intell. Robots Syst. (IROS)*. 2006, pp. 4909–14. doi: `10.1109/IROS.2006.282449`.

[171] Shimano, B. and Roth, B. “On force sensing information and its use in controlling manipulators”. In: *Proc. IFAC Int. Symp. Information-Control Problems*. 1977, pp. 119–26.

[172] Siciliano, B. and Khatib, O., eds. *Springer Handbook of Robotics*. Berlin, Heidelberg, New York: Springer, 2008. isbn: 978-3-540-23957-4.

[173] SKF Linearsysteme GmbH. *Ball screws*. Product catalog. Schweinfurt/Germany, June 2008. url: `http://www.linearmotion.skf.com/`.

[174] Slatter, R., ed. *Leichtbau in der Antriebstechnik*. (in German). Aachen: Shaker, 2004. isbn: 3-8322-2805-5.

[175] Sodeyama, Y., Nishino, T., Namiki, Y., Nakanishi, Y., Mizuuchi, I., and Inaba, M. “The designs and motions of a shoulder structure with a spherical thorax, scapulas and collarbones for humanoid ‘Kojiro’”. In: *Proc. IEEE/RSJ Int. Conf. Intell. Robots Syst. (IROS)*. 2008, pp. 1465–70. doi: `10.1109/IROS.2008.4651221`.

[176] Sugahara, Y., Hashimoto, K., Sunazuka, H., Kawase, M., Ohta, A., Tanaka, C., Lim, H.-o., and Takanishi, A. “WL-16RII: Prototype of Biped Walking Wheelchair”. In: *Proc. CISM-IFToMM Symposium on Robot Design, Dynamics, and Control (RoManSy)*. 2006, pp. 313–20.

[177] Taghirad, H.D. and Bélanger, P.R. “Modeling and parameter identification of harmonic drive systems”. In: *J. Dyn. Sys., Meas., Control* **120**, 4 (1998), pp. 439–44. doi: `10.1115/1.2801484`.

[178] Tajima, R., Honda, D., and Suga, K. “Fast Running Experiments Involving a Humanoid Robot”. In: *Proc. IEEE Int. Conf. Robot. Autom. (ICRA)*. 2009, pp. 1571–6.

[179] Takahashi, M., Nishiwaki, K., Kagami, S., and Mizoguchi, H. “Development and Evaluation of An Attitude Measuring System that uses Acceleration Information of Walking for Biped Robots”. In: *Proc. IEEE Conf. on Sensors (Sensors)*. 2007, pp. 292–5. doi: `10.1109/ICSENS.2007.4388394`.

[180] Takao, S., Ohta, H., Yokokohji, Y., and Yoshikawa, T. “Function analysis of human-like mechanical foot, using mechanically constrained shoes”. In: *Proc. IEEE/RSJ Int. Conf. Intell. Robots Syst. (IROS)*. 2004, pp. 3847–52. doi: `10.1109/IROS.2004.1390014`.

[181] Takenaka, T., Gomi, H., Hamaya, K., Akimoto, K., Shirokura, S., Asatani, M., and Tanaka, K. “Leg Joint Assist Device of Legged Mobile Robot”. Pat. EP 1 820 612 (A1). Honda Motor Co., Ltd. Aug. 22, 2007.

[182] Takenaka, T., Gomi, H., S., Shigemi, and Matsumoto, T. “Leg-type Moving Robot and Floor Reaction Force Detection Device Therefor”. Pat. EP 1 475 193 (A1). Honda Motor Co., Ltd. Nov. 10, 2004.

[183] Takenaka, T., Matsumoto, K., Gomi, H., and Hamaya, K. “Leg Type Moving Robot”. Pat. EP 1 702 725 (A1). Honda Motor Co., Ltd. Sept. 20, 2006.

[184] Takenaka, T., Matsumoto, K., Gomi, H., and Hamaya, K. “Legged Mobile Robot”. Pat. EP 1 785 235 (A1). Honda Motor Co., Ltd. May 16, 2007.

[185] Takenaka, T., Matsumoto, T., Yoshiike, T., and Shirokura, S. “Real time motion generation and control for biped robot —2nd report: Running gait pattern generation—”. In: *Proc. IEEE/RSJ Int. Conf. Intell. Robots Syst. (IROS)*. 2009, pp. 1092–9. doi: `10.1109/IROS.2009.5354654`.

[186] Tellez, R., Ferro, F., Garcia, S., Gomez, E., Mora, J.D., Pinyol, D., Poyatos, J., Torres, O., Velazquez, J., and Faconti, D. “Reem-B: an Autonomous Lightweight Human-size Humanoid Robot”. In: *Proc. IEEE-RAS Int. Conf. Humanoid Robot. (Humanoids)*. 2008, pp. 462–8. doi: `10.1109/ICHR.2008.4755995`.

[187] Tränkler, H.-R. *Sensortechnik. Handbuch für Praxis und Wissenschaft*. Ed. by Obermeier, E. Springer, 1998. isbn: 978-3-540-58640-1.

[188] Tsagarakis, N.G., Metta, G., Sandini, G., Vernon, D., et al. “iCub: The Design and Realization of an Open Humanoid Platform for Cognitive and Neuroscience Research”. In: *Adv. Robotics* **21**, 10 (2007), pp. 1151–75. doi: `10.1163/156855307781389419`.

[189] Uchiyama, M., Bayo, E., and Palma-Villalon, E. “A Systematic Design Procedure to Minimize a Performance Index for Robot Force Sensors”. In: *J. Dyn. Sys., Meas., Control* **113**, 3 (1991), pp. 388–94. doi: `10.1115/1.2896422`.

[190] Umberger, B.R. “Effects of suppressing arm swing on kinematics, kinetics, and energetics of human walking”. In: *J. Biomech.* **41**, 11 (2008), pp. 2575–80. doi: `10.1016/j.jbiomech.2008.05.024`.

[191] Vanderborght, B., Verrelst, B., Ham, R. van, Damme, M. van, Lefeber, D., Meira Y Duran, B., and P., Beyl. “Exploiting Natural Dynamics to Reduce Energy Consumption by Controlling the Compliance of Soft Actuators”. In: *Int. J. Robot. Res.* **25**, 4 (2006), pp. 343–58. doi: `10.1177/0278364906064566`.

[192] VDI 2206. *Design methodology for mechatronic systems*. June 2004.

[193] VDI 2209. *3D-product modeling*. June 2006.

[194] Vishay Micro-Measurements, Inc. *Fatigue Characteristics of Vishay Micro-Measurements Strain Gages*. Tech Note. Malvern, PA (USA), 2007. url: `http://www.vishay.com/doc?11058`.

[195] Voyles, R., Morrow, J., and Khosla, P. “The Shape from Motion Approach to Rapid and Precise Force/Torque Sensor Calibration”. In: *J. Dyn. Sys., Meas., Control* **119**, 2 (1997), pp. 229–35. doi: `10.1115/1.2801238`.

[196] Vucobratović, J. and Borovac, B. “Zero-Moment Point – Thirty Five Years Of Its Life”. In: *Int. J. Humanoid Robot.* **1**, 1 (2004), pp. 157–73. doi: 10.1142/S0219843604000083.

[197] Vukosavić, S.N. and Stojić, M.R. “Suppression of torsional oscillations in a high-performance speed servo drive”. In: *IEEE Trans. Ind. Electron.* **45**, 1 (1998), pp. 108–17. doi: 10.1109/41.661311.

[198] Watson, P.C. and Drake, S.H. “Pedestal and wrist force sensors for automatic assembly”. In: *Proc. Int. Symp. Industrial Robots*. 1975, pp. 501–11.

[199] Whittle, M.W. “Generation and attenuation of transient impulsive forces beneath the foot: a review”. In: *Gait Posture* **10**, 3 (1999), pp. 264–75. doi: 10.1016/S0966-6362(99)00041-7.

[200] Whittle, M.W. and Levine, D. “Three-dimensional relationships between the movements of the pelvis and lumbar spine during normal gait”. In: *Hum. Mov. Sci.* **18**, 5 (1999), pp. 681–92. doi: 10.1016/S0167-9457(99)00032-9.

[201] Wisse, M., Schwab, L., and Van der Helm, F.L.T. “Passive walking dynamic model with upper body”. In: *Robotica* **22**, 6 (2004), pp. 681–8. doi: 10.1017/S0263574704000475.

[202] Wittenstein cyber motor GmbH. *Full-line catalog*. Igersheim/Germany, 2003. url: http://www.wittenstein-cyber-motor.de/.

[203] Wright, D.G., Desai, S.M., and Henderson, W.H. “Action of the subtalar and ankle-joint complex during the stance phase of walking”. In: *J. Bone Joint Surg. Am.* **46**, A (1964), pp. 361–82.

[204] Yamaguchi, J., Soga, E., Inoue, S., and Takanishi, A. “Development of a Bipedal Humanoid Robot–Control Method of Whole Body Cooperative Dynamic Biped Walking”. In: *Proc. IEEE Int. Conf. Robot. Autom. (ICRA)*. 1999, pp. 368–74. doi: 10.1109/ROBOT.1999.770006.

[205] Yamaguchi, J., Takanishi, A., and Kato, I. “Experimental Development of a Foot Mechanism with Shock Absorbing Material for Acquisition of Landing Surface Position Information and Stabilization of Dynamic Biped Walking”. In: *Proc. IEEE Int. Conf. Robot. Autom. (ICRA)*. 1995, pp. 2892–9. doi: 10.1109/ROBOT.1995.525694.

[206] Yamamoto, K., Sugihara, T., and Nakamura, Y. “Toe Joint Mechanism Using Parallel Four-bar Linkage Enabling Humanlike Multiple Support at Toe Pad and Toe Tip”. In: *Proc. IEEE-RAS Int. Conf. Humanoid Robot. (Humanoids)*. 2007.

[207] Yamazaki, Y., Kobayashi, N., and Koshiishi, T. “Head Support Structure of Humanoid Robot”. Pat. JP 2006-167 832 (A) (Japanese). Honda Motor Co., Ltd. June 29, 2006.

[208] Yoon, J., Nandha, H., Lee, D., and Kim, G. “A Novel 4-DOF Robotic Foot Mechanism with Multi-platforms for Humanoid Robot (SICE-ICCAS 2006)”. In: *Proc. Int. Joint Conf. SICE-ICCAS*. 2006, pp. 3500–4. doi: 10.1109/SICE.2006.314621.

[209] Zhang, G. and Furusho, J. “Speed control of two-inertia system by PI/PID control”. In: *IEEE Trans. Ind. Electron.* **47**, 3 (2000), pp. 603–9. doi: 10.1109/41.847901.